Karlsruhe Institute of Technology

In-Depth Analysis of the Micro-Bunching Characteristics in Single and Multi-Bunch Operation at KARA

Zur Erlangung des akademischen Grades eines
DOKTORS DER NATURWISSENSCHAFTEN (Dr. rer. nat.)

von der KIT-Fakultät für Physik des
Karlsruher Instituts für Technologie (KIT)
genehmigte

DISSERTATION
von

M.Sc. Miriam Brosi
aus Malsch

Tag der mündlichen Prüfung:	31.01.2020
Referentin:	Prof. Dr. Anke-Susanne Müller
Korreferent:	Prof. Dr. Marc Weber

Contents

1 Introduction

In recent times synchrotron radiation plays an ever increasing role in many areas of state-of-the-art research. Synchrotron radiation is utilized for microscopy, spectroscopy, and for time-resolved experiments as a versatile tool in a multitude of fields such as solid-state physics, geology, material science as well as biology, pharmacy, and medicine. In order to fulfill the growing demands of such experiments, new synchrotron light sources consisting of electron accelerators are being build providing increasingly higher brilliance. The higher brilliance is achieved by increasing the photon flux and reducing the transverse emittance of the electron beam down to where diffraction limits a further reduction of the source point of the photon beam. Longitudinal coherence can be achieved by longitudinal compression of the electron bunch to shorten the photon pulses. A further effect caused by short electron bunches, is the emission of coherent synchrotron radiation (CSR) at wavelengths larger than the emitting electron structures. Compared to incoherent synchrotron radiation, coherent synchrotron radiation exhibits a beneficial power amplification by the number of emitting electrons. For realistic short bunch lengths of the order of sub-mm at circular light sources, CSR is emitted at frequencies up to the THz range. This amplification in the emitted power has proven to be beneficial for certain applications of THz radiation such as imaging techniques for various materials without the ionizing side effects of X-ray radiation.

Under certain circumstances the emitted CSR interacts with the emitting structure resulting in complex dynamics and fluctuations in the emitted power. This manifests itself in a nondestructive instability which complicates the usage of the THz radiation and causes fluctuations of the transverse bunch dimensions, interfering with the stable operation of the light source. The instability is called micro-bunching instability and was observed at several electron storage rings, among others at Advanced Light Source [1], BESSY II [2], DIAMOND [3], MAX-I [4], MLS [5], NSLS VUV Ring [6], Stanford linear collider damping ring [7], SOLEIL [8], and SURF III [9]. Theoretical descriptions and models were discussed, for example, in [7; 10; 11; 12; 13].

To operate with and around this instability, a deep understanding thereof is necessary. Even though the instability was simulated and observed, a full understanding of the complex

dynamics as well as of all the possible influences and contributions is still missing. As the operation of KARA, the KArlsruhe Research Accelerator, is highly flexible, many parameters (like energy, acceleration voltage, momentum compaction factor, bunch length, filling pattern, ...) can be varied within a wide range. This thesis exploits this fact in order to systematically study the dependencies of the micro-bunching instability on these different machine parameters as well as on special conditions like short bunch lengths combined with low bunch currents and even multi-bunch operation. The comparison of the comprehensive measurement results with simulations shows the strength as well as the shortcomings of the used model. This is a big step towards the longterm-goal of having a complete as possible understanding and model of all contributing impedances and parameters, which finally would allow to influence and control the instability in order to suppress it if needed or increase the usability of the emitted CSR.

This thesis starts with a short introduction into accelerator physics with a focus on the longitudinal beam dynamics in Chapter 2. Furthermore, it is described how the CSR impedance can be combined with the Vlasov-Fokker-Planck equation to simulate the dynamics in the longitudinal phase space. The resulting micro-bunching instability is introduced based on the empirical understanding developed, in a way that it will serve as underlying working model for this thesis. Additionally, an existing prediction for the threshold current of the instability is introduced.

In Chapter 3, a brief overview of KARA, its short-bunch operation mode and some key components is given, including the performed calibration for the acceleration voltage. The used diagnostics infrastructure present at KARA is described in Chapter 4 with focus on the filling pattern measurement used for the determination of the bunch currents. The systematic measurement artifacts caused by the dead time of the time-correlated single photon counting set-up are discussed as well as the correction scheme implemented within the scope of this thesis and the limitations thereof. The main parameter the measurements in the thesis rely on are the changes in the emitted coherent synchrotron radiation power in the THz frequency range. To record the CSR power emitted by each bunch at every turn simultaneously, the dedicated data acquisition system KAPTURE was developed further and improved in a KIT-internal cooperation, resulting in the new version KAPTURE-2. KAPTURE, the fast THz detectors, and other components of the THz diagnostics are described in Chapter 5. The bunch-by-bunch detection capability of KAPTURE allowed the development of a faster measurement method to study the current dependency of the instability. Chapter 6 explains how using the information of all bunches in a multi-bunch fill can reduced the measurement time of such a snapshot measurement down to one second compared to typically one up to several hours for a decay measurement. Furthermore,

it is discussed how the bunch current is interpolated at the time of each individual THz measurement followed by a description how the three characteristic features used to study the bursting behavior are determined from the resulting data.

At the beginning of Chapter 7, the observed behavior of a bunch subject to the micro-bunching instability is described and its dependencies on the machine parameters the momentum compaction factor and the acceleration voltage is systematically mapped. The results are discussed and compared with the expectations based on the working model as well as simulation results by Vlasov-Fokker-Planck solvers. To study the influence of the longitudinal damping time on the instability, a prototype of a CLIC damping ring wiggler was used. With the prototype installed in KARA it is possible to increase the synchrotron radiation loss of the particles and therefore reduce the longitudinal damping time.

Afterwards in Chapter 8, it is investigated how the detected frequency range of the CSR emission affects the observed behavior under the instability, which provides insight into the changes in the emitted CSR spectrum. Additionally, it is shown that by measuring the longitudinal and horizontal bunch profile synchronously to the emitted CSR power even further insight can be gained.

In Chapter 9, the additional region of the instability predicted for short bunch length and bunch currents below the micro-bunching instability threshold is observed. The expected dependence of this second instability on the product of the synchrotron frequency and the longitudinal damping time is evaluated and confirmed. Afterwards, systematic measurements of the limits of this instability are compared in detail with simulations based on the description of the micro-bunching instability via the simplified parallel plates model of the CSR impedance and possible explanations for the observed differences are stated.

After studying the instability through the behavior of a single bunch, the instability is studied in a multi-bunch environment in Chapter 10. First, it is shown that the overall behavior reflects the behavior observed in single-bunches in the previous chapters. Then, precision measurements are conducted to reveal small changes caused by the presence of the other bunches in the multi-bunch environment. The observed differences in the threshold current, the bursting frequency, and the low bursting frequency of the individual bunches are used for an in-depth analysis of the influence the multi-bunch environment has on the behavior of the micro-bunching instability.

The thesis is concluded in Chapter 11 by a summary and an outlook on various aspects of the results.

2 Fundamentals of Accelerator Physics and the Micro-Bunching Instability

In the first part of this chapter, the accelerator physics of synchrotrons and storage rings will be reviewed with focus on the longitudinal beam dynamics including a description of synchrotron radiation and its properties. Next, the concept of impedances and wake fields is introduced and several examples including two simple models for the coherent synchrotron radiation (CSR) impedance are presented. Furthermore, the chapter describes the Vlasov-Fokker-Planck equation, which allows for calculations of the dynamics under the influence of e.g. the CSR impedance, as well as simulation tools incorporating this principle. Based on this, the micro-bunching instability resulting from the interaction of a bunch with the CSR impedance is introduced.

2.1 Motion of Charged Particles in Electromagnetic Fields

The motion of charged particles in electromagnetic fields is described by the Lorentz force [14]:

$$\vec{F} = q(\vec{E} + \vec{v} \times \vec{B})$$

For the acceleration of a charged particle the energy gain is given by:

$$\Delta E = \int_{\vec{r_1}}^{\vec{r_2}} \vec{F}_{Lorentz} \cdot \mathrm{d}\vec{r} = q \cdot \int_{\vec{r_1}}^{\vec{r_2}} \left(\vec{v} \times \vec{B} + \vec{E}\right) \cdot \mathrm{d}\vec{r}$$

With $\mathrm{d}\vec{r} = \vec{v} \cdot \mathrm{d}t$ this leads to:

$$\Delta E = e \cdot \int_{\vec{r_1}}^{\vec{r_2}} \vec{E} \cdot \mathrm{d}\vec{r} = e \cdot U$$

Only the electrical part of the field contributes to the energy gain while the magnetic fields leads to a deflection of the charged particles perpendicular to their direction of motion and the magnetic field component. The resulting circular motion in a constant magnetic field is given by the balance of the centripetal force and the perpendicular part of the Lorentz

force:

$$\frac{mv^2}{R} = qvB \tag{2.1}$$

The deflection radius R is then given by $R = \frac{p}{qB} \overset{v \to c}{\to} \frac{E}{qcB}$, for highly relativistic particles. It is common to use electrical fields for acceleration and magnetic fields for deflection and guiding of the particle beam in accelerators. Due to this separation, the two parts can be described separately to good approximation.

The first accelerators were based on electrostatic fields for acceleration. The upper limit of the achievable electrostatic potential of several megavolt has led to the usage of alternating electromagnetic fields instead. The used sinusoidal alternating voltage can be described by $V(t) = V_0 \cdot \sin \omega t$. To avoid exposure of the particles to the decelerating part of the alternating voltage, they are only exposed to the field at a fixed phase Ψ_s. The overall energy gain after i passages through the accelerating voltage is given by

$$E_i = i \cdot q \cdot V_0 \cdot \sin \Psi_\mathrm{s} \tag{2.2}$$

This could be the passage through the i-th accelerating structure in a linear accelerator (short: linac) or the i-th passage of the same structure in a circular accelerator.

2.2 Synchrotrons and Storage Rings

The radius of circular accelerators increased in the past decades due to the increasing particle energy and the strength in magnetic field limited by the magnetic saturation of non-superconducting magnets. To avoid gigantic magnets the radius is kept fixed while accelerating the particles. For that the magnetic field used for guidance has to grow synchronously with the increase in energy $R = \frac{E}{qcB}$, when assuming near speed of light velocities and following Equation 2.1. This has led to the name synchrotron.

Storage rings on the other hand store particles at a constant energy. Often synchrotrons are operated as pre-accelerators for pure storage rings, with the pre-accelerator providing the particles a the end energy (full energy injector). Some of these machines can be operated in top-up operation, where regularly particles are injected from the pre-accelerator into the storage ring to keep the number of stored particles constant. Other machines can operate as both a synchrotron and a storage ring. They are called ramping machines and operate as synchrotron to accelerate the particles and then store them with a constant magnetic field at different end energies.

In these circular machines, the magnets are normally placed with gaps in-between leading

to a polygon instead of a perfect circle. The resulting straight sections can then be used for the accelerating structures, insertion devices or different diagnostics.

To allow the usage of alternating electromagnetic fields for acceleration the accelerating cavities are resonators at a specific radio frequency (RF) f_{RF}. The particle beam is not continuous but bunched in packages (referred to as bunches) as the particles experience the necessary acceleration only at a certain phase Ψ_{s}. The relation between the frequency of the acceleration voltage f_{RF} and the revolution frequency $f_{\mathrm{rev}} = \frac{C}{v}$ (with circumference C) gives the maximal number of particle bunches in a machine, called harmonic number

$$h = \frac{f_{\mathrm{RF}}}{f_{\mathrm{rev}}} \tag{2.3}$$

This directly demands that the parameters are chosen in such a way that h is an integer.

The number of accelerated particles is connected to the beam current I via the revolution time T of the particles in a circular accelerator:

$$I = \frac{Q}{T} = \frac{qvN}{C} \tag{2.4}$$

with the circumference C, the number of particles N, their charge q, and their velocity v. Analogously, the number of particles per bunch is connected to the bunch current I_{b}.

The position of a particle will be given relative to a reference particle (referred to as synchronous particle) on the ideal trajectory $\vec{s}(t)$ with the ideal momentum p_0. The relative coordinates per particle are given as Cartesian coordinates (x, y, z). While z is the distance to the synchronous particle for each point in time tangential to the ideal orbit, x and y are the relative transverse positions. Including the momentum, the coordinates of a particle are given at a time t as $\vec{x}\,(t) = (x, x\prime, y, y', z, z', t)^{\intercal}$, with $x' \approx \frac{\mathrm{d}x}{dz}$ and $y' \approx \frac{\mathrm{d}y}{dz}$ being the momentum, written as divergence of the beam.

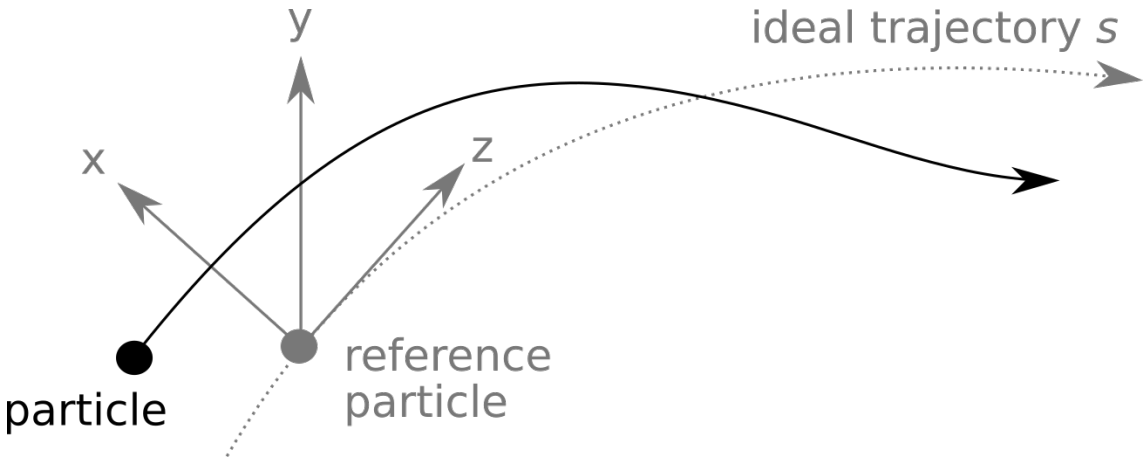

Figure 2.1: The position of each particle is given in Cartesian coordinates (x, y, z) relative to the reference particle (synchronous particle) moving on the ideal trajectory $\vec{s}(t)$.

2.3 Transverse Beam Dynamics

The transverse divergence of the particle beam can be controlled and partially circumvented through correctly chosen magnetic fields. Following Equation 2.1 and employing a Taylor expansion around the ideal orbit ($x = 0$) gives:

$$\begin{aligned}\frac{q}{p}B_y(x) &= \frac{q}{p}B_y(0) + \frac{q}{p}\frac{dB_y(x)}{dx}x + \frac{1}{2!}\frac{q}{p}\frac{d^2B_y(x)}{dx^2}x^2 + \dots \\ &= \underbrace{\frac{1}{R}}_{\text{Dipole}} + \underbrace{k \cdot x}_{\text{Quadrupole}} + \underbrace{\frac{1}{2}m \cdot x^2}_{\text{Sextupole}} + \dots\end{aligned}$$

The different orders represent the different poles used in the magnet optics. The dipole fields are constant in the horizontal direction and are used to deflect the particles on the close circular orbit. This gives them the name bending magnets (with the bending radius R) and causes them to be the main source of synchrotron radiation. Synchrotron radiation with a higher intensity and a partly adjustable spectrum can be generated with so called insertion devices. An example will be discussed shortly in Section 3.5.

The next order in the expansion depends linearly on the horizontal position and therefore corresponds to a quadrupole magnet with the strength $k = \frac{q}{p}\frac{dB_y(x)}{dx}$. Due to the position-dependent strength, the particles will experience a force towards the center and, in this way, will be focused. So quadrupoles are used like focal lenses to collimate the beam. But opposite to normal optical focusing lenses, quadrupoles only ever focus in one of the

two transverse planes while defocusing in the other. So multiple and differently oriented quadrupoles are necessary for an overall net focusing effect.

Using only the two types of magnet optic components (dipoles and quadrupoles) is enough to roughly hold together and guide the particle beam. This is often used as approximation in simulations of the particle trajectories, as it simplifies the calculations, as the traverse planes are not coupled in this first order description. Nevertheless, most storage rings use at least the next order, the sextupole magnets. Their strength is defined as $m = \frac{1}{2!}\frac{q}{p}\frac{d^2 B_y(x)}{dx^2}$ and they can correct field errors in the dipole and quadrupole magnets as well as chromatic errors. Chromatic errors can be described analogously to color aberration in optics, as energy-dependent focusing of the particles. Some storage rings additionally use higher orders magnets for an even better control of the particle motion and distribution.

Using the approximation of the linear optic, the motion of the particles in the transverse planes are determined by Hill's differential equations [15]:

$$x''(s) + \left(\frac{1}{R^2(s)} - k(s)\right) \cdot x(s) = \frac{1}{R(s)} \cdot \frac{\Delta p}{p_0} \tag{2.5}$$

$$y''(s) + k(s) \cdot y(s) = 0 \tag{2.6}$$

While the vertical particle position $y(s)$ only depends on the quadrupole strength $k(s)$ at the position s around the ring, the horizontal position $x(s)$ also depends on the bending radius of the dipole magnets and therefore on the particle momentum (relative momentum deviation $\frac{\Delta p}{p_0}$ from the ideal momentum p_0).

Following [16], the assumption $\frac{\Delta p}{p_0} = 0$ results in a solution for both planes $u = (x, y)$:

$$u(s) = \sqrt{\varepsilon \beta(s)} \cdot \cos\left(\Psi_u(s) + \Phi\right)$$

with the beta function $\beta(s)$, the emittance $\varepsilon$and the phase $\Psi_u(s)$ of the oscillation at the position s around the ring. The motion described by this solution are oscillations in each of the respective planes, which are referred to as betatron oscillations. As long as there is no coupling between the planes they can be viewed separately. The particles move along an ellipse in the phase space (u, u') of both planes $u = (x, y)$. Following Liouville's theorem [17], the area $F = \pi\varepsilon$ enclosed by each ellipse as a function of the position s in the ring is constant if only conservative forces act on the particles. As this is not true for the longitudinal plane due to the emitted synchrotron radiation and the acceleration, this plane will be treated separately in Section 2.5. The amplitude of the betatron oscillation is given by the emittance ε and the beta function $\beta(s)$, which is the reciprocal change

of the phase $\Psi_u(s)$ at the position s around the ring. $\int_{s_1}^{s_2} \frac{1}{\beta(s)} \mathrm{d}s$ therefore is the phase advance on the way from position s_1 to position s_2. This phase advance (in units of 2π) per revolution is referred to as tune Q_u:

$$Q_u = \frac{f_{\text{Betatron, } u}}{f_{rev}} = \frac{1}{2\pi} \oint \frac{\mathrm{d}s}{\beta_u(s)}$$

The working point (Q_x, Q_y) of an accelerator is given by the horizontal and vertical tune.

As normally $\frac{\Delta p}{p_0} \neq 0$, the horizontal equation of motion Equation 2.5 has to be solved as an inhomogeneous differential equation. With the dispersion $D(s)$ defined as the horizontal deposition $x(s)$ relative to the momentum deviation $\frac{\Delta p}{p_0}$:

$$D(s) = \frac{x(s)}{\frac{\Delta p}{p_0}}$$

the specific solution is given by:

$$\begin{aligned} x(s) &= x_{p=p_0}(s) + D(s) \cdot \frac{\Delta p}{p_0} \\ &= \sqrt{\varepsilon \beta(s)} \cdot \cos\left(\Psi_u(s) + \Phi\right) + D(s) \cdot \frac{\Delta p}{p_0} \end{aligned}$$

The dispersion orbit $\left(\frac{\Delta p}{p_0} = 1\right)$ can be calculated from Equation 2.5 for $k = 0$, as the highly relativistic particles only move differently in the dipole magnets and not in the quadrupole magnets. The resulting equation

$$D''(s) + \frac{1}{R^2} \cdot D(s) = \frac{1}{R}$$

has the solutions

$$\begin{aligned} D(s) &= D_0 \cos\frac{s}{R} + D_0' R \sin\frac{s}{R} + R\left(1 - \cos\frac{s}{R}\right) \\ D'(s) &= -\frac{D_0}{R}\sin\frac{s}{R} + D_0' \cos\frac{s}{R} + \sin\frac{s}{R} \end{aligned}$$

In Equation 2.14, it will be covered later that the length of the dispersion orbit is not necessarily linear with the momentum deviation.

While the quadrupole strength should only depend on the position of the particle, there can be effects similar to chromatic aberrations of focusing lenses in optics. This leads to slightly different focusing of particles with deviating momentum and therefore to a small change in the tunes. The relative tune change as a function of the relative momentum

deviation is referred to as chromaticity ξ

$$\begin{aligned}\xi &:= \frac{\Delta Q}{\frac{\Delta p}{p}} \\ &= -\frac{1}{4\pi}\oint k(s)\,\beta(s)\,ds\end{aligned}$$

The natural chromaticity (without correction) has usually a negative value. Sextupole magnets are used to change the chromaticity to small positive values [16].

2.4 Synchrotron Radiation

Charged particles emit electromagnetic radiation when their momentum is changed. If the change of momentum occurs due to an acceleration in the transverse direction of motion, the resulting radiation is called synchrotron radiation, as this kind of radiation was first observed at a synchrotron. The power emitted during the circular motion of highly relativistic particles due to their deflection in the dipole magnets is given by [16]:

$$P_\mathrm{s} = \frac{q^2 c}{6\pi\varepsilon_0}\frac{1}{\left(m_0c^2\right)^4}\frac{E^4}{R^2}$$

For non-relativistic particles their total energy is close to their rest energy m_0c^2 so the emitted power is negligible.

The energy loss of a particle per revolution results from $U_0 = \oint P_\mathrm{s}\mathrm{d}t$ with Sand's radiation constant (for electrons) $C_\gamma = \frac{4\pi}{3}\frac{r_c}{(m_ec^2)^3} = 8.8575\cdot 10^{-5}\,\mathrm{m/GeV^3}$:

$$U_0 = \frac{q^2E^4}{3\cdot\varepsilon_0\left(m_0c^2\right)^4}\oint\frac{ds}{R(s)^2} = \frac{C_\gamma E^4}{2\pi}\oint\frac{ds}{R(s)^2} = \frac{C_\gamma}{R}E^4 \tag{2.7}$$

The particles regain the lost energy in the cavities. If the energy loss needs to be minimal, like in colliders, the bending radius R can be increased, leading to huge machines like LEP. For heavy particles like protons, used in hadron colliders like LHC, the energy loss is smaller at the same particle energy than for electrons. Opposed to colliders, accelerators dedicated to the production of synchrotron radiation, referred to as light-sources, use light particles, mostly electrons.

The opening angle Θ of the tangentially emitted synchrotrons radiation is $\tan\Theta \approx \frac{1}{\gamma}$ which

simplifies for highly relativistic particles to :

$$\Theta \approx \frac{1}{\gamma} \tag{2.8}$$

As an example, electrons with an energy of 2.5 GeV emit with an opening angle of 0.2 mrad $\approx 0.01°$. This typically extremely narrow emission cone leads to a broad spectrum of emitted frequencies $P(\omega)$.

The equation for the spectral distribution is described nicely in [18]:

$$P(\omega) = \frac{P_\mathrm{s}}{\omega_\mathrm{c}} S\left(\frac{\omega}{\omega_\mathrm{c}}\right)$$

with $\omega = 2\pi f$ and the critical frequency ω_c defined as

$$\omega_\mathrm{c} = \frac{3}{2}\frac{c\gamma^3}{R}$$

and the normalized function S

$$S(\xi) = \frac{9\sqrt{3}}{8\pi}\xi \int_\xi^\infty K_{5/3}\left(\hat{\xi}\right) \mathrm{d}\hat{\xi}$$

where $K_{5/3}$ is a modified Bessel function [18]. Figure 2.2 shows the spectrum emitted by a single electron calculated for an energy of 1.3 GeV and a bending radius of 5.559 m (which corresponds to the bending radius of the KIT light source).

The emitted power does not only depend on the number of particles N, but also on their spatial distribution. The power emitted at wavelengths larger than the emitting structure (here the length of the particle bunch) is coherently amplified. The resulting spectrum is given by [15]:

$$\begin{aligned} P(f) &= N\left[1 + (N-1)F(f)\right] \cdot P_\mathrm{s}(f) \\ &= N \cdot P_\mathrm{s}(f) + N(N-1)F(f) \cdot P_\mathrm{s}(f) \\ &= P_\mathrm{ISR}(f) + P_\mathrm{CSR}(f) \end{aligned} \tag{2.9}$$

with the form-factor $F(f)$ being the absolute square of the Fourier transform of the normalized longitudinal charge distribution $\varrho(t)$[1]: $F(f) = \left|\int_{-\infty}^{\infty} \varrho(t) \cdot \mathrm{e}^{-i2\pi f t} \mathrm{d}t\right|^2$

P_ISR scales linearly with the number of particles and corresponds to the power of the

[1] $\varrho(t) = \frac{\rho(t)}{eN}$ with the longitudinal charge distribution $\rho(t)$, the number of electrons N and the elementary charge e

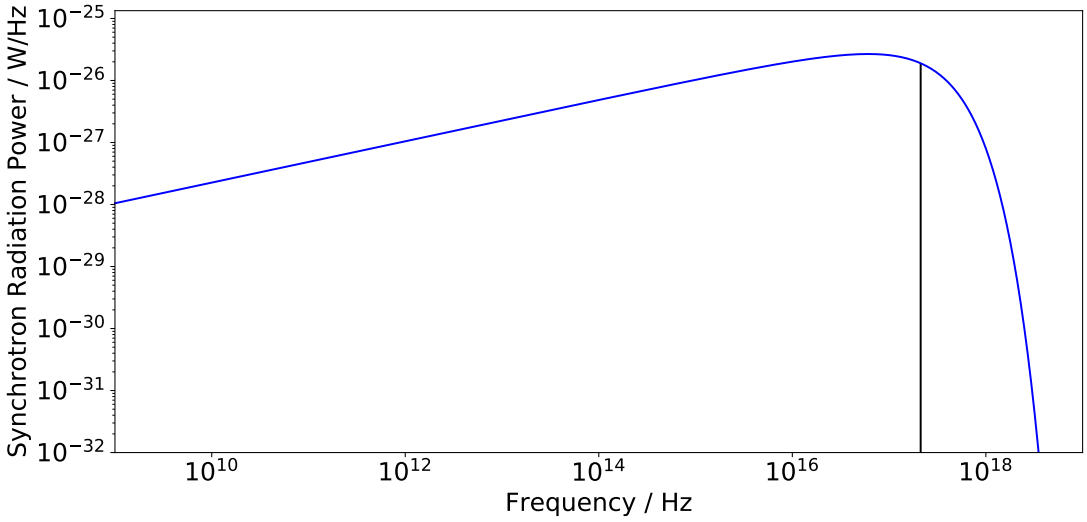

Figure 2.2: Emitted incoherent synchrotron radiation power as a function of frequency for a single electron at 1.3 GeV and a bending radius of 5.559 m. The critical frequency is displayed as vertical line at $f_\mathrm{c} = \omega_\mathrm{c} / (2\pi)$.

incoherent synchrotron radiation. Meanwhile, $P_\mathrm{CSR}(f)$ corresponds to the coherently emitted synchrotron radiation (CSR) power and depends on the square of the number of particles as well as on the form-factor of the particle bunch and therefore the longitudinal charge distribution.

For a Gaussian charge distribution the form-factor is also a Gaussian $F(f) = e^{-(\sigma_z 2\pi f/c)^2}$ with σ_z being the RMS bunch length. This directly shows that for wavelengths shorter than the bunch length ($\lambda = c/f \ll \sigma_z$) the form-factor becomes small and Equation 2.9 is reduced to the incoherent radiation power.

2.5 Longitudinal Beam Dynamics

As for the transverse plane, the longitudinal dynamics depend on the momentum of each particle. A highly relativistic particle with the ideal energy moving on the ideal orbit gains in the cavity exactly the power it has lost due to synchrotron radiation. The phase at which it passes the acceleration field is called the synchronous phase Ψ_s and derived from that this ideal particle is called the synchronous particle with the momentum p_0. Particles with a slightly deviating momentum sample a different phase of the acceleration voltage. Due to Equation 2.1 particles with a lower momentum, than the synchronous particle, are deflected stronger in the bending magnets and therefore take a shorter time for a revolution

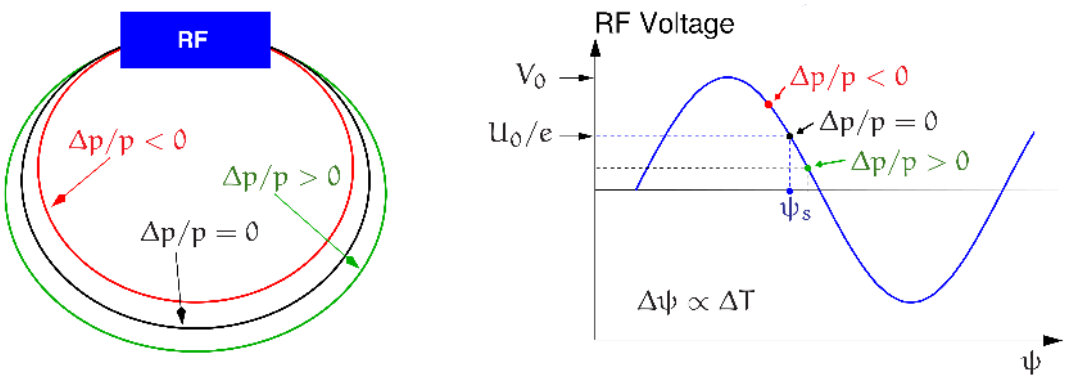

Figure 2.3: Particles with a lower momentum $\frac{\Delta p}{p_0} < 0$ have a shorter path around the storage ring and therefore sample the acceleration voltage at a earlier phase and thus gain slightly more energy. While particles with a higher momentum $\frac{\Delta p}{p_0} > 0$ arrive slightly later and gain less energy, leading to a focusing effect, referred to as phase focusing. [19]

and reach the acceleration voltage at an earlier phase[2]. Vice versa, particles with higher momentum arrive at a later phase. For a synchronous phase on the falling edge of the acceleration voltage, an earlier phase ($p < p_0$) leads to a stronger acceleration while a later arriving particle ($p > p_0$) is accelerated less. Overall, this effects always corrects the energy to the ideal value, focusing the particle momentums. This effect, referred to as phase focusing, is depicted in Figure 2.3.

To display the connection between longitudinal position and energy, the movements and/or distribution of particles are usually studied in the longitudinal phase space. While on the x axis the relative position to the ideal longitudinal position (sometimes as phase or in units of the bunch length) is plotted, the y axis gives the particle energy (often in units of the energy spread or as time derivative of the phase) as shown in Figure 2.4. Out of the multiple possible particle trajectories displayed, the outermost closed one (red) is called separatrix. It separates the stable (inside, often also referred to as RF-bucket) from the unstable (outside) trajectories. This already indicates that the longitudinal particle motion can be described as an oscillation.

As nicely described in [20], the equation of longitudinal motion can be derived from the energy gain of off-momentum particles and the phase focusing described above. The result

[2]This holds true for a positive momentum compaction factor. For a negative momentum compaction factor the connection would be inverted.

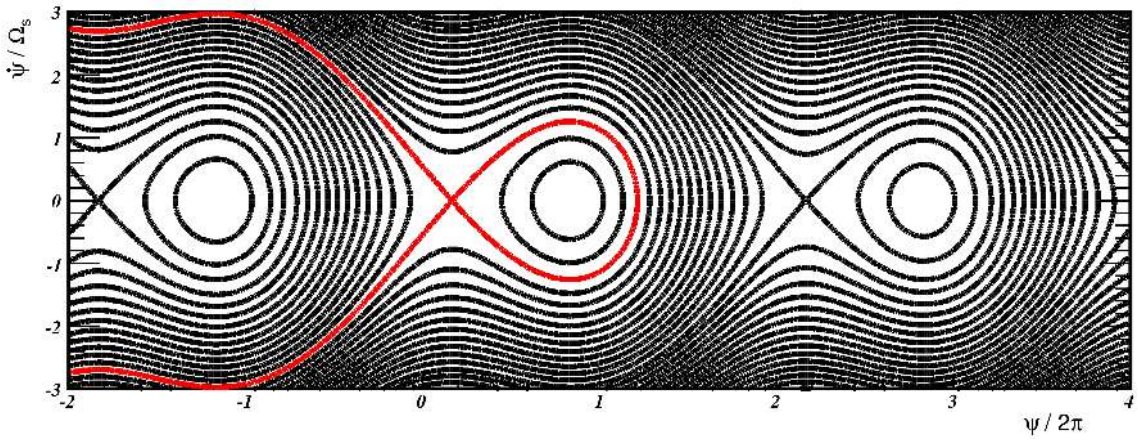

Figure 2.4: Possible particle trajectories are displayed in the longitudinal phase space. The trajectory displayed in red is called separatrix and separates the stable (inside) from the unstable (outside) trajectories. [19]

is an equation for an harmonic oscillator for the energy deviation ΔE:

$$\Delta\ddot{E} + \frac{2}{\tau_d}\Delta\dot{E} + \omega_s^2 \Delta E = 0$$

or as given in [15] for the phase deviation $\varphi = \Psi - \Psi_\mathrm{s}$:

$$\ddot{\varphi} + 2\alpha_z\dot{\varphi} + \Omega^2\varphi = 0$$

with the longitudinal damping time $\tau_\mathrm{d} = 1/\alpha_z$ and the longitudinal oscillation frequency, referred to as synchrotron frequency $f_\mathrm{s} = {}^{\omega_\mathrm{s}}/_{2\pi} = \Omega$:

$$f_\mathrm{s} = \frac{\omega_\mathrm{s}}{2\pi} = f_{rev}\sqrt{\frac{h\eta}{2\pi\beta^2 E} e \left.\frac{\mathrm{d}V_\mathrm{RF}}{\mathrm{d}\Psi}\right|_{\Psi_\mathrm{s}}} \tag{2.10}$$

with the transition factor $\eta = \alpha_c - \gamma^{-2}$ and the harmonic number h. As the synchronous phase is defined as the phase where a particle receives exactly the amount of energy it lost, it is given that

$$V_0 \sin\Psi_\mathrm{s} = \frac{U_0}{e} \tag{2.11}$$

So the derivative of the acceleration voltage with respect to the phase at the point of the synchronous phase is given by $e\left.\frac{\mathrm{d}V_\mathrm{RF}}{\mathrm{d}\Psi}\right|_{\Psi_\mathrm{s}} = eV_\mathrm{RF}\cos\Psi_\mathrm{s} = \sqrt{e^2V_\mathrm{RF}^2 - U_0^2}$. Leading to the following equation for the synchrotron frequency:

$$f_\mathrm{s} = f_\mathrm{rev}\sqrt{\frac{h\eta}{2\pi\beta^2 E}\sqrt{e^2V_\mathrm{RF}^2 - U_0^2}} \tag{2.12}$$

For highly relativistic particles the transition factor converges to the momentum compaction factor $\eta = \alpha_\mathrm{c} - \frac{1}{\gamma} \overset{v\to c}{\to} \alpha_\mathrm{c}$ and $\beta \overset{v\to c}{\to} 1$.

The longitudinal damping time is given by [18]:

$$\frac{1}{\tau_\mathrm{d}} = \frac{1}{2T_0}\frac{\mathrm{d}U}{\mathrm{d}E} = \frac{1}{2T_0}\frac{U_0}{E_0}\mathcal{J}_z \tag{2.13}$$

with the damping partition number $\mathcal{J}_z = 2 + \mathcal{D} \approx 2$, which depicts the coupling $\mathcal{D}$ between the different planes. The coupling parameter depends on parameters of the magnet optics, namely the Dispersion D, quadrupole strength k, and bending radius R:

$$\mathcal{D} = \frac{\oint \left[\frac{D}{R}\left(2k + \frac{1}{R^2}\right)\right]\mathrm{d}s}{\oint \frac{\mathrm{d}s}{R^2}}$$

Similar to the longitudinal damping time the damping times in the other planes are given by:

$$\frac{1}{\tau_x} = \frac{1}{2T_0}\frac{U_0}{E_0}(1-\mathcal{D}) = \frac{1}{2T_0}\frac{U_0}{E_0}\mathcal{J}_x$$
$$\frac{1}{\tau_y} = \frac{1}{2T_0}\frac{U_0}{E_0} = \frac{1}{2T_0}\frac{U_0}{E_0}\mathcal{J}_y$$

From this follows directly the theorem discovered by K. W. Robinson [21]:

$$\mathcal{J}_x + \mathcal{J}_y + \mathcal{J}_z = 4$$

While the sum of the damping partition numbers is always four, $\mathcal{J}_z$ and $\mathcal{J}_z$ can be changed accordingly to the value of $\mathcal{D}$. At rings with separated function magnets (as it is the case for KARA) $\mathcal{D}$ is generally very small [16] and the damping is distributed naturally, i.e. $\mathcal{J}_x = 1$, $\mathcal{J}_y = 1$, $\mathcal{J}_z = 2$, leading to a damped oscillation in all three planes.

Another important aspect of the longitudinal beam dynamics is the momentum compaction. As described for the phase focusing, due to the dispersion, particles with an momentum deviating from the ideal momentum travel on a deviating orbit. The ratio between the path length difference resulting from an momentum difference is referred to as momentum compaction factor α_c [15]:

$$\alpha_\mathrm{c} = \frac{\Delta L/L}{\Delta p/p} = \frac{1}{L_0} \oint \frac{D\left(s\right)}{R\left(s\right)} ds \tag{2.14}$$

α_c shows how the longitudinal compression depends on the optical functions and plays a vital role in the calculation of the length of a bunch.

The natural bunch length $\sigma_{z,0}$ is the length of a bunch with a low charge, for which the effects from the statistic emission of photons and the energy gain are in equilibrium [22]:

$$\sigma_{z,0} = \frac{c\sigma_{\delta,0}\left|\alpha_\mathrm{c}\right|}{2\pi f_\mathrm{s}\beta} \tag{2.15}$$

With Equation 2.12 the natural bunch length can be written as

$$\sigma_{z,0} = \frac{c\sigma_{\delta,0}\left|\alpha_\mathrm{c}\right|}{2\pi\beta f_\mathrm{rev}\sqrt{\frac{h\eta}{2\pi\beta^2 E} e \left.\frac{\mathrm{d}V_\mathrm{RF}}{\mathrm{d}\Psi}\right|_{\Psi_\mathrm{s}}}} = \frac{c\sigma_{\delta,0}\sqrt{E\left|\alpha_\mathrm{c}\right|}}{f_\mathrm{rev}\sqrt{2\pi h e \left.\frac{\mathrm{d}V_\mathrm{RF}}{\mathrm{d}\Psi}\right|_{\Psi_\mathrm{s}}}}$$

which directly shows the dependencies of the natural bunch length on the different adjustable machine parameters:

$$\begin{aligned} \sigma_z &\propto \alpha_c^{\frac{1}{2}} \\ \sigma_z &\propto E^{\frac{3}{2}} \\ \sigma_z &\propto \left(\left.\frac{\mathrm{d}V_\mathrm{RF}}{\mathrm{d}\Psi}\right|_{\Psi_\mathrm{s}}\right)^{-\frac{1}{2}} \end{aligned} \tag{2.16}$$

Additional to the momentum compaction factor and the synchrotron frequency, the natural bunch length also depends on the natural energy spread $\sigma_{\delta,0}$ due to the motion in the longitudinal phase space. As the name implies, the energy spread gives the relative spread of the energy deviations the different particles in a bunch have from the ideal synchronous particle: $\sigma_\delta = \frac{\sigma_E}{E_0}$. The natural energy spread $\sigma_{\delta,0} = \frac{\sigma_{E,0}}{E_0}$ is the equivalent to the natural bunch length and is valid for bunches containing a low number of particles. For bunches containing a high number of particles the actual bunch length and for even higher particle numbers also the energy spread deviate from the natural one.

The potential well distortion is one effect that leads with increasing bunch charge to a lengthening of the bunches due to collective effects, but does not effect the energy spread. Further description of this effect can be found in [23; 24]. The influence on the bunch length is given by:

$$\left(\frac{\sigma_z}{\sigma_{z,0}}\right) - \left(\frac{\sigma_z}{\sigma_{z,0}}\right)^3 = \frac{I_\mathrm{b}}{\left(2\pi\right)^4} Z_\mathrm{c} \frac{\dot{V}_\mathrm{RF}\sqrt{2\pi}}{f_\mathrm{rev}^3 \sigma_{z,0}^3} \tag{2.17}$$

which directly depends on various beam parameters as the bunch current I_b and the impedance Z_c leading to the potential well distortion caused by the electromagnetic field (wake field) co-propagating with the bunch. Impedances and wake fields are a way to describe the interaction of a bunch with its surroundings, as explained further in the next chapter.

2.6 Impedances and Wake Fields

The energy an electron gains depends on the potentials it experiences. The most prominent and important one is the RF potential the electrons in a bunch see when the bunch passes the RF cavities. As described above (Section 2.5) the energy gained in the cavities compensates the energy loss caused by synchrotron radiation. There are also other sources for potentials interacting with the bunch. These can be described by the concept of wake potentials $V(t)$ as a convolution of the wake function $W(t)$ [3] with the charge distribution $\rho(t)$ of the electron bunch. The resulting potential defines the energy gain dependent on the longitudinal position t of the particles in the longitudinal phase space. While the RF potential can be assumed in good approximation to be linear at the position of the bunch, other wake potentials might not be linear. The linear RF potential in combination with the phase focussing leads to a simple rotation of the charge distribution in the phase space. Particles in the front of the bunch gain more energy than they lost due to synchrotron radiation and, therefore, move up in the phase space. Whereas particles at the end gain less energy and move down in the phase space. And due to the phase focussing particles with more energy take a longer way around the ring and, thus, move back in the bunch and the other way round for particles with less energy[4]. A non-linear potential, on the other hand, can lead to the deformation of the charge distribution in the phase space.

Sometimes, also the description in frequency domain is used. The Fourier transform of the wake function is defined as the impedance $Z(f)$. So, instead of the convolution of the wake function with the charge distribution, the impedance can be multiplied with the Fourier transform of the charge distribution $\tilde{\rho}(f)$ (referred to as bunch spectrum) resulting in the Fourier transform of the wake potential $\tilde{V}(f) = \tilde{\rho}(f)\, Z(f)$ and therefore giving

$$V(t) = \int_{-\infty}^{\infty} \tilde{V}(f)\, e^{i2\pi f t} \mathrm{d}f = \int_{-\infty}^{\infty} \tilde{\rho}(f)\, Z(f)\, e^{i2\pi f t} \mathrm{d}f \tag{2.18}$$

[3] The wake function is the potential which a single particle would create for a test charge.

[4] The direction of rotation would be opposite for an operation with a negative momentum compaction factor. In this case also the RF Voltage would need to be phase shifted by $\approx 180\,^\circ$ to achieve phase focussing and therefore stable operation.

Depending on the frequency-dependent behavior of the impedance as well as the bunch length and the charge distribution, the functions overlap for different frequency ranges. This leads to different shapes of the resulting wake potential creating a different position-dependent energy gain. The different changes of the energy distribution in the bunch cause different changes in the bunch profile (charge distribution) via the rotation of the phase space due to the synchrotron motion. Thus, the resulting charge distribution depends not only on the impedance but also on the initial distribution. This cycle does not necessarily lead to an equilibrium. It can under the right conditions lead to a self-enhancing effect as for example under the influence of the CSR impedance causing the micro-bunching instability, which will be described in Section 2.9.

Thus, an important parameter is the shape of the impedances that is sampled by the frequencies present in the bunch profile. For long Gaussian-shaped bunches, mainly the low frequency components are of interest, while for shorter and deformed bunches (e.g. non-Gaussian shapes or shapes modulated with substructures (higher frequency components)) also the higher frequency ranges can have an influence. As most impedances are complex, their effect on the bunch depends on the real and imaginary part. The real part can be associated with a resistive effect. A positive real part leads to an energy loss and the bunch leaning forward, while a negative real part corresponds to an energy gain. For the imaginary part of the impedance a negative sign has a capacitive effect and leads to a shortening of the bunch while a positive imaginary part has an inductive effect and lengthens the bunch[25].

As stated above, interactions of the bunch with its surrounding and itself can be described in the form of impedances. For example, the vacuum camber is not constructed from an ideal conductor, so the interaction of the electromagnetic field of the charged particles with the vacuum camber surface material leads to energy losses depending on the material and the distance of the charged particles to the chamber wall. This effect is referred to as resistive wall impedance. A formula for the corresponding impedance is given in for example ([25], equ. 1.58):

$$\frac{Z_{\mathrm{RW}}(f)}{L} = [1 - i\,\mathrm{sign}(f)]\sqrt{\frac{\mu_{\mathrm{r}} Z_0}{2c\sigma_{\mathrm{c}}}}\frac{1}{2\pi b}\sqrt{|f|}$$

with the conductivity σ_{c}, the permeability μ_{r}, the length L of the vacuum camber, the radius b of the assumed round beam pipe and the vacuum impedance $Z_0 \coloneqq \mu_0 \cdot c \approx 377\,\Omega$.

Many more impedances can be grouped as geometric impedances. They describe the influence on the beam which geometric changes in the dimensions of the vacuum chamber have. The cross section of the chamber often changes due to external constrains, for

example the ports for vacuum pumps or a reduced chamber height in insertion devices. A localized widening of the chamber can act as a passive resonating structure, which can, driven by the beam itself, act back on it. Another example for a geometric impedance is a collimator which temporally decreases the opening of the vacuum chamber. These and many more can be found in the collection by K. Y. Ng and K. Bane [26].

Another kind of interaction is described by the CSR impedance. The coherent synchrotron radiation emitted by a bunch can act back on the bunch itself. As it is emitted in a small cone (Equation 2.8) tangentially to the direction of motion of the bunch, it can catch up with the front of the bunch, when the bunch moves on a curved trajectory. Thus, the CSR emitted at one point of the bunch can change the potential for electrons at other positions in the bunch. Different models exist to describe this interaction of a bunch with its own coherent synchrotron radiation. A simple model, only considering a bunch moving on a perfect circular trajectory in vacuum, is the free space model deducted by J. Murphy, S. Krinsky, and R. Gluckstern in 1995 [27]. The impedance is given as ([28], eqn. 6.18):

$$\begin{aligned} Z_{\mathrm{FS}}(n) &= Z_0 \frac{\Gamma(2/3)}{3^{1/3}} \left(\frac{\sqrt{3}}{2} + \frac{i}{2}\right) n^{1/3} \\ \Rightarrow \quad \frac{Z_{\mathrm{FS}}(f)}{L} &= Z_0 \frac{\Gamma(2/3)}{2\pi} \left(\frac{\sqrt{3}}{2} + \frac{i}{2}\right) \left(\frac{2\pi f}{3R^2 c}\right)^{1/3} \end{aligned} \tag{2.19}$$

with $n = f/f_0$ multiples of the revolution frequency f_0 for a circle of length $L = 2\pi R$, the vacuum impedance Z_0, and the Gamma-function $\Gamma(x)$.

The parallel plates model of the CSR impedance additionally considers two infinitely wide, perfectly conducting, parallel plates between which the bunch is moving on its perfect circular trajectory. An equation for the impedance is given in [29]:

$$\frac{Z_{\mathrm{PP}}(f)}{L} = Z_0 \frac{2\pi}{\beta h_{\mathrm{c}}} \left(\frac{2f_0}{f}\right)^{\frac{1}{3}} \sum_{p=0}^{\infty} F_0(\beta_p) \tag{2.20}$$

with $F_0(\beta_p) = \mathrm{Ai}'(\omega_p)\,\mathrm{Ci}'(\omega_p) + \beta_p^2 \mathrm{Ai}(\omega_p)\,Ci(\omega_p)$, the Airy function Ai, the Airy function of the second kind Bi, $\mathrm{Ci}(z) = \mathrm{Ai}(z) - i\mathrm{Bi}(z)$, $\beta = v/c$, $\beta_p = \frac{\pi}{h_c}(2p+1) \cdot \left[\frac{2}{R}\left(\frac{2\pi f}{c}\right)^2\right]^{-1/3}$, and $\omega_p = \beta_p^2 + \left(2\frac{f^2}{f_0^2}\right)^{1/3} \frac{1}{2\gamma^2}$. The distance between the parallel plates is h_{c} and represents the height of the vacuum chamber. Figure 2.5 shows the parallel plates impedance for a chamber height of 32 mm. It is visible that for low frequencies the real part of the impedance is suppressed, which originates in the fact that for long wavelength electromagnetic fields can not propagate in the vacuum chamber. The suppression of wavelengths longer than a cut-off wavelength is called shielding by parallel plates. For short enough bunches the

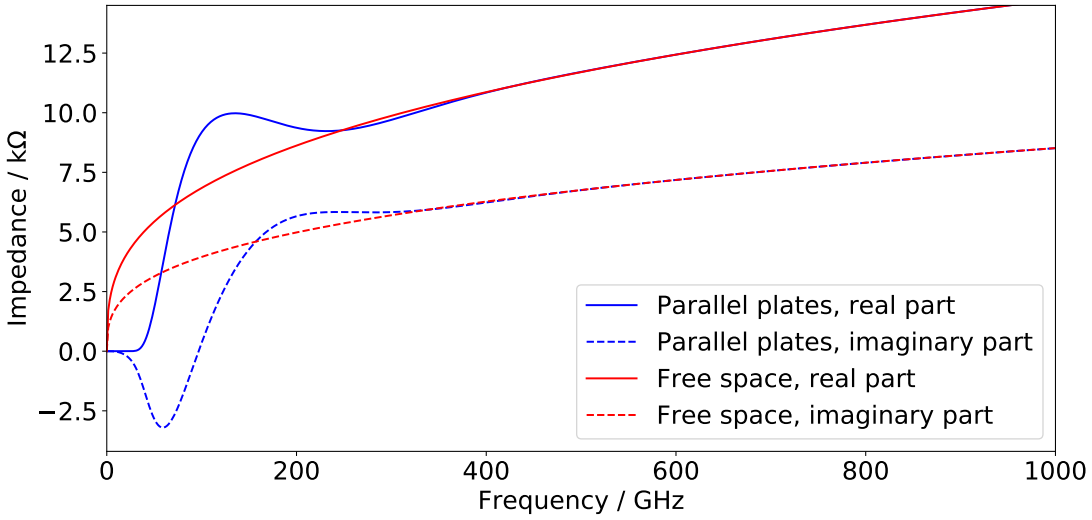

Figure 2.5: Real and imaginary part of the parallel plates as well as the free space model of the CSR impedance (see Equation 2.19 and Equation 2.20) calculated for an vacuum chamber height of 32 mm and a bending radius of $R = 5.559\,\mathrm{m}$ for one revolution. For high frequencies the parallel plates impedance approaches the free space impedance.

CSR impedance can lead to the micro-bunching instability studied in this thesis, where due to the additional wake potential micro-structures form on the charge distribution in the longitudinal phase space and the emitted CSR power changes continuously.

The detailed influence of an impedance on the dynamics of the bunch can be calculated using the Vlasov-Fokker-Planck equation. This is described in the next section for the longitudinal plane.

2.7 Vlasov-Fokker-Planck Equation

As discussed in Section 2.5, the dynamics in the longitudinal phase space can be simplified to an harmonic oscillator. The Hamiltonian for such a system is given by

$$\mathcal{H} = \frac{1}{2}\left(q^2 + p^2\right)$$

The dimensionless, generalized coordinates are in this case defined as [10]

$$q \coloneqq \frac{z}{\sigma_{z,0}}$$
$$p \coloneqq \frac{E - E_0}{\sigma_{E,0}}$$

with $z = -\frac{\beta c T_0}{2\pi h}\Psi$ transforming the phase to a position. As dimensionless time axis multiples of the synchrotron oscillation period T_s are used

$$\theta := \frac{t}{T_\mathrm{s}}$$

the Hamiltonian of the longitudinal phase space then results to

$$\mathcal{H} = \pi h f_\mathrm{rev} \alpha_\mathrm{c} \sigma_\delta^2 + \frac{1}{2}\frac{e V_\mathrm{RF} f_\mathrm{rev}}{E_0}\Delta\Psi^2 \tag{2.21}$$

For conservative systems, which is not given for synchrotrons, the development of the charge density $\psi(z, E, t)$ in the phase space can be described by the Vlasov equation [30]:

$$\frac{\mathrm{d}\psi}{\mathrm{d}\theta} = \frac{\partial\psi}{\partial\theta} + \frac{\partial\mathcal{H}}{\partial p}\frac{\partial\psi}{\partial q} - \frac{\partial\mathcal{H}}{\partial q}\frac{\partial\psi}{\partial p} = 0$$

To account for non-conservative effects in a system, like in this case the emission of synchrotron radiation, the Vlasov-Fokker-Planck (VFP) equation can be used [30]:

$$\frac{\mathrm{d}\psi}{\mathrm{d}\theta} = \frac{\partial\psi}{\partial\theta} + \frac{\partial\mathcal{H}}{\partial p}\frac{\partial\psi}{\partial q} - \frac{\partial\mathcal{H}}{\partial q}\frac{\partial\psi}{\partial p} = \beta_\mathrm{d}\frac{\partial}{\partial p}\left(p\psi + \frac{\partial\psi}{\partial p}\right) \tag{2.22}$$

where $\beta_\mathrm{d} = T_\mathrm{s}/\tau_\mathrm{d}$ gives the longitudinal damping time in units of synchrotron period.

Until now only a simple Hamiltonian including only single particle effects has been considered. This can be changed by modifying and extending the Hamiltonian to include further effects [31] for example collective effects

$$\begin{aligned}\mathcal{H}(q, p, \theta) &= \underbrace{\mathcal{H}_l(q, p, \theta)}_{\text{unperturbed}} + \underbrace{\mathcal{H}_c(q, \theta)}_{\text{collective}} \\ &= \frac{1}{2}\left(q^2 + p^2\right) + \frac{e f_\mathrm{rev}}{\sigma_E f_{\mathrm{s},0}}\int_q^\infty V_c(q', t)\,\mathrm{d}q'\end{aligned} \tag{2.23}$$

The potential V_c multiplied by the elementary charge e gives the energy of the collective effects in one revolution. To adjust it to the dimensionless time in units of the synchrotron period it is multiplied by the revolution frequency and divided by the synchrotron frequency.

To also include higher orders of the momentum compaction factor and the accelerating voltage further modifications of the Hamiltonian would be necessary [31].

Combining the Vlasov-Fokker-Plank equation (Equation 2.22) with one or several of the impedances described in Section 2.6 allows a prediction of the dynamics a particle beam

would show under their influence. With Equation 2.18 the Hamiltonian can be rewritten to directly depend on the impedance

$$\mathcal{H}(q,p,\theta) = \frac{1}{2}\left(q^2+p^2\right) + \frac{e f_{\mathrm{rev}}}{\sigma_E f_{\mathrm{s},0}} \int_q^\infty \int_{-\infty}^\infty \varrho(f)\, Z(f)\, e^{i2\pi f q'} \mathrm{d}f \mathrm{d}q'$$

From here it is visible that the Hamiltonian not only depends on the impedance but also on the charge distribution, which itself can change under the influence of the impedance. As briefly noted in Section 2.6, this can lead to a self-enhancing effect and under certain conditions to an instability, e.g. the micro-bunching instability (see more in Section 2.9). The VFP equation converges for a stable distribution. In the case of an instability, an iterative approach provides insight into the longitudinal dynamics, where the calculation steps describe the temporal evolution of the system.

2.8 Vlasov-Fokker-Planck Solver

There have been several implementations of the VFP equation to simulate the phase space evolution by solving the equation in time domain (based on wake fields) for each time step after the other [10; 13; 32]. A relatively new and massively parallelized implementation, Inovesa Numerical Optimized Vlasov Equation Solver Application (Inovesa) [Sch18c; Sch17a], was developed by Patrik Schönfeldt (KIT) and solves the VFP equation based on impedances in the frequency domain.

In Inovesa, the charge density $\psi(z,E,t)$ in the phase space is implemented as a 2D matrix of grid cells, each entry representing the amount of charge present in the corresponding phase space volume.

Starting from an initial charge distribution, the longitudinal bunch profile is calculated and from that the emitted radiation spectrum as well as the wake potential for the next step is calculated. Then, the phase space is rotated by shifting the density along the position axis by an amount depending on the energy coordinate of each grid cell and derived from the VFP equation. Afterwards, a kick along the energy axis is applied, with a kick strength resulting from the RF potential and the wake potential calculated from the previous distribution. As the wake potential is position-dependent the kick strength is different for each grid column. The rotation results in a slightly changed charge distribution for which the process starts over. This leads to a stepwise simulation of the dynamics happening in the phase space under the influence of the selected impedance. A much more detailed description can be found in [31; Sch17b].

Already implemented in Inovesa are the parallel plates impedance and the free space impedance. Further impedances can be provided via input files. Furthermore, the charge distribution to start a simulation run with can be defined by specifying a gaussian distribution or given as an input file. As stated in [Sch17b], depending on the form and size chosen as starting distribution, it will take a certain number of simulation steps until the simulation results converge to the physical state. All other parameters present in Equation 2.21 are defined in configuration files or can be passed as a command line parameter. This is convenient for automatized parameter scans.

The resulting phase space distributions as well as many derived quantities and additional information of all simulation steps are written into an HDF5 file [33], allowing to analyze and display the simulated dynamics afterwards. An example for a simulated phase space distribution under the influence of the parallel plates impedance is displayed in Figure 2.6.

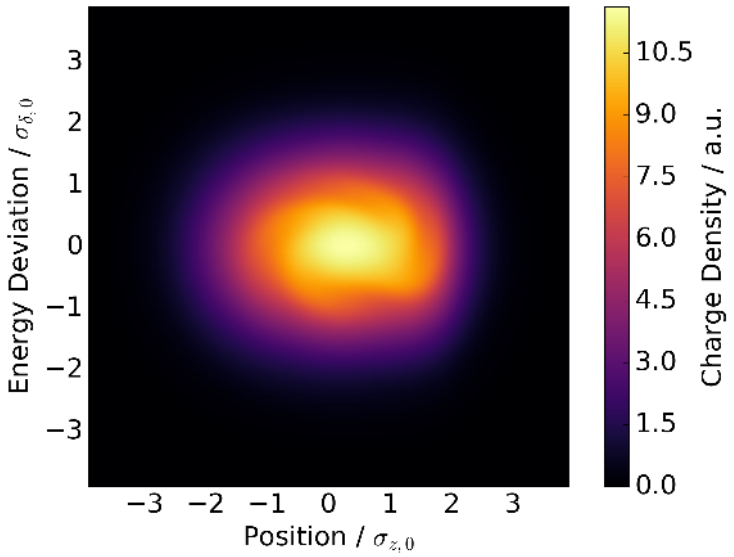

Figure 2.6: Deformed charge distribution displaying substructures in the longitudinal phase space simulated using Inovesa with the parallel plates model for the CSR impedance.

2.9 Micro-Bunching Instability

As described above, the interaction of a bunch with its surrounding is described by impedances and can lead to a deformed longitudinal bunch profile or even to instabilities where the bunch profile continuously changes with time. Such an instability is the micro-bunching instability which will be studied in this thesis. The micro-bunching instability arises from the interaction of the bunch with its own emitted coherent synchrotron radiation.

As described in Section 2.6, the CSR emitted by a bunch can act back on the bunch as a position-dependent potential and thus cause a deformation of the longitudinal bunch profile. The simple parallel plates model of the CSR impedance has proven to describe this interaction quite well for the experimental results at KARA [Bro16a] and will be used in the scope of this thesis to compare the experimental results with. In general, CSR is only emitted at wavelength longer than the emitting structure, meaning the shorter the emitting structure the larger the frequency range in which CSR is emitted. Simply stated, the micro-bunching instability arises as soon as the bunch is short enough for its bunch spectrum[5] to significantly overlap with the impedance. This then causing substructures to occur on the charge distribution in the longitudinal phase space.

In the following, an empirical working model is introduced, describing the dynamics under the instability in more detail. This model will be used as preconceived understanding throughout this thesis to put the experimental findings into perspective. First, the overlap of the bunch spectrum with the impedance in frequency domain causes an additional wake potential. This additional potential provides a position-dependent energy gain causing the electrons in the bunch to gain energy depending on their longitudinal position in the bunch. The change in the energy distribution in the bunch eventually results, due to the synchrotron oscillation, in a deformation of the longitudinal bunch profile [Bol19a]. For low bunch currents this manifests in an asymmetric longitudinal bunch profile (given by Haissinski solution [34]). Due to the deformation of the longitudinal bunch profile, the bunch spectrum contains higher frequencies leading to an even bigger overlap with the impedance and thus a stronger potential acting back on the bunch. This self-interaction will increase and result in stronger deformations the higher the bunch current becomes, as the potential depends on the actual longitudinal charge distribution and not only on the normalized charge distribution. Meaning, the resulting potential scales with the number of electrons contributing to it. At a certain bunch current the instability threshold is reached. Above this current, the deformation of the charge distribution in the longitudinal phase space forms finger-like substructures, now also affecting the energy distribution (see measurement in e.g. [35]) additionally to the longitudinal charge distribution. These substructures modulated on the charge distribution rotate in the longitudinal phase space and cause continuous changes in the projection onto the position axis. As then the longitudinal bunch profile is not constant in time anymore, also the emitted CSR power fluctuates over time. Here the self-interaction results in the changes in the longitudinal bunch profile causing changes in the wake potential which again drives the changes in the longitudinal bunch profile,

[5] The bunch spectrum $\tilde{\rho}(f)$ is the Fourier transform of the longitudinal charge distribution $\rho(t)$ of the bunch.

leading to a continuous presence of finger-like substructures in the charge distribution on the longitudinal phase space. At even higher bunch currents an additional and slower behavior can be observed. The interaction of the emitted CSR with the bunch is even stronger and leads to a kind of self-amplification of the substructures. The substructures grow in amplitude over the turns while they also are subject to diffusion. After some synchrotron periods the substructures are so spread out that the corresponding wake potential no longer leads to a further enhancement. This means, as the charge distribution in the longitudinal phase space is then washed out, the bunch length is increased and the longitudinal bunch profile is smoothened. The resulting bunch spectrum contains less high frequency components thus leading to a lower wake potential. At this point, the radiation damping out-weighs the driving wake potential remaining and the charge distribution in the longitudinal phase space shrinks. When the bunch length is short enough, the wake potential increases again and starts to drive the formation of new substructures. The cycle is starting again.

This behavior is visible in the emitted CSR power as well as in the bunch length and the energy spread as saw-tooth shaped pattern (see Figure 2.7), sometimes also called burst. This was early on observed at the SURF III electron storage ring at the NIST [9]. Due

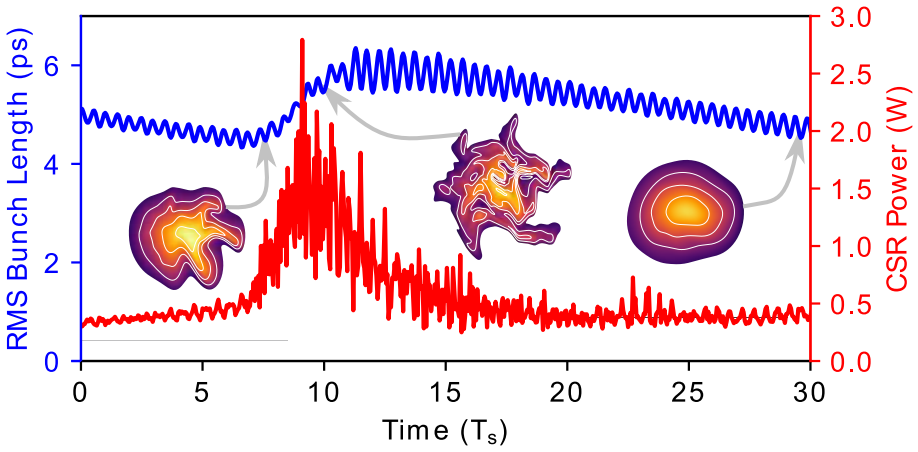

Figure 2.7: Simulated example for one burst, showing the changes in the emitted CSR power, the bunch length and for three points in time the charge distribution in the longitudinal phase space. Courtesy of Patrik Schönfeldt

to the shape, the micro-bunching instability is sometimes also referred to as sawtooth instability in literature (e.g. [10]).

The complex dynamics in the longitudinal phase space is directly visible in the fluctuations of the emitted CSR power. Displaying the fluctuation frequencies as a function of the bunch current, results in a spectrogram[6] like the one shown in Figure 2.8. The onset of

[6] A spectrogram visualizes the temporal changes of the spectrum of frequencies of a signal. In this case,

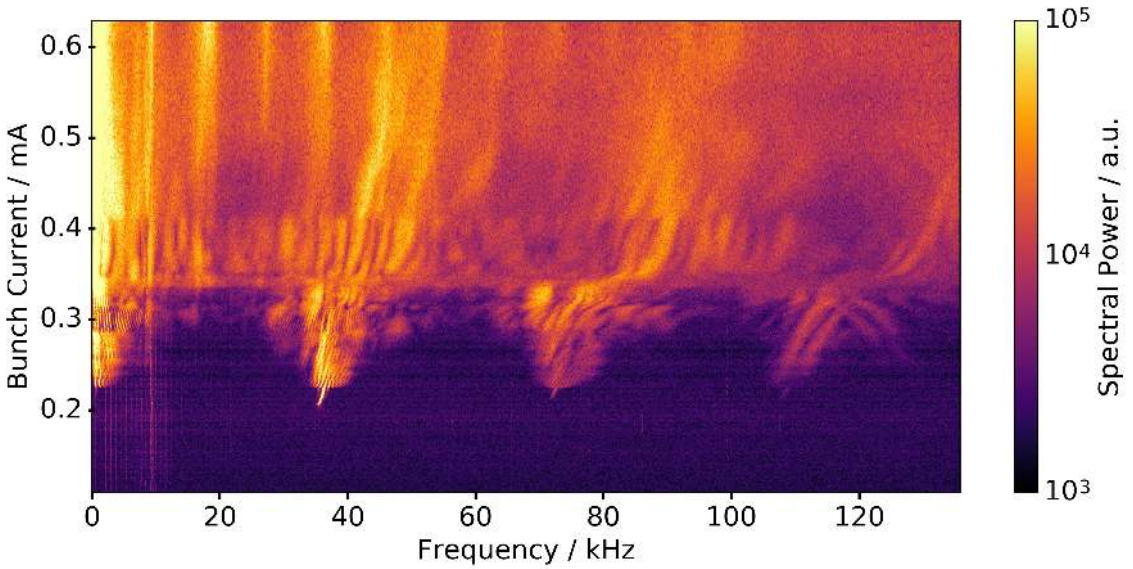

Figure 2.8: The spectrogram shows the fluctuation frequencies of the emitted CSR power as a function of the bunch current. At $\approx 0.2\,\mathrm{mA}$ the threshold of the instability is visible as the fluctuations only occur for higher bunch currents.

fluctuations at the bunch current of $\approx 0.2\,\mathrm{mA}$ indicates the instability threshold above which, as discussed before, the longitudinal bunch profile is not constant in time anymore. Above the threshold current a complex dynamic is visible in the changes of the fluctuation frequencies, which will be described in more detail in Section 7.1. While the dynamics in the longitudinal phase space under the micro-bunching instability is complex, it is completely reproducible for the exact same conditions. This allows to study its dependency on different machine parameters, like the momentum compaction factor, the acceleration voltage, or the longitudinal damping time later on in this thesis.

The previous section described that a Vlasov-Fokker-Planck solver in combination with an model of the CSR impedance can be used to simulate the dynamics of a bunch under the influence of the micro-bunching instability. In [13], Bane, Cai, and Stupakov used such a VFP solver, based on the algorithm devised by Warnock and Ellison [10], to formulate an equation for the threshold current of the micro-bunching instability, assuming a bunched beam and the parallel plates model for the CSR impedance. They applied a linear fit to the simulated threshold currents for different parameters, resulting in the linear scaling

the bunch current changes with time corresponding therefore to the time axis.

law [13]:

$$(S_{\mathrm{CSR}})_{\mathrm{th}} = a_{\mathrm{th}} + b_{\mathrm{th}}\,\Pi \tag{2.24}$$

$$(S_{\mathrm{CSR}})_{\mathrm{th}} = 0.5 + 0.12\;\Pi \tag{2.25}$$

$$\text{with } \Pi = \frac{\sigma_{z,0} R^{1/2}}{h^{3/2}} \tag{2.26}$$

$$\text{and } S_{\mathrm{CSR}} = \frac{I_{\mathrm{n}} R^{1/3}}{\sigma_{z,0}^{4/3}} \tag{2.27}$$

where $a_{\mathrm{th}} = 0.5$ and $b_{\mathrm{th}} = 0.12$ are the fit parameters, $\sigma_{z,0}$ is the natural bunch length, R the bending radius, $h = \frac{1}{2}h_{\mathrm{c}}$ half of the spacing between the parallel plates, and I_{n} the normalized current:

$$I_{\mathrm{n}} = \frac{r_{\mathrm{e}} N_{\mathrm{b}}}{2\pi\nu_{\mathrm{s},0}\gamma\sigma_{\delta,0}} = \frac{I_{\mathrm{b}}\sigma_{z,0}}{\gamma\alpha_{\mathrm{c}}\sigma_{\delta,0}^2 I_{\mathrm{A}}}$$

with N_{b} the number of electrons, I_{b} the bunch current, r_{e} the classical electron radius, $\nu_{\mathrm{s},0}$ the nominal synchrotron tune, $\sigma_{\delta,0}$ the nominal energy spread, α_{c} the momentum compaction factor, γ the Lorentz factor, and I_{A} the Alfvén current [7]. This linear scaling law fits best for high values of Π ($\Pi > 3$); however, at lower values the simulated thresholds are higher than the fit (see Figure 2.9).

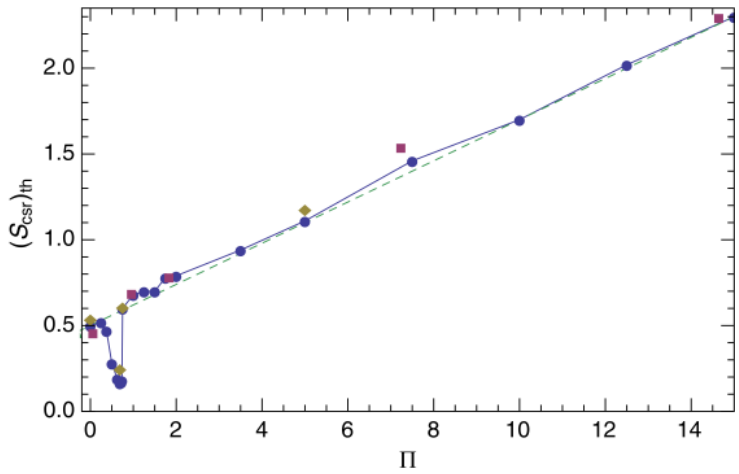

Figure 2.9: Simulated instability thresholds on which the simple linear scaling law was based, by [13]. "For the CSR wake, threshold value of S_{csr} vs shielding parameter, $\Pi = \rho^{1/2}\sigma_{z0}/h^{3/2}$. Symbols give results of the VFP solver (blue circles), the LV code (red squares), and the VFP solver with twice stronger radiation damping (olive diamonds)." ([13], figure 3)

In Figure 2.9, a dip around $\Pi \approx 0.7$ is visible, which is ignored by the fit leading to simple

[7] Alfvén current $I_{\mathrm{A}} = 4\pi\varepsilon_0 m_{\mathrm{e}} c^3/e = 17045\,\mathrm{A}$

linear scaling law (Equation 2.24). It was shown in [13] that this dip contains a second unstable region in the bunch current, with a threshold below the one expected from the standard micro-bunching instability. This new region corresponds to the short-bunch-length bursting studied in Chapter 9. [13] predicts that the occurrence of this additional region of instability depends additionally to the shielding parameter Π also on $\beta = 1/(2\pi f_s \tau_d)$, which relates the synchrotron frequency f_s and the longitudinal damping time τ_d [13; 36]. It was therefore termed a weak instability [13].

3 KARA - Short Bunch Operation

KARA, the KIT storage ring (KArlsruhe Research Accelerator), will be described in this chapter and important features and parameters will be highlighted. The first part of the chapter is about the structure and the operation of KARA. Afterwards, the importance of the RF system providing the acceleration voltage is described. It is discussed that to achieve the accuracy necessary for the systematic measurements in this work, a calibration of the set values of the acceleration voltage was performed within the framework of this thesis. This is followed by a brief introduction of the KARA timing system and in the end a brief description of the CLIC damping ring wiggler will be given.

3.1 KARA - KArlsruhe Research Accelerator

KARA stands for the KArlsruhe Research Accelerator and is an electron synchrotron. There is a complex infrastructure supporting KARA consisting amongst others of a chain of pre-accelerators. To generate the electrons a thermionic electron gun is used. Afterwards, the electrons are accelerated in a racetrack microtron to an energy of $\approx 53\,\mathrm{MeV}$. In the following booster synchrotron ring they reach an energy of $\approx 500\,\mathrm{MeV}$ before they are transferred to the main ring. KARA serves as a synchrotron and storage ring. The pre-accelerated electrons can be stored at the injection energy of 500 MeV or accelerated further to the maximum operation energy of 2.5 GeV. Predefined and tested settings for the magnet optics exist for 500 MeV, 1.3 GeV, 1.6 GeV, and 2.5 GeV, but in principle KARA could be operated at any energy between 500 MeV and 2.5 GeV.

The magnet optics in KARA consist of dipole, quadrupole, and sextupole magnets as well as multiple small corrector and kicker magnets. The magnetic lattice is divided in four mostly identical sectors each consisting of two double-bend-achromat (DBA) structures [15]. This results in four short and four long straight sections (see Figure 3.1).

Most of these straight sections are used to place insertion devices like wigglers or undulators (e.g. Section 3.5) [16]. These insertion devices consist of a sequence of dipole magnets. Depending on the geometry and configuration the synchrotron radiation emitted by the

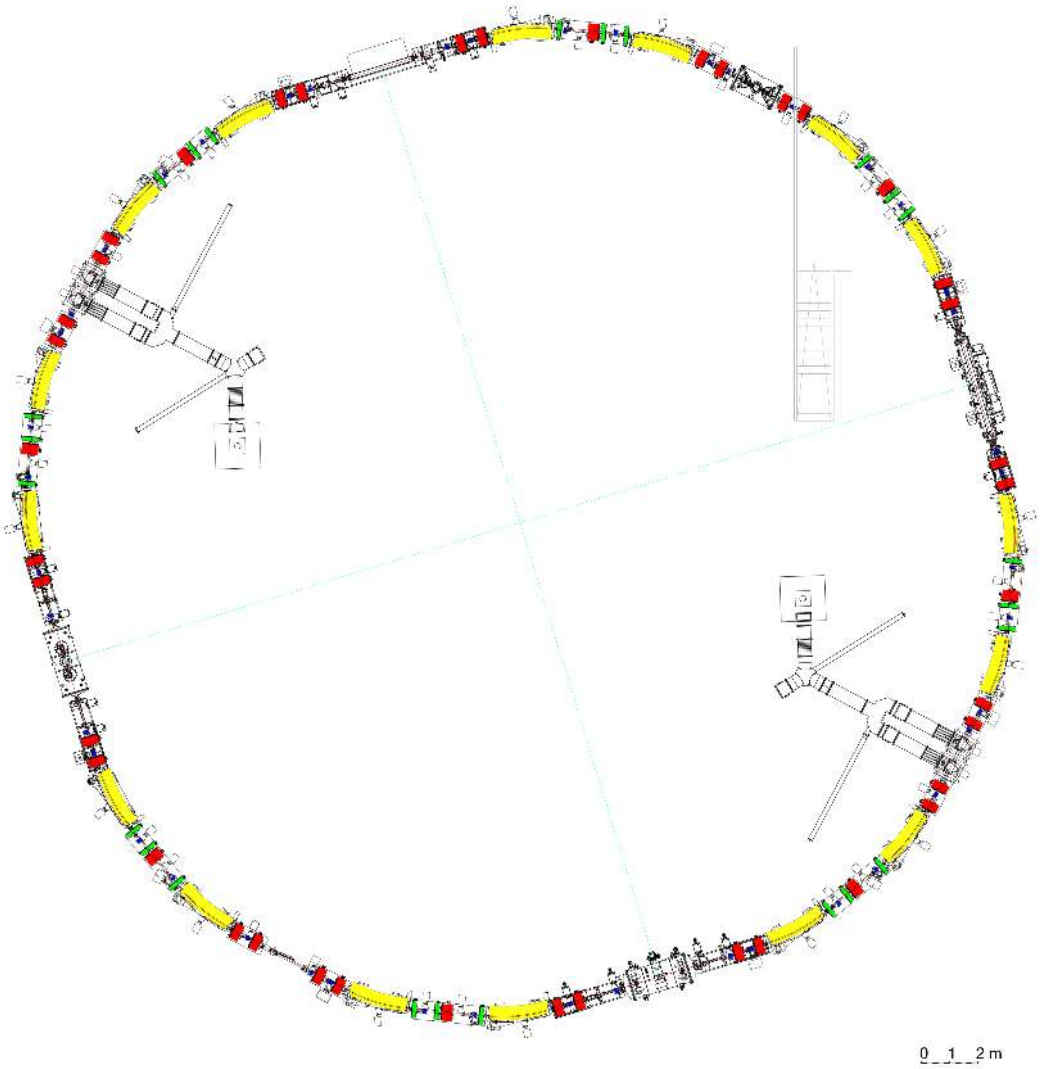

Figure 3.1: Sketch of KARA. It shows the different types of magnets (dipoles in yellow, quadrupoles in red, and sextupoles in green) and the RF system infrastructure. The ring consists of four sectors which are identical except for the RF cavities and the insertion devices in the straight sections. [37]

electrons, can be more intense, can have a higher photon flux or the radiation spectrum can be changed, compared to the synchrotron radiation emitted in a standard dipole magnet. In two of the short straight sections the accelerating cavities are placed. At KARA, the electrons are accelerated in 2×2 500 MHz cavities. The two pairs sit on opposite sides of the ring and each pair of cavities is fed by a 500 MHz klystron.

The vacuum chamber used at KARA has an roughly elliptical shape with a height of 32 mm and a width of 72 mm. The exact dimensions vary depending on the position in the ring. The transverse size of the vacuum camber restricts the maximum wave length

able to propagate in the chamber. The cut-off wavelength below which the propagation of electromagnetic waves is suppressed is given by $\lambda_c \approx \sqrt{4h_c^3/\rho}$ [38] with ρ being the bending radius of the dipole magnets and h_c the vacuum chamber height. For $\rho = 5.559\,\mathrm{m}$ and $h_c = 32\,\mathrm{mm}$ at KARA this results in $\lambda_c \approx 4.9\,\mathrm{mm}$ and a cut-off frequency of $f_c \approx 61\,\mathrm{GHz}$. This suppression in the emission of synchrotron radiation in the low frequencies is where the parallel plates CSR impedance differs from the free space CSR impedance (see 2.6). Also the material, especially the electric conductivity, of the chamber and the different widenings in the vacuum chamber play a role in the dynamics of the stored beam and can be considered in the shape of impedances and wake fields as described in Section 2.6.

3.2 Short Bunch Operation Mode

Operation of KARA is highly flexible. Many parameters (e.g. energy, acceleration voltage, momentum compaction factor, bunch length, and filling pattern) can be varied in a wide range. This thesis makes heavy use of this fact to measure the dependencies of the micro-bunching instability on these parameters. For the measurements conducted the energy was fixed to 1.3 GeV.

As written in Section 2.2, the harmonic number is given by the ratio of the RF frequency and the revolution frequency and defines the number of possible bunches in a storage ring. For KARA with a circumference of 110.4 m the revolution frequency is $\approx 2.715\,\mathrm{MHz}$. Together with the used RF frequency of $\approx 499.65\,\mathrm{MHz}$ this leads to a harmonic number of 184. For normal operation approximately 100 to 136 of these 184 possible bunches are used. They are grouped by approximately 34 bunches[1]. Three to four of these bunch groups (trains) are typically injected. The resulting gaps help to minimize the effects of ion instabilities on the beam quality and lifetime [40; 41]. For this work, nevertheless, the number of filled bunches, their position, and even their individual bunch current were chosen freely, allowing to operate KARA with all kinds of filling patterns, ranging from a single bunch, having every second/third/n-th bunch filled [Ste16] to pyramid shaped or completely random filling patterns. These custom filling patterns are necessary for example for the snapshot measurements presented in Subsection 6.1.2.

While the natural bunch length in normal operation at 2.5 GeV is $\approx 45\,\mathrm{ps}$, a shorter bunch length is necessary to investigate the micro-bunching instability. One way to decrease the bunch length is by modifying the magnet optics to reduce the momentum compaction

[1] The booster has a harmonic number of 44. This batch of bunches is transferred to the storage ring and leads to the train structure. Due to the rise time of kicker and septa magnets during the transfer process $8 - 12$ bunches are lost. [39]

factor α_c as described in Equation 2.15. Therefore, the quadrupole strength is adjusted to obtain partially negative dispersion in the dipole magnets (see Figure 3.2).

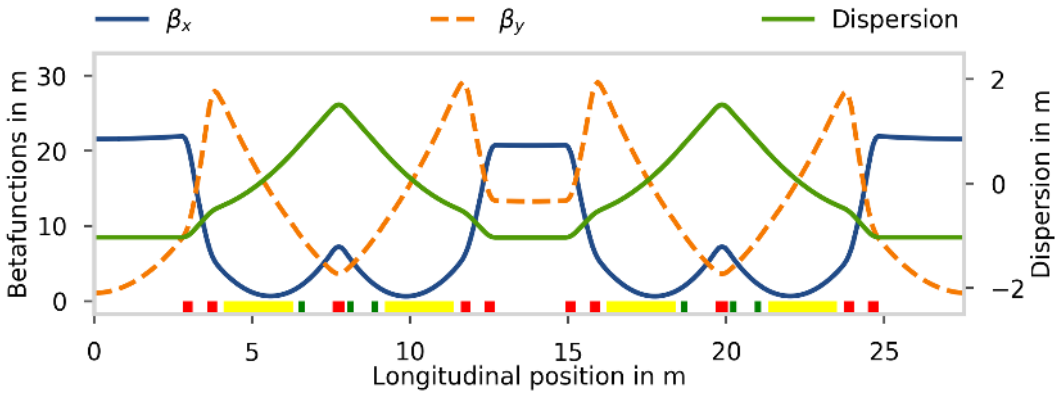

Figure 3.2: Optical functions including the dispersion simulated for a low alpha optics in one sector of KARA. It shows nicely the partially negative Dispersion in the dipole magnets (indicated at bottom in yellow). Courtesy of Patrick Schreiber.

This reduces the integrated dispersion around the ring resulting in a smaller momentum compaction factor α_c (Equation 2.14). This kind of magnet optics is often referred to as low-alpha optics. Different settings for the quadrupole strength are predefined (with matched sextupole values to keep the chromaticity close to 1), allowing operation at different values of the momentum compaction factor ranging from $\alpha_c = 10^{-2}$ (normal operation) to $\alpha_c = 10^{-4}$. This operation mode will be referred to as low-alpha operation. The lower α_c is the smaller the momentum acceptance of the lattice becomes [Pap19]. Hence, fluctuations in the magnet current and therefore a temporally further reduction of α_c can cause the beam to be lost. The lowest reachable value of alpha depends on the stability of the power supplies of the quadrupole magnets. At the moment, operation of KARA at values lower than $\alpha_c = 10^{-4}$ is not reliable.

A complementary way to shorten the bunches is via the amplitude of the acceleration voltage. Equation 2.16 shows that the natural bunch length depends on the local derivative of the acceleration voltage at the (synchronous) phase of the electron bunches. By increasing the amplitude V_{RF} the slope gets steeper leading to a reduction of the bunch length.

Combining these two methods can lead to natural bunch length as short as 1.8 ps for KARA at 1.3 GeV in low-alpha operation. Typical machine parameters for the measurements presented in this thesis are listed in Table A.1.

3.3 RF System and Calibration

As stated above and given by Equation 2.16 the acceleration voltage is, beside the momentum compaction factor, a second possibility to reduce the natural bunch length of the electron bunches. The acceleration voltage is provided by two 500 MHz klystrons which each feed a pair of 500 MHz RF cavities. The typical maximum voltage that can be used for the acceleration is in total 1600 kV.

The amplitude of the acceleration voltage is a set value of the RF system of the machine. As it is also necessary for the calculation of the momentum compaction factor from the measured synchrotron frequency (Equation 2.12, Section 7.2), it is an important parameter and a discrepancy between the set value and the actual voltage in the RF cavities can have an huge impact on measurement and calculation results. So for the analog RF system used until 2015, the set value for V_{RF} was calibrated. This was accomplished via a direct measurement of the beam energy by measuring the Compton back scattering (CBS) of a laser shot at 90° on the electron beam [42]. The dependency of the beam energy on the RF frequency provided then the momentum compaction factor (Equation 6.2 in [43]). With the measured values of α_{c} and f_{s} taken from the CBS measurements [43] the exact value of V_{RF} were calculated ($V_{\mathrm{RF,\,calc}}$) within this thesis. For the calibration of V_{RF} (of the old RF-system) the measurements were conducted at four different magnet optics corresponding to different values of the momentum compaction factor. The set-value of V_{RF} was 140 kV per cavity for all four measurements. The momentum compaction factor determined by the CBS measurement ([43]) as well as the measured synchrotron frequency and the acceleration voltage calculated from that are given in Table 3.1. The resulting calibration factor $f_{\mathrm{calibration}}$ is simply calculated by $f_{\mathrm{calibration}} = \frac{V_{\mathrm{RF,\,calc}}}{V_{\mathrm{RF,\,set}}}$. The uncertainties are calculated using linear error propagation.

Table 3.1: Values obtained by the CBS measurement of the momentum compaction factor and the resulting calibration factors for V_{RF}

α_{c}	$(1.8 \pm 0.5) \cdot 10^{-4}$	$(4.7 \pm 0.2) \cdot 10^{-4}$	$(6.8 \pm 0.2) \cdot 10^{-4}$	$(8.2 \pm 0.1) \cdot 10^{-3}$
f_{s}	4.52 ± 0.09 kHz	6.29 ± 0.13 kHz	7.44 ± 0.18 kHz	25.78 ± 0.52 kHz
$V_{\mathrm{RF,\,set}}$	140 kV	140 kV	140 kV	140 kV
$V_{\mathrm{RF,\,calc}}$	168.82 ± 47.38 kV	125.16 ± 7.31 kV	121.07 ± 6.01 kV	120.55 ± 5.04 kV
$f_{\mathrm{calibration}}$	1.21 ± 0.34	0.89 ± 0.05	0.87 ± 0.04	0.86 ± 0.04

As the set value of V_{RF} was the same for all four measurements, the resulting voltage obtained from the measurements should also be the same. This is only true for the last three measurements while the first measurement is significantly off and also shows a huge error. So, this measurement was ignored and the final calibration factor was taken as the

mean of the other three measurements (0.87 ± 0.03). A cross check of the chosen calibration factor via measured threshold currents is shown in Appendix A.3. In the following, the correction factor is always included in the value of V_{RF} given for measurements, resulting in seemingly random set-values.

A new digital low-level RF (LLRF) system was installed in September/October 2015 [44]. It allows a more flexible control and provides an accurate intrinsic calibration. The remaining error on the acceleration voltage V_{RF} is assumed to be 1%.

Additionally, the new system provides the possibility for synchronized changes of the setting with machine wide trigger signals via the KARA timing system to multiple measurement stations. For example, making triggered shifts of the phase of the acceleration voltage or switching modulations of the phase or the amplitude on and off, synchronized to the data acquisition e.g. with KAPTURE. This is used as a cross check of the synchronization for synchronous measurements described in Section 8.2.

3.4 Timing System

The timing system at KARA [45; 46] consists of one event generator and multiple event receivers. The event generator is directly connected to the master oscillator and provides a reference signal with one quarter of the RF frequency of $\approx 500/4\,\mathrm{MHz} = 125\,\mathrm{MHz}$. The event receivers are situated at the different experimental stations and at all time critical components like the LLRF system (Section 3.3) and Bunch-by-Bunch (BBB) feedback system (Section 4.1). The event receivers are connected to the event generator via fibers. They can provide the received reference frequency at one quarter of the RF frequency as well as different derived frequencies such as the revolution frequency. Additionally, trigger signals can be send to all receivers, e.g. every 10 seconds, which allow the synchronized readout of multiple turn-by-turn capable detector systems (see Section 8.2). It also allows the recording of triggered events like an RF phase modulation (switching between on and off) or for example RF phase jumps or beam dumps [Keh18b].

3.5 CLIC Damping Ring Wiggler

The CLIC damping ring wiggler (CLICDW) is a superconducting wiggler designed to increase the radiation damping in the CLIC damping rings. CLIC is the Compact LInear Collider study [47]. The concept of the CLIC damping rings is to increase the radiation damping and therefore reduce the emittance of the beam after a pre-acceleration before

they are inserted into the main linear accelerator of CLIC itself. Therefore, the rings will contain many damping wigglers.

One prototype is installed in KARA since 2016 for testing of the technical design as well as for studies on its influence on the beam. It can be operated in the 2.5 GeV operation mode of KARA with a field of up to 2.9 T [48]. Despite a strong vertical tune shift created by the wiggler, it can be operated with up to 2 T in KARA's 1.3 GeV operation mode. The CLIC wiggler is a superconducting wiggler and has a fixed gap which means it does not change the geometric impedance like an in-vacuum insertion device would do. Experiments have been conducted to study the influence of CLICDW on the beam quality and the beam dynamic [48; 49]. One experiment will be discussed in Section 7.3, where the influence of the wiggler on the micro-bunching instability was studied. The additional radiation emitted in the wiggler leads to an increase of the energy loss which results in a faster damping (Equation 2.13). This damping can be utilized to study the influence of the longitudinal damping time on the behavior of a bunch in the micro-bunching instability.

4 Diagnostic Infrastructure

This chapter describes the different diagnostic tools used in this thesis. Starting with the measurement of the beam position and the beam current the chapter will cover some standard diagnostics as well as more specialized setups, which allow the observation of the changes in the longitudinal phase space.

The measurement of the filling pattern will be described in detail as it is necessary to determine the bunch currents in multi-bunch fills. For measurements of multi-bunch effects on the micro-bunching instability (Chapter 10) it became necessary to reduce the systematic errors in the measured bunch currents drastically. Therefore, a correction of the dead time effect in the filling pattern measurement was implemented and tested in cooperation with Benjamin Kehrer (KIT, [50]).

As described in Section 2.9, the micro-bunching instability leads to substructures forming in the longitudinal phase space of the electron bunches. These substructures form, dissolve, and rotate in the phase space. Due to the deformations in the phase space, also the energy spread and the longitudinal charge density (the projection of the phase space on the time axis) changes dynamically. The changes in the energy spread are measured by monitoring the horizontal bunch size. For the longitudinal profile, as the substructures are in the order of picoseconds at KARA, a high temporal resolution as provided by the electro-optical measurement setup is necessary. The diagnostics used to observe the coinciding strong fluctuations in the emitted radiation in the THz regime will be presented in the next chapter.

4.1 Bunch-by-Bunch Beam Position Monitor and Feedback

The Bunch-by-Bunch (BBB) feedback system is a digital, three-dimensional, fast feedback system to interact with the individual electron bunches [51].

Bunch position monitors (BPM) are used to measure the three-dimensional position of the center of charge of each bunch. In standard operation, the BBB feedback system is used to calculate the oscillation spectrum from the measured X and Y positions as well

as the arrival time and then to apply the necessary correction (phase corrected) to damp unwanted oscillations and instabilities. The feedback is applied with two strip lines for X and Y direction and a small longitudinal kicker cavity for the longitudinal component [51; 52]. The kind and strength of the feedback can be configured. So that not only the damping but also the excitation of specific frequencies is possible. This is done for each bunch individually and can improve the lifetime and stability of the stored electron beam [52].

The BBB does not only provide feedback but naturally also functions as a bunch-resolved measurement device for the position and the arrival time. As the whole oscillation spectrum of all three dimensions can be calculated this gives the tunes respective the betatron and synchrotron frequencies. But also any other dominant frequency in the motion of the center of charge can be identified from these measurements. This was for example used in a related master thesis [53] where the low fluctuation frequency of the micro-bunching instability was detected in the oscillation spectrum of the longitudinal as well as the transverse center of charge positions measured with the BBB system.

In the course of this work, the BBB system was used to generate custom filling patterns and measure the synchrotron frequency. The synchrotron frequency is determined with an automated peak finder directly from the spectrum of the arrival time oscillation measured by the BPMs. Depending on the frequency resolution of the spectrum and the signal-to-noise ratio the peak finder can identify the synchrotron frequency with an accuracy between 100 Hz and down to 10 Hz. This results in an uncertainty of less than 1.5 % for the measurements in the framework of this thesis.

To shape the filling pattern, which is the distribution of the electrons onto the bunches around the ring, the individual bunches can be exited so that they lose electrons faster until each bunch contains its designated bunch charge. In this way all kind of filling patterns are possible. A single bunch can be obtained by exiting all other bunches in a way that all contained electrons are lost. Within the scope of this thesis, mostly filling patterns covering a wide bunch current range were necessary to study current-dependent effects in a short time (see Subsection 6.1.2). For this, the bunch current in the individual bunches was reduced to different values. Depending on the application, the bunch current values can be distributed on the bunches in any pattern wanted. Figure 4.1 shows a filling pattern where the currents were sorted in an increasing order for the first train, a decreasing for the second train, and are randomly distributed in the third train.

Furthermore, the BBB gives a rough estimation of the charge per bunch via the sum signal of the BPM and was used as rough first estimation when the precise filling pattern measurements explained in Subsection 4.3 are not directly available.

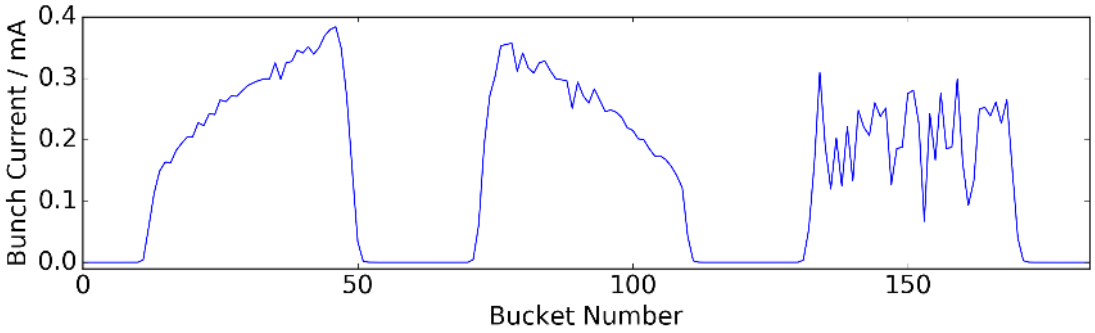

Figure 4.1: Bunch current in the 184 bunches with a filling pattern of three trains. The current is increasing over the first train, decreasing over the second train and shows a random distribution within the third train.

4.2 Beam Current Measurement

The beam current, as defined in Equation 2.4, can be measured non-destructively with a current transformer. It measures the magnetic field of the electron beam by defining the beam as the primary winding of the transformer and measuring at the secondary winding. The device used at KARA is a commercially available parametric current transformer (PCT) from Bergoz (Figure 4.2) [54]. The measurement range goes up to 600 mA with a resolution of $< 0.5\,\mu A$ for an integration time of 1 s. With an integration time at KARA of 0.7 s an uncertainty of 0.6 µA is expected. Measurements at very low currents (≈ 0.1 mA) gave an uncertainty of 0.55 µA [55]. In the following, this error will be used for beam current measurements.

(a) (b)

Figure 4.2: Photographs of the parametric current transformer from Bergoz installed at KARA.

How the beam current is distributed on the bunches in a multi-bunch fill can be determined by measuring the normalized filling pattern and multiplying it with the beam current. Further information on this method as well as an estimate of the uncertainties on the

resulting bunch currents is given in Subsection 4.3.

4.3 Filling Pattern Monitor

The distribution of the current over the bunches in the ring is called filling pattern. It can be determined e.g. by the technique of Time Correlated Single Photon Counting (TCSPC) [56]. This setup is located at the visible light diagnostics port (VLD) [56] of KARA. The visible part of the synchrotron radiation at KARA is purely incoherent. It can therefore serve as a convenient diagnostic tool. An incoherent synchrotron radiation pulse directly represents the distribution of the emitting electrons. The power of this radiation is proportional to the amount of electrons emitting [15]. The VLD port uses incoherent synchrotron light in the visible range from a 5° port front end of a dipole magnet. The light is transported via two off-axis paraboloid and two planar mirrors onto an optical table. To distribute the light to different setups, the light is split into different spectral parts by two bandpass filters. The light passing the first bandpass with a central wavelength of $\lambda = 400\,\mathrm{nm}$ is guided to the time correlated single photon counting device used for measuring the filling pattern.

The TCSPC setup at KARA consists of a single photon avalanche diode and a histogramming device. As diode a single photon avalanche diode (id100-20) from IDquantique is used. It detects the emitted photons in the visible range of the synchrotron radiation. In this wavelength region, the synchrotron radiation is incoherent and thus the emitted number of photons is proportional to the number of electrons emitting and proportional to the stored current. Using a two channel histogramming device, such as the PicoHarp 300 from PicoQuant [57], the detected photons are counted and sorted into a histogram according to their arrival time relative to the revolution clock. After accumulating for several seconds, the resulting histogram gives the temporal distribution of all electrons relative to the revolution clock (see Figure 4.3 for the signal of a few bunches). To get the current of each bunch, 46025 (of the total 65536, each 8 ps long) bins of the histogram are divided in packets of 2 ns duration (corresponding to the RF-bucket size) to count the number of photons emitted per bunch [50]. Then the filling pattern is normalized and multiplied with the beam current measured by the PCT (Section 4.2) giving the absolute current of each bunch.

For single bunch operation, this measurement is used to determine the purity of the single bunch filled.

As the bunch current is an important parameter for nearly all measurement conducted in

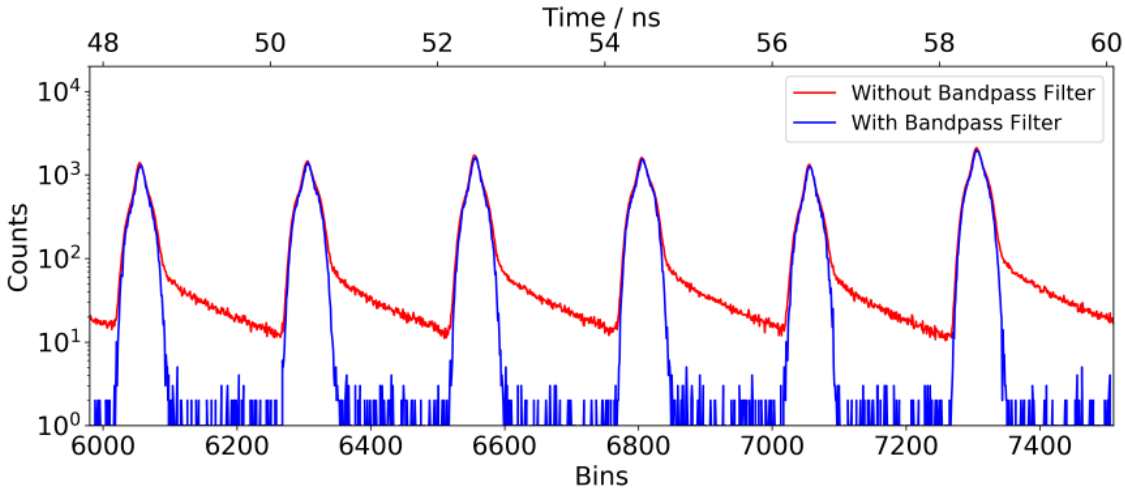

Figure 4.3: PicoHarp counts as a function of time. The histogramming device sorts the detected photons in bins of 8 ps width according to their detection time in reference to the revolution clock. By using a bandpass filter for the incoming photons, the diffusion tail is reduced and the influence from one bunch on the measured value of the following bunch is suppressed.

this thesis, it is important to have a correct approximation and detailed knowledge of the uncertainties and measurement errors on the bunch current. The following sections will give an overview of the biggest effects and contributions to the uncertainty.

4.3.1 Statistical Error

The statistical error on the filling pattern is dominated by the Poisson statistics and therefore can be calculated from the measured counts ν_b per bunch b as:

$$\frac{\sigma_{\mathrm{I_b}}}{\mathrm{I_b}} = \frac{1}{\sqrt{\nu_\mathrm{b}}} \tag{4.1}$$

This results in a higher relative error for smaller bunch currents as the count rate is proportional to the bunch current. To reduce the measurement error a high number of counts is necessary. But as a too high count rate leads to strong systematic measurement errors due to the dead time effect (see following section and [Bro17a]), a lower count rate combined with a longer integration time is favorable. On the other hand it needs to be considered that the bunch current changes (decreases) during the measurement, resulting in a decreased temporal resolution for longer measurement durations. With an attenuation reducing the count rate below the impact of the dead time effect, or to a correctable impact, the integration time per measurement was chosen to be 30 s.

The overall error on the bunch current measurement consists of the statistical error on the

beam current measurement (see Section 4.2) and the error on the filling pattern. It will be derived in Subsection 6.2.

4.3.2 Systematic Errors and Dead Time Correction

Systematic errors on the filling pattern measurement can falsely look like systematic effects of the measured parameter depending on the bunch currents. For example, an incorrectly measured distribution of the beam current on the bunches would lead to incorrectly determined bursting thresholds and thus potentially displaying a similar signature as multi-bunch effects as was shown in [Bro17a]. Hence, it is crucial to avoid deformations in the measured filling pattern. They can originate for example from a dead time of parts of the setup, which will be discussed in more detail below. Another possible source is the accuracy achieved by the setup in measuring the bunch purity. It can be limited by the diffusion tail effect, which is described nicely in [50; 56]. Using a narrow bandpass filter suppresses the effect (see Figure 4.3) and results in a dynamic range for bunch purity measurements of approximately 10^3 to 10^4.

Measurement of the Dead Time of the System

The dead time of the used PicoHarp 300 was measured to be $\tau_{\mathrm{d,\,PH}} = 86.8 \pm 0.2\,\mathrm{ns}$, which is significantly longer than the distance between bunches and can therefore lead to missed counts and a systematic deformation of the measurement results. To measure the dead time the input channel was connected to a frequency generator that generates logical pulses with an adjustable frequency. Then the count rate was determined as a function of the input count rate (see Figure 4.4). The count rate is equal to the input rate as long as it is below $1/\tau_{\mathrm{d,\,PH}}$. As soon as the input rate is higher than the inverse dead time, the detected count rate drops to half the input rate, as every second event falls in the dead time and is therefore missed. The same drop in count rate appears when the input rate exceeds twice the inverse dead time. In Figure 4.4, these two drops are clearly visible. The dead time of the single photon avalanche diode (SPAD) was measured to be $\tau_{\mathrm{d,\,SPAD}} = 37 \pm 1\,\mathrm{ns}$ by displaying the detector response to bright light on an oscilloscope with infinite persistence mode. The dead time is clearly visible in Figure 4.5 as the time where no second pulse after the initial pulse is detected. As the dead time of the SPAD is shorter than the one of the PicoHarp, it only becomes relevant when an event detected by the SPAD falls in the last 37 ns of the PicoHarp dead time. This will then extend the total dead time to a maximal value of $87 + 37\,\mathrm{ns}$. So the dead time of the SPAD can be considered an second order effect [50; Bro17a] and will be neglected in the following calculations.

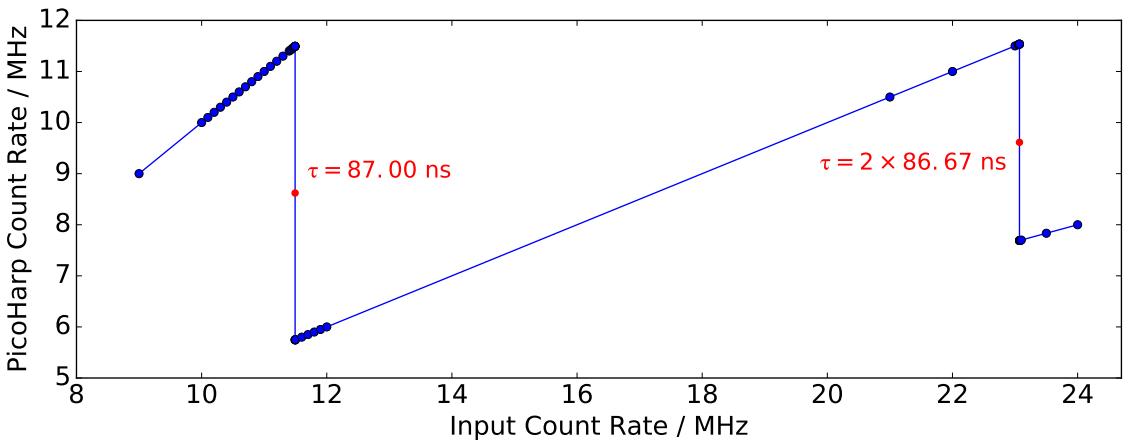

Figure 4.4: PicoHarp count rate over input count rate generated by a frequency generator. As the input rate is varied the count rate drops to half the input rate when it exceeds the inverse dead time of 87 ns. A similar drop occurs when the input rate exceeds twice the inverse dead time.

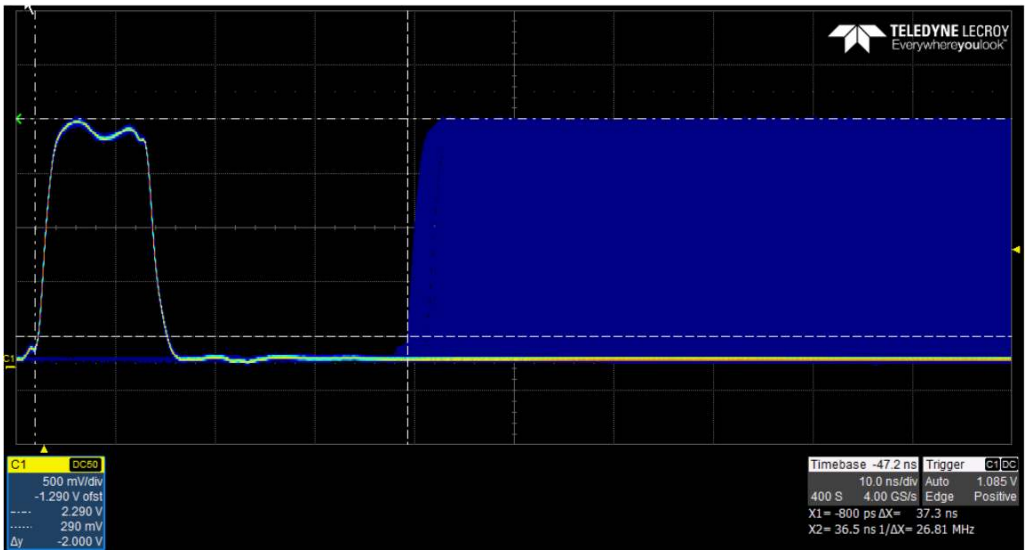

Figure 4.5: Dead time of the single photon avalanche diode measured in infinite persistence mode on an oscilloscope. The dead time is visible as time during which the next event after an initial one can not be observed. A second event could be observed as early as 37 ns after the initial one, defining the dead time.

Correction for the Dead Time

The effects due to this dead time on the measured filling pattern can be estimated as described in [58]. The probability p_{b} that a photon is detected from bunch b at one passage is proportional to its bunch current. In a circular light source, the probability $p_{\mathrm{b,\ dead\ time}}$ for a photon from bunch b being detected per revolution can be derived from the probability $p_{\mathrm{b,\ no\ dead\ time}}$ of a photon being detected without the dead time effects present, multiplied with the product of the probabilities that no photon was detected in the 44 previous bunches ($\hat{=}\,87\,\mathrm{ns}$):

$$p_{\mathrm{b,\ dead\ time}} = p_{\mathrm{b,\ no\ dead\ time}} \prod_{j=\mathrm{b}-44}^{\mathrm{b}-1} (1 - p_j)$$

This is valid under the assumption that only one photon is emitted per bunch and revolution so that only the photons emitted by previous bunches need to be taken into account. This assumption was considered to be true for the calculations within the scope of this work. The corrected number of photons ($\nu_{\mathrm{b}} = N_{\mathrm{rev}} \cdot p_{\mathrm{b}}$) is given by

$$\nu_{\mathrm{b,\ corrected}} = \frac{\nu_{\mathrm{b,\ dead\ time}}}{\Pi_{j=\mathrm{b}-44}^{\mathrm{b}-1} \left(1 - \frac{\nu_j}{N_{\mathrm{rev}}}\right)}$$

with the number of turns N_{rev} per acquisition time. With the assumption that the probability $p = \nu/N$ is small, the product can be replace by a sum. Additionally this leads to a higher numerical stability as higher order terms are neglected.

$$\nu_{\mathrm{b,\ corrected}} \approx \frac{\nu_{\mathrm{b,\ dead\ time}}}{1 - \sum_{j=\mathrm{b}-44}^{\mathrm{b}-1} \left(\frac{\nu_j}{N_{\mathrm{rev}}}\right)} \tag{4.2}$$

Test of Correction

Using Equation 4.2 the measured filling patterns can be corrected for the influence of the dead time of the detection system. To test this correction, two measurements of the same filling pattern were taken. For the reference measurement without an influence of the dead time effect, the count rate was decreased to $\approx 250\,\mathrm{counts/s}$ per bunch using a 0.01 neutral optical density filter and the measurement duration was 2 minutes. From this measurement the reference filling pattern was calculated. The second measurement was taken without a filter at a count rate of $\approx 1.5 \cdot 10^4\,\mathrm{counts/s}$ for each bunch (over 1 minute). The resulting filling pattern once calculated with and once without the correction is compared to the reference one in Figure 4.6.

The distortion due to the dead time effect in the uncorrected high count rate measurement is directly visible in the difference to the reference measurement. With the correction applied this difference is reduced from a maximal deviation of $\pm 53\,\mu A$ ($\approx 15\,\%$) to a maximal deviation of $\pm 12\,\mu A$ ($2.4\,\%$) and is now closer to the resolution limit of the reference measurement ($\approx 0.58\,\%$), given by the Poisson statistics (Equation 4.1). For these test measurements the high count rate of $\approx 1.5 \cdot 10^4\,\text{counts}/\,(\text{s} \cdot \text{bunch})$ (statistical error $\approx 0.11\,\%$) was used to test the limits of the correction.

To reduce the error remaining after applying the correction, it was decided for following measurements to keep the count rate at a lower value balancing the advantage of a smaller remaining error of the dead time effect and the disadvantage of increasing the statistical uncertainty due to the reduced number of counts. As written in the section above a longer integration time improves the statistical uncertainty for low count rates. A measurement duration of 30 s was chosen to still have an reasonable time resolution when studying the bunch current over time. For example, a statistical uncertainty of $0.5\,\%$ can be achieved for a 30 s measurement with a count rare of $\approx 1.3 \cdot 10^3\,\text{count}/\,(\text{s} \cdot \text{bunch})$ which is more than a factor of ten smaller than the one in the test measurement. Extrapolating from the deviation of the test measurement (with high count rate) before and after correcting to the now assumed lower count rate, results in an estimated dead time error after the correction of approximately $0.2\,\%$.

Figure 4.7 shows an example of how the uncorrected dead time effect can have a strong influence on measurement results. Without the correction the filling pattern is distorted and leads to wrong bunch current values for the different bunches when they cross the bursting threshold. This difference in the bursting threshold of bunches in a multi-bunch fill is drastically reduced when the dead time influence is corrected [Bro17a].

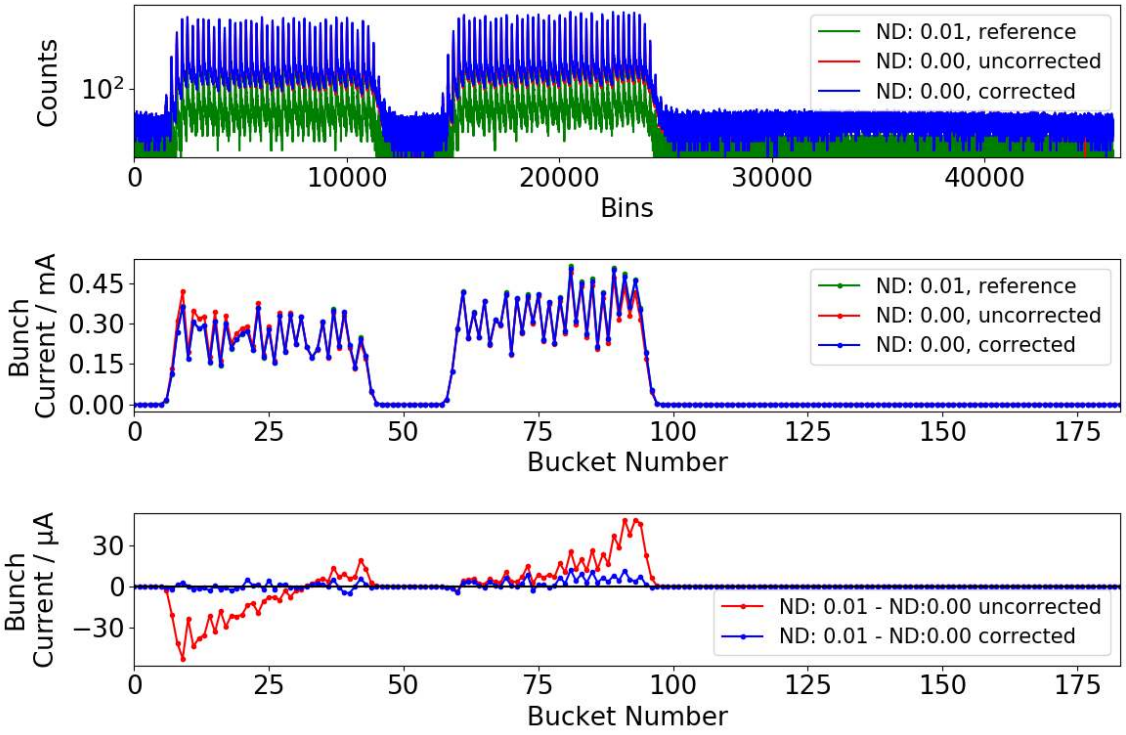

Figure 4.6: Measurement to test the correction algorithm for the dead time effect. A measurement with a neutral density filter (ND: 0.01) was taken as reference and directly afterwards a measurement without the filter (ND: 0.00) was taken. The upper panel shows the measured histograms for the reference measurement as well as the uncorrected and dead time corrected values for the measurement without filter. The 2nd panel shows the resulting bunch currents for the three cases. And the difference between the reference measurement to the uncorrected and the corrected respectively is shown in the lower panel.

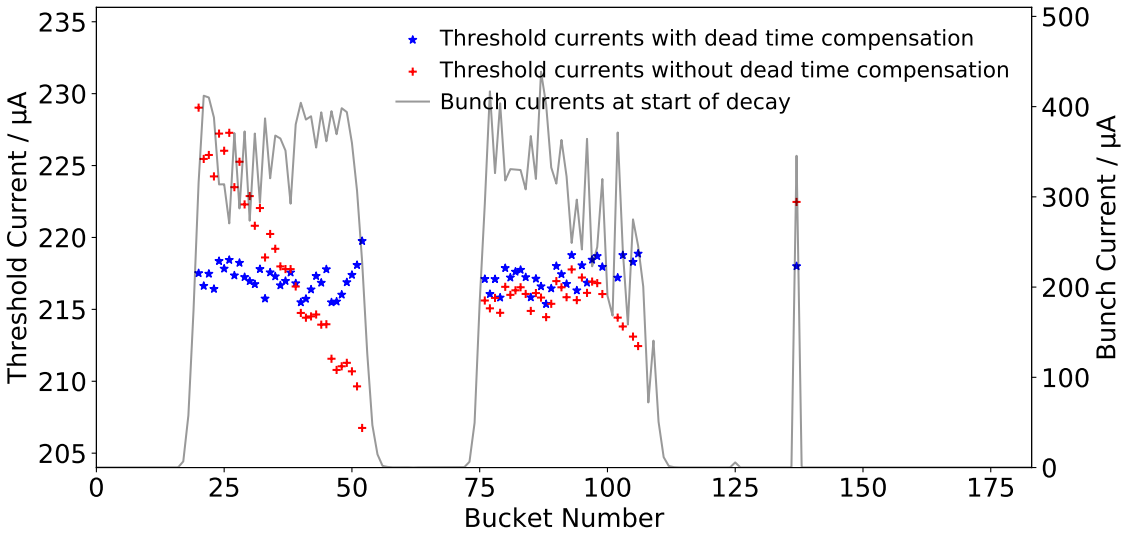

Figure 4.7: Threshold current per bunch as function of bunch number. Due to the dead time effect the bunch current is determined falsely, leading to differences in the threshold currents (in red). The systematic in the differences originates from the combination of the dead time duration of 87 ns (44 buckets) and the filling pattern (in grey). After the compensation of the dead time effect the systematic differences vanish and the spread decreases (in blue).

4.4 Horizontal Bunch Size Monitor

Another experiment situated at the VLD port is a horizontal bunch size monitor. It uses light passing the $\lambda = 500\,\mathrm{nm}$ bandpass filter at the VLD port. As the horizontal bunch size is coupled to the energy spread via the dispersion [15], it is an important parameter for the study of the longitudinal phase space. The changes occurring in the horizontal bunch size estimated from the measured profile are used as an indication for the changes in the energy spread [50].

The source point of the light in the VLD port lies within a dispersive section and therefore provides the necessary coupling between the longitudinal and horizontal plan. The measurement setup consists of optics which provide a source point image of the transverse beam profile. The spot, which is enlarged horizontally while the vertical size is reduced, is put on an image sensor to record the development over turns. This can either be done via a fast rotating mirror onto a fast gated intensified camera [Keh17; 53; 50; Ste18c]. In this way, the gate of the camera can be used to select the pulse of a specific bunch in a multi-bunch fill at every 6th turn (or more seldom). The rotating mirror sweeps the light over the sensor resulting in several spots (max. 80) next to each other on the CCD sensor, showing the temporal evolution.

Another possibility realized at KARA is using a single line array detector with an ultra-fast readout system (KALYPSO [59]), which was originally designed for usage with the electro-optical setup (see Section 4.5) [50; Ste18c; Keh19a]. In this case the spot of a single bunch can be detected and readout at every turn (2.7 MHz). The latter option has the advantage that every turn can be recorded for a long time, while the first setup only allows every 6th turn or slower (max 450 kHz) and only up to 80 spots can be fitted on the screen. Nevertheless, the first option has the advantage that due to the gating (which is realized by a micro-channel plate intensifier) one bunch can be observed in a multi-bunch environment and that due to the intensifier the increased sensitivity allows to measure at significantly lower bunch currents.

This setup can be triggered so it can be used for synchronous measurements with e.g. the electro-optical setup and the THz intensity measurements (see Section 8.2) [Keh17].

4.5 Electro-Optical Setup

To measure the longitudinal bunch position and bunch profile as directly as possible a near-field electro-optical setup (Figure 4.8) was installed at KARA. It was the first to

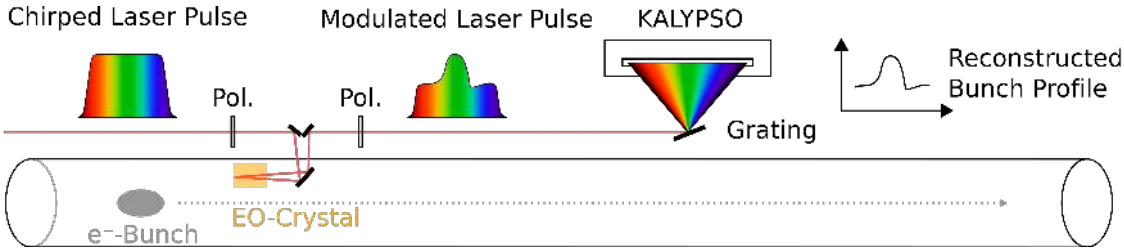

Figure 4.8: The electro-optical setup for measuring the longitudinal bunch profile consists of a GaP crystal inside the vacuum pipe. A laser pulse chirped in frequency is send through the crystal to sample the change in the birefringence due to the passing electro-magnetic field of the electron bunch flying by. In this way, the longitudinal bunch profile is imprinted on the laser pulse and can be decoded with a spectrometer, in this setup a grating and a fast line array detector (KALYPSO).

be installed at a storage ring directly in the vacuum camber [60; Bie19]. In single bunch operation it can be lowered into the vacuum chamber close to the path of the electron beam.

The setup inside the vacuum consists mainly of a gallium phosphite (GaP) crystal. Due to the pockels effect, this crystal becomes birefringence when it is exposed to the electromagnetic near-field of an electron bunch flying by. This change of polarization is detected by measuring the intensity change of a pre-polarized, short laser pulse guided through the crystal. As the intensity change of the laser pulse can be correlated to the strength of the electromagnetic field, the crystal is exposed to, the longitudinal charge density of an electron bunch can be sampled by shifting the laser pulse relative to the arrival time of the bunch for each revolution. This method, referred to as Electro-Optical-Sampling (EOS), does not allow the determination of the whole field distribution per turn, it only provides a sampled charge distribution.

A more complex measurement method, Electro-Optical-Spectral-Decoding (EOSD), overcomes this drawback, by sending a longer laser pulse with a frequency chirp through the crystal. In this way, the temporal information of the field strength is modeled on the long laser pulse as frequency information and can be decoded with a spectrometer. EOSD therefore provides a single-shot measurement of the longitudinal charge distribution and can thus resolve the development and potential deformation of the longitudinal bunch profile over the turns [Nie18; 61].

The detection of substructures on the longitudinal bunch profile gives important insight on the dynamics in the longitudinal phase space, as described in Section 2.9. To get continuous information about the development of the bunch profile over the turns, a new and faster spectrometer was developed by KIT-IPE [59; 62]. It can detect the bunch profile of a single

bunch at every turn for several seconds. It consists of a grating plus a line array detector with an ultra-fast readout system called KALYPSO, which is based on the same design as KAPTURE (see Subsection 5.3.2).

The usage of KALYPSO also allows triggered measurements synchronized to measurements of e.g. the THz emission with KAPTURE (see Section 8.2).

5 THz Diagnostics

THz radiation is an important tool (and the main tool in this thesis) in the investigation of the micro-bunching instability. As described in Section 2.9, the substructures occurring on the bunch during the instability lead to the emission of coherent synchrotron radiation in the low THz frequency range. The intensity of this radiation fluctuates due to the dynamics of the instability and therefore gives an insight in the time scales of the dynamics. Therefore, it is of interest how the emitted THz power changes for each bunch over time. To detect these changes, the amplitude of the THz detector pulse for each bunch at every turn is recorded.

In the following, the used equipment is described from the beam line, the optics, and the fast THz detectors over the fast readout systems signal digitization to a short overview of the data analysis.

5.1 IR Beam Lines

The synchrotron radiation emitted in each bending magnet, can be extracted from three ports per magnet and then guided in a vacuum tube to the experimental hutches to be used. These ports sit at an bending angle of the particle beam of 0° (corresponding to the entry edge of the magnet), 5°, and 11.25°, respectively.

The different source point in the bending magnet has an influence on some properties of the emitted synchrotron radiation. Due to this, the two infrared beamlines at KARA are situated at 0° degree ports and provide edge radiation. This radiation is a combination of the radiation emitted by the electron beam at the exiting edge of the previous dipole magnet and the entry edge of the present dipole magnet as well as a (small) proportion of normal bending radiation from the electron flying out of focus further along the bending magnet. This can be seen in the spacial distribution of the visible light spot at the beamline. As shown in [63], a small point of high intensity caused by the edge radiation can be seen on top of a slightly curved streak of weaker intensity caused by the bending radiation contribution. As described in [64], this combination results in the emission of a different

synchrotron radiation spectrum compared to normal synchrotron radiation emitted in a dipole magnet, with a higher intensity in the longer wavelengths. The Infrared1 beamline was one of the first far-infrared beamlines to use edge radiation [65]. Even though the infrared beamlines were built and optimized for the infrared range (2.5 mm and 1 µm (0.12 THz to 300 THz)) [66; 67] they partially transmit down to some tenth GHz and also visible light. Therefore, enough intensity is provided for the THz measurements, from 80 GHz up to several THz, presented in this thesis. And the additional emission of some (incoherent) synchrotron radiation in the visible range is useful for e.g. the synchronization of the readout systems described in Section 8.2. The (measured) coherent edge radiation will be simply referred to in the following as coherent synchrotron radiation (CSR) as the properties concerning the coherence are identical.

The standard approach of geometrical optics assumes that all components and the dimension of the beam are significantly larger than the wavelength so that diffraction effects can be neglected. Due to the rather long wavelength of THz radiation, the dimensions of the used optics are only a few times the wavelength. In this regime, the geometrical optics can not be applied anymore and it is referred to as quasi-optics [68]. As the size of the synchrotron light beam is only a couple times the wavelength, it typically can be described as Gaussian beam and the Gaussian beam propagation formalism can be used, which includes diffraction [68].

The IR beamlines use flat and toroidal mirrors to guide the infrared component of the emitted synchrotron radiation to the diagnostic port [65]. The beamlines were designed to provide a collimated beam for the different experimental stations, but the beam is divergent if coupled out at the diagnostic port window. Profile measurements of the provided THz beam, showed that for THz frequencies, the beam is slightly diverging [55]. To focus the radiation on the detector an offaxis parabolic mirror is used.

5.2 THz Detectors

To detect the emitted THz power of each bunch individually, sufficiently fast detectors have to be used. At the same time they need to be sensitive enough to detect and resolve the expected fluctuation in the emitted power. The RF frequency of KARA of 500 MHz (see Chapter 3) results in a spacing between the bunches of 2 ns. So the pulse response of the detector needs to be shorter than 2 ns.

The length of an emitted synchrotron light pulse is, for ultra-relativistic particles, of the same length as the emitting bunch, which range, for the presented studies, from 2 ps for low

Figure 5.1: The photo shows the zero-bias, quasi-optical, room-temperature Schottky barrier diode detector from ACST. It consists of an silicon lens, a log-spiral antenna, the actual zero bias Schottky barrier diode, and the built-in 4 GHz amplifier.

bunch currents up to 25 ps and more for higher currents and higher momentum compaction factors. To resolve the pulse form or even determine the pulse length, the detector would need to be faster. This includes the detection mechanism, the analog output bandwidth, and also the analog input bandwidth of the readout system used. While some detection mechanisms exist that provide fast enough responses, the analog output bandwidth is mostly limited to below 100 GHz, due to the lack of electrical connections and cables with a higher bandwidth. Also only a few oscilloscopes can provide such a high analog input bandwidth and sampling rate. As the most important parameter in the scope of this thesis is to resolve the fluctuation in the emitted THz power per bunch per turn, detectors were chosen that are fast enough to resolve the different bunch but are to slow to determine the bunch length or the pulse shape.

This requirement is satisfied by zero-biased Schottky barrier diode (SBD) detectors. A Schottky diode is a standard electrical component consisting of a metal-semiconductor junction and is used as a rectifying circuit. Due to its nonlinear current-voltage characteristic (I-V curve) it can be used to measure the RF power in a signal. For this thesis several detectors were available. The used broad-band quasi-optical Schottky barrier diode detector from ACST GmbH (Advanced Compound Semiconductor Technologies [69; 70; 71]), shown in Figure 5.1, consists of a spherical silicon lens on a log-spiral planar antenna, the detector element and an internal 4 GHz amplifier. The spectral sensitivity is given by the characteristics of the antenna and ranges from 50 GHz up to 1.2 THz, with a maximal sensitivity at 70 GHz. Due to the low analog bandwidth of the internal amplifier the response time of the detector is ≈ 160 ps FWHM.

Additionally waveguide coupled Schottky barrier diode detectors from Virginia Diodes, Inc. (VDI, [72]) were used. The synchrotron radiation is coupled via horn antennas into waveguides guiding the radiation onto the detection element. The spectral sensitivity

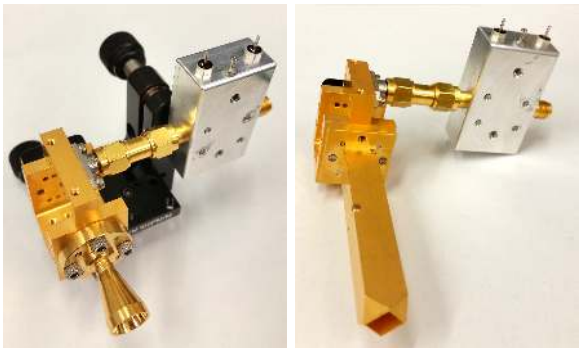

(a) (b)

Figure 5.2: Photographs of VDI SBD detectors with a spectral sensitivity band of 140 − 220 GHz (a) and 220 − 325 GHz (b). Different horn antennas, fitting the spectral sensitivity, are attached to couple the radiation into the waveguide. The silver block is an external 18 GHz amplifier.

depends on the dimensions of the waveguide. The lowest sensitivity band of the used detectors is from 90 − 140 GHz while the highest band ranges from 500 − 750 GHz. The photographs in Figure 5.2 show diodes sensitive in the range of 140 − 220 GHz and 220 − 325 GHz. All of the used VDI detectors have an analog output bandwidth higher than 12 GHz and can be combined with external 18 GHz amplifiers if necessary.

A diagram with the spectral responsivity of the different Schottky barrier diode detectors can be found in Figure A.1. The narrow-band waveguide coupled VDI detectors have a higher responsivity in their frequency band while the ACST quasi-optical broad-band detector has a lower responsivity but over a significantly wider spectral range.

Due to the different analog output bandwidth of the different detectors their response times differ (see Figure A.2). The response of the ACST detector consists of a initial, relatively long pulse due to the low analog output bandwidth of 4 GHz, followed by ringing which takes nearly the 2 ns bunch spacing to damp down. The response of VDI detector shows a significantly shorter pulse and less ringing afterwards.

5.3 Fast Detector Readout

The study of the micro-bunching instability puts high demands on the detector readout systems. To study each bunch in a multi-bunch environment the readout needs to be able to resolve the THz pulses from different bunches with a bunch spacing of 2 ns. Or at least for single bunch measurements, the revolution frequency of 2.7 MHz. The biggest challenge is the combination with the time scale of the dynamics in the instability ranging from

multiples of the synchrotron frequency (some tenth of kHz) over milliseconds (periodicity of bursts) to hours for bunch current-dependent effects. This monitoring of a long time scale with a high temporal resolution is not easily met by standard readout systems like oscilloscopes.

In the following, two operation modes (peak detect mode and segmented mode) for oscilloscope are shortly presented, which can satisfy parts of the demands listed above. To meet all the requirements, a dedicated readout system, called KAPTURE, was developed in an in-house cooperation with the Institute for Data Processing and Electronics (IPE). KAPTURE stands for KArlsruhe Pulse Taking and Ultra-fast Readout Electronics. In the last section, the handling and analysis of the resulting large datasets will be outlined briefly.

5.3.1 Readout via Oscilloscope

There are commercially available oscilloscopes which provide a fast enough sampling rate to resolve the bunch spacing of 2 ns. However, due to the limited memory depth, the high temporal resolution leads to a short time for which the signal can be recorded continuously. Figure 5.3 shows the temporal evolution of the detected THz signal of one train with ≈ 33 bunches.

Instead of sampling continuously also the uninteresting time between the THz pulses, two possible recording modes are available. The peak detect mode saves only the maximum value of a certain time range (e.g. several turns) omitting the rest of the signal and, therefore, being more memory efficient. This mode has the disadvantage that it can only be used in single bunch operation. The time range in which the maximum is determined can not be short enough for resolve every bunch in a multi-bunch filling pattern. This

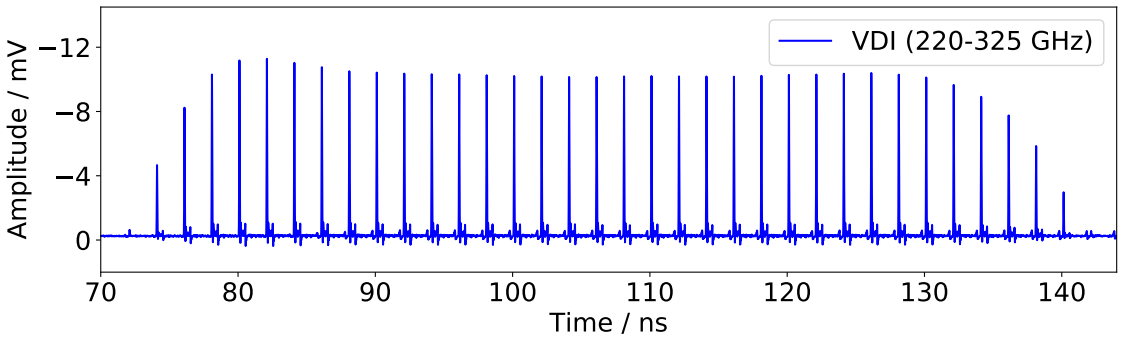

Figure 5.3: THz signal of one train detected with narrow-band VDI detector showing the long time between the THz pulses by the different bunches.

would lead to only the bunch with the highest signal being sampled.

The second recording mode is called segmented mode and can be in multi-bunch operation. In this mode, several thousand short segments are taken with a high temporal resolution shortly after each other. The duration of one segment could range from some bunches ($\approx 4\,\mathrm{ns}$) to one turn (368 ns). The minimal distance between the different segments depends on the specific oscilloscope used (for example between 300 ns and 4.5 µs for the devices used in this thesis). This saves memory space compared to continuous sampling but at the same time can show the development of the signal better as the segments can follow faster on each other, than normal acquisitions could.

The exact times and durations an oscilloscope can record, depend strongly on its price. But the memory depth will always limit the maximal recorded time. To circumvent this, a dedicated readout system was developed. KAPTURE was designed to sample only the interesting parts of the detector signal and provide continuous readout indefinitely. It is described in the following chapter.

5.3.2 Readout via KAPTURE System

KAPTURE stands for KArlsruhe Pulse Taking and Ultra-fast Readout Electronics. It was developed in an in-house cooperation with the KIT institute IPE (Institute for Data Processing and Electronics) [Cas14a]. KAPTURE is designed to digitize the signal of each bunch at every revolution individually over a long time up to continuously. And at the same time saving memory by not sampling the long "dark" time between the bunches.

The complete KAPTURE system consists of 4 sampling channels on a digitizing board connected to an FPGA, which itself is connected via PCI-Express to a control PC. Each channel contains a Track and Hold unit (T/H) with an analog bandwidth of 18 GHz and a 12-bit, 500 MSa/s analog-to-digital converter (ADC) [Cas14a]. Via a PLL (phase locked loop) KAPTURE is connected to the timing system of the storage ring. In this way, it is assured that the ADCs are synchronized to the RF system and the sampling point does not shift relative to the RF phase with time. To sample exactly at the point in time a bunch comes by, the timing can be delayed globally and between the channels with a minimal step size of 3 ps [Cas14b].

Two different operation modes are possible. One single detector can be connected to a 1:4 splitter, splitting the signal to the four channels equally. Shifting the timing between the channels, allows to sample the pulse a four different points in time. Depending on the chosen delays between the channels a local sampling rate of up to 330 GSa/s can be achieved. In Figure 5.5, a sketched detector pulse with four sampling points is shown.

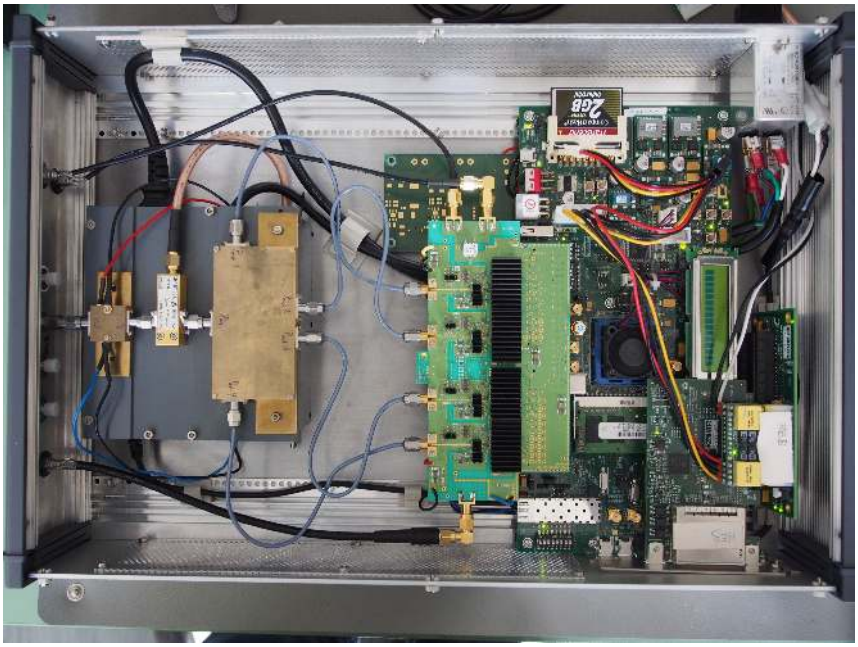

Figure 5.4: The Photo of KAPTURE is showing the 1-4 splitter, the V connection cables to the four sampling channels (consisting of a T/H unit and 500 MHz ADC each) on the digitizing board, the FPGA board below, and the PCI-Express connector (bottom right) for the connection to the control PC. Courtesy of Michelle Caselle.

Ideally the pulse width, height, and arrival time could be reconstructed from the four values and the corresponding delays. In this way, the amplitude of the detector pulse (as measure for the emitted THz power) can be determined from possible arrival time fluctuations. That is especially important when the detector pulse is short compared to the arrival time fluctuations. For slow detector pulses, which are much broader than the arrival time fluctuations, the change in detected amplitude at a fixed sampling point would be negligible. Therefore, a second operation mode becomes possible. In this mode, one detector is only connected to one sampling channel. So that up to 4 detectors can be sampled synchronously. Possible delays between the different detector signal in the optical and/or electrical signal path can be compensated by shifting the delays of each sampling channel. It has to be assured that the delays are chosen such that the peak of each detector pulse is sampled. Again, if the detector pulses are short compared to arrival time fluctuations this will lead to amplitude modulations which can not be distinguished from real changes in the detector pulse height. Such changes in arrival time could originate from the synchrotron oscillation of the bunches as well as from timing jitter. The multi-detector mode was for example used to measure the emitted THz power with two narrow band THz detector or an eight channel on-chip Schottky diode array, to gain insight into the changes

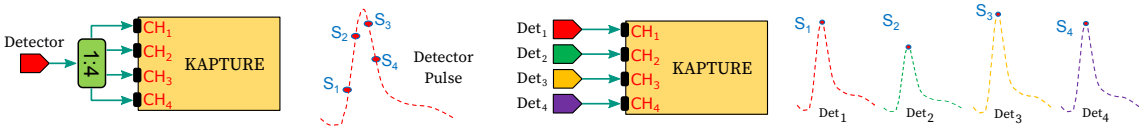

Figure 5.5: Sketch of the two different modes of KAPTURE. One detector via splitter to sample at four points and reconstruct pulse height, width, and arrival time. Alternatively one detector per channel with the sampling point at the peak to synchronously sample different detectors. Courtesy M. Caselle.

in the emitted radiation spectrum (Section 8.1). For most measurements presented in this thesis, the detectors had a sufficiently large pulse widths (between 4 GHz and 18 GHz) and were, therefore, directly connected to only one readout channel.

With the newest version, KAPTURE-2 [Cas17], up to eight readout channels are provided. Additionally, the sampling rate of the ADCs can be increased from 500 MHz up to 1 GHz, therefore allowing to sample the baseline of the detector between two pulses emitted by neighboring bunches. As KAPTURE-2 was still in testing, all measurements in this thesis were conducted with a four channel KAPTURE system, if not stated otherwise.

In principle the sampling channels sample continuously. The data is accumulated on the 2 GB flash memory of the FPGA from where the control PC can read and save it as binary files (the data contained in one file is in the following referred to as one dataset) on the PCs internal hard drive.

The operation of KAPTURE is controlled via PCI-Express from an graphical user interface (GUI) on the control PC. The GUI is called KCG (KAPTURE control GUI, see Figure 5.6) and serves as abstraction of the registers on KAPTURE's FPGA that need to be set to control and provide values to KAPTURE).

Different parameters can be set (see Table 5.1), like the number of turns to be recorded before the dataset is saved to the disk. Whether each turn is saved or only every n-th turn (n=10 is often sufficient to make the measured effects visible and will save memory and allows for a longer recording duration). The time between the acquisition of two datasets, and how many datasets should be taken at all. If the PC should trigger the start of the next dataset acquisition or if this should happen on an external trigger directly connected to KAPTURE (see synchronous measurements Section 8.2). And also the whole timing settings and delay values can be defined. To find the correct settings the KCG provides a time scan mode (see Figure 5.7), where short datasets are taken for different delays and the mean signal for each delay is displayed, resulting in a sampling scan of the input signal, allowing to select the correct delays for each sampling channel.

Furthermore, the KCG can display the recorded data directly and provides three acquisition

Figure 5.6: Screenshot of the graphical user interface to control KAPTURE. The different parameters can be set and the acquired measurement data can be displayed.

Table 5.1: Selected parameters for operation of KAPTURE

parameter	range	typical value	description
observed orbits	1-...	2700000	number of turns happening during the acquisition
skipped orbits	0-...	9	the numbers of revolutions that are not saved (9≙every 10th turn saved)
acquisitions	1-...		number of datasets to be taken during e.g. decay measurement
wait (s)	0-...	10	number of seconds to wait before starting next acquisition
use external trigger	0-1	0	select if a external trigger should be used to start each acquisition (replaces wait (s))
timeout (s)		12	if external trigger, this gives the number of seconds after a timeout error is thrown without receiving a trigger pulse
course delay	0-14	-	global delay (on all channels) to move the sampling point relative to the RF clock to find detector pulse (1 step ≙150 ps, maximum shift 2.25 ns)
fine delay	0-31	-	individual delay for each channel to distribute the sampling point over the detector pulse (1 step ≙3 ps, maximum shift 92 ps)

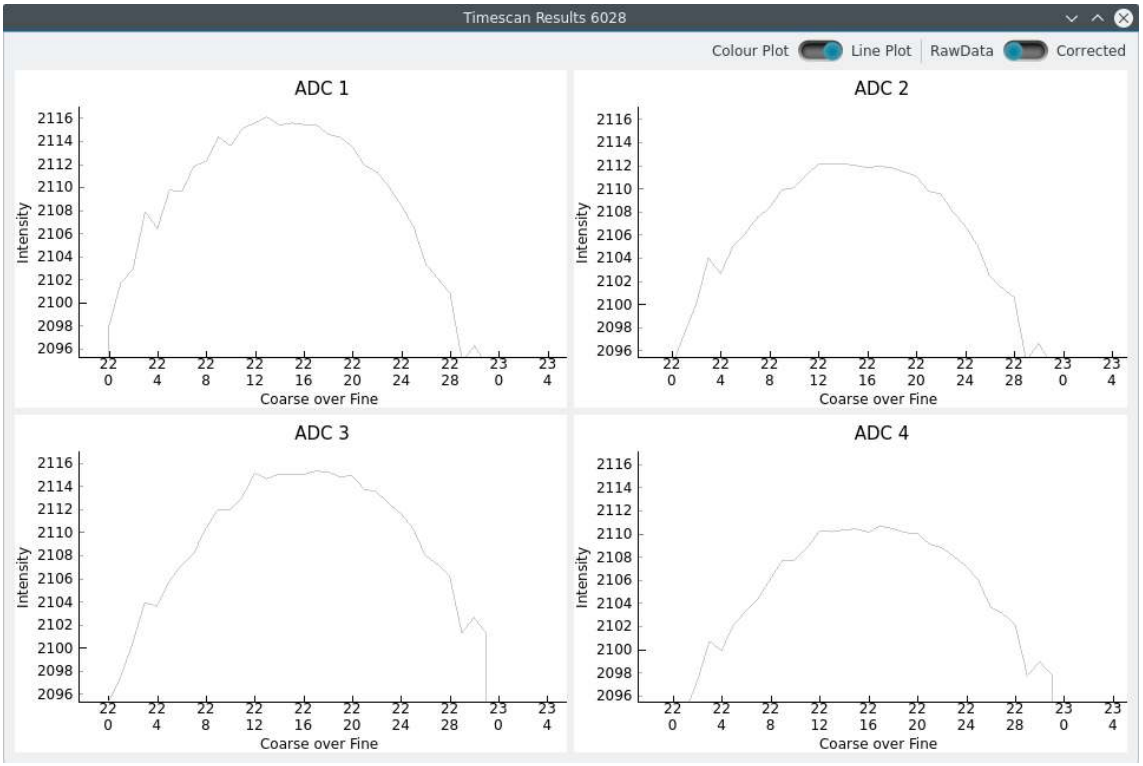

Figure 5.7: Screenshot of a time scan showing the raw data for each of the four ADC channels over the different delay steps.

modes. The standard 'Acquisition' which takes several datasets according to the given settings. 'Single Read' directly takes and saves one measurement without the need to change any acquisition settings. 'Continuous Read' takes continuously measurements as fast as possible (or distanced by the input 'interval (s)' parameter), displaying them without saving them to disk. This simplifies the process of setting up tremendously and the possibility to display the measured data directly functions as live feedback during a running measurement.

For the detailed analysis of the measurements the data is processed afterwards.

5.3.3 Post-Processing and Analysis

The recorded datasets are saved as binary files on the control PC. For the post processing and detailed analysis, the data is structured and transferred into HDF5 files [33]. As HDF5 allows partial file read-in, this drastically reduces the memory access necessary to plot only parts of the measurement data. All datasets recorded during one measurement (e.g. during one fill) will be saved in one HDF5 file together. Additional meta data, like the bunch currents over time, the used machine settings, the measurement type (see Section

6.1) and goal, and the used detectors is added.

The following analysis is done on these HDF5 files. To ease the access to certain data parts and to handle all the additional information saved in the HDF5 files (e.g. interpolate the bunch current at the point of time a measurement was done (Subsection 6.2)), an abstraction layer [Bro14] was written in Python [73]. Multiple Python scripts allow to plot the measurement data in different styles and over different parameters. Also the measurement and current class provided by the abstraction layer make it easy to create new scripts for plotting and analyzing the data.

6 Measurement Techniques and Methods

This chapter introduces the methods and measurement techniques used throughout this thesis to observe the effects of the instability on an electron bunch. The main focus of this thesis was the observation of the synchrotron radiation in the THz regime. The first part of this chapter will describe the two methods employed to study the dependence of the micro-bunching instability on the bunch current. One being the comparatively slow standard approach and second a newly developed approach called snapshot measurement, which reduces the measurement time drastically and allows the fast systematic studies described in the third part of the chapter. The second part explains how the current of each bunch is deduced from the beam current measurement and the filling pattern measurement by interpolation for the times of the THz measurements. The last part will discuss some representative properties used to characterize the behavior under the instability and the methods to extract them from the measurement data for easier comparison during systematic studies.

6.1 THz Measurement Methods

In this section, the two different methods of measuring the current dependence of the dynamics in the micro-bunching instability will be explained. As KARA is a ramping machine and can not be operated in top-up operation (see Section 2.2) the beam current decreases over time due to particle losses in the beam and a therefore limited beam lifetime. Hence, the beam current always changes making it an important parameter to display the dynamics of the instability over. Additionally, the current dependence of the fluctuations in the emitted THz radiation is, like the entire dynamics, reproducible for otherwise fixed settings and is consequently used as fingerprint of the instability behavior for each specific setting.

If not stated otherwise, all measurements of the emitted THz signal were recorded with KAPTURE.

6.1.1 Measurement during Current Decrease

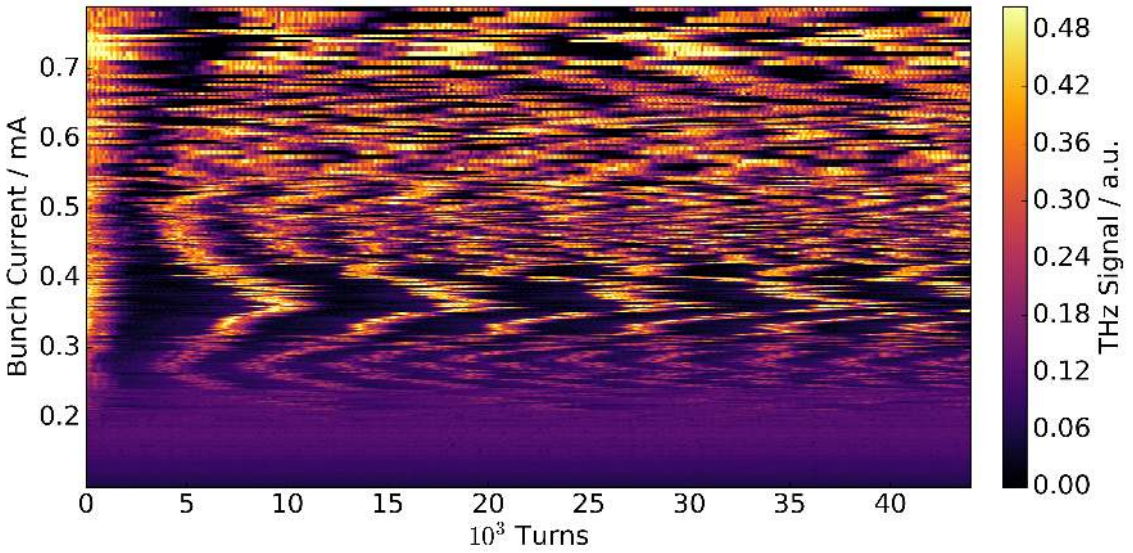

Figure 6.1: THz signal (color coded) of one bunch as a function of turn number during the decrease of the bunch current. Both, the temporal evolution and the repetition rate of an outburst, show a strong dependence on bunch current. For better visibility, the THz signals were shifted in time so that the first bursts are aligned. Also published in [Bro16a].

The simplest and most robust method of measuring the dependence of the dynamics under the instability on the current is to measure while the current decreases with time. This method will be referred to as decay measurement.

Using KAPTURE (or in a single bunch fill an oscilloscope) the amplitude of the THz detector response to the emitted THz pulse is measured, for each bunch at every turn individually for a certain time. Typically a measurement duration of one second was chosen. If the peak amplitudes are plotted for each bunch separately, the fluctuations in the emitted THz radiation are visible over the turns. The dominant frequencies of the fluctuations can be seen in an FFT of the data for each bunch individually. As the dominant fluctuation frequencies depend on the bunch current, the measurement is repeated over and over for several hours while the bunch current decreases. For the studies in the following a one second measurement was recorded every ten seconds, resulting in a 2D dataset with a fast and a slow time axis as shown in Figure 6.1 (with the slow time axis mapped to the corresponding bunch current). The changes in the dynamics with decreasing bunch current are visible in the changing repetition rate and the duty cycle of the fluctuations. The changes can be visualized even better by plotting the Fourier Transform of the signals. Such a spectrogram is shown in Figure 6.2. Bunch currents that mark a change in the

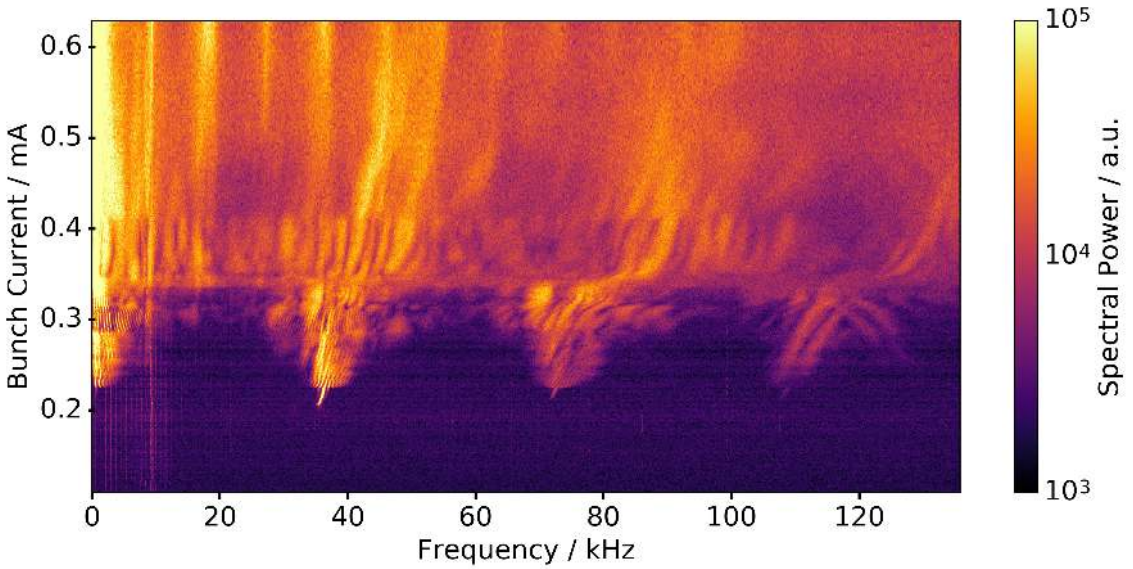

Figure 6.2: Spectrogram showing the fluctuation frequencies of the THz signal of one bunch as a function of the bunch current. The changes in the fluctuation frequencies with decreasing current are clearly visible.

fluctuation of the THz signal and therefore in the driving micro-bunching instability are easily accessible in the visualization [74]. The different regimes with different dominant frequencies will be discussed in Section 7.1.

The advantages of this method are its independence on the number of bunches and the high resolution of the slow time axis (bunch current) due to the long overall measurement time. The disadvantages follow directly: the long measurement time (up to several hours) and the significant amount of data ($184\,\text{buckets} \cdot 12\,\text{bit} \cdot 4\,\text{ADCs} \cdot 2.7\,\text{MHz} \cdot 1\,\text{h} = 10.7\,\text{TB}$). The typical setting to record only one second of data every ten seconds reduces the amount already by a factor of 10. Additionally, in most cases it is sufficient to skip some turns and only record every n-th turn, which will reduce the amount of data even further. As the fluctuations due to the instability are mainly below $\approx 200\,\text{kHz}$ (see Section 7.1) often only every 10-th turn was recorded, resulting in the highest resolved frequency of $\approx 270\,\text{kHz}$. Still the resulting data amounts up to 100 GB/h.

6.1.2 Snapshot Measurement

To overcome the long measurement times and the huge amount of recorded data, a new measurement method was refined in the framework of this thesis, based on the foundation laid by my master thesis [Bro14]. It has been published in [Bro16a]. The fast mapping technique (the so-called “snapshot” measurement) is enabled by the unique combination of

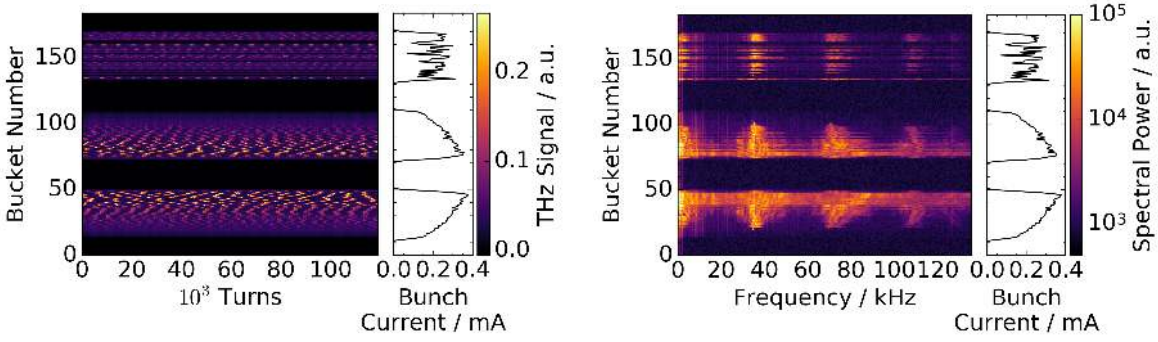

Figure 6.3: The fluctuating THz signal (color coded) of each of the 184 RF-buckets is shown in (a) for the first 130 thousand consecutive turns, out of the total recorded 2.7 million in one second. The bursting behavior differs visibly for bunches with different currents. On the right hand side, the filling pattern, consisting of three trains, is indicated by the bunch current. Also published in [Bro16a]. In (b) the Fourier transforms of the individual THz signals are displayed. The change in the dominant fluctuation frequencies with bunch current is already visible.

fast THz detectors with the high-data-throughput DAQ system KAPTURE (Subsection 5.3.2). It drastically reduces the time required to cover the full bunch current range of interest. Instead of following all bunches (or also a single bunch) during an hour-long beam current decrease, the technique makes use of the simultaneous acquisition of pulses for all bunches by KAPTURE. Combined with a special filling pattern, which covers the full current range of interest, the same information can be acquired in just one second.

The tailored filling pattern required for the measurements is achieved with the help of the bunch-by-bunch feedback system (Section 4.1). An example of such a filling pattern is displayed in the right side panel of Figure 6.3a. The current of the individual bunches was chosen in such a way that the bunch currents are distributed as evenly as possible between the minimal and the maximal current of interest. In the first train the bunch currents increase over the bunches, in the second train the currents decrease, and in the third train the current values are distributed randomly on the bunches. The bunch currents were measured with a time-correlated single-photon counting setup (Subsection 4.3).

With this filling pattern, the amplitude of the detector response for the individual THz pulse of each bunch is recorded for every n-th turn (typically $n = 10$) of over 2.7 million consecutive revolutions. Such a dataset contains the THz traces of all bunches during the measurement time of one second. The first 130 thousand turns of such a dataset are displayed in Figure 6.3a. Each horizontal row shows the THz signal as a function of the

turn number for one bunch. A vertical column yields the THz signal for all bunches at a specific turn. The fluctuations in the THZ power due to the bursting are clearly visible for each bunch. As before, to show the prominent frequencies of the fluctuation, the FFT of the THz signal is calculated for each bunch (see Figure 6.3b). For the first two trains with the ordered bunch currents, the change of frequency with bunch current is already visible similar to Figure 6.2. By sorting the lines according to the corresponding bunch currents, the spectrogram shown in Figure 6.4b is created.

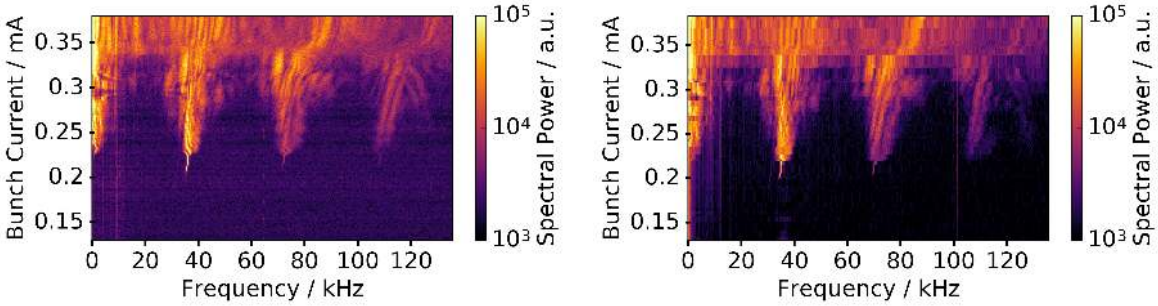

(a) (b)

Figure 6.4: The spectrogram shown in (a) was obtained from measurements of a single bunch for slowly changing beam current lasting two and a half hours, while the spectrogram in (b) was obtained from a snapshot measurement lasting just one second by using the FFT of the THz signals shown in Figure 6.3. For the snapshot measurement the bunch current resolution is limited by the number of bunches and their current distribution. Compared to this, the decay measurement during a slow current decrease results in a higher current resolution. Despite the limited current resolution of the snapshot spectrogram, the dominant bursting frequencies and the thresholds between different bursting regimes are clearly visible. Also published in [Bro16a].

The resulting spectrogram has a lower resolution on the current axis, due to the limited number of bunches and hence current bins, than the spectrogram obtained from measurements of a single bunch for different bunch currents shown in Figure 6.4a. However, the different dominant frequencies and regions are clearly visible and give an overview of the bursting behavior for these accelerator settings. The comparison between the snapshot spectrogram and the spectrogram taken during a standard current decrease of one bunch at the same accelerator settings shows the excellent agreement of the two methods and that the dominant structures can easily be observed with the time-saving snapshot measurement.

For the snapshot approach, it is assumed that the observed behavior is mostly dominated by single bunch effects, meaning the behavior of the bunches is not changed by the presence of other bunches. The validity of this assumption can already be deduced from

the good agreement of the two spectrograms in Figure 6.4 and will be studied in more detail in Chapter 10. For the determination of e.g. the bursting threshold with snapshot measurements, the determined small influence of multi-bunch effects will be included as part of the error propagation on the detected bursting thresholds.

Snapshot measurements offer the opportunity to acquire fast, comprehensive maps (like fingerprints) of the micro-bunching instability in dependence of various accelerator parameters. This allows, for example, to go to different machine settings in one fill and measure the bursting behavior (via one snapshot spectrogram) at each stetting within one second. A more detailed description of this is given in Section 7.2.

Compared to a decay measurement, snapshot measurements are significantly faster (one second instead of hours), but also more complex. As the current resolution is limited due to the limited number of bunches, an even distribution of the bunch currents in the filling pattern is necessary to avoid "gaps" on the current axis in the spectrogram and to cover the whole current range of interest. Nevertheless, with enough consideration of the difficulties, this technique was used successfully for many of the measurements presented in Chapter 7.

6.2 Determination of the Bunch Current at the Time of a Measurement

As the bursting behavior of a bunch experiencing the micro-bunching instability strongly changes with the current of the bunch, the bunch current is one of the most important parameters and plays a role in almost every measurement. The two possible methods to systematically measure the influence of the bunch current on the instability are the decay measurement and the snapshot measurement described in the previous section (Section 6.1). Most of the time, the behavior of a bunch under the influence of the instability will be studied as a function of its current as it decreases naturally, because no top-up operation is available at KARA, and the current can thus not be kept constant like other parameters.

The bunch current is determined by measuring the beam current with a PCT (Section 4.2) and the filling pattern with the TCSPC setup described in Subsection 4.3. The measured filling pattern is normalized and multiplied with the beam current yielding the absolute current of each bunch. To determine the bunch current as a function of time for each bunch, an interpolation of the measured bunch currents is necessary, as only every 30 seconds (or less often) a TCSPC measurement is available while for example the THz power is typically measured every 10 seconds.

To interpolate the current, different functions can be fitted to the measured bunch currents over time of each bunch individually. A higher-order polynomial, for example, follows the temporal development well, while smoothing out fast statistical fluctuations (Figure 6.5). Another possibility used, is a double exponential fit to model the current decrease respecting two contributions to the continuous current losses. For each measurement set the fit function returning the smallest error on the bunch currents was used. Applying the fit not only serves as interpolation between the measurements, but also reduces the statistical error. Due to the Poisson characteristic of the measurement, a fit incorporating all measurements reduces the relative statistical error by a factor of $f = \frac{1}{\sqrt{N}}$, where N is the number of measurements. For measurements taken twice every minute over four hours this results to $f \approx 0.05$. For a smaller number of measurements in a measurement set this factor increases. In this case, the fitted function represents the measurement less accurately and therefore does not improve the measurement error as much.

Figure 6.5 shows the bunch current of one bunch over a time period of 155 minutes. A single measurement is an integration over 30 seconds and one measurement was taken approximately every minute. At the highest bunch current of 0.511 mA 26603 events were counted by the TCSPC setup (Subsection 4.3). At the end 3337 counts were recorded for the lowest current of 0.056 mA. The resulting relative errors due to the Poisson statistics are 0.6 % and 1.7 % respectively. Due to the interpolation with a fit over the 147 measurements in the set, the final statistical, relative error accounts to $0.6\,\% \cdot \frac{1}{\sqrt{147}} \approx 0.05\,\%$ ($\approx 0.2\,\mu A$) and 0.14 % ($\approx 0.08\,\mu A$). For this example the reduction of the statistical fluctuations by the interpolation can be directly seen in Figure 6.5. The reduced χ^2 value of the used fit close to one indicates that the combination of the fit function and the estimated errors (poisson statistic) describe the measurement data well.

The uncertainty on the measurement of the overall beam current with the PCT was determined to be 0.55 µA (see Section 4.2). For a single bunch fill this will be the dominant error on the current. How big the influence of the beam current error is compared to the uncertainty on the filling pattern depends for multi-bunch fills on the number of bunches and the stored current. For most multi-bunch measurements the contribution of the filling pattern measurement will dominate the uncertainty so that the other will be neglected.

Systematic errors arise mainly from two different effects. The remaining signal of the previous bunch at the position of a bunch is about 0.05 % of the signal of the previous bunch (Subsection 4.3.2). Additionally, even with the correction of the dead time of the PicoHarp device in place, a resulting error due to the dead time effect of $\approx 0.2\,\%$ remains.

The errors on the measured bunch currents were therefore conservatively estimated to be around 0.2 % for the statistical uncertainty when a fit was applied and 1 % when a

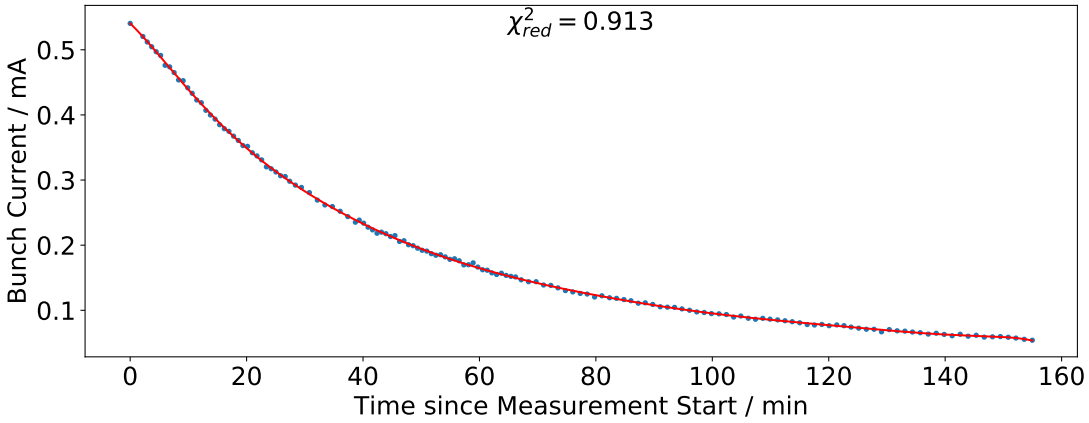

Figure 6.5: Bunch current determined via the filling pattern measured with TCSPC and the beam current measured with a PCT. For each individual measurement the resulting bunch current is displayed as a dot at the time since the measurements started. To interpolate between the single measurement points a polynomial of 10th order is fitted to the data and displayed as red line. The interpolation reproduces the curvature of the decreasing bunch current nicely while smoothing the statistical fluctuations.

simple linear interpolation was used. For the systematic uncertainty a value of 0.21 % was estimated. If not stated otherwise, these values were assumed for the measurements presented in this thesis.

6.3 Identification of Characteristic Properties of the Instability

The data gained with the above measurements can be quite complex, as seen in the spectrograms in Figure 6.4. To compare the behavior of the bunches under the influence of the instability at different machine settings, the most prominent properties are extracted. In this thesis, they were identified as the threshold current of the instability often referred to as bursting threshold, the main frequency of the fluctuations in the THz signal directly above the threshold current and the low frequency corresponding to the repetition rate of the THz bursts. All three properties can be equally identified and extracted from simulation data. This section will elaborate why these are important properties of the micro-bunching instability and how these properties are extracted from the measurement data.

For the analysis described in the following, it does not matter whether the data was recorded during the decay of a single bunch or with a snapshot measurement. Both result in time domain data for different bunch currents.

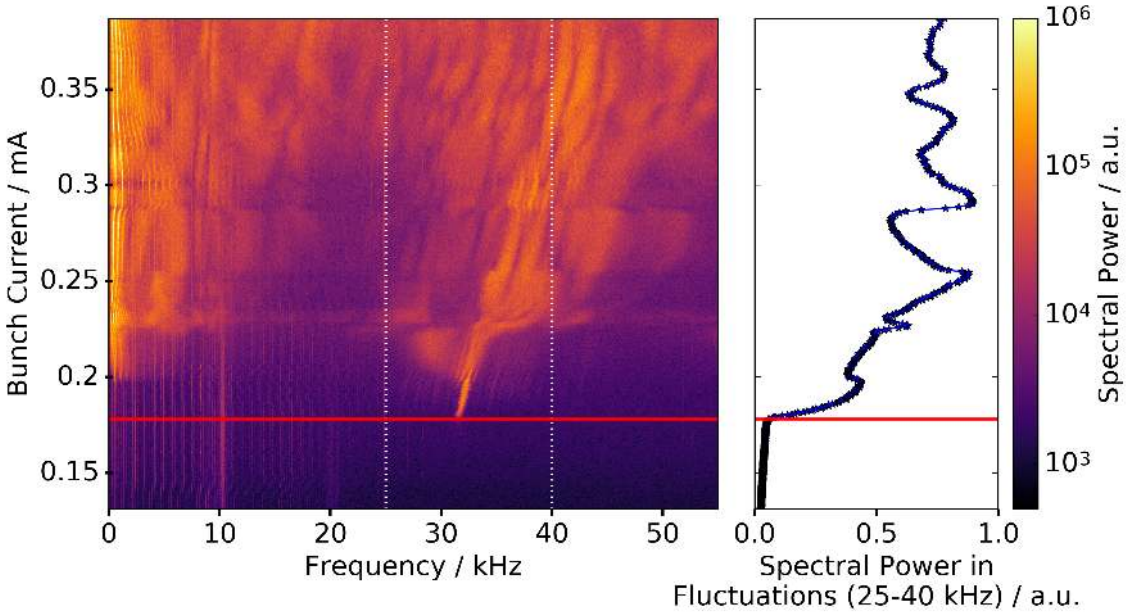

Figure 6.6: Temporal emission spectrum of THz power as function of decreasing bunch current. The red line indicates the onset of the fluctuations due to the micro-bunching instability. In the right panel, the sum of the fluctuation power in frequency range $25 - 40$ kHz shows a strong increase at the threshold current. Also published in [Bro17a].

6.3.1 Threshold Current

The threshold current I_{th} of the micro-bunching instability is the bunch current above which the first fluctuations in the emitted CSR power occur. It is an important property of the instability as it gives the instability threshold below which the beam is stable and not affected by the instability. The standard deviation of the temporal emission describes the strength of the fluctuations and can therefore be used to determine the bursting threshold, as the fluctuations drastically increase at the threshold current [Bro16a]. Fluctuations seen below the threshold current (see for example Figure 6.6) are mainly caused by the synchrotron oscillation and 50 Hz noise and are therefore generally at lower frequencies than the first instability frequency (which was observed to always be higher than the synchrotron frequency as described later in Subsection 7.2.2). To improve the threshold determination, those lower frequency fluctuations can be omitted by using the integrated power in fluctuations at a specific frequency range around the first instability frequency instead of the standard deviation. In Figure 6.6 exemplary, the power of the fluctuations in the frequency range from $25 - 40$ kHz is displayed. The threshold is strongly visible as the first increase (kink).

For snapshot measurements the procedure is similar. The standard deviation of the THz

signal of each bunch is calculated and displayed as a function of the momentary current of the bunch in question (Figure 6.7). The bursting threshold is immediately visible as a kink in the standard deviation. Figure 6.7 shows that the THz signals of bunches below the threshold (0.2 mA at these specific settings) show hardly any fluctuations compared to the signal of bunches with higher current. In the framework of my master thesis, an algorithm was developed for the automated detection of the kink in the standard deviation corresponding to the threshold [Bro14]. It was used in this dissertation for the analysis of parameter scans with snapshot measurements, as they result in a set of measurements for each of which the threshold needs to be determined. Such a study was published in [Bro16a] and the methods will be discussed in Section 7.2 and the results in Subsection 7.2.1.

Another possibility to determine the threshold current is to read it out off the spectrogram directly by eye. This was used in some cases where a lot of noise on the signal caused an increase in the fluctuation already well below the threshold current. Due to the recognizable shape of the onset of the fluctuations directly above the threshold it was still possible to determine the threshold for these cases.

The error in the determined threshold contains the error of the threshold detection algorithm including the uncertainty due to the finite current resolution, the errors on the bunch current measurement itself, and for the snapshot measurements the expected spread of the thresholds due to residual multi-bunch effects (see Chapter 10).

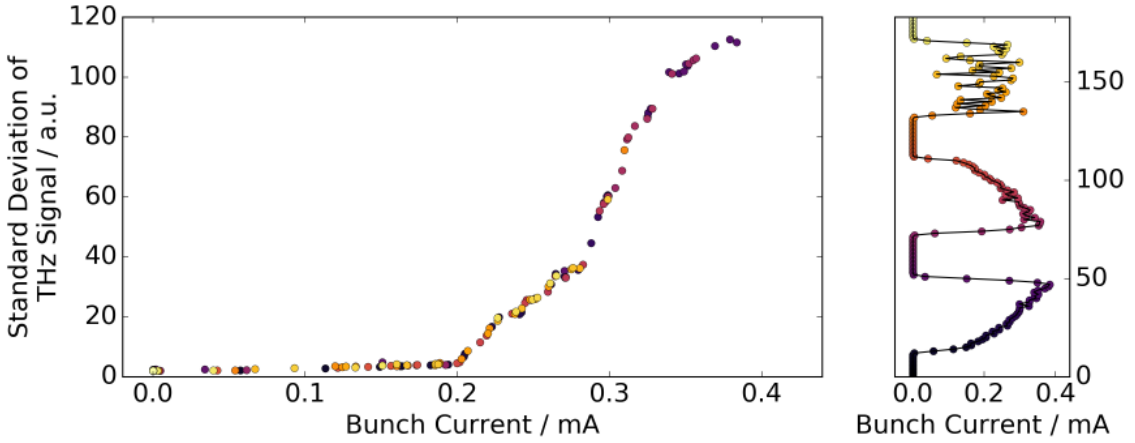

Figure 6.7: Standard deviation of the THz signal of each bunch as a function of the corresponding bunch current from a snapshot measurement, revealing the onset of bursting emission ("bursting threshold") at 0.2 mA. The individual bunch currents (shown on the right) were patterned to equally sample the whole bunch current range (published in [Bro15; Bro16a]).

6.3.2 Bursting Frequency ("Finger" Frequency)

The bursting frequency f_{th} is the most dominant frequency of the power fluctuations above the synchrotron frequency and is the first frequency to occur when the instability starts to affect the beam at the threshold current. It is connected to the rotating substructures on the charge distribution in the longitudinal phase space caused by the instability, which will be explained and discussed in more detail in Subsection 7.2.2. With increasing bunch current this frequency component shifts, which makes it look like a finger in the spectrogram. It will therefore be referred to as finger or finger frequency.

To have a comparable value between measurements at different settings, the frequency of the finger directly above the instability threshold is used. This value is easily identified in the FFT as the strongest frequency above the synchrotron frequency at the determined threshold current. A simple maximum finder was applied after some smoothing of the FFT data (e.g. with a moving average) to get rid of narrow noise peaks. Figure 6.8 shows the FFT of the THz signal of one bunch recorded directly at its bursting threshold.

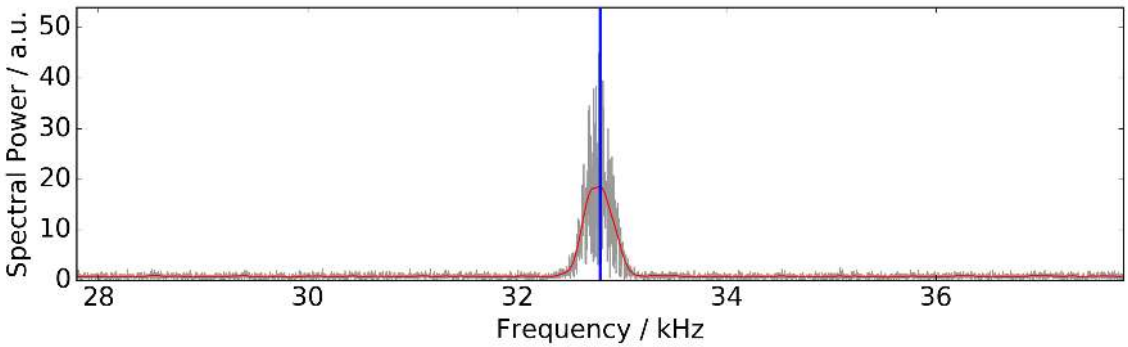

Figure 6.8: A section of the FFT of the THz signal at a current directly above the threshold current containing the bursting frequency is displayed in grey. Additional the smoothed signal is displayed in red and the determined bursting frequency (finger frequency) is marked (black line). For this measurement a moving average with a width of 75 Hz was used to smooth the signal.

The error on the determined bursting frequency at the threshold current depends mostly on the frequency resolution and the width of the frequency line (width of finger frequency). For a one second measurement the frequency resolution is 1 Hz.

6.3.3 Low Bursting Frequency (Repetition Rate)

The third characteristic property of the micro-bunching instability, is the repetition rate of the low-frequency bursts which is also referred to as low bursting frequency. It is given by

the repetition rate of the slow, sawtooth-like bursts in the THz emission. It is the most prominently visible feature of the instability if observed in time domain, which is why the micro-bunching instability is also referred to as sawtooth instability. These sawtooth-like bursts do not occur directly above the threshold but at higher bunch currents (see Section 2.9). The repetition rate is always below the synchrotron frequency and can therefore be separated from the bursting frequency described above. Similar to the finger the low bursting frequency changes over current. As it is not present at the threshold there is no comparable point at which a single value can be extracted to serve as comparison value. Hence, the low bursting frequency is extracted as a function of the bunch current and the whole behavior is used for comparison between different measurements (for example in Subsection 7.2.3).

To extract the low bursting frequency at each current, a frequency range on the FFT of the THz signal is defined, in which the frequency with the highest contribution is identified. Sometimes, it is necessary to apply a moving average with a small window (width mostly around 10 Hz) to avoid falsely identifying narrow noise peaks. The lower limit of the frequency range is defined to be 75 Hz to avoid the 50 Hz line and still be low enough for the studied settings to always be below the asked frequency. The upper limit is calculated from the individual synchrotron frequency of the analyzed measurement minus 20%. In this way, the synchrotron frequency line can not be falsely detected instead of the low frequency, but even for low synchrotron frequencies the search area is still broad enough to cover the whole dynamics of the low bursting frequency of the bunch current. For most machine settings at KARA, the low bursting frequency is between $200 - 600$ Hz ($5 - 1.7$ ms period).

7 Micro-Bunching Instability and its Dependencies

As described in Section 2.6, the micro-bunching instability occurs due to the interaction of the coherent synchrotron radiation (CSR) emitted by a bunch with the bunch itself. In short (for more see Section 2.9), the emitted CSR causes an additional wake potential. This leads to a change of the energy gained by the electrons dependent on their position in the longitudinal bunch profile. The result is a deformation of the distribution in the longitudinal phase space, which again changes the power and spectrum of the emitted CSR and therefore the additional wake potential. Due to this cycle, the emitted CSR fluctuates continuously for bunches experiencing the micro-bunching instability.

The following systematic study of the micro-bunching instability is structured in four chapters. This chapter will focus on mapping and discussing the precise characteristics of the CSR power fluctuations as well as their dependence on different machine and beam parameters. In Chapter 8, it will be first discussed which influence the frequency range detected by the used THz detector has on the observed CSR fluctuations by measuring simultaneously with different THz detectors. Then the influence the instability has on beam parameters other than the emitted CSR power will be studied by additionally measuring the longitudinal as well as horizontal bunch profile synchronously. Next, Chapter 9 provides a detailed study of the behavior of a single bunch under the influence of the weak instability. Which is a second region of instability also caused by CSR self-interaction. Under special conditions it occurs additionally to the micro-bunching instability. While already in the first chapters the measurements will be compared to simulations, the measurements in this chapter are used for a detailed comparison with simulations based on the description of the micro-bunching instability via the simplified parallel plates model of the CSR impedance (see Section 2.6). The last chapter (Chapter 10) focusses on measurements in multi-bunch operation, which is not included in the description of the micro-bunching instability via the simplified parallel plates model of the CSR impedance. An in-depth analysis is presented of the influence the multi-bunch environment has on the behavior of the micro-bunching instability. Therefore, the differences observed in the threshold current, the bursting

frequency, and the low bursting frequency of the individual bunches are discussed.

7.1 Observed Bursting Behavior

The first and most direct effect of the micro-bunching instability visible at KARA is the fluctuation in the emitted CSR. If the CSR power emitted by one bunch is observed at every revolution the fluctuations are clearly visible. Such a measurement is shown in Figure 7.1. It is also directly visible that the fluctuations are not completely chaotic but seem to form patterns, which change over the decreasing bunch current.

The changes in the fluctuation patterns are more distinctly visible if the frequency of the fluctuations is displayed. Figure 7.2 shows the Fourier transform of Figure 7.1.

Around 0.2 mA the instability threshold is visible. For bunch currents below this current no fluctuations are present except for changes with the synchrotron frequency and some 50 Hz lines. Above the threshold current, several areas showing different fluctuation frequencies are present. The borders between these different regimes are not very distinct.

The first regime, directly above the threshold, is dominated by a single frequency (and its higher harmonics). This frequency will be referred to as bursting frequency or finger frequency (Subsection 6.3.2) and discussed in more detail in Subsection 7.2.2. In all conducted measurements, the bursting frequency was observed to be higher than the synchrotron frequency f_s. The changes in the longitudinal profile, which cause the emitted CSR to fluctuate with the bursting frequency, originate from the name-giving substructures in the longitudinal phase space distribution rotating with frequencies close to but not exactly the synchrotron frequency [75].

With increasing bunch current the dominant frequencies shift to higher values and broaden. At a certain current another dominant fluctuation frequency arises at significantly lower values than f_s (see Figure 7.2b). The structures in the phase space distribution are now not stable anymore in amplitude but grow and shrink over time. As before, the self-interaction leads to the presence of substructures. In this regime, contrary to before, the excitation by the wake potential and the damping due to radiation damping and diffusion do not balance each other out. So that the structures grow over several synchrotron periods, just to be washed out by diffusion and filamentation. The resulting smoothness of the charge distribution as well as the increase in bunch size leads to a lower wake potential. At this point, the radiation damping outweighs the driving wake potential so that the substructures and the overall bunch length are damped down to the point, where the wake potential increases enough to lead to the formation of substructures again. The repetition

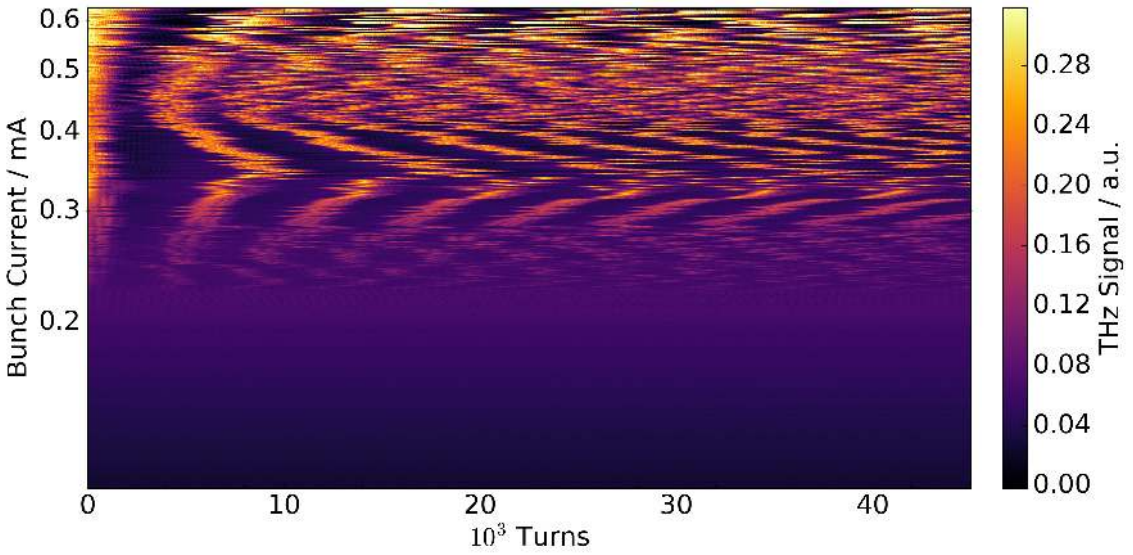

Figure 7.1: The turn-by-turn measured CSR power of one bunch is displayed as a function of decreasing bunch current. Each row displays the first 45000 revolutions of each measurement. Many measurements were taken while the bunch current decreased (different rows). The fluctuation of the emitted CSR due to the presence of the micro-bunching instability is clearly visible as well as the change in the fluctuation with changing bunch current. For better visibility, the first bursts of each measurement were aligned. Another example of such a measurement is shown in Figure 6.1 for a different set of machine settings.

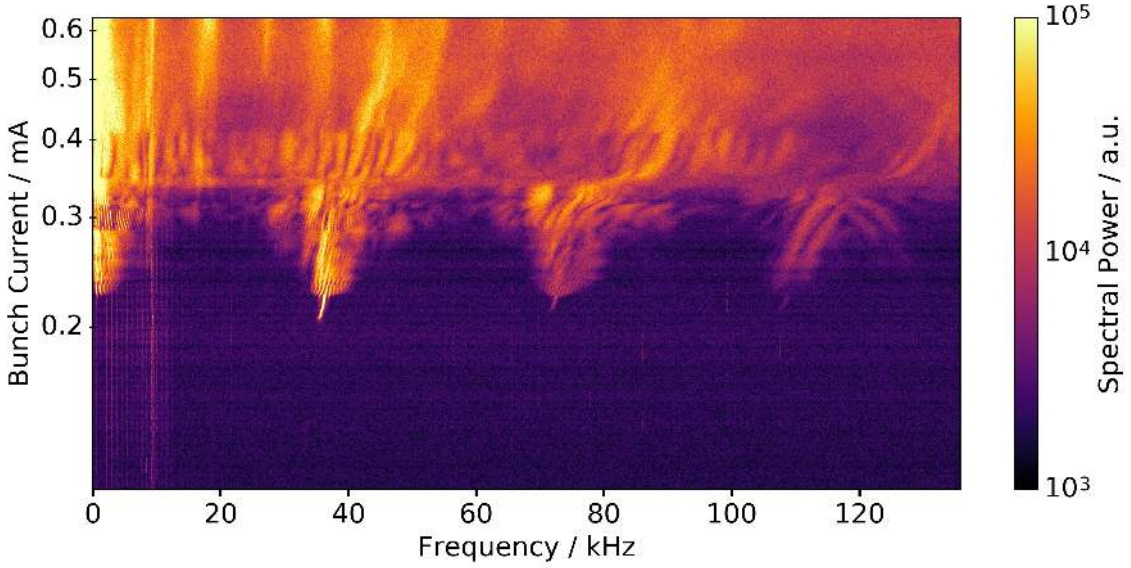

(a)

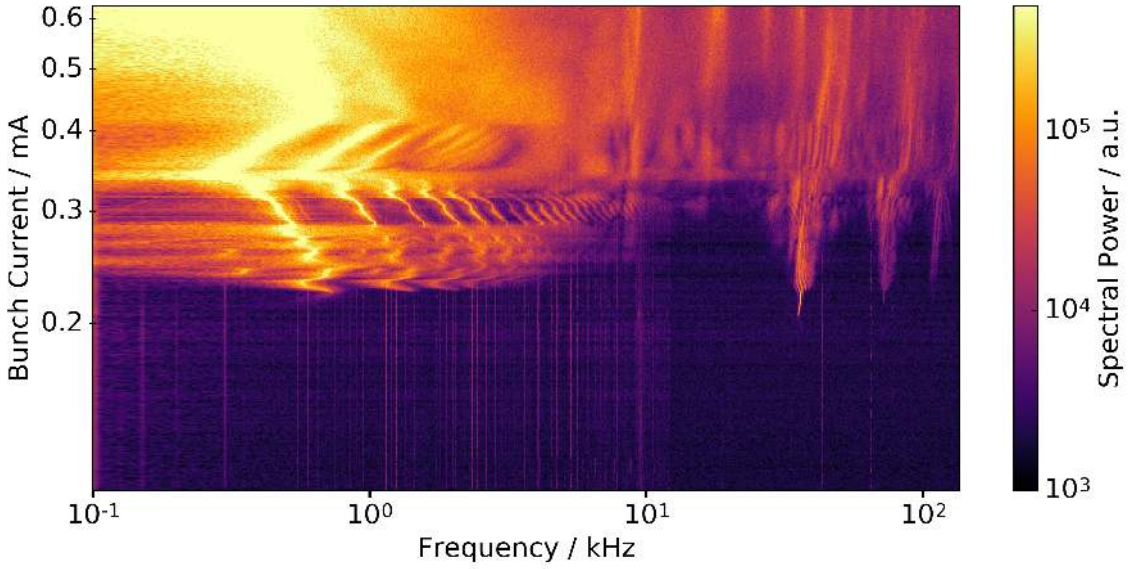

(b)

Figure 7.2: The spectrogram of the CSR emitted by one bunch displays the spectrum of the fluctuations as a function of the bunch current. The representation in the frequency space shows directly the dominant frequencies of the fluctuation, revealing different regimes of bunch current with different dominant frequencies. Subfigure (a) has a linear frequency axis while subfigure (b) has a logarithmic frequency axis to make the changes in the lower frequencies visible.

rate of these bursts shows up as the additional low frequency. It will be referred to as low bursting frequency or bursting repetition rate (Subsection 6.3.3) and is studied in more detail in Subsection 7.2.3. Figure 7.2b shows the low bursting frequency changing with increasing current, but contrary to the finger frequency, it is not only increasing but also decreasing in some bunch current ranges. At even higher bunch currents the frequency lines become even broader and/or wash out completely, indicating a more irregular behavior (see Subsection 7.2.3).

The behavior a bunch displays under the influence of the micro-bunching instability while its current decreases seems to follow a blueprint. The measured fluctuations in the CSR are completely reproducible for the same settings of the machine. For different machine settings the resulting spectrogram of the CSR fluctuations looks different (see Figure 7.3) but the main features are still recognizable, including the instability threshold, the bursting frequency starting as a single finger at the threshold current, and the low bursting frequency starting at higher currents. The currents where they occur as well as the values of the frequencies change depending on the used machine parameters (like momentum compaction factor and acceleration voltage). A sequence of spectrograms measured at decreasing values of α_c (see Appendix A.4) shows how the pattern changes. The bursting frequency gradually shifts to lower frequencies and the bursting threshold decreases in current (with decreasing α_c).

For easier comparison of the bursting behavior at different machine settings, the already identified characteristic features (Section 6.3), threshold current, bursting frequency, and low bursting frequency will be investigated and their dependence on different machine settings will be studied in the following subsections.

Another helpful feature is the mean detected CSR power as well as the standard deviation (strength of fluctuation) of the detected CSR. They can also reveal changes over current in the bursting behavior, which is for example used in the determination of the threshold current (Subsection 6.3.1) as well as in the investigation of the short-bunch-length bursting (the weak instability, Chapter 9), a second region of instability occurring for certain conditions below the instability threshold. Additionally, the mean and standard deviation of the detected CSR depend on the frequency range which the used detector is sensitive to [Ste18b]. This indicates that not only the emitted power of the coherent synchrotron radiation fluctuates but also the emitted spectrum changes, which would confirm the expectation based on the simulations (Section 2.9) and will be discussed shortly in Section 8.1.

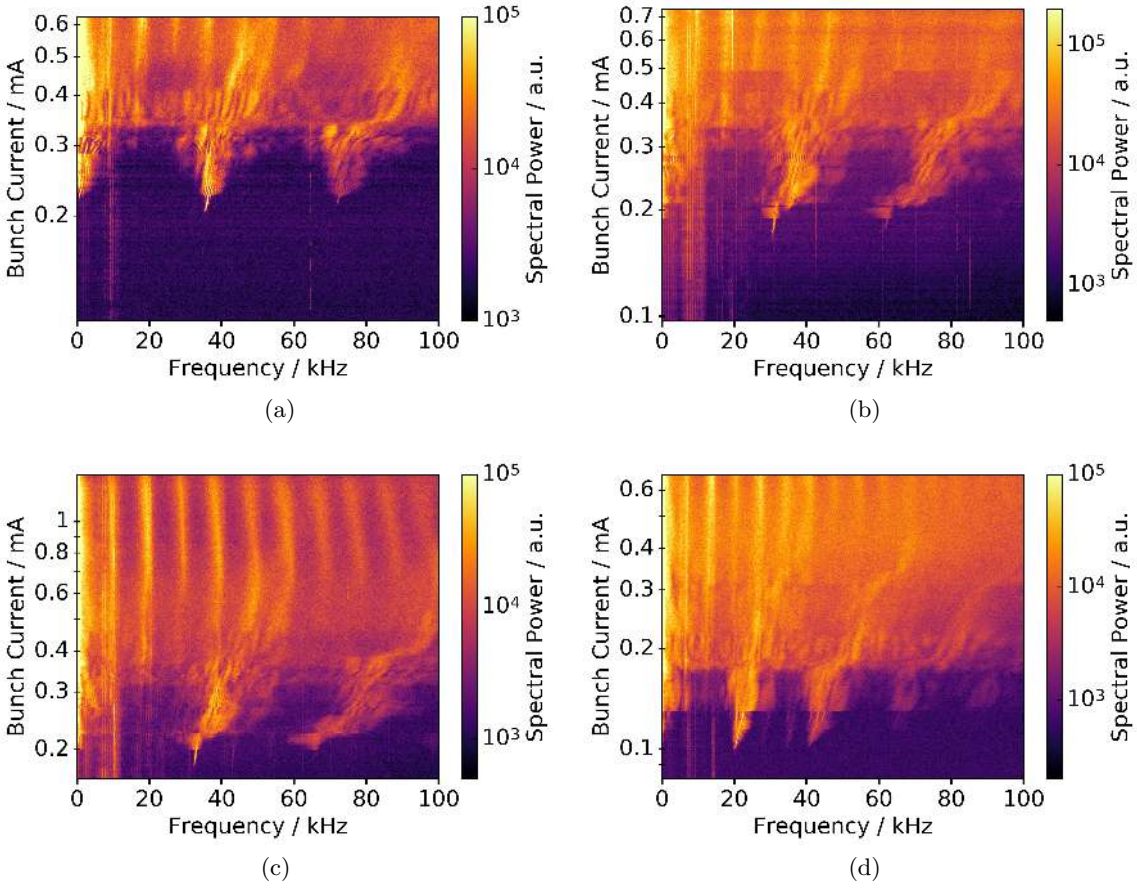

Figure 7.3: Spectrograms of the emitted CSR power for different values of the momentum compaction factor and the acceleration voltage. Measurements (a) to (c) were taken with the same momentum compaction factor ($\alpha_c \approx 5 \cdot 10^{-4}$) at different acceleration voltages resulting in different synchrotron frequencies. (a) $f_s = 8,9\,\mathrm{kHz}$ and $V_{RF} = 4 \times 300\,\mathrm{kV}$; (b) $f_s = 9,8\,\mathrm{kHz}$ and $V_{RF} = 4 \times 325\,\mathrm{kV}$; (c) $f_s = 10,3\,\mathrm{kHz}$ and $V_{RF} = 4 \times 350\,\mathrm{kV}$; Measurement (d) was taken at a lower value of $\alpha_c \approx 3 \cdot 10^{-4}$ with $V_{RF} = 4 \times 300\,\mathrm{kV}$ resulting in $f_s = 7,2\,\mathrm{kHz}$. (adapted from [Bro14])

7.2 Influence of Momentum Compaction Factor and Acceleration Voltage

The assumption that the bunch length plays an important role not only in the occurrence but also in the behavior of the instability seems not far-fetched, considering that the micro-bunching instability is caused by the interaction of a bunch with its own emitted coherent synchrotron radiation. And this radiation is only emitted for wavelengths longer than the emitting structures and at the same time the vacuum pipe cut-off limits the maximal emitted wavelength. Two machine parameters, which have an influence on the natural bunch length $\sigma_{z,0}$ (see Equation 2.16) and at the same time can be changed relatively easy at KARA, are the momentum compaction factor α_c and the acceleration voltage V_RF.

The momentum compaction factor α_c (Equation 2.14) can be changed via the magnet optics (Section 3.2). A reduction of α_c reduces the path length difference of particles with different energies inside a bunch with a certain energy spread and therefore reduces the length of the bunch. As it can be changed independently from other parameters it is ideal for systematic scans. A typical measurement would be to take a snapshot measurement then change the magnet optics in such a way that α_c is reduced, take again a snapshot measurement and so on, while the acceleration voltage is kept constant. This results in a set of snapshot measurements for different values of α_c. To measure the exact value of α_c several precise beam energy measurements (at different settings of the RF frequency) are necessary. Therefore, α_c is not measured online but calculated from the measured values for the synchrotron frequency f_s and the acceleration voltage V_{RF} using Equation 2.12, which couples the three parameters. Thus, if V_RF is kept constant, the synchrotron frequency is used as indicator for the momentum compaction factor for each snapshot measurement. Figure 7.4 shows for several snapshot measurements at different magnet optics and a fixed value of V_RF (indicated by different values of f_s) the standard deviation of the THz signal at different bunch currents. It directly shows that the behavior changes for different values of f_s and therefore different values of α_c.

Also the amplitude of the acceleration voltage V_RF influences the natural bunch length and therefore the behavior under the instability. As given in Equation 2.16, the natural bunch length $\sigma_{z,0}$ depends on the local derivative of the acceleration voltage at the synchronous phase. Figuratively speaking, the steeper the slope of the acceleration voltage at the position of the bunch, the smaller are the longitudinal position changes the electrons in the bunch have to do to compensate a certain energy mismatch, resulting in a shorter overall bunch. So, by increasing the amplitude of the acceleration voltage the slope at the phase of the bunch gets steeper and the phase difference an off-energy particle in the bunch has

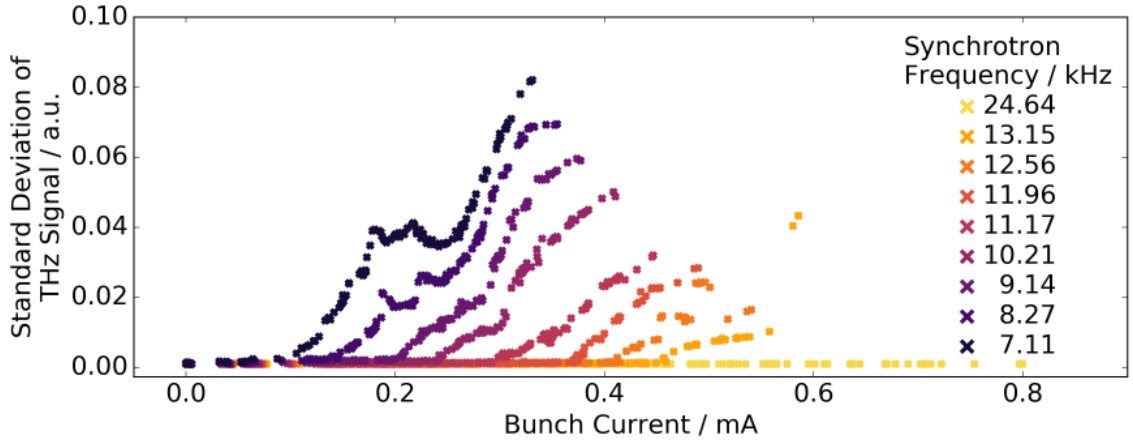

Figure 7.4: Standard deviation of the THz signal as a function of the bunch current for a constant acceleration voltage of 1047 kV and different settings of the magnet optics, resulting in different synchrotron frequencies and hence different bursting thresholds [Bro16a] (adapted from [Jud14]).

to have to correct for its slightly different energy becomes smaller.

So, similar to a scan over different settings of the magnet optics, a scan over different values of V_{RF} can be done. A change of V_{RF} also leads to a change of f_{s}. Therefore, the value of f_{s} alone does not describe the machine settings. It has to be accompanied additionally by either V_{RF}, α_c or $\sigma_{z,0}$. As described above, a bunch length reduction due to a change of the magnet optics that leads to a lower momentum compaction factor reduces the synchrotron frequency. On the other hand, for a fixed momentum compaction factor, a shortening of the bunch by an increase in the acceleration voltage is accompanied by an increase of the synchrotron frequency (Equation 2.10). The reduction of the bunch length (independent of the cause) leads to a reduced threshold current of the instability (see Equation 2.24 and Subsection 7.2.1). These connections are sketched in Figure 7.5a. In Figure 7.5b, the same is shown for measured threshold currents. For changes of the acceleration voltage, the relative change of the threshold with the synchrotron frequency is smaller and has the opposite sign than the change due to variations of the momentum compaction factor. The currents were extracted from scans over α_c ("magnet sweep") and from scans were α_c as well as V_{RF} were changed ("combined sweep").

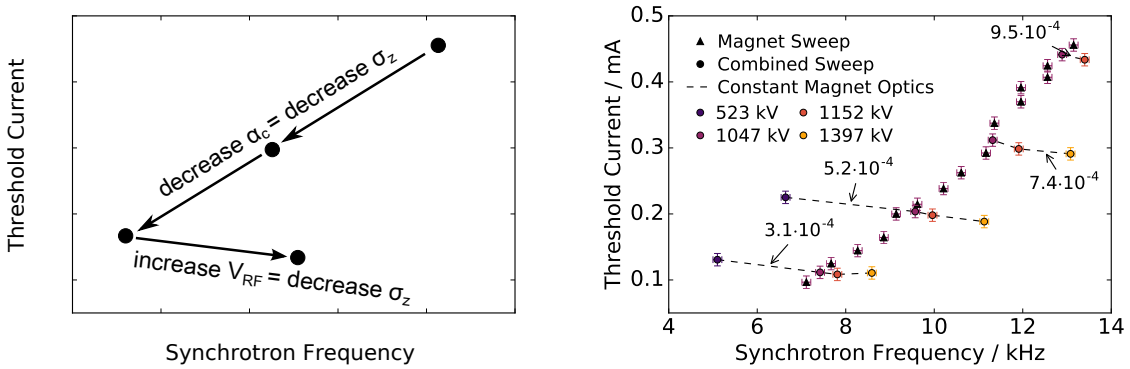

(a) (b)

Figure 7.5: Dependence of the threshold current on the momentum compaction factor and on the acceleration voltage as a function of the synchrotron frequency. On the left hand side, the connections between the different parameters are sketched. The same is shown on the right hand side for measurements of the threshold current. Points obtained at the same magnet optics (therefore same momentum compaction factor) are connected by dashed lines. Same color means the threshold was measured at the same voltage.

7.2.1 Threshold Current

The bunch current at the instability threshold is one of the most, if not the most, important property of the micro-bunching instability as it describes above what current a bunch is affected by the instability such that it is not stable over time anymore. For the context of this thesis, the threshold current was defined as the current above which clear fluctuations (other than the synchrotron frequency) are visible in the emitted CSR power of a bunch. Different methods of determining the threshold from the measured CSR emission are discussed in Subsection 6.3.1.

Measurements show that the threshold current is always the same for the same machine settings but changes significantly for different settings. In Figure 7.6, measured threshold currents for different settings of α_c and V_{RF} are displayed as a function of the measured synchrotron frequency. The measurement was taken in several sets and over the course of one year. The typical machine parameters for these measurements are summarized in Table A.1. The measurements show that at a fixed value of V_{RF} the threshold current decreases for a reduction of α_c (reduction of f_s). And for a higher V_{RF} (higher f_s) the threshold current decreases if the magnet optics are kept constant (fixed value of α_c). This supports the assumption that the bunch length plays an important role. A reduction of α_c as well as an increase in V_{RF} leads to a reduced natural bunch length. Shorter bunches have a higher

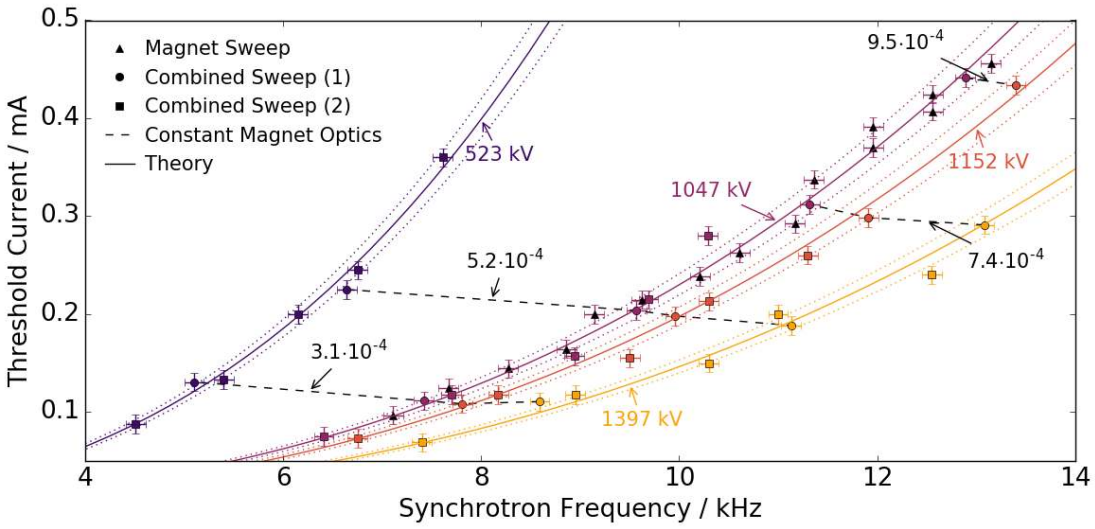

Figure 7.6: Measured bursting thresholds from three sets of measurements as a function of the synchrotron frequency. Here "combined sweep (2)" refers to the same measurements taken 11 months apart from "combined sweep (1)". For "combined sweep (1)", measurement with the same magnet optics (and therefore same α_c) are connected by dashed lines. The different colors indicate the different acceleration voltages. The horizontal error bars indicate the systematic error on the measured synchrotron frequency. The vertical error bars include the error of the algorithm for the automated threshold detection, the bunch current measurement as well as the expected spread of the threshold due to multi-bunch effects. The solid lines show the theoretical expectation according to Equation 7.1 from the bunched beam theory. The dotted lines indicate the one standard deviation uncertainties on the theoretical predictions. Within uncertainties all measurements agree with the bunched beam theory. (published in [Bro16a])

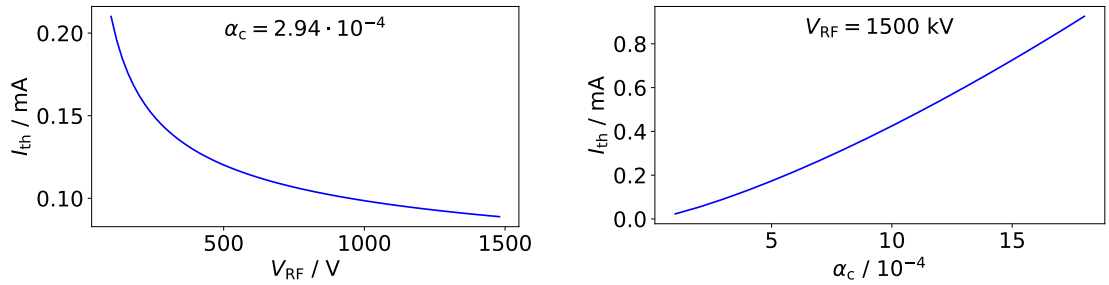

(a) (b)

Figure 7.7: Theoretical prediction of the threshold current as a function of the acceleration voltage and the momentum compaction factor respectively, according to Equation 7.1.

overlap of their bunch spectrum with the CSR impedance than longer bunches. So the critical charge density necessary for the wake potential to have a significant contribution is lower resulting in a lower threshold current. A change in α_c seems to have a bigger effect than a change of V_{RF}. It can be shown that this is in full agreement with the theory.

In [13], systematic studies of the threshold current are conducted by solving the Vlasov-Fokker-Planck equation (Section 2.7) for the bunched beam theory and the parallel plates impedance model (Section 2.6) with a VFP solver. Equation 2.24 was derived from these simulation results. Expanded to only contain measurable machine parameters, this results in:

$$I_b^{th} = \frac{2\pi\gamma I_A \left(c\,\sigma_\delta^7\,E^4\,f_s^7\,h^4\right)^{\frac{1}{3}}}{R^{\frac{1}{3}}\left(f_{RF}^2\sqrt{e^2V_{RF}^2 - U_0^2}\right)^{\frac{4}{3}}}\left(a_{th} + b_{th}\frac{\sqrt{8}c\,\sigma_\delta\,E\,f_s\,h\,R^{\frac{1}{2}}}{h_c^{\frac{3}{2}}\,f_{RF}^2\sqrt{e^2V_{RF}^2 - U_0^2}}\right) \tag{7.1}$$

with the determined fit parameters $a_{th} = 0.5$ and $b_{th} = 0.12$ [13]. In Figure 7.6, the expected thresholds are displayed for different values of V_{RF}. Within the uncertainties, the measured thresholds agree extremely well with the predicted ones. This is quite astonishing, as the simulation only considers the machine as two parallel, perfectly conducting, infinite plates for the calculation of the used CSR impedance. When displaying the expected threshold current as a function of V_{RF} for a fixed α_c and vice versa (see Figure 7.7), the same correlations as described above for the measurement are visible. At least for the parameter ranges available at KARA, the effect of α_c on the threshold is stronger than the one of V_{RF}. This is not surprising. While the bunch length equally depends on the square root of both parameters, the threshold current has a factor of α_c additional to the

dependency on $\sigma_{\mathrm{z},0}$:

$$I_{\mathrm{b,th}} = \frac{\gamma \alpha_{\mathrm{c}} I_{\mathrm{A}} \sigma_{\delta,0}^{2} \sigma_{\mathrm{z},0}^{\frac{1}{3}}}{R^{\frac{1}{3}}} \left(a_{\mathrm{th}} + b_{\mathrm{th}} \frac{\sqrt{8} \sigma_{\mathrm{z},0} R^{\frac{1}{2}}}{h_{\mathrm{c}}^{\frac{3}{2}}} \right)$$

In [13], the dimensionless quantities Π (shielding, Equation 2.26) and S_{CSR} (CSR strength, Equation 2.27) are used to express the threshold equation. If the measurements displayed in Figure 7.6 are now displayed as a function of Π and S_{CSR}, they should all form a straight line independently of their V_{RF}. This can be seen in Figure 7.8. Without the dependence on V_{RF} in this representation, is was possible to add more measurements at further voltages to Figure 7.8 without the figure becoming unclear. Now, small differences between the expectation based on the simulations by [13] become visible, but are still mostly within the uncertainties of the measurement. The purple stars represent thresholds taken from single bunch decays while the other points where taken from snapshot measurements or decays with multiple bunches filled. As expected, no systematic differences within the uncertainties of the measurements are visible. The additional region of instability below the expected threshold will be discussed in Chapter 9.

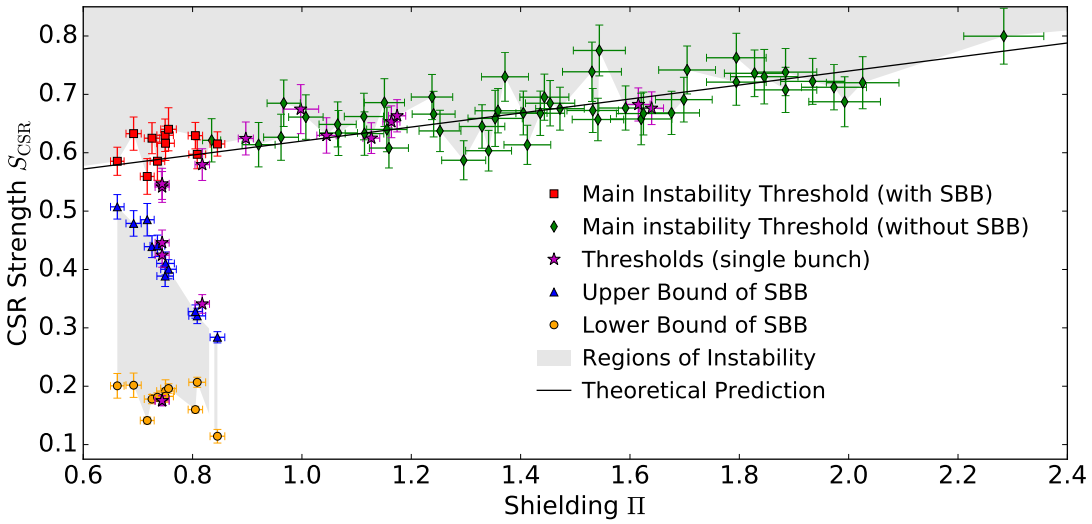

Figure 7.8: CSR strength vs. shielding of thresholds from snapshot measurements at different settings of the machine parameters compared to the linear scaling law given by Equation 7.1(line). The lower bound (orange discs) as well as the upper bound (blue triangles) of the short-bunch-length bursting (SBB) are shown. The main bursting threshold is shown in red (squares) for machine settings where short-bunch-length bursting occurred and in green (diamonds) for settings where it did not occur. The purple stars represent thresholds and bounds which were obtained from a full decay of a single bunch and not from snapshot measurements. The error bars display the one standard deviation uncertainties calculated from the measurement errors.

7.2.2 Bursting Frequency

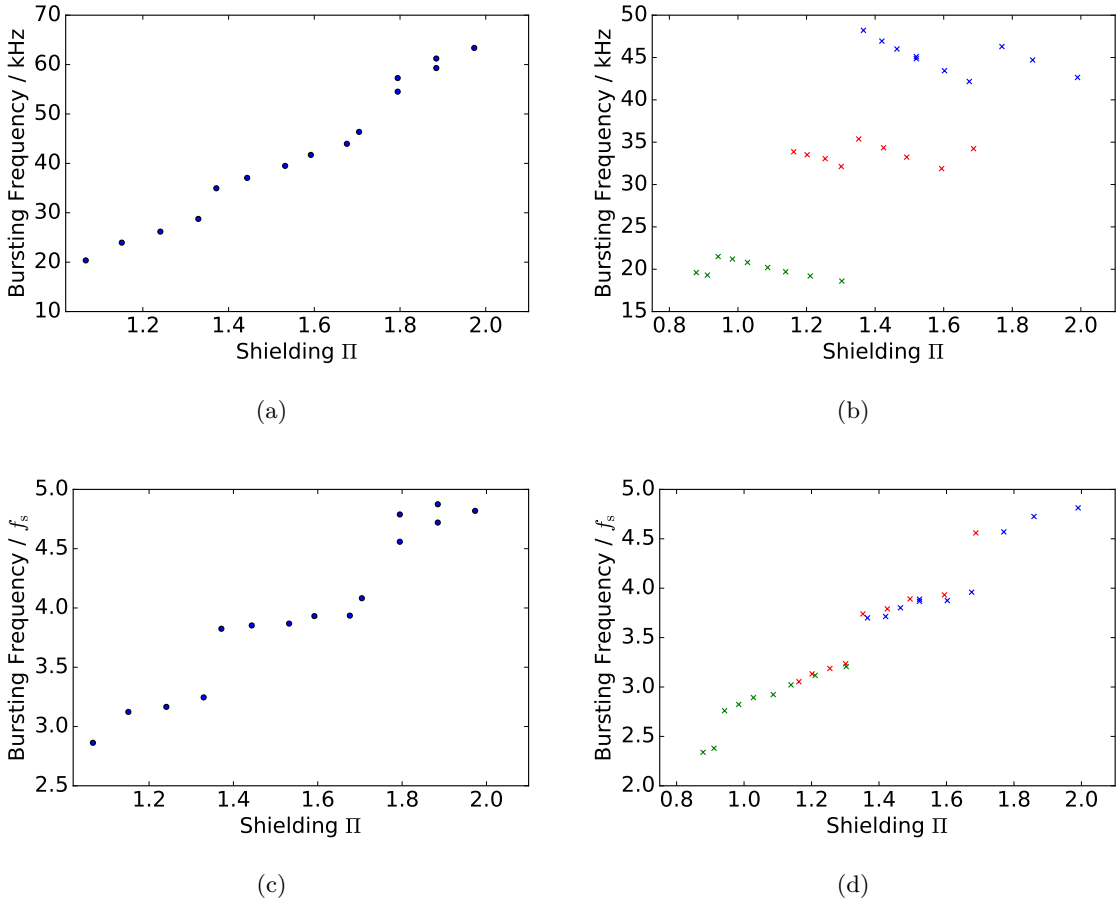

Figure 7.9: Bursting frequency at instability threshold as a function of the shielding parameter. In (a) only the momentum compaction factor was changed (from $2.9 \cdot 10^{-4}$ to $9.9 \cdot 10^{-4}$) while the acceleration voltage was constant at 1048 kV. In (b) the acceleration voltage was changed (from 700 kV to 1500 kV) while the momentum compaction factor was kept constant at $6.8 \cdot 10^{-4}$ (blue points), $4.9 \cdot 10^{-4}$ (red points) or $2.85 \cdot 10^{-4}$ (green points). In subfigures (c) and (d) the bursting frequency (from subfigure (a) and (b) respectively) is displayed in multiples of the synchrotron frequency.

The bursting frequency f_{th} is the first dominant fluctuation frequency arising directly above the threshold current. The observations always show it to be higher than the synchrotron frequency. The exact frequency value changes for different settings of α_{c} and V_{RF}. In Figure 7.9, the bursting frequency is displayed as a function of the shielding parameter Π, which is the natural bunch length scaled with the bending radius and the height of the vacuum chamber (see Equation 2.26), which both stay unchanged. For the measurements shown in Figure 7.9a only the momentum compaction factor was changed, while the acceleration

voltage was left unchanged. Here, the bursting frequency decreases for settings with smaller natural bunch length (smaller Π). On the other hand, Figure 7.9b shows how the bursting frequency changes if the momentum compaction factor is kept constant and instead the acceleration voltage is changed (each color indicates one fix value of α_c). The frequency mostly increases for a smaller bunch length, except for some downward steps, which is contrary to the behavior for changes of α_c. Additionally, it is visible that different settings (combinations of α_c and V_{RF}) can lead to the same value of the shielding parameter Π, but with different values for the bursting frequency. This and the difference in how α_c and V_{RF} change the bursting frequency indicate that f_{th} not solely depends on the bunch length.

Due to the change of α_c and V_{RF} also the synchrotron frequency changes. This means the rotation frequency of the charge distribution in the longitudinal phase space changes. So, when the bursting frequency originates from substructures on the distribution rotating in the phase space, one could assume that the change in bursting frequency solely originates from the change of f_s. In Figure 7.9c and Figure 7.9d, the bursting frequency is displayed as multiples of f_s. In this representation, the measurements taken at the same value of Π also show the same value of (f_{th}/f_s), even though they can have different values of f_{th} as shown before in Figure 7.9b. Additionally, the slope now has the same direction for both parameters that were changed. This implies that the different behaviors originated in the different influence of α_c and V_{RF} on f_s, which is now canceled out through the division by f_s similar to plotting the threshold in Figure 7.8 as dimensionless quantities (S_{CSR} and Π). Now the dimensionless quantity is (f_{th}/f_s). The quotient (f_{th}/f_s) for multiple measurements at different settings (including the ones in Figure 7.9 and more) is displayed in Figure 7.10. As (f_{th}/f_s) does not stay constant but reduces with decreasing Π, it is clear that the change of f_{th} can not solely be caused by the change in synchrotron frequency. Additionally, clear steps can be seen in (f_{th}/f_s) around integer multiples of f_s. Similar steps were also observed in measurement at the Canadian light source [76], Bessy II, and MLS [32].

The steps could be explained by the theory that the number of substructures n decreases for lower values of Π leading to a lower symmetry in the phase space distribution and thus to a lower finger frequency [31]. Substructures not rotating exactly with the synchrotron frequency, but, depending on Π, with slightly different frequencies, could explain why the plateaus between the steps are not completely flat [77; 75]. The simulations overlaid in Figure 7.10 were calculated with a Vlasov-Fokker-Planck solver by Peter Kuske (HZB). While the simulation results show a similar overall behavior, the steps are significantly less pronounced and mainly only visible for $\Pi < 1.1$ (see Figure 4 in [78] which was prepared in the framework of this thesis).

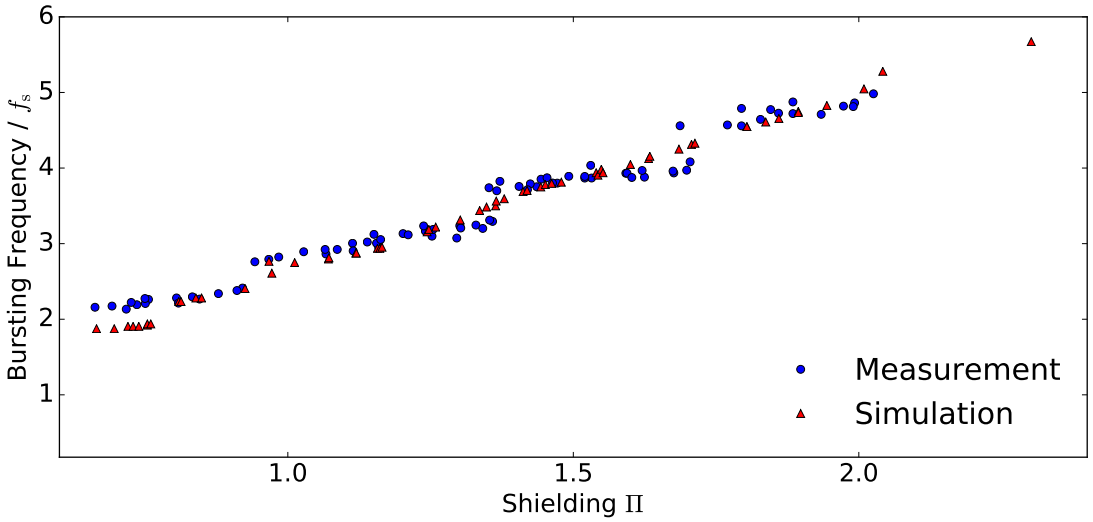

Figure 7.10: Bursting frequency (finger frequency) at the instability threshold in multiples of the synchrotron frequency as a function of the shielding parameter. The measurements were conducted at different settings of α_c and V_{RF} (including the measurements displayed in Figure 7.9. The simulations were conducted by P. Kuske (HZB).

Additional simulations were conducted, in the framework of this thesis, with the Vlasov-Fokker-Planck solver Inovesa, in the same range of Π as the measurements. The simulated charge distributions in the longitudinal phase space (with the mean distribution subtracted [79]) for different values of Π show different numbers of substructures as expected (see Figure 7.11). Four substructures are visible for $\Pi = 1.05$ and for the higher value $\Pi = 1.95$ more substructures, in this case six, are visible, supporting the initial proposition that for different settings (values of Π) different numbers of substructures are present. In more detail, this dependency of the number of substructures on Π can be seen in Figure 7.12. The bursting frequency observed in the simulation is displayed as multiples of f_s as well as the number of substructures present in the simulated charge distribution in the longitudinal phase space (counted by eye) [77]. The rather linear change of the bursting frequency with Π shows, as observed in other simulations, close to no steps and thus deviates from the number of substructures significantly, at values of Π where the number of substructures changes from one to the next higher integer value. A closer look in the phase space distribution for such a case ($\Pi = 1.35$), displayed in Figure 7.11c, reveals that one counts four substructures on the outer edge and five in the inner part of the distributions. First observations of a charge distribution showing not only a single number of substructures were already reported in [31]. This effect is displayed in Figure 7.12 as "half" integer numbers of substructures. The resulting x-symbols (connected by a dashed

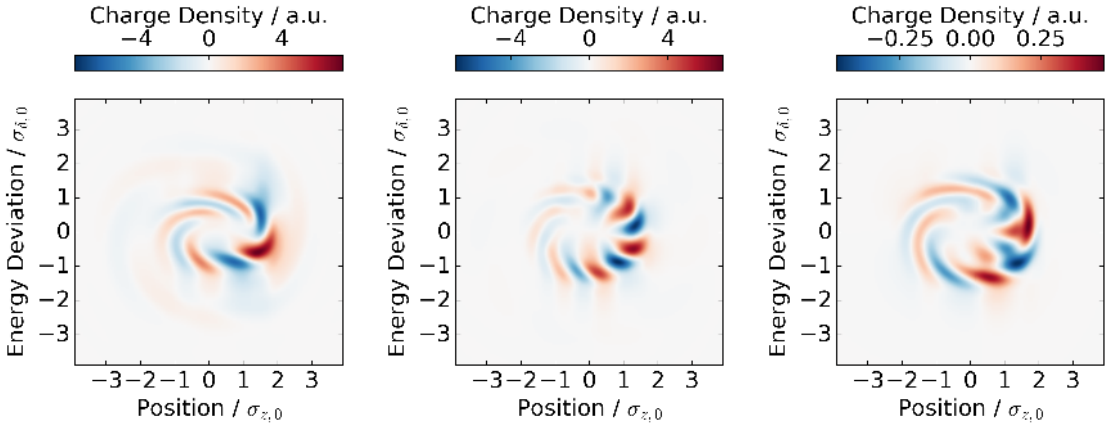

(a) (b) (c)

Figure 7.11: Charge distribution in phase space simulated with Inovesa. By subtracting the mean distribution over time the changing substructures are more pronounced [79], with positive values indicating additional charge and negative values indicating less charge. (a) Four substructures are visible for $\Pi = 1.05$ while for (b) $\Pi = 1.95$ six substructures are present. (c) If counted in outer area four substructures are present and if counted in the inner area five substructures are visible for $\Pi = 1.35$.

line) fit the relative trend of the bursting frequency better than the solid line connecting the plus symbols only taking integer numbers of substructures into account. It is not possible to conclude, whether the coexistence of $n = i$ and $n = i + 1$ substructures in the outer and inner part of the charge distribution for values of Π marking the transition from $n = i$ to $n = i + 1$ substructures directly causes the change in the bursting frequency or if both effects are symptoms of another underlying effect. In [31], it was proposed as a possible explanation that the substructures form in dynamic processes and therefore do not consist of the same electrons over time. This would allow the substructures to rotate with different frequencies than the electrons themselves. In this case, the rotation frequency would be decoupled from f_s and the quotient $(f_\mathrm{th}/f_\mathrm{s})$ is not a direct indicator for the number of substructures present. Based on the presented simulations, it can only be stated that at settings where the bursting frequency is not close to an integer multiple of f_s, the charge distribution shows a different number of substructures on the outer than on the inner part. Additionally, it is noteworthy that even with considering "half" integer values for the number of substructures the quotient $(f_\mathrm{th}/f_\mathrm{s})$ has an offset of one to the number of substructures[1]. The red symbols in Figure 7.12 show that the number of substructures minus one $(n - 1)$ shows a better agreement with $(f_\mathrm{th}/f_\mathrm{s})$. This again implies that the dynamics are more complex than a pure rotation of the structures with the synchrotron

[1] Found in discussions with T. Boltz (KIT)

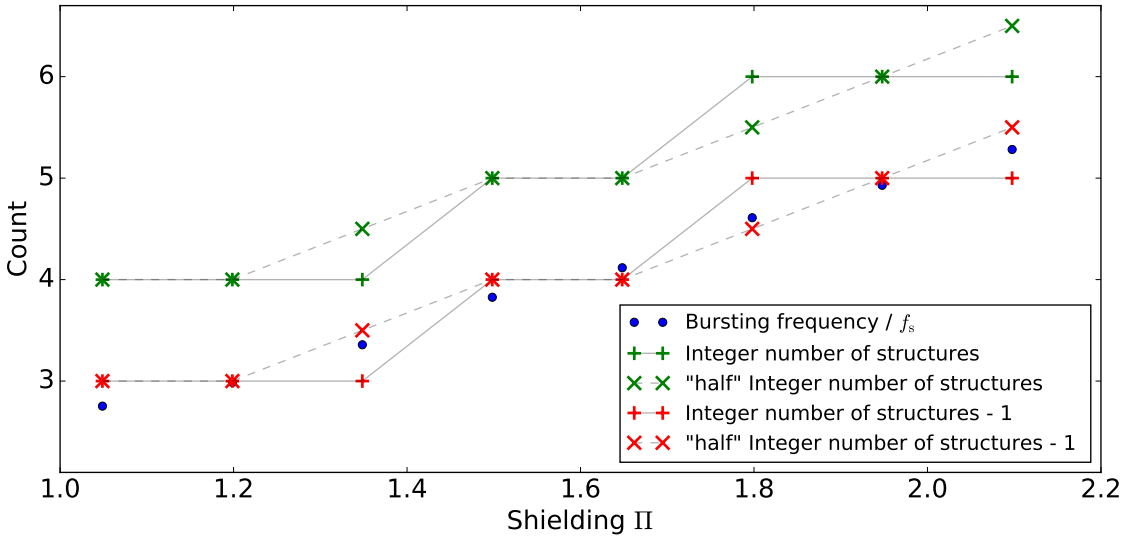

Figure 7.12: Simulated bursting frequency in multiples of f_s compared to the number of substructures n(counted manually) as a function of the shielding parameter. The simulations were conducted with Inovesa. The green plus symbols show the counted number of substructures as integers, while the green x-symbols account a changing number of substructures over the radius of the phase space (see Figure 7.11c) as "half" integers. The red symbols show the integer and "half" integer numbers of substructures subtracted by one $(n-1)$ accordingly.

frequency. Recent studies on this, based on simulations are foreseen for publication [75].

So to conclude, the bursting frequency at the instability threshold is not exactly multiples of the synchrotron frequency, which indicates a rotation frequency different from f_s. Additionally, there are steps observed in the measured quotient (f_{th}/f_s) as a function of the shielding parameter. This could be caused by a change in the number of substructures for different settings, which is observed in simulations. In the simulations, the coexistence of $n = i$ and $n = i + 1$ substructures in the outer and inner part of the charge distribution is observed for values of Π at the transition between settings with purely $n = i$ and $n = i + 1$ substructures. On the other hand, the steps in the bursting frequency for different values of Π are less distinct in simulations than in the measurements. This difference might indicate a sharper transition from $n = i$ to $n = i + 1$ substructures when changing Π in the measurements, hinting at a short-coming in the model used in the simulations (Section 2.8). Nevertheless, it can be presumed that at each value of Π there is a specific number of substructures present in the phase space distribution and the resulting bursting frequency depends on the actual rotation frequency, which is not exactly f_s but seems to depend on it. For measurements the bursting frequency can be influenced by changing α_c and V_{RF}, but it has to be kept in mind that this will also change the threshold current as discussed

in the previous section.

7.2.3 Low Bursting Frequency - Burst Repetition Rate

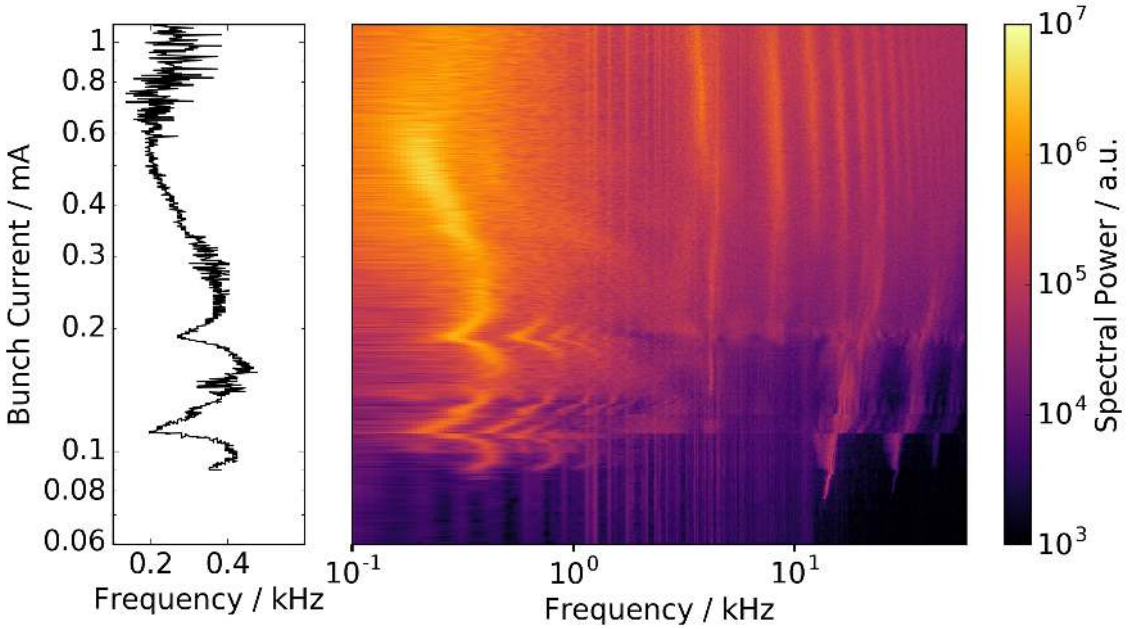

Figure 7.13: Spectrogram in a double logarithmic plot, prominently displaying the low bursting frequency. In the left panel, the extracted values of the low bursting frequency are shown as a function of the bunch current to make the changes better visible.

The low bursting frequency corresponds to the repetition rate of the bursts in emitted CSR power occurring at bunch currents significantly above the threshold current. The burst are caused by a slow growth and a following slow shrinkage of the modulation amplitude of the substructures in the charge distribution over several thousand revolutions. It is independent of the shape of the bursts as this is encoded in the higher frequency components of the spectrogram. In Figure 7.13, the low bursting frequency is clearly visible at the low frequencies of the spectrogram. In the left panel, the extracted frequency is displayed. It can be seen that the low bursting frequency changes as a function of the bunch current. It does not increase or decrease monotonously but changes the direction at different points, showing kinks at certain bunch currents. Some of the kinks align with changes in the higher frequencies, indicating the transition into a different bursting regime. At certain bunch currents the low bursting frequency is quite blurred out and hard to identify. This means that no (clear) bursts occur (e.g. directly above the threshold current) or the bursts do not have a fixed periodicity as for higher currents (see above 0.6 mA in Figure 7.13).

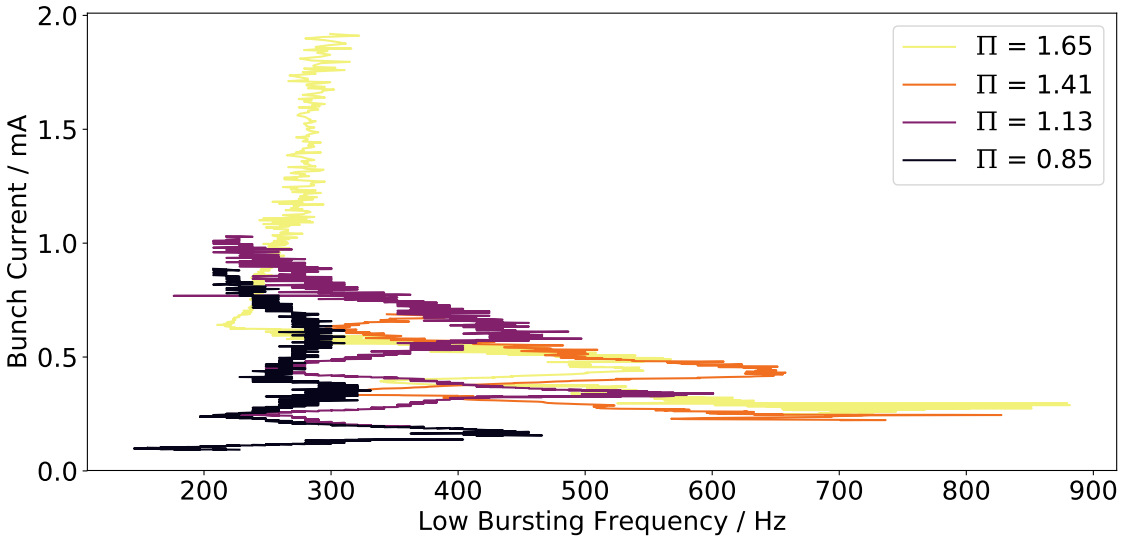

Figure 7.14: Low bursting frequency as a function of bunch current for multiple measurements with different shielding parameter. The darker the color of the curve the lower the value of Π is. A similar figure can be found in Figure A.5 showing more measurements.

The evolution of the low bursting frequency over bunch current is different if the value of Π is changed by changing the momentum compaction factor and the acceleration voltage. Figure 7.14 shows the extracted low bursting frequency as a function of bunch current for multiple different measurements with different values of Π. For lower values of Π the kinks in the low bursting frequency as a function of bunch current seem to occur at lower currents, which is probably correlated to the lower threshold for lower values of Π as shown in Figure 7.8. While the absolute values of the threshold and the bursting frequency change with Π, the overall behavior is still similar for different settings. The same regimes can be observed in all four spectrograms shown in Figure 7.3 but at different bunch currents, which seem somehow correlated to the threshold current. This is reflected in the kinks of the low bursting frequency and the fact that they are lower for measurements with lower Π.

Also, for lower values of Π (shorter natural bunch length) the span between minimum and maximum frequency of the low bursting frequency over current is smaller than for higher values of Π. In Figure 7.14, the three measurements for $\Pi \approx 1.6$ span from about $\approx 230\,\mathrm{Hz}$ up to $\approx 900\,\mathrm{Hz}$ while the two measurements with ≈ 0.85 and ≈ 0.81 span from $\approx 150\,\mathrm{Hz}$ to only $\approx 460\,\mathrm{Hz}$. The other measurements with values of Π in-between show a span of the low bursting frequency lying between these values. The result is a visible trend of increasing span with increasing Π (increasing color brightness), as can be also seen in Figure 7.15.

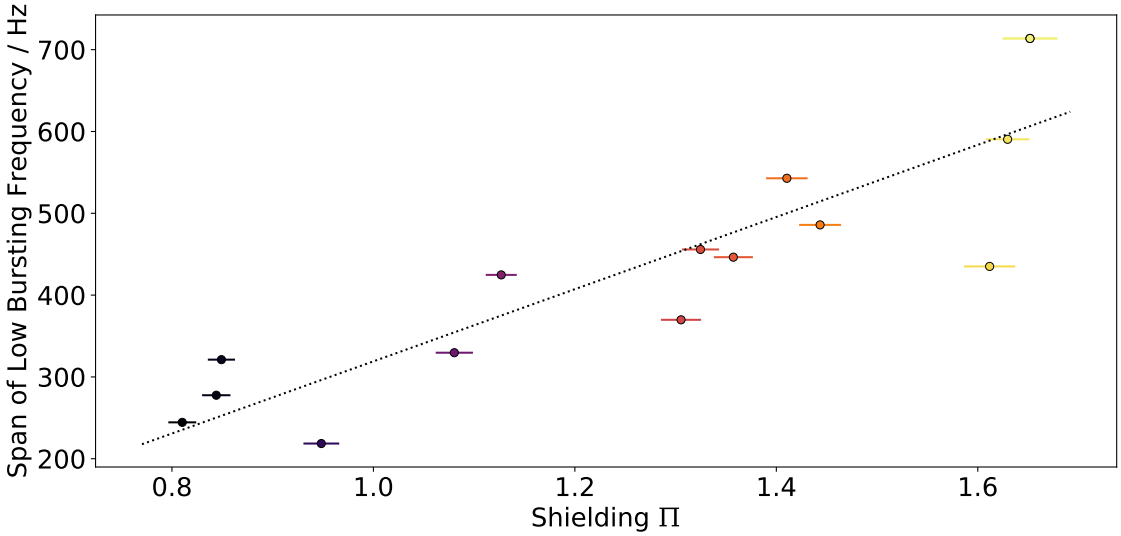

Figure 7.15: Span of the low bursting frequency calculated for different measurements including the four measurements shown in Figure 7.14 as a function of the shielding parameter. The dotted line is a linear fit to point out the increasing trend with increasing values of Π.

While the reasons for the exact behavior of the low bursting frequency as a function of the bunch current are not yet understood (and can not be exactly reproduced with Vlasov-Fokker-Planck simulations under the assumption of the parallel plates impedance), it was observed that the low bursting frequency in all measurements lies between 150 Hz − 900 Hz, which corresponds to a period of the bursting of ≈ 6.7 ms − 1.1 ms. This is in the order of the longitudinal damping time, which is according to Equation 2.13 approximately 10.5 ms. The influence of the damping time is discussed in the following chapter.

7.3 Influence of Longitudinal Damping Time

Another interesting parameter to study its influence on the behavior of the micro-bunching instability, is the longitudinal damping time τ. It depends, among other things, on the energy lost by the electrons due to synchrotron radiation (Equation 2.13). The synchrotron radiation loss can be increased by using an insertion device, like a wiggler. For the presented studies a prototype wiggler for the CLIC damping rings (CLICDW, Section 3.5, [80]), currently installed in KARA, was used and operated together with Julian Gethmann [81]. The main part of this section has also been published in [Bro18b].

As described in Section 3.2, a low alpha optics is used to achieve the short natural bunch length during the short bunch operation mode. In the used optics, the beta function at the

Table 7.1: Machine Parameters

Parameter	Value
Energy	1.3 GeV
Acceleration voltage	771 kV
Filling pattern	mixed currents
Synchrotron frequency	7.5, 7.7, 7.95 kHz
Horizontal tune	0.7863(1)
Vertical tune	0.7992(1)

position of the CLICDW is quite large, which, in combination with the strong magnetic field of the wiggler, leads to a vertical tune shift that can not be neglected [Bro18b]. The wiggler has to be switched on while the beam is already present and the machine is in the short bunch operation mode. In order to not deviate too much from the working point and potentially cross resonances leading to beam losses, the tune shift has to be compensated synchronously during the increase of the magnetic field of the wiggler. A local tune compensation is not possible as the quadrupoles at KARA are powered in five families and not individually. To find the magnet optics correcting for the tune shift, the magnetic field of the CLICDW was increased step-wise to the final value of 2 T, while the tunes were measured with the Bunch-by-Bunch system (Section 4.1,). At each step, the changes in the tunes were corrected using the quadrupoles and the RF frequency if necessary. Calculations (based on equation 61 in [82] done by Julian Gethmann [Bro18a]) show that the momentum compaction factor changes, when CLICDW is switched on, by an absolute amount of $1.2 \cdot 10^{-7}$which is negligible compared to the momentum compaction factor of about $3 \cdot 10^{-4}$ for the case where CLICDW is off.

Due to the necessary changes in the magnet optics, when switching between CLICDW on and off, the measurements (discussed in Section 7.3) were conducted as decay measurements with either the CLICDW being on during the whole decay or off. The only exception is fill C where the wiggler was switched on (and the optics corrected accordingly) after half of the decay. Not switching between CLICDW on and off and on again, also avoids unwanted changes in the optics, due to possible hysteresis effects in the magnets.

The measurements were done in separate fills (A - E) for the machine parameters given in Table 7.1. The synchrotron frequency f_s of fill A and B differs slightly from the others. With this set of fills two cases are covered, CLICDW on ($B_{wig} = 2\,T$) and CLICDW off ($B_{wig} = 0\,T$), for the same range of bunch currents. Furthermore, fill C includes the transition from one case to the other.

The THz fluctuation spectrograms for the cases with wiggler on or off show an overall similar appearance (Figure 7.16). While some differences are visible in the shape of the

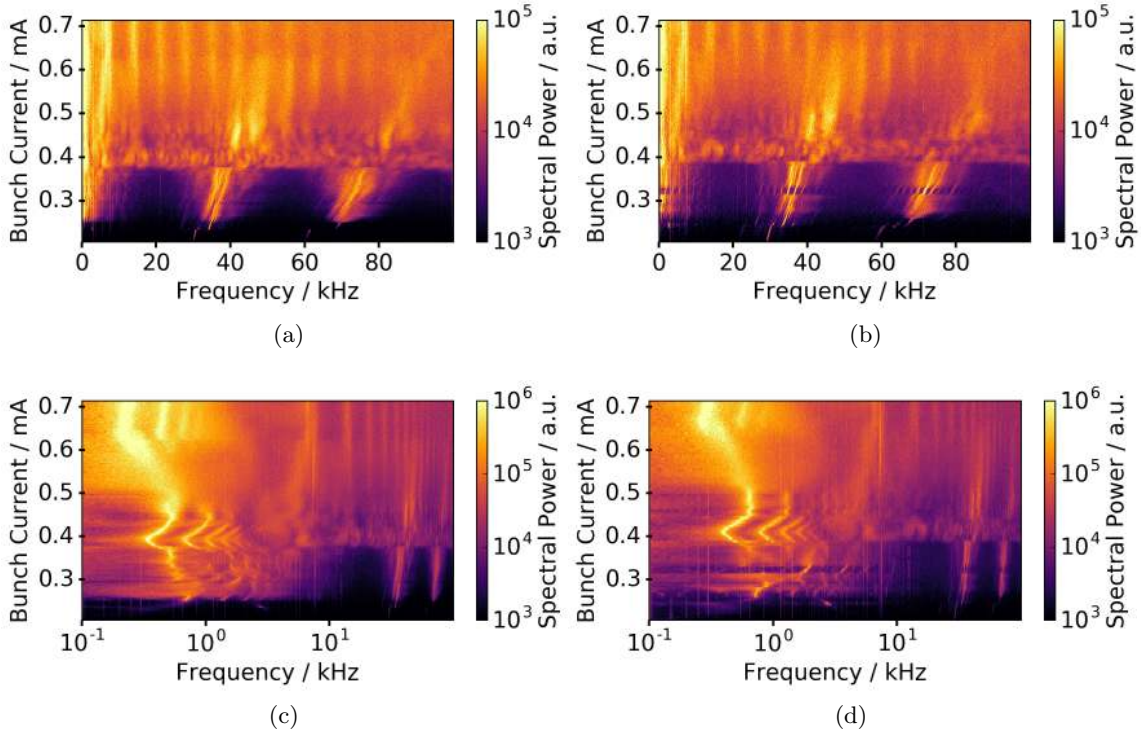

Figure 7.16: Spectrograms of the measured fluctuations in the emitted CSR power. For the data shown in (a) as well as in (c) the CLIC damping ring wiggler was off (fill B), while for (b) and (d) its magnetic field was at 2 T (fill D). In (c) and (d) the same data is shown as in (a) and (b) respectively on a logarithmic frequency axis make the low bursting frequency visible.

frequency finger shortly above 0.3 mA , other properties of the instability are unchanged. For example, the threshold I_{th} of the instability, the current above which fluctuations in the emitted THz power occur, is similar for all fills (see Table 7.2, fill D did not reach low enough currents). This shows that the momentum compaction factor was not changed significantly during the measurements, as this would lead to a change of the threshold current (as shown in the previous chapter). Therefore, it can be said that the CLICdw and therefore the longitudinal damping time has no significant influence on the threshold current. This is in agreement with the statement in [13] that the micro-bunching instability is a strong instability and hence its threshold should be independent from the damping time. The approximation for the threshold current resulting from their simulations is independent from the damping time (Equation 2.24). As shown in Subsection 7.2.1. this approximation concurs with measurements at KARA to a great extent (see also [Bro16a]). For the settings used in this experiment, the simple scaling law predicts a threshold current of $I_{\mathrm{th}} = 207\,\mu\mathrm{A}$ for $f_{\mathrm{s}} = 7.7\,\mathrm{kHz}$.

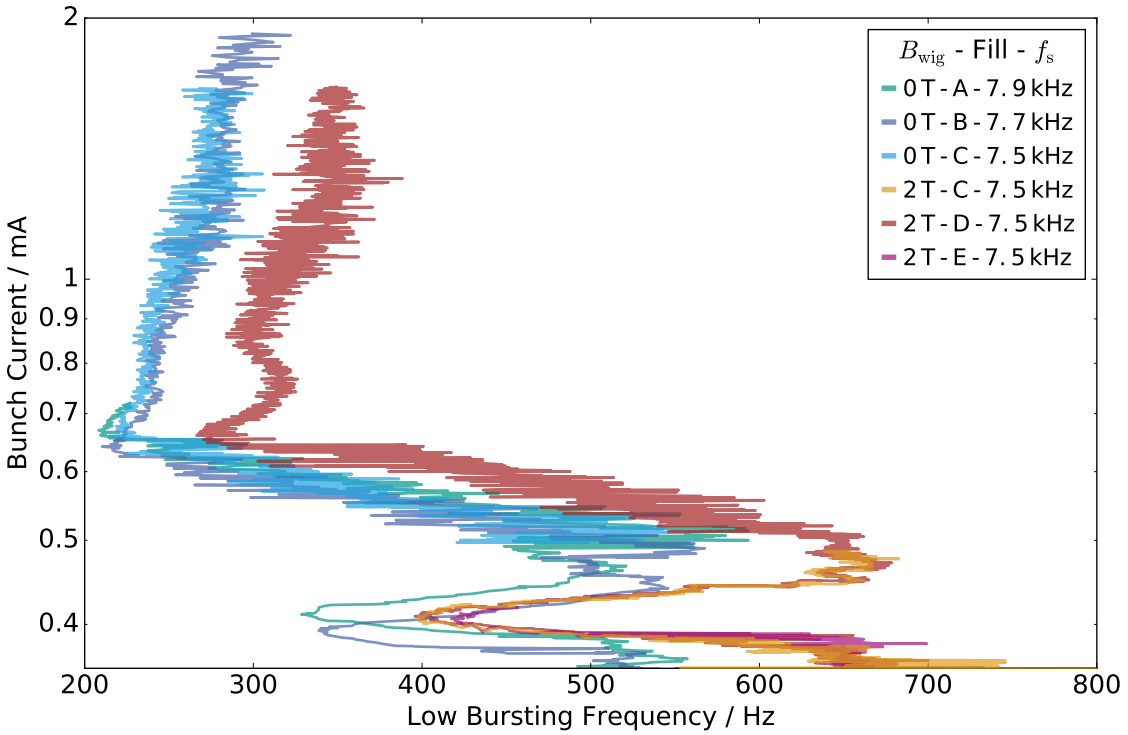

Figure 7.17: Low bursting frequency (periodicity of radiation outbursts) as a function of bunch current for different fills. A shift in the frequency is visible for fills with CLICDW at 0 T compared to fills with CLICDW at 2 T.

Also, the bursting frequency, the fluctuations directly above the instability threshold have similar frequencies f_{th} (Table 7.2) and don't seem to be changed significantly by changes of the damping time.

The low frequency of the fluctuations in the emitted THz power (the periodicity of the radiation outbursts), however, shows a significant difference between the measurements with CLICDW on and CLICDW off. This low bursting frequency is displayed as a function of the bunch current in Figure 7.17 for the different fills. For all fills the curves show similar features, like the kinks at approximately 0.65 ± 0.01 mA and 0.40 ± 0.01 mA. Nevertheless, the curves for CLICDW off lie at lower frequencies whereas the ones with CLICDW on are shifted to higher frequencies. Contrary to the effect a change of α_c and V_{RF} has on

Table 7.2: Bunch Current and Frequency at Instability Threshold

Property	A	B	C	E
B_{wig}/ T	0	0	$0 \rightarrow 2$	2
I_{th}/ µA	217± 3	213± 3	215±2	220± 4
f_{th}/ kHz	30.9±0.3	30.1±0.3	29.6±0.3	29.7±0.3

the low bursting frequency (see Subsection 7.2.3), the frequencies are only shifted and no clear change in the behavior over current is visible. For example for a current of 0.8 mA the frequency is shifted from 240 ± 5 Hz to 310 ± 5 Hz but the kinks at e.g. 0.65 mA stay at the same current.

The dependency of the low bursting frequency on the damping time is not unexpected as will be explained with a simple model of the longitudinal dynamics during a THz bursts in the following. The additional potential acting on the bunch during the micro-bunching instability, is the convolution of the wake function and the bunch profile (see Section 2.6). The shorter the bunch is the stronger this additional wake potential is acting on the bunch and driving the growth of substructures. These substructures lead to the emission of coherent synchrotron radiation above the vacuum chamber cut-off, which is visible as an outburst of THz radiation. Due to filamentation and diffusion the substructures get smeared out over time, making the bunch longer. For a longer bunch the wake potential is significantly weaker and the bunch length is damped down until it is short enough to generate a strong wake potential leading again to the growth of substructures and another repetition of this cycle. Such a cycle is visible in the bunch length σ_z and the energy spread σ_δ as a saw-tooth like pattern [83; Keh17].

The time span between two outbursts at a given bunch current I_b consists of two parts. The first part, the rise time of the bunch length is caused by the occurrence and filamentation of the substructures. This time changes as a function of I_b. The second part, is the time it takes to damp the bunch length down from its maximum to its minimum. On the one hand, this depends strongly on the longitudinal damping time and explains how the damping time affects the repetition rate of the outbursts. On the other hand, it depends on the minimal and maximal bunch length at I_b.

Assuming there is no exciting force from the impedance (as the blown-up bunch has no high enough frequency components to overlap with the impedance) during the second part (the damping of the bunch length) which is then exponential, the low bursting frequency can be described as follows. The rise time of the bunch length $\Delta t_\mathrm{rise}\,(I_\mathrm{b})$ plus the time it takes to damp the bunch length from its maximal blown-up length to the minimal bunch length (Δt_shrink) at a each bunch current determines the low bursting frequency[2]:

[2]Instead of the bunch length, one can also argue via the energy spread. The resulting equation would look the same.

$$f\left(I_\mathrm{b}\right) \approx \left(\Delta t_\mathrm{rise}\left(I_\mathrm{b}\right) + \underbrace{\frac{\tau}{2} \cdot \ln\left(\frac{\sigma_{z,\mathrm{max}}\left(I_\mathrm{b}\right) - \sigma_{z,0}}{\sigma_{z,\mathrm{min}}\left(I_\mathrm{b}\right) - \sigma_{z,0}} \right)}_{\Delta t_\mathrm{shrink}} \right)^{-1} \tag{7.2}$$

with the longitudinal damping time τ, the minimal and maximal bunch length ($\sigma_{z,\mathrm{min}}$, $\sigma_{z,\mathrm{max}}$) during one bursting cycle, the natural bunch length $\sigma_{z,0}$ towards which it is damped, and the rise time Δt_rise of the bunch length at the bunch current I_b. $\frac{\tau}{2}$ is used in the equation to reflect that the bunch size damps approximately twice as fast as the center of mass. A sketch of this model is displayed in Figure 7.18. As the bunch length decreases

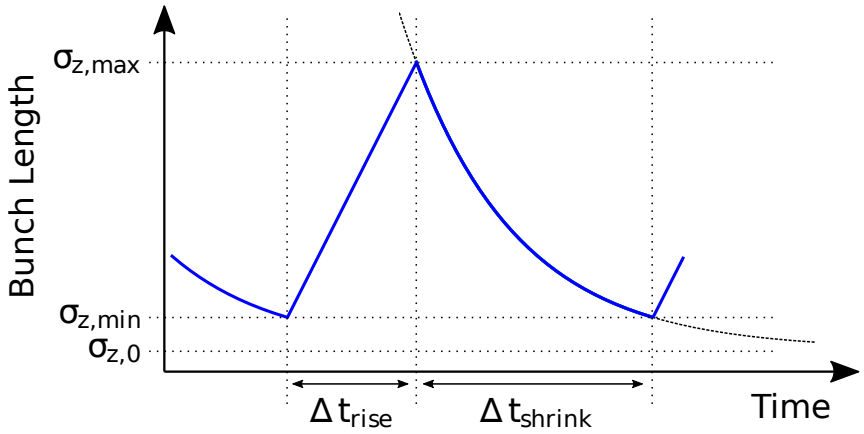

Figure 7.18: Sketch of the simple model illustrating the parameters contributing to the duration of one burst. The blue line shows the increase of the bunch size up to the maximal bunch length $\sigma_{z,\mathrm{max}}$ followed by its damping to the minimal bunch length $\sigma_{z,\mathrm{min}}$. The dotted curve indicates the exponential damping towards the natural bunch length.

with current also the interaction between the longitudinal charge distribution and the impedance changes. Therefore, the low bursting frequency can change as a function of bunch current even for a constant damping time as seen in Figure 7.17. A faster damping (which is the case with CLICDW on) results in a similar behavior but shifted to higher frequencies due to the shorter time necessary to shrink down from $\sigma_{z,\mathrm{max}}$ to $\sigma_{z,\mathrm{min}}$, therefore supporting the observations in the measurements.

The dependency of the low bursting frequency on the longitudinal damping time was also studied with simulations using Inovesa (Section 2.8). For this, two bunch current decays were simulated with the machine settings given in Table 7.1 and different values for the longitudinal damping time. The values for τ were estimated from optics simulations using elegant [84] and a LOCO based model [85] by Julian Gethmann (KIT, [Bro18a]). The input to Inovesa was then set to $\tau_{\mathrm{s,\ CLICDW\ off}} = 11\,\mathrm{ms}$ and $\tau_{\mathrm{s,\ CLICDW\ on}} = 9\,\mathrm{ms}$. The

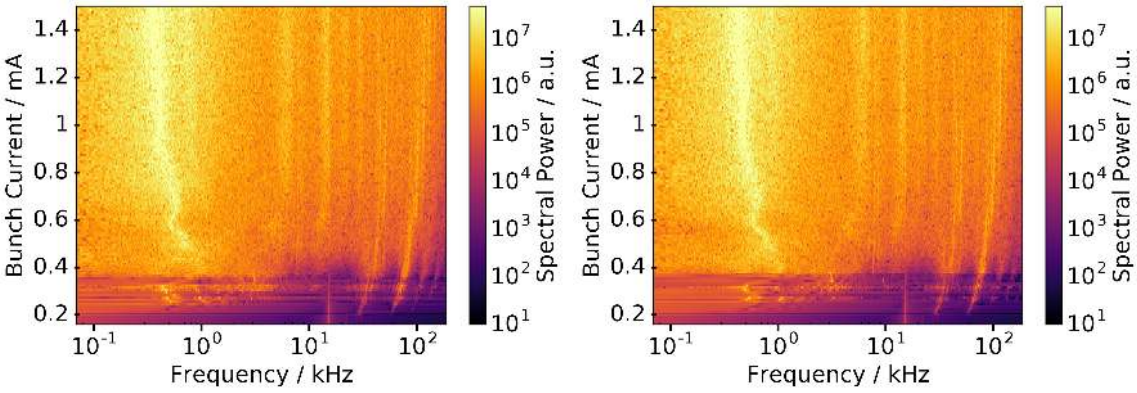

(a) (b)

Figure 7.19: Simulated spectrograms with logarithmic frequency axis, prominently showing the low bursting frequency. (a) CLICDW off ($\tau = 11\,\mathrm{ms}$). (b) CLICDW on ($\tau = 9\,\mathrm{ms}$)

Table 7.3: Simulated Bunch Current and Frequency at Instability Threshold

$B_{\mathrm{wig}}/\mathrm{T}$	0	2
$\tau_{\mathrm{s}}/\mathrm{ms}$	11	9
$I_{\mathrm{th}}/\mathrm{mA}$	205.0 ± 0.5	205.0 ± 0.5
$f_{\mathrm{th}}/\mathrm{kHz}$	29.27 ± 0.05	29.26 ± 0.05

resulting spectrograms are shown in Figure 7.19. Similar to the measurements the overall appearance is the same.

The simulation shows no change at all in the threshold current as well as in the bursting frequency at the threshold (see Table 7.3). Supporting the conclusion that the threshold current I_{th} as well as the fluctuation frequency f_{th} at the threshold do not depend on the longitudinal damping time.

In Subsection 7.2.2, it was discussed that the fluctuation frequency at the threshold is expected to originate from the changes in the longitudinal bunch profile caused by the rotation of substructures in the phase space and that the rotation frequency of the substructures is close to (but not exactly) the synchrotron frequency. The hypothetical idea that the difference between the substructure rotation frequency and the synchrotron frequency might depend on the damping time, as τ influences the shrinking of the phase space, is directly disproven, as the change of damping time had no effect on the finger frequency (bursting frequency). Probably the time scales of the longitudinal damping time and the synchrotron frequency are too different and the difference in the rotation frequency of the substructures and the synchrotron frequency has a different origin.

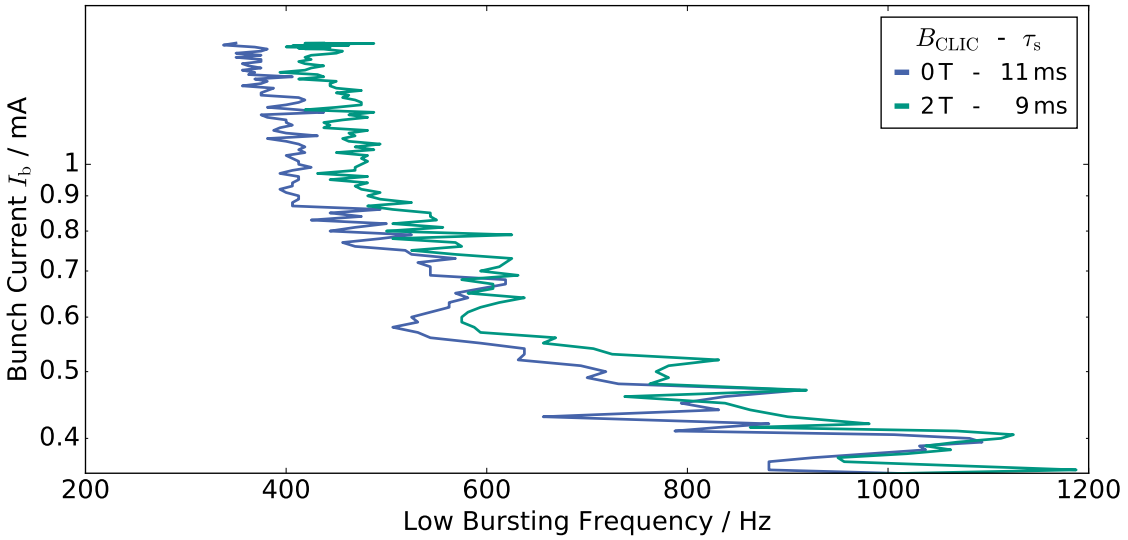

Figure 7.20: Simulated low bursting frequency as a function of bunch current for damping times of 11 ms (corresponds to CLICDW off) and 9 ms (corresponds to CLICDW on). Shift of frequency curve to higher frequencies is clearly visible.

In the simulated low bursting frequency a shift occurs for the changed damping time (Figure 7.20). While the overall course of the low frequency over bunch current does not quantitatively match the measurements, the shift to higher frequencies with decreased damping time matches qualitatively the effect observed in the measurements. This supports the thesis of the dependency of the low bursting frequency on the longitudinal damping time.

As the simulations provide access to the whole charge distribution in the phase space and therefore every derived parameter, like the bunch length or the energy spread, the model introduced above (Equation 7.2) can be directly tested on the simulated data (which had a set value of $\tau = 9\,\mathrm{ms}$). In the following the energy spread is used for the discussion as the energy loss leading to the synchrotron radiation damping affects directly the energy of the electrons. The following discussion and calculations can be done as well on the bunch length and would yield the same results (see Appendix A.6).

Figure 7.21 shows the minimal and maximal energy spread $\sigma_{\delta,\mathrm{min/max}}(I_{\mathrm{b}})$ reached during the bursting for each bunch current of the decay. It is visible that the difference between the minimal and the maximal value decreases for decreasing current but at the same time both values come closer to the natural energy spread at zero current (see Figure 7.21b). Both effects affect the time ($\Delta t_{\mathrm{shrink}}$) it takes with a pure exponential damping to shrink down from $\sigma_{\delta,\mathrm{max}}(I_{\mathrm{b}})$ to $\sigma_{\delta,\mathrm{min}}(I_{\mathrm{b}})$ differently. The reduced difference between minimal and maximal value shortens $\Delta t_{\mathrm{shrink}}$, while coming closer to the natural energy

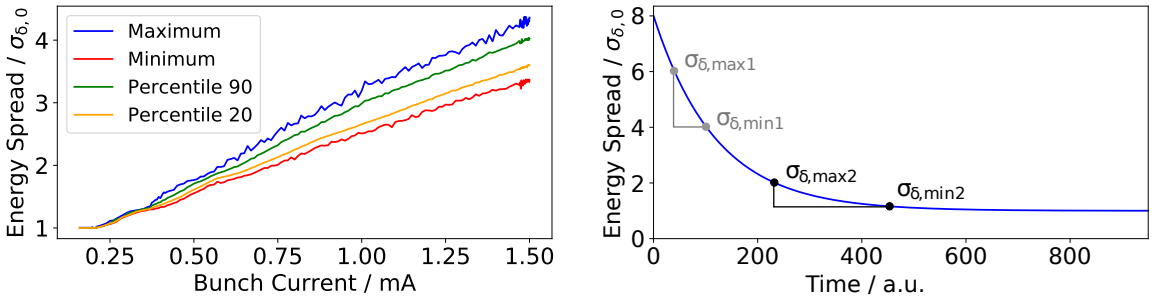

(a) (b)

Figure 7.21: Figure (a) shows the simulated minimal and maximal energy spread as well as the 90th and 20th percentile of the energy spread at each bunch current as a function of the bunch current. (b) shows a sketch of an exponential decay from $\sigma_{\delta,\mathrm{max2}}$ to $\sigma_{\delta,\mathrm{min2}}$ for a case where the energy spread is close to the natural energy spread and a case with high values of $\sigma_{\delta,\mathrm{min1}}$ and $\sigma_{\delta,\mathrm{max1}}$.

spread again increases $\Delta t_{\mathrm{shrink}}$. So, the actual time it takes to shrink down the energy spread depends on the balance between both effects. It can be easily calculated for each bunch current how long ($\Delta t_{\mathrm{shrink}}$) it would take for a pure exponential damping of the energy spread from the highest value to the lowest value. To accustom for outliers the 90th percentile for the upper and the 20th percentile for the lower value was used instead. $\Delta t_{\mathrm{shrink}}$ was calculated for different values of the damping time ranging from 2 to 18 ms and is displayed in Figure 7.22. As expected, the resulting lines show no simple decrease or increase with bunch current, but a quite complex behavior, as the distance between minimal and maximal energy spread and the effect from a higher or lower position on the exponential decay change with different rates. This behavior over current looks similar to the one of the actual repetition rate of the bursts (low bursting frequency) even so the model completely neglects the first part (the rise time) of the bursting cycle. Furthermore, a change in damping time leads to a change of the behavior over current in the same way as the observed shift of the frequency in the measurements. A stronger damping (smaller damping time) leads to a short time necessary to shrink down the energy spread, which corresponds to a higher repetition rate and therefore higher frequency as observed in the measurements with the CLICDW on.

Additionally, the actual time it took the energy spread to damp down after each burst was extracted from the simulations using a software Schmitt trigger with the switching thresholds at the same 90th and 20th percentile values. The time it takes to shrink down was defined as the time the Schmitt trigger took from starting the transition (crossing the upper level downwards) to reaching the lower level and is displayed as blue curve in Figure 7.22. The curve shows a similar but not exactly the same behavior as the ones calculated

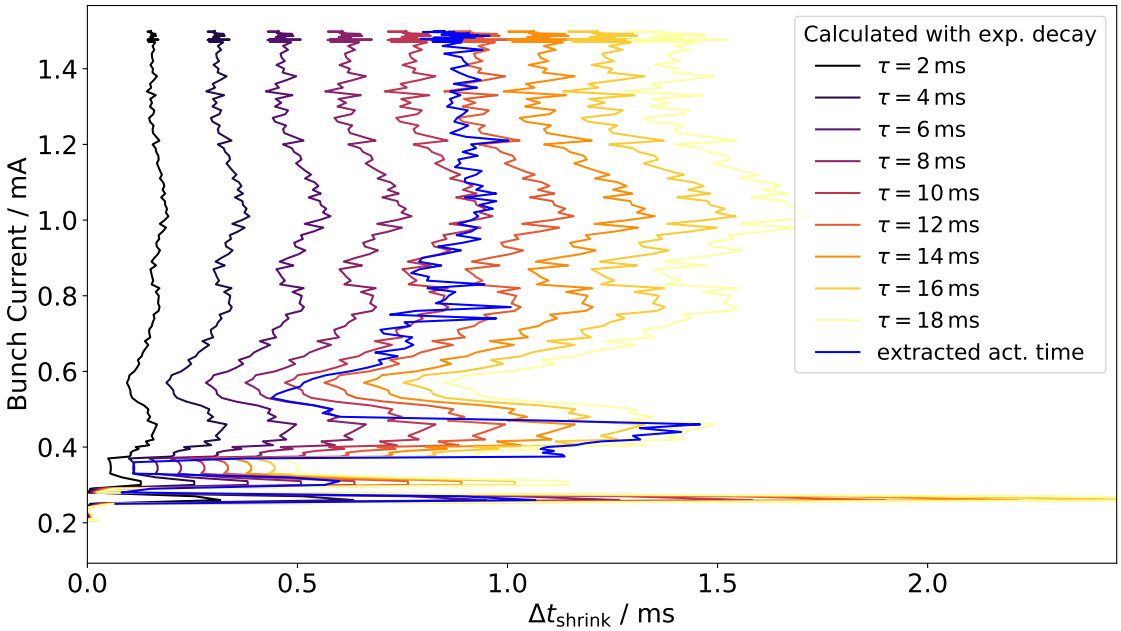

Figure 7.22: Time it would take the energy spread to shrink down between bursts calculated based on the model that it is damped down from $\sigma_{\delta,\max}$ to $\sigma_{\delta,\min}$ with a pure exponential damping with damping time τ. For $\sigma_{\delta,\max}$ and $\sigma_{\delta,\min}$ the values displayed in Figure 7.21 are used and the damping time is varied. Additionally, the actual shrinking time it took in the simulation was extracted with a Schmitt trigger and is displayed in blue. The simulation this is based on was run with a damping time of 9 ms.

for different damping times, as it even crosses several of these. This difference between the curve for the extracted actual time and the curves for the calculated time indicates that the damping can not be assumed to be purely exponential with a fixed value of τ for one current decay. For different currents there seem to be different effective damping times. For example, at bunch currents above 0.6 mA the extracted actual time is mostly above the value for $\tau = 10$ ms even though the underlaying simulation was run with a damping time of 9 ms. This is not surprising, considering the initial excitation by the wake potential is not switched off instantly but gradually decreases as the substructures filament out. And also at the end of the damping of the energy spread, the excitation starts gradually to increase again to drive the next burst, leading to a non-exponential damping process with different (in this case higher) effective damping times depending on the bunch current.

Coming back to the model, the shift caused by the change in damping time is linear in τ as the original assumption was that it damps purely exponentially with the given damping time from the maximal to the minimal value ($\Delta t_{\text{shrink}} = \frac{\tau}{2} \ln(\frac{\sigma_{\delta,\max} - \sigma_{\delta,0}}{\sigma_{\delta,\min} - \sigma_{\delta,0}})$, see Equation 7.2). So, if the damping time changes, Δt_{shrink} changes proportionally. Plotting the inverse of Δt_{shrink} (analog to a repetition rate but without Δt_{rise}) as a function of damping time, it results in a pure $1/\tau$ dependency as visible in Figure 7.23b. To compare this with the actual repetition rate of the bursts (the low bursting frequency), the bursting behavior at a fixed bunch current (1.5 mA) was simulated with Inovesa for different damping times. Figure 7.23a shows the resulting low bursting frequency as a function of damping time. The result does not precisely follow $1/\tau$. Which is not surprising as it also contains the rise time of the burst. Also, it was not considered in the model that $\sigma_{\delta,\max}$ and $\sigma_{\delta,\min}$ might change with the damping time as well. A fit with the function $a/(\tau - b) + c$, which describes the data better, results in an y-offset of $c \approx 250$ Hz and an offset in time of $b \approx 0.003$ s. This could indicate that for a damping time shorter than 3 ms there are no bursts anymore and therefore no repetition rate defined. The y-offset could indicate that even for long damping times a minimal repetition rate of 250 Hz is kept. These are two interesting points which should be investigated with further simulations. On the other hand, the bad fit of $1/\tau$ could be attributed to the fact that $1/\tau$ is just not the right function to describe the damping time dependency of the low bursting frequency when taking into account the rise time and other effect ignored by the model. The difference by a factor of approximately 2 between the simulated low bursting frequency and the calculated shrink time from the simple model indicates that the rise time, which is missing in the model is roughly the same size as the shrink time.

By using the CLIC damping wiggler prototype installed at KARA, it was shown that the low bursting frequency depends strongly on the longitudinal damping time. For the

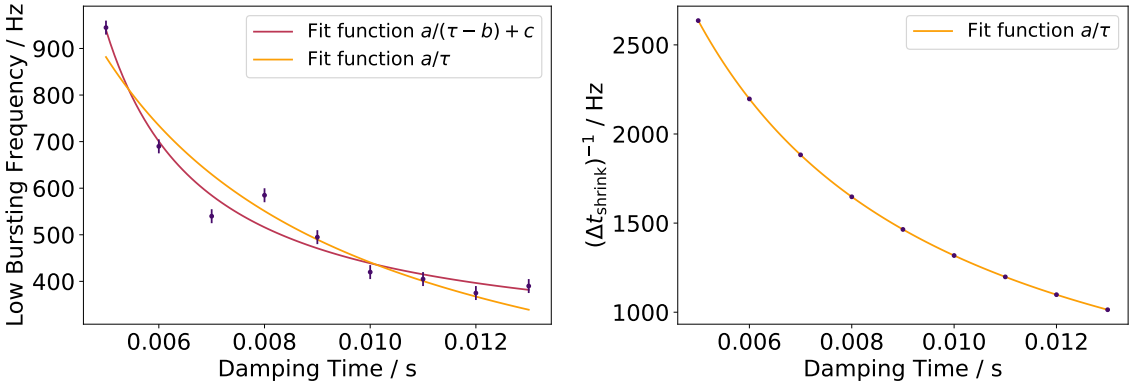

(a) (b)

Figure 7.23: (a) Simulated low bursting frequency as a function of damping time. All other settings like α_c, V_{RF} and the current (1.5 mA) were the same. (b) Inverse of calculated shrink time (via exponential damping) of the energy spread. The data are taken from Figure 7.22 at 1.5 mA for the different assumed damping times.

threshold current as well as the bursting frequency at the threshold no change was observed. The findings could be reproduced by simulations with Inovesa. In principle, insertion devices can be used to increase the energy loss and shift the low bursting frequency to a desired frequency range as well as further study the dependency of instabilities on the longitudinal damping time. It would be interesting to do this, for example, for the weak instability discussed in Chapter 9 as this instability is predicted to depend on the damping time [13].

8 Signature of the Micro-Bunching Instability in Alternative Observables

After studying the effects of the micro-bunching instability based on the detection of the emitted CSR power with broad-band Schottky diode detectors in the previous chapter. In this chapter, the effects of the instability will be measured with multiple different detectors. The first part will focus on measurements conducted with narrow-band Schottky diode detectors sensitive in different frequency ranges. Based on this, it is discussed how the spectrum of the emitted CSR changes and leads to the observed bursts in the emitted CSR power. In the second part, additionally to the emitted CSR also the horizontal and longitudinal bunch profile is measured turn-by-turn. These synchronous measurements provide a further insight into the longitudinal beam dynamics under the instability. In comparison with simulations the expected behavior based on working model, described in Section 2.9, is discussed and verified.

8.1 Observation in Different CSR Frequency Ranges

In the previous chapters, THz detectors sensitive in a broad frequency range were used to detect the CSR power emitted by a bunch at each turn. The emitted CSR spectrum depends on the longitudinal bunch profile, which is, as discussed in Section 2.9, assumed to change under the influence of the micro-bunching instability. Using multiple THz detectors sensitive in different frequency ranges will allow to study the fluctuations in the emitted CSR power not only for the overall integrated spectrum but separately in the spectral range of each detector. This will help to understand how the spectrum of the emitted CSR changes under the instability and what effects this has on the observed characteristics.

Measurements with multiple synchrotron radiation detectors can be conducted in a way that the different detectors are synchronously read out with KAPTURE. As described in Subsection 5.3.2, KAPTURE supports an operation mode where different detectors are each connected directly to one sampling channel leading to an inherent synchronization on a bunch-by-bunch basis. This was, for example, used to test the synchronization

of KAPTURE to the other measurement setups during the synchronous measurements (Section 8.2), by connecting an optical photo diode sensitive to visible light in addition to the THz detector. For the studies presented in the following, narrow-band waveguide-coupled Schottky barrier diodes from VDI (Subsection 5.2) were used.

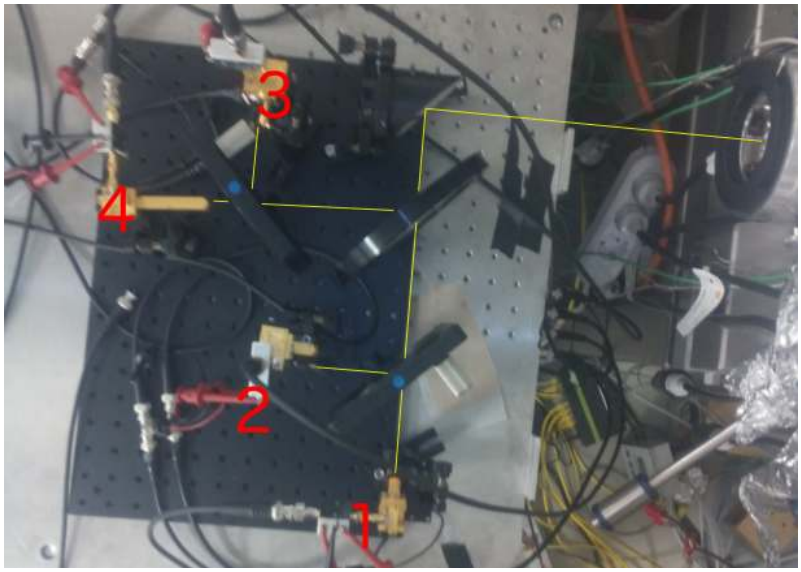

Figure 8.1: Photo of the setup for the 4 Schottky detector single-shot spectrometer. The incoming synchrotron radiation is focussed with an off-axis paraboloid mirror and split into four equal parts with three wire-grid polarizers. The path of the light is sketched as yellow lines.

For this set-up the synchrotron radiation coming from the beam port is first focussed with an off-axis paraboloid mirror and then split with wire-grid polarizers. A setup with four THz detectors, as it was used for the measurements published in [Ste18b], is depicted in Figure 8.1. This joint publication looked into the differences in the mean and the standard deviation of the CSR power, as a function of the bunch current, if detected in different frequency ranges. Additionally, the onset of a burst when observed in different frequency ranges was compared and for a bunch current directly above the threshold current, a phase shifts between the signals of different detectors was observed and compared with simulations by Inovesa. Additional to the observations reported in [Ste18b], further effects can be observed in other measurements and will be described in this section.

The first measurements of this type at KARA were conducted with only two Schottky diodes from VDI [72], sensitive in the frequency range $140 - 220\,\mathrm{GHz}$ (detector A) and $325 - 500\,\mathrm{GHz}$ (detector B). Figure 8.2 shows the spectrograms recorded with the two Schottky diodes connected to KAPTURE. Both spectrograms show overall the same behavior. In both, only a single frequency line (with the bursting frequency of $32.5\,\mathrm{kHz}$)

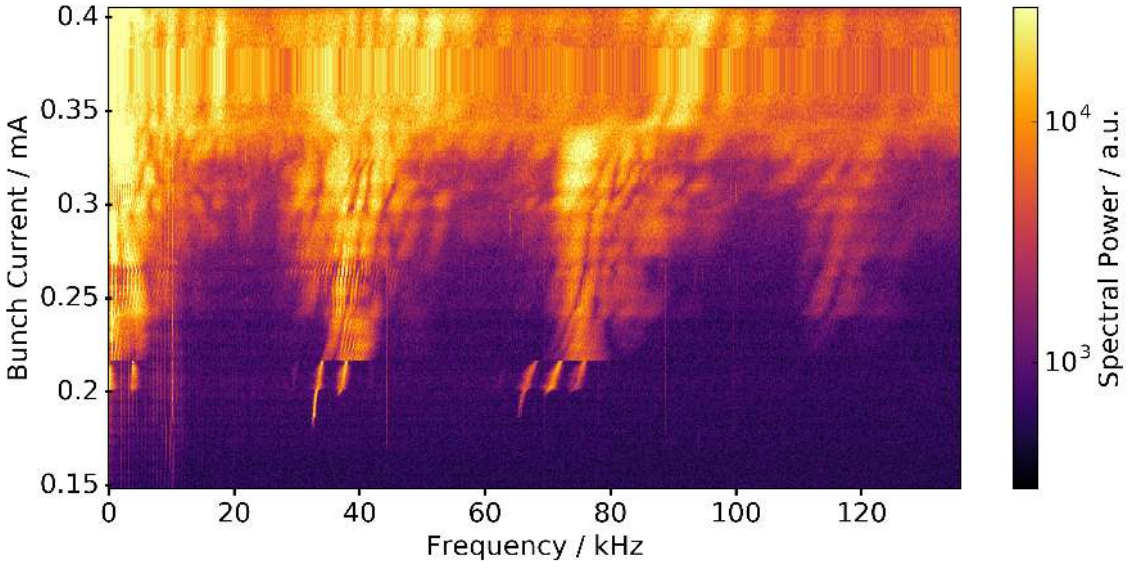

(a)

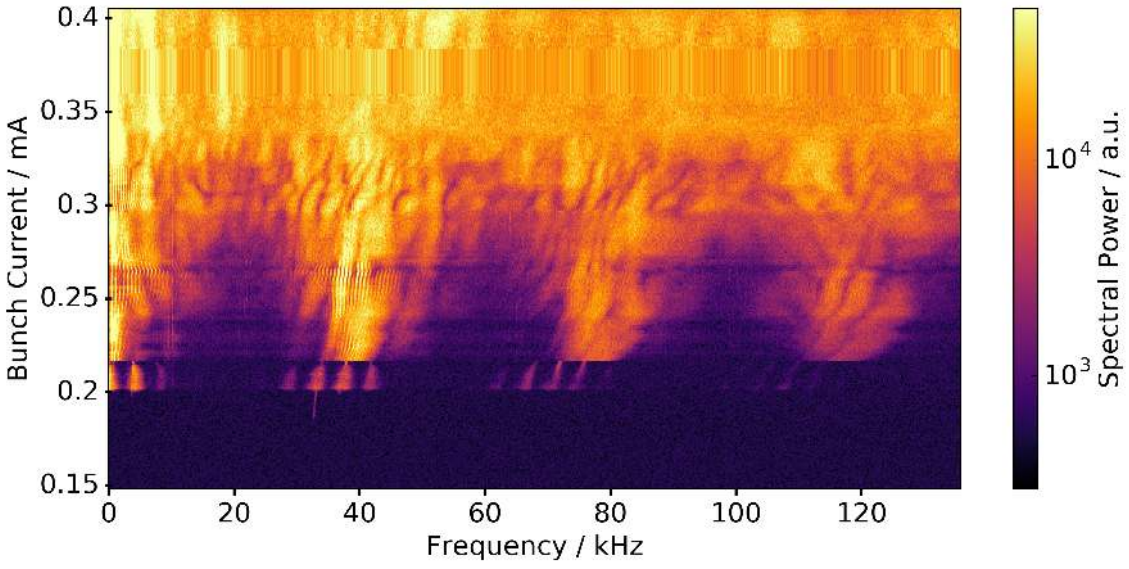

(b)

Figure 8.2: Spectrograms of the fluctuation in the emitted CSR power detected simultaneously with two different Schottky diode detectors from VDI. (a) Detector A is sensitive for $140 - 220\,\mathrm{GHz}$. (b) Detector B is sensitive for $325 - 500\,\mathrm{GHz}$.

occurs at the threshold. At higher bunch currents (around 205 µA), additional frequency components become prominent until starting around 330 µA up to the top of the spectrogram mainly a broad frequency band is visible.

On the other hand, also distinct differences can be observed. First, some frequency components within one spectrogram show a different spectral power relative to each other. For example, in the spectrogram obtained with detector B, the narrow line starting at the bursting frequency (32.5 kHz) at the threshold, is weaker (darker in color) compared to the frequency content for the same frequency at higher bunch currents. While in the spectrogram obtained with detector A, this line is similar in strength (similar in color) as the frequency content at higher bunch currents. Second, at the upper end of this frequency line, around 200 µA, several further lines occur left and right of it (in total three additional lines). For the spectrogram taken with detector B these lines all have more or less the same strength. While in the spectrogram detected with detector A these lines differ significantly in strength, so far that the ones furthest to the left and right are hardly visible. In general, the relative power in the higher harmonics is bigger in the measurement obtained with detector B than for the one with detector A. For example, the third harmonic of the frequency structure between $215 - 300$ µA (original around 38 kHz and 3rd harmonic around 114 kHz) is better visible in B than in A even so the original structures were similar in strength (in color) for both spectrograms.

The effects of the different distribution of power in the fluctuation frequencies are also clearly visible in the time domain representation of the two detector signals, as differences in the shape of the detected CSR bursts. The upper two figures in Figure 8.3 show the detected CSR power over turns at a bunch current of 326 µA, for each detector respectively. Both signals look similar with a steeper increase than the following decrease of the detected CSR power for each burst. On the signal recored with detector B, the amplitude of the fast fluctuation during the decrease are slightly higher. The signals recorded at a bunch current of 218 µA are displayed in the lower two figures of Figure 8.3. Contrary to the signals at the previous bunch current, now the two signals have a huge difference in amplitude. Furthermore, their shape differs significantly. While the signal recorded with detector A starts increasing again directly after the last decrease, the signal of detector B shows some low and constant signal between the bursts. Additionally, the bursts detected with detector B look quite symmetric concerning the increase and decrease in each burst, opposed to the asymmetric shape of the bursts in the signal of detector A. For signals recorded at further bunch currents see Appendix A.7.

These observations lead to the conclusion that the fluctuations in the emitted CSR power come along with changes in the emitted CSR spectrum and do not simply originate from

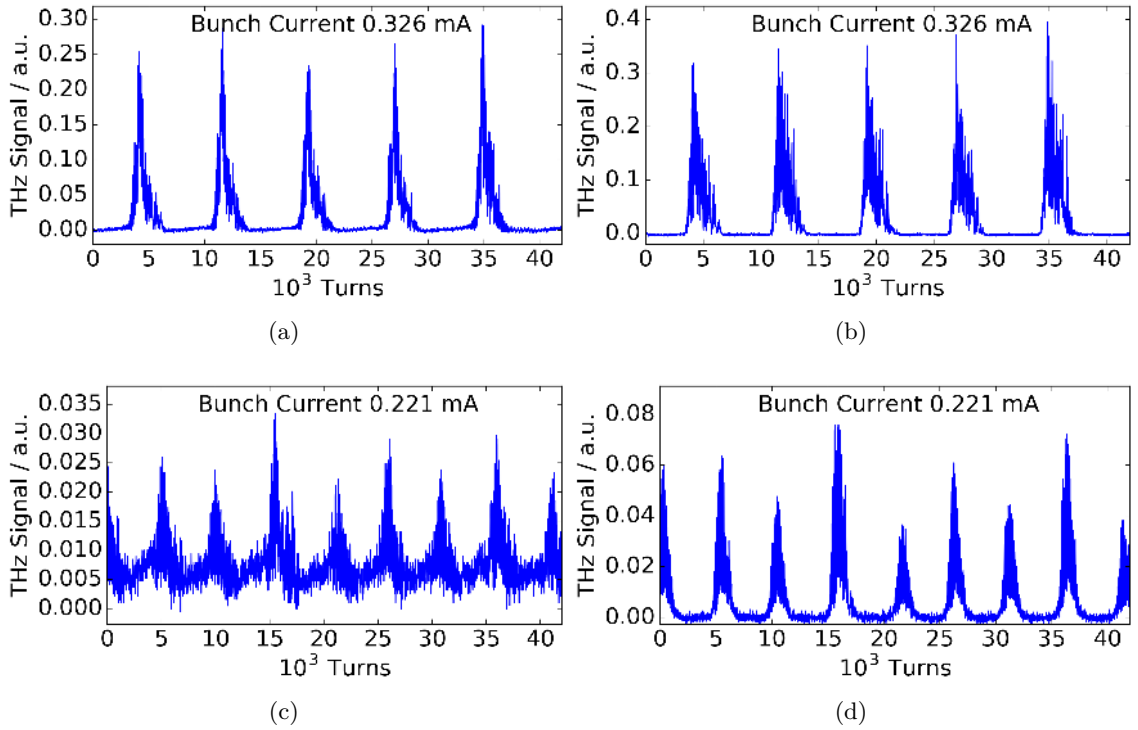

Figure 8.3: CSR power per turn simultaneously detected with two waveguide-coupled Schottky diode detectors sensitive in different frequency ranges (A: 140 – 220 GHz and B: 325 – 500 GHz). (a) was measured with detector A and (b) was measured with detector B, at a bunch current of 326 µA. (c) and (d) were taken at a lower bunch current of 221 µA with A and B respectively.

a scaling of the emitted power with a fixed spectrum. The spectrum changes due to temporally more power being emitted in different frequencies, depending on the momentary shape of the longitudinal bunch profile. This supports the model discussed in Section 2.9, as the occurrence of substructures changes the bunch shape and therefore leads to changes in the emitted CSR spectrum.

This leads to the following question. When the fluctuations of the emitted power differ for different frequency ranges, is there then a difference in the current at which the first fluctuations are observed, depending on the detected frequency range? This could be the case, if the distortion of the bunch profile (at and directly above the bursting threshold) would consist mainly of a modulation with a single frequency which is higher than the frequency contributions in the undisturbed bunch profile. In this case, there would be frequency ranges in the spectrum where the emitted power is not increased by the deformation, as the form-factor is zero in these ranges. To detect this, a detector with a respectively narrow spectral sensitivity would be necessary. In the measurement with the two detectors (A: 140 – 220 GHz and B: 325 – 500 GHz) this is not observed. As seen in

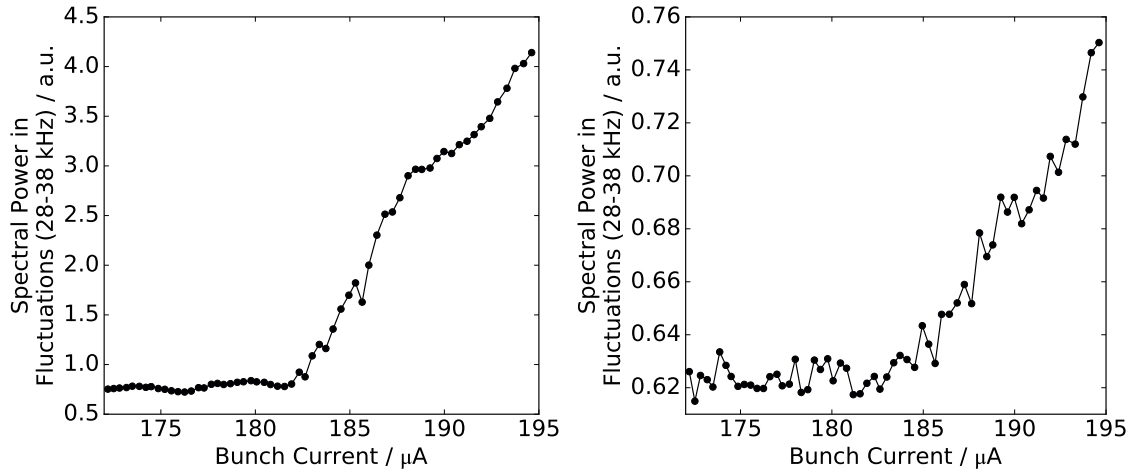

(a) (b)

Figure 8.4: Power in the fluctuations with frequencies from $28 - 38\,\mathrm{kHz}$ in the detected CSR power, as function of bunch current. Only the current range around the bursting threshold (onset of increase) is shown. (a) For the signal detected with detector A the threshold is estimated at $182\,\mu\mathrm{A}$. (b) For the signal detected with detector B the threshold is harder to determine due to the smaller signal to noise ratio. It is estimated to be around $182.5 \pm 1\,\mu\mathrm{A}$.

Figure 8.4, both detector signals show an increase in fluctuation strength at practically the same bunch current $\approx 182\,\mu\mathrm{A}$, even though the signal for detector B is much more noisy. Probably, this is caused by the combination of two things. The modulation on the bunch profile is not narrow band, thus leaving only very small to no regions in the spectrum unchanged. And the detectors while being narrow-band waveguide-coupled detectors, still cover a reasonable frequency range. Another effect leading to a difference in observed threshold currents for different detected frequency ranges, is the potentially different total responsivity of the different detectors, causing differences in the signal to noise ratio. For a low signal to noise ratio it can't be distinguished, if the fluctuations stopped or if the signal got to low and can't be detected any more. In all cases, the effect of a frequency range and/or detector dependence of the observed threshold current, would always overestimate the threshold current. Meaning the determined threshold current would be higher than the one, the bunches actually experience.

It is noteworthy that even with the fluctuations depending on the observed frequency range of the emitted CSR, the repetition rate of the bursts is the same. The frequency dependence only leads to different shapes of observed bursts. This is also visible in the newest measurements, presented in the following. As alternative to the individual waveguide-coupled Schottky detectors, an on-chip Schottky diode array, newly developed

by the group of Niels Neumann (TU Dresden) [86], was tested in a joint measurement campaign at KARA[1]. The array consists of eight Schottky detector elements with different antennas sensitive in different frequency ranges (50 ± 3 GHz, 100 ± 6.5 GHz, 200 ± 21 GHz, 300 ± 7.5 GHz, 400 ± 8.5 GHz, 500 ± 9.5 GHz, 600 ± 13 GHz, and 700 ± 14 GHz)[2] situated next to each other on one chip ($2.4\,\text{mm} \times 1.4\,\text{mm}$) [86]. Thus, the whole chip can be put in the focus of the synchrotron radiation and the beam does not need to be split (see Figure 8.5). For these recent measurements the usage of KAPTURE-2 made it possible to connect each of the eight detector elements to an individual channel.

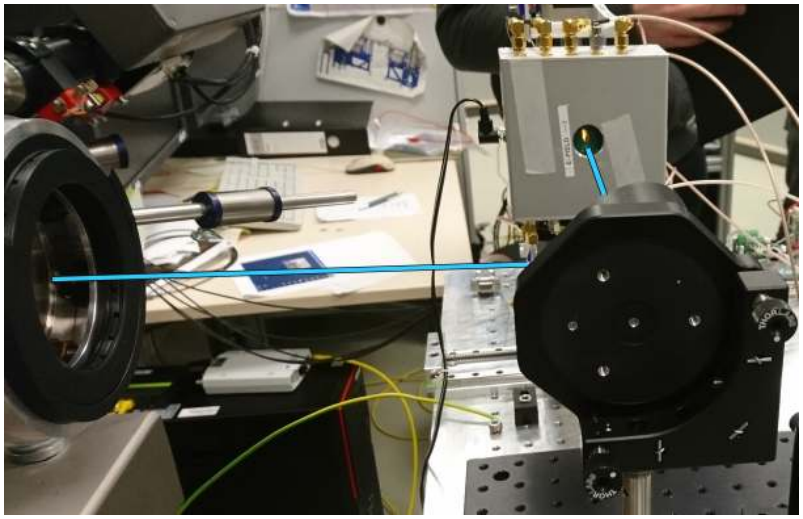

Figure 8.5: Photo of the on-chip spectrometer setup. Only a focussing mirror is needed in front of the detector chip containing eight Schottky diode detector elements with individual antennas sensitive in different frequency ranges. The light path is sketched in blue.

For each detector channel a spectrogram is calculated (see Appendix A.8). The extracted low bursting frequency which corresponds to the repetition rate of the bursts, is displayed in Figure 8.6. No differences are visible between the extracted frequencies of the different detectors. This shows again that the low bursting frequency is independent of the detected frequency range, at least for the spectral range in the emitted CSR power up to the maximal observed frequency of ≈ 700 GHz. By this, the measurements prove the assumption of what is causing this low frequency to be correct: The repetition rate should not change when observed in different CSR frequency ranges as it corresponds to the growing and shrinking of substructures on the charge distribution in the longitudinal phase space. If there would be a difference in the low bursting frequency detected with the different detectors, this

[1] together with Niels Neumann (TU Dresden), Carsten Mai (TU Dortmund), Matthias Martin, Johannes Steinmann, Patrick Schreiber (all KIT)

[2] The width of the frequency range is taken from the simulated bandwidth given in [86].

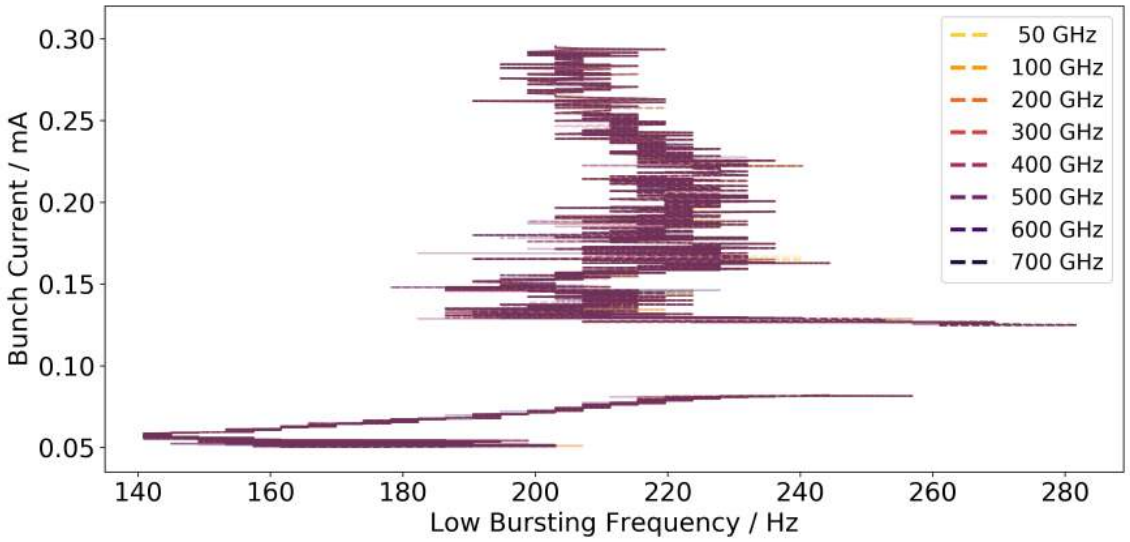

Figure 8.6: Low bursting frequency measured with on-chip Schottky diode array consisting of eight channels sensitive in different frequency ranges from 50 GHz up to 700 GHz. The frequency resolution is 5 Hz due to a measurement duration of only ≈ 250 ms per dataset.

would require the substructures to be (and therefore emit) quite narrow-band and these different narrow-band structures would need to grow and shrink with different repetition rates. Nevertheless, the measurement not showing these differences makes this very unlikely within the observed frequency range. What happens at the upper end of the emitted CSR spectrum, not studied with the presented measurements, needs to be investigated. It can only be assumed that, as these frequencies are only emitted coherently due to the presence of substructures, these frequencies are also subject to the growing and shrinking of these substructures and therefore should show the same low bursting frequency.

Observing different frequency ranges of the CSR emitted during the micro-bunching instability provides further insight into the dynamics during the instability. The measurements showed, for example, that the low bursting frequency (the repetition rate of the occurring bursts) is independent of the observed frequency range while the shape of the bursts can differ. Therefore, proving the current working model of the dynamics occurring in the charge distribution in the longitudinal phase space to be correct, concerning the growth and shrinkage of the substructures. Further studies using the on-chip diode array could help to prove or disprove the potential dependence of the observed "threshold" current on the detected frequency range.

8.2 Behavior of Beam Parameters in the Micro-Bunching Regime

Another type of systematic studies conducted are synchronous measurements [Keh18b; Bro19a]. From the experimental side, a direct measurement of the longitudinal phase space distribution is not feasible. It was shown in previous sections that the measurement of the THz power provides an insight into the dynamics of the charge distribution in the longitudinal phase space. Still, it can not reveal the whole dynamics. So additionally, the projection of the charge density on the time axis as well as the projection on the energy axis can be measured to gain a deeper insight. Several different synchronized measurement systems are used to measure these multiple properties of the beam. These studies do not (like the above) investigate the dependence of the behavior from a certain machine parameter, but instead observe time-resolved how the different properties of the electron beam change during the occurrence of the instability. In the following, the synchronous measurement of the fluctuations in the THz signal, the changes in the energy spread (via the measurement of the horizontal bunch size, see Subsection 4.4) and the longitudinal bunch profile over turns (Section 4.5) will be discussed. Parts of this section have also been published in [Bro19a].

The experimental setups present at KARA allow for a synchronization accuracy of down to some turns as demonstrated in [Keh18a; Ste18c]. This is achieved via the distributed timing system (Section 3.4). A common trigger can be sent to all acquisition systems around the ring, as well as the Bunch-by-Bunch feedback system (Section 4.1) and the Low-level RF system (Section 3.3). The trigger was typically sent every 10 seconds. For the KAPTURE and KALYPSO systems, used for measuring the THz signal, the longitudinal profile, and the horizontal size, the trigger arms the systems and the acquisition of one dataset (typically the recording of one second) is started on the next flank of the additionally provided revolution clock ($\approx 2.7\,\mathrm{MHz}$). This should result in an intrinsic on-turn synchronization between these devices. To synchronize, the Fast Gated Camera (Subsection 4.4) takes more adjusting as described in [Keh16; 50]. Also, the BBB and LLRF system can take triggered measurements or perform operations triggered by the 10 seconds trigger. The synchronization of the detector systems can be checked by triggered jumps in the RF phase. These are visible as the onset of strong synchrotron oscillations. This is directly visible in the longitudinal profile as a change in arrival time oscillation and in the horizontal bunch position due to the coupling via the dispersion. As the change in synchrotron oscillation amplitude is not reliably visible on the THz signal due to the bursts caused by the micro-bunching instability, an ultra-fast optical diode is connected to one of the

channels of KAPTURE. A measurement during such an RF phase jump is displayed in Figure 8.7.

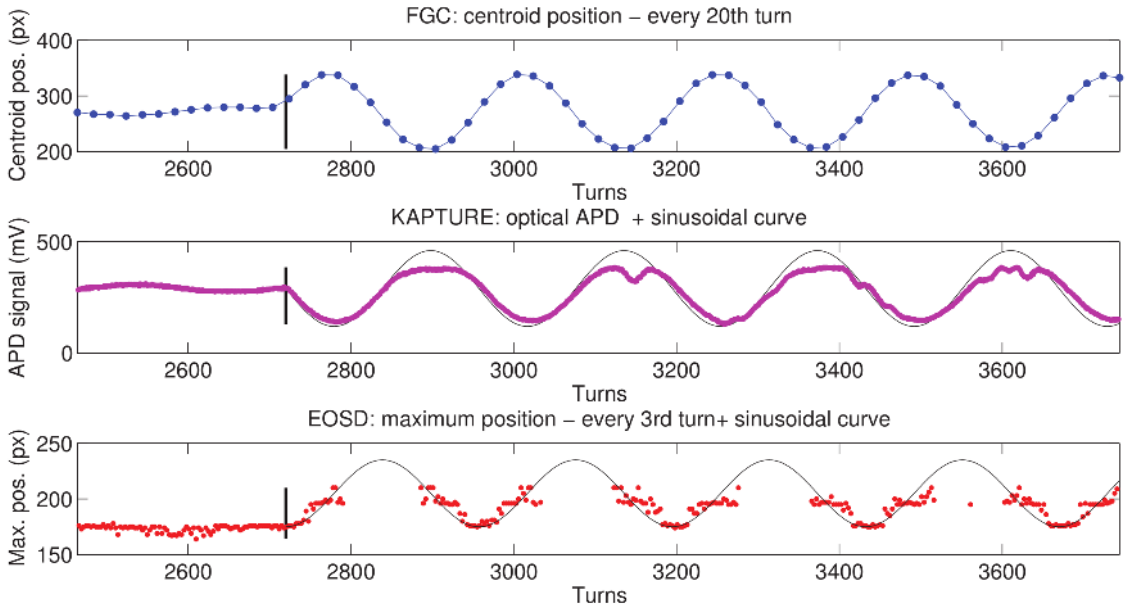

Figure 8.7: The triggered RF phase jump is visible on the different properties of the beam. From top to bottom: The horizontal position was recorded by the FGC. The signal of the optical diode recorded with KAPTURE. The longitudinal position was measured with the electro-optical setup and KALYPSO. In black, a sinus with the synchrotron frequency f_s is overlaid to illustrate the synchrotron oscillation. The thick, vertical black line in all plots shows the occurrence of the RF phase step. The sudden increase in the oscillation amplitude is clearly visible in all three signals. [Keh16]

The synchronization test shows that the synchronous acquisition of the three setups is better than at least the resolution of the FGC of 20 turns. Due to the uncertainties on the signal the expected on-turn synchronization between KAPTURE and KALYPSO can not be proven, but it should be in the order of several turns. If KALYPSO is also used for the horizontal measurements, all three setups achieve a synchronization with this accuracy. Even without a deliberate excitation the synchrotron oscillation amplitude changes sometimes significantly, which can be seen in Figure 8.8 in the measured bunch length and longitudinal position as well as in the horizontal size and position. This serves as intrinsic check of the synchronization.

The horizontal as well as the longitudinal setup delivers “pictures” of the bunch in the corresponding projection. For the following analysis, derived parameter are used. The calculation of these derived parameters like size (length) and center of mass (phase) from the measured horizontal and longitudinal profiles is done in post processing. Due to the

deformation of the bunch caused by the instability, the bunch shape is not Gaussian any more and even varies with time. So, instead of extracting the information by a fit, the statistical moments (center of mass and standard deviation) are calculated. For example, the horizontal position is determined from the first statistical moment (center of mass) of the individual profile. As the measurement of the longitudinal profile has a slightly tilted base line[3], the position of the maximum of the charge distribution is calculated instead of the center of mass, which results in a smaller but still not negligible error. For the bunch length and the horizontal size, the standard deviation is calculated. The way the derived parameters are calculated has to be taken into account when interpreting the results presented in the following as it can have an influence on the observed behavior.

Such a synchronous measurement is shown in Figure 8.8[4]. It shows over a time range of several ten-thousand turns the development of the measured longitudinal bunch profile, the longitudinal bunch position and length calculated from the profile, as well as the measured horizontal bunch profile, the thereof calculated horizontal bunch position and size which are connected to the energy and the energy spread of the bunch via the dispersion. In the bottom panel, the THz power measured with a detector sensitive from 220 GHz to 325 GHz is displayed. The characteristic bursts in the emitted CSR power are visible with a period of approximately 5000 turns. Similarly, the horizontal bunch size shows a sawtooth shaped pattern with the increase and decrease correlated to the bursts in the CSR power. Also, in the bunch length a change is visible with the repetition rate of the bursts, although not as clear as it is in the horizontal bunch profile. Between turn number 7500 and 22500 (Figure 8.8) two shorter bursts occur in the CSR emission. These are also visible in the bunch length and horizontal bunch size, supporting the seen correlation between the changes in bunch size and the emitted CSR power.

This can be observed in more detail in Figure 8.9, where a short time range around the onset of a CSR burst is shown. Around turn 24700 ($\approx$ 9.1 ms), substructures on the longitudinal bunch profile start to form. Due to the changes in the longitudinal bunch profile the bunch spectrum changes. In this case, the occurrence of substructures leads to higher frequency components in the bunch spectrum. The therefore increased overlap with the CSR impedance (Section 2.6) results in an increase of emitted CSR power. As expected from this, the measured THz power starts to increase significantly around the same time as the substructures occur. This drives the self-amplification of the substructures via the wake potential until, after approximately 2.5 to 3 synchrotron periods (at approx. turn 25300 $\approx$ 9.3 ms), the substructures start to be less pronounced and begin to wash out due

[3] More information and a detailed error analysis can be found in [31].
[4] Measurement data were taken together with P. Schönfeldt, B. Kehrer, and J. Steinmann.

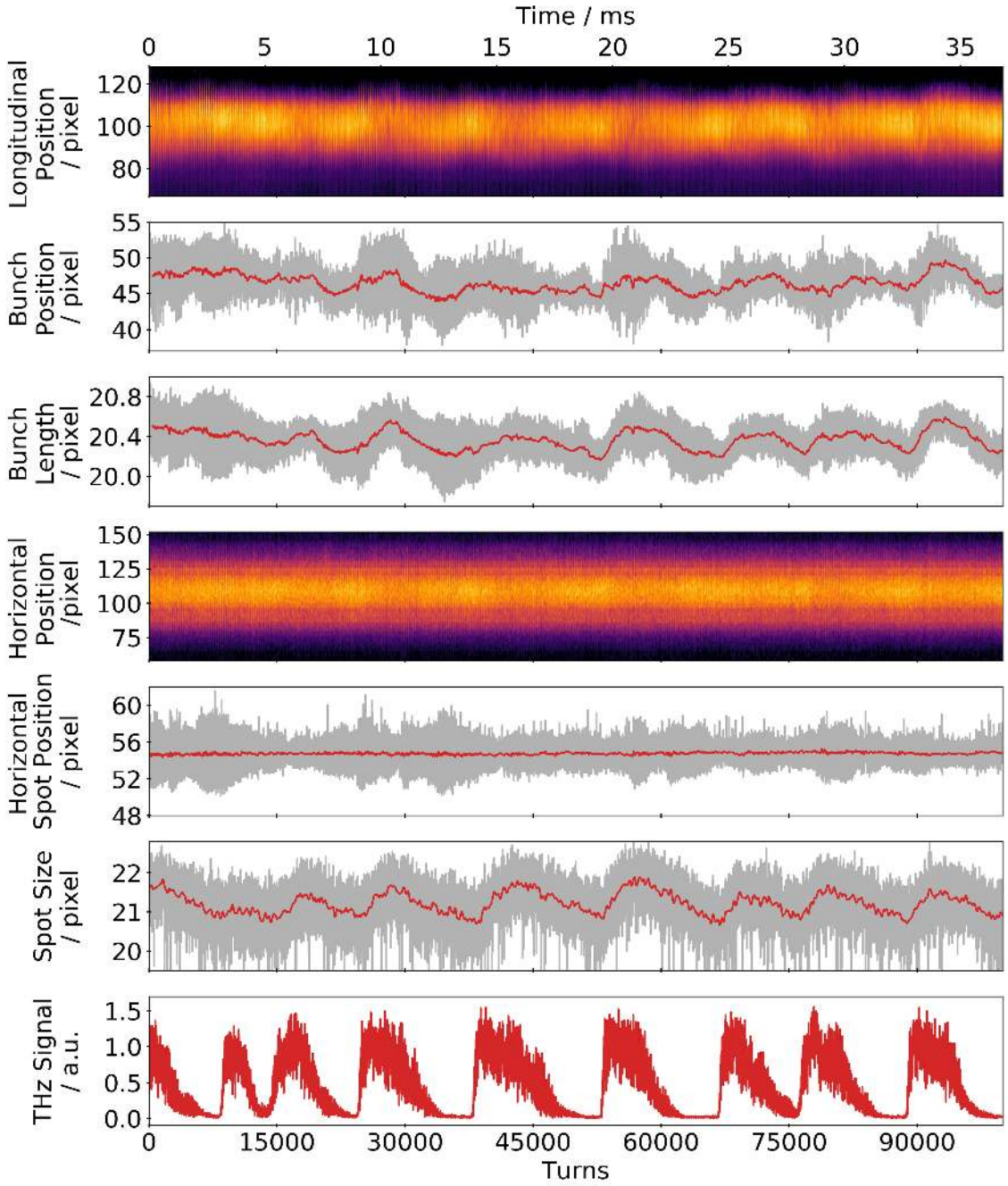

Figure 8.8: Synchronized measurement showing from top to bottom: the longitudinal profile, the longitudinal position, the longitudinal bunch length, the horizontal profile, the horizontal position, the horizontal bunch size, and the THz power. For panel 2, 3, 5, and 6 in the actual signal including the synchrotron oscillation (and noise) is shown in grey and overlaid a slowly changing moving average (with a window of 450 turns) in red.

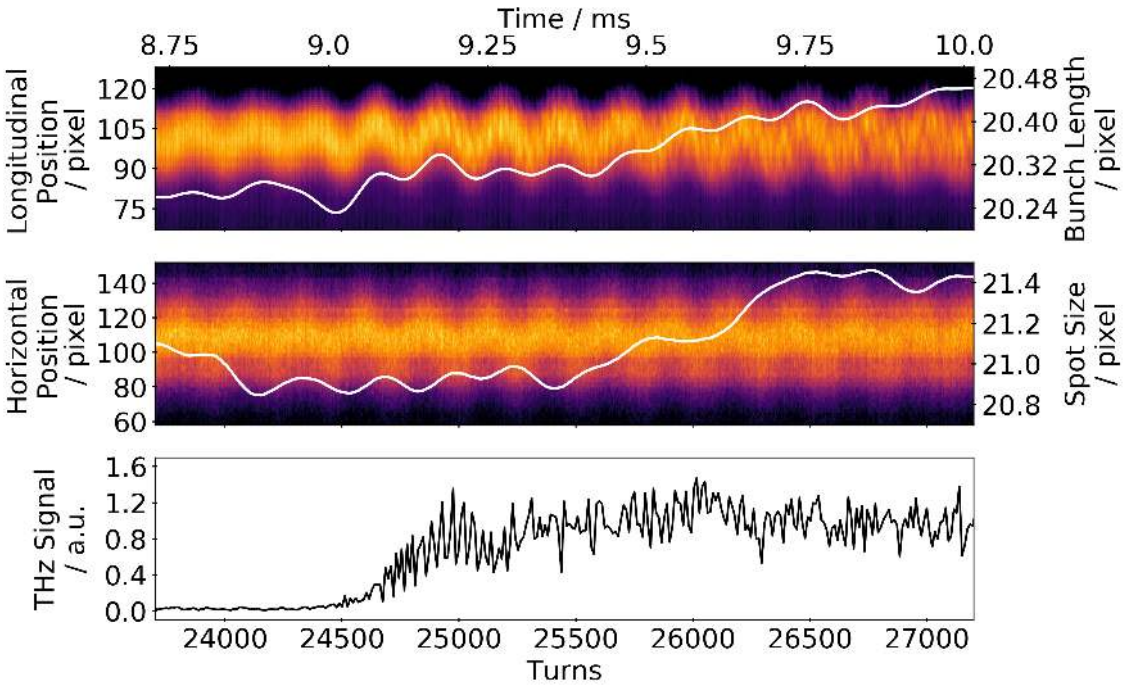

Figure 8.9: Zoom-in on the onset of one measured CSR burst in Figure 8.8. The longitudinal and the horizontal bunch size are shown as white lines on corresponding profiles. The lines were smoothed with a moving average (450 turns) to show the overall trend without the fluctuation due to the synchrotron oscillation and the noise present in the measurements (same as in Figure 8.8).

to diffusion and filamentation. In Figure 8.9, it is visible that over several thousand turns this results in an increased bunch size and therefore a lower wake potential. At this point, the radiation damping outweighs the driving wake potential, the substructures dissolve and the overall bunch length is damped down to the point, where the wake potential increases and leads again to the formation of substructures, starting the cycle over again.

While, at the beginning of the burst cycle, the bunch length (calculated as standard deviation of the bunch profile) starts to increase around the time the substructures occur, the horizontal bunch size (corresponding to the energy spread) seems to stay constant at a low value until the substructures start to wash out (which is approx. 2.5 to 3 synchrotron periods later) before increasing as well. The time difference between the increase in bunch length and the increase in horizontal bunch size could possibly be explained by the calculation of the bunch length and size via the standard deviation of the profile. The standard deviation is sensitive to the occurrence of the substructures and therefore a first increase of the calculated bunch length is observed during the rising of the substructures. On the measured horizontal bunch profile no substructures are visible [50]. This could be caused by the diffraction limit of the optical beam path and the fact that the horizontal

size also contains a contribution from the emittance. Therefore, the calculated horizontal size remains constant until the substructures filament out and increase the overall size of the charge distribution in the phase space and consequently the energy spread and the measured horizontal bunch size accordingly. The washed out and blown up distribution in phase space is then damped down, leading to the decrease in bunch length as well as energy spread visible in Figure 8.8.

In Figure 8.10, simulation results by Inovesa are displayed similarly to the measurements in Figure 8.8. As in the measurements a sawtooth pattern of increasing and decreasing can be observed in the energy spread σ_δ as well as in the bunch length σ_z with the same period than the bursts in emitted CSR power. The correlation is clearly visible as the increase in σ_δ and σ_z always occurs around the time the CSR power increases even when this is happening slightly irregular.

A zoom onto one burst (Figure 8.11) shows that in contrast to the measurements some structures are always visible on the longitudinal as well as the energy profile. As soon as the substructures become prominent, the emitted CSR power increases. The bunch length as well as the energy spread start to grow both at the same time. The simultaneous increase in bunch length and energy spread supports the hypothesis that the delayed increase of the measured horizontal size could be attributed to the observation, that the substructures are not visible on the measured horizontal profile. The slow increase in the CSR power in the simulation makes it hard to tell if the bunch length starts to increase at the same time as the CSR power, as it seems to be the case in the measurements. As shown in the previous chapter, the shape of the burst depends on the frequency range the THz detector is sensitive to (Section 8.1). If only summing up the power emitted in the frequencies the detector used in the measurement is sensitive to[5], the onset of CSR power and of the bunch length are closer and it looks closer to what was observed in the measurement. Similar to the measurement, the simulation shows that the substructures are washed out after some synchrotron periods, which is then followed by a damping of the overall size.

During the burst the bunch loses more energy due to the increased emission of CSR. The simulation shows this as a small shift in the longitudinal position (phase) of the bunch. The bunch moves to a slightly different phase of the acceleration voltage to compensate for the increase in radiation loss. Figure 8.12 (1st panel) shows that this shift in phase is in the order of the amplitude of the synchrotron oscillation ($\approx 3\,\mathrm{ps}$). Calculated from the

[5] Only the upper and lower limit of the detector sensitivity, in this case $220\,\mathrm{GHz} - 325\,\mathrm{GHz}$, were taken into account and not the exact detector response.

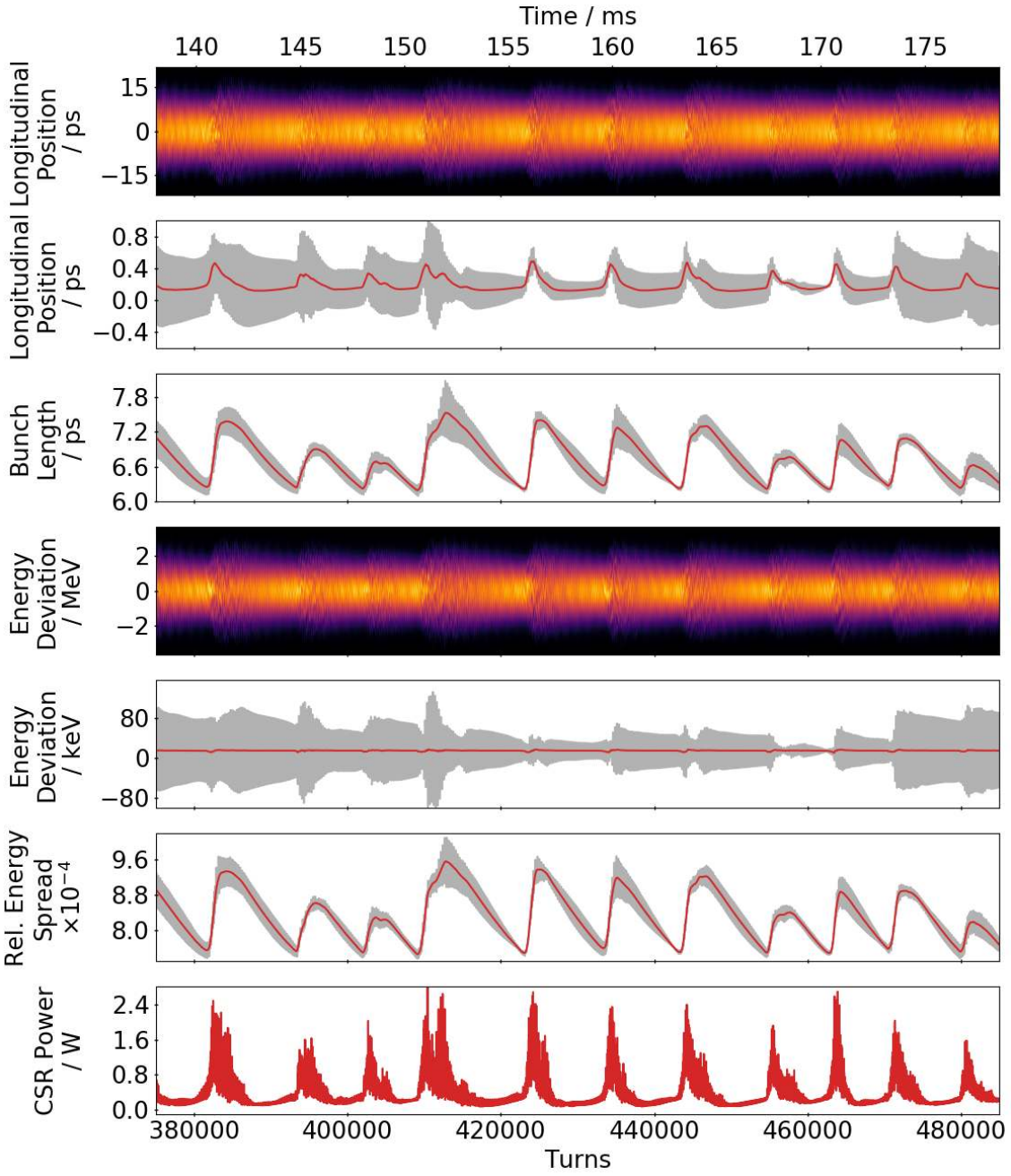

Figure 8.10: Simulation results displayed similarly to Figure 8.8 showing the longitudinal bunch profile, the longitudinal position (phase), the bunch length as well as the energy profile, the energy offset, the energy spread, and the emitted CSR power. For panel 2, 3, 5, and 6 a moving average (520 turns) is displayed in red to show the overall trend without the fluctuations caused by the synchrotron oscillation.

simulation, the additional radiation loss (for one revolution) at the peak of a burst is

$$\Delta U_{CSR} = \frac{P_{\text{peak}} T_{\text{rev}}}{N_{\text{electrons}}} = \frac{P_{\text{peak}} \cdot e}{I_{\text{b}}} = 2.48\,\text{keV}$$

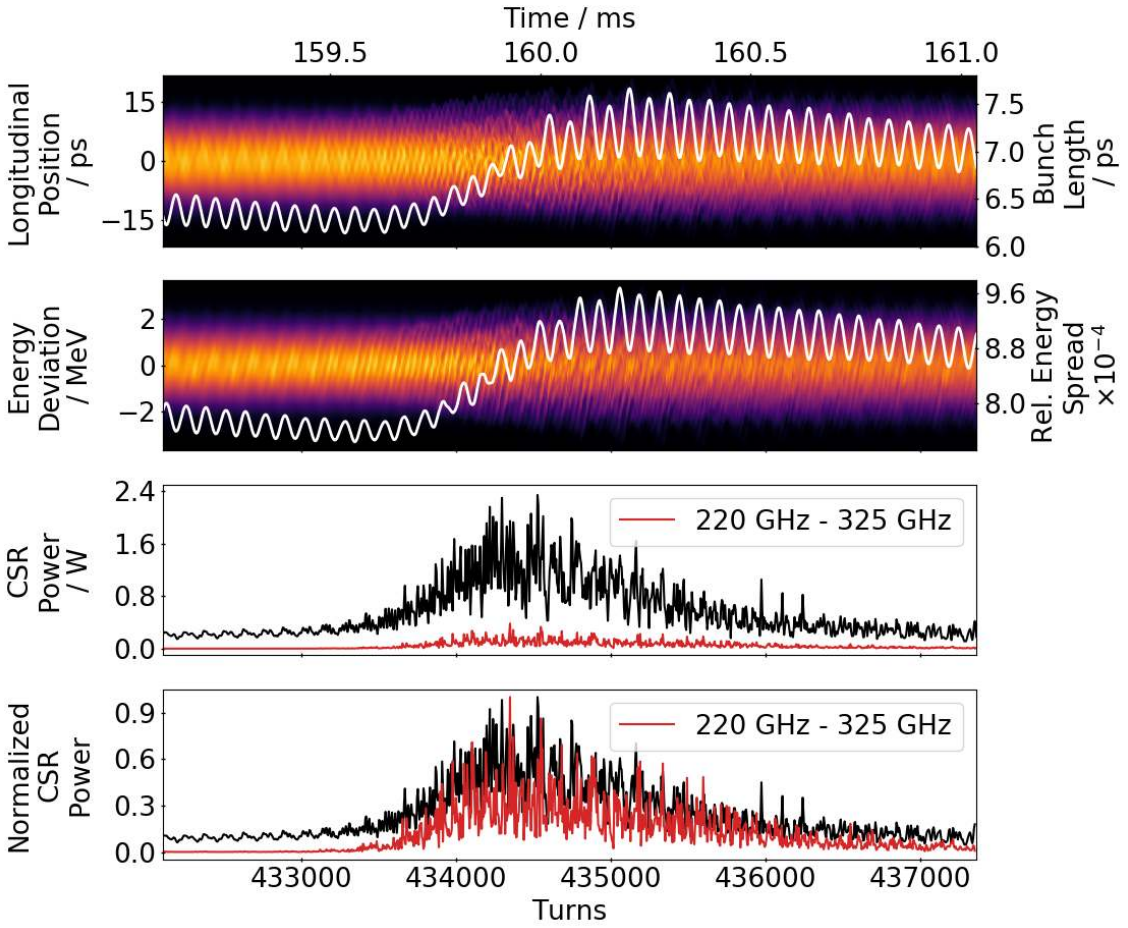

Figure 8.11: Zoom into one simulated burst of Figure 8.10. Showing the bunch length and the energy spread as white line over the corresponding profile. In the 3rd panel, additional to the emitted CSR power in black, the CSR power emitted in the frequency range the detector used in the measurements is sensitive in (220 GHz - 325 GHz) is displayed in red. The 4th panel shows the same data normalized to make the small difference in onset better visible.

assuming an emitted peak CSR power of $P_{\text{peak}} = 2.2\,\text{W}$ for the simulated bunch current of $I_{\text{b}} = 0.886\,\text{mA}$. e is the elementary charge. For comparison the radiation loss due to incoherent synchrotron radiation results in $\Delta U_{\text{ISR}} = 46\,\text{keV}$ using Equation 2.7. With an acceleration voltage of $V_{\text{RF}} = 1.3\,\text{MV}$ and Equation 2.11 the phase shift is expected to be approximately

$$\Delta\Psi = \Psi_{\text{burst}} - \Psi_{\text{s}} = \sin^{-1}\left(\frac{46\,\text{keV} + 2.48\,\text{keV}}{1.3\,\text{MV}\cdot e}\right) - \sin^{-1}\left(\frac{46\,\text{keV}}{1.3\,\text{MV}\cdot e}\right) = 0.11\,^\circ$$

This corresponds to a temporal shift of $\frac{2\,\text{ns}}{360\,^\circ}\cdot\Delta\Psi \approx 0.61\,\text{ps}$, which is slightly bigger than the one observed in the simulation.

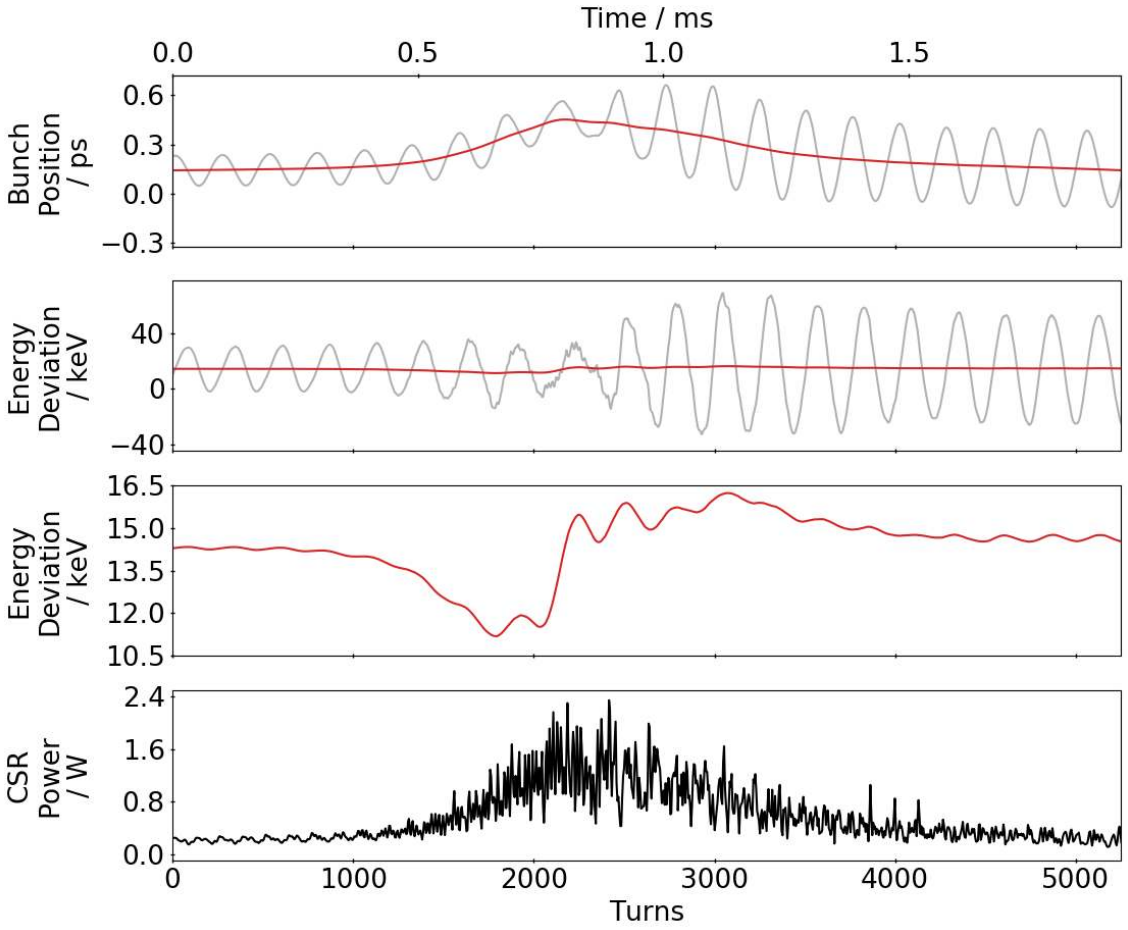

Figure 8.12: Zoom into one simulated burst of Figure 8.10. For the phase (longitudinal position) of the bunch in the 1st panel and the energy offset in the 2nd panel a moving average (520 turns) is displayed in red while the actual values including the synchrotron oscillation are displayed in grey. The 3rd panel shows a zoom of the smoothed energy deviation.

The energy loss visible on the energy deviation is significantly smaller than the synchrotron oscillation amplitude. It is in the order of 2.5 keV (see 3rd panel Figure 8.12), which fits well to the estimated additional radiation loss. Within a few synchrotron oscillations, the energy mismatch is compensated as the bunch has moved to the different phase Ψ_{burst} to gain the necessary additional energy in the RF cavities. Thus, the energy deviation already returns to the original value during the burst and shows a light overshoot when the emitted CSR power decreases again, as it takes a moment for the bunch to compensate by a phase shift back.

The phase shift triggers an increase in the amplitude of the synchrotron oscillation around the new phase. This can be seen in the grey curve in the 1st and 2nd panel of Figure 8.12 and, for example, in the 5th panel of Figure 8.10. In the simulations, the excitation of

synchrotron oscillations by RF noise was not considered [87], thus the change in synchrotron oscillation amplitude caused by the phase shift is visible and not overlaid by other effects as it is the case for the measurements. The measurement in Figure 8.13 shows the phase and the energy deviation as well as the emitted CSR power for one burst, similar to the simulation displayed in Figure 8.11. The measured amplitude of the synchrotron oscillation changes but no clear correlation is visible between changes of the synchrotron oscillation amplitude (visible in the 1st and 3rd panel of Figure 8.13 or e.g. on the horizontal bunch position (grey curve in 5th panel of Figure 8.8)) and the state of the CSR bursts. This is not unexpected as the synchrotron oscillation is strongly driven by RF phase noise [88].

The expected phase shift is also visible in the measured longitudinal position. No absolute values can be given as no calibration for time to pixel of the EO measurement setup for these particular measurements was performed. In contrast to the simulation, the phase shift is smaller than the amplitude of the synchrotron oscillations. This could indicate a smaller phase shift or stronger synchrotron oscillations. The latter is plausible due to the aforementioned additional excitation of the synchrotron oscillation by RF noise and other noise sources. The shift of the horizontal bunch position due to the change in energy deviation expected during the burst is not visible on the horizontal bunch position. Even when smoothed further no clear change correlated to the burst is observed (see 4th panel of Figure 8.13). It might not be possible to resolve the small energy deviation via the dispersion on the horizontal bunch profile similarly to the non-resolved substructures.

Overall, the measurements and the simulations draw a clear and consistent picture of the expected behavior of the bunch under the influence of the micro-bunching instability. As expected, the effects are visible on the longitudinal as well as the horizontal plane, which is used as access to the energy plane. The synchronization of the different measurement setups allows to study the connection between the different parameters. All observed features are also present in the simulation results. The small deviations between the behavior in the measurement and the simulation, can probably be attributed to some limitations in the measurement setup or a limitation in the simulation. For example, the difference between measurement and simulation in the onset of the CSR power during a burst compared to the onset of the bunch length increase, could probably be resolved if the exact detector sensitivity would be considered in the simulation. And the difference in the onset of the increase of the horizontal bunch size ($\simeq$ energy spread) might be caused by the fact that the parameters of the energy plane can only be indirectly obtained with the presented measurement setups.

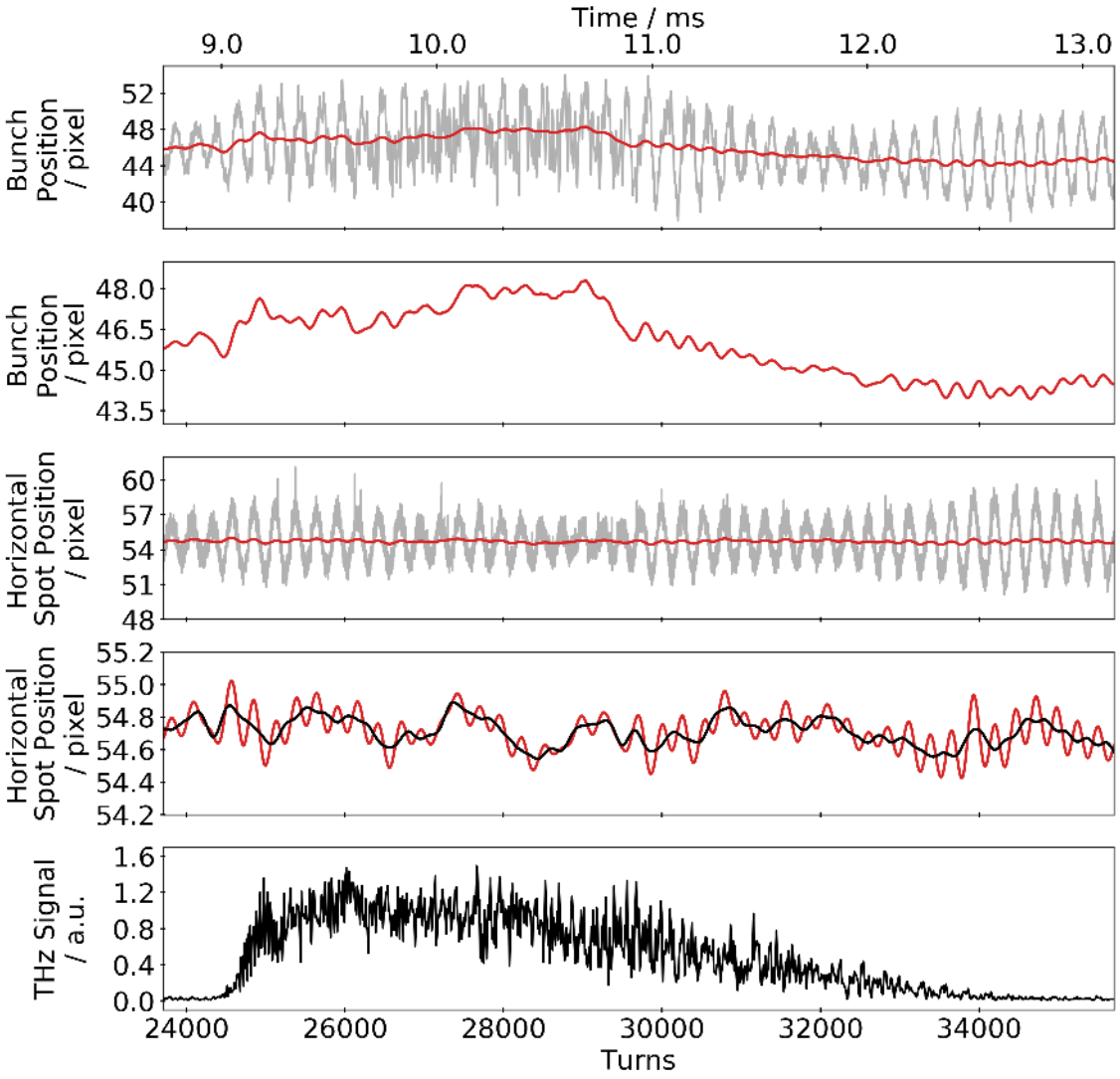

Figure 8.13: Zoom-in on one CSR burst in the measurement shown in Figure 8.8. The longitudinal and the horizontal bunch position corresponds to the phase of the bunch and its energy deviation. The red lines are the smoothed positions (moving average with 450 turns) to show the overall trend without the strong fluctuation due to the synchrotron oscillation and the noise present in the measurements (same as in Figure 8.8). The 2nd and the 4th panel show a zoom-in on the smoothed longitudinal and horizontal bunch position respectively. In the 4th panel, additionally, a black curve depicting the moving average with a window of 550 turns of the horizontal bunch position is displayed, to further suppress all fluctuations due to the synchrotron oscillation.

9 Weak Instability (Short-Bunch-Length Bursting)

For most machine settings, the beam is stable for all currents below the bursting threshold (see Figure 9.1a). Nevertheless, observations show that at KARA, for a momentum compaction factor $\alpha_c \leq 2.64{\cdot}10^{-4}$ combined with high acceleration voltages ($V_{RF} > 1100\,\mathrm{kV}$) leading to a natural bunch length $\sigma_{z,0} \leq 0.723\,\mathrm{mm} \mathrel{\hat{=}} 2.43\,\mathrm{ps}$, an additional region of instability occurs for bunch currents below the main bursting threshold, as shown in Figure 9.1b. In the following, this instability is referred to as short-bunch-length bursting (SBB). The main part of this section has also been published in [Bro19b].

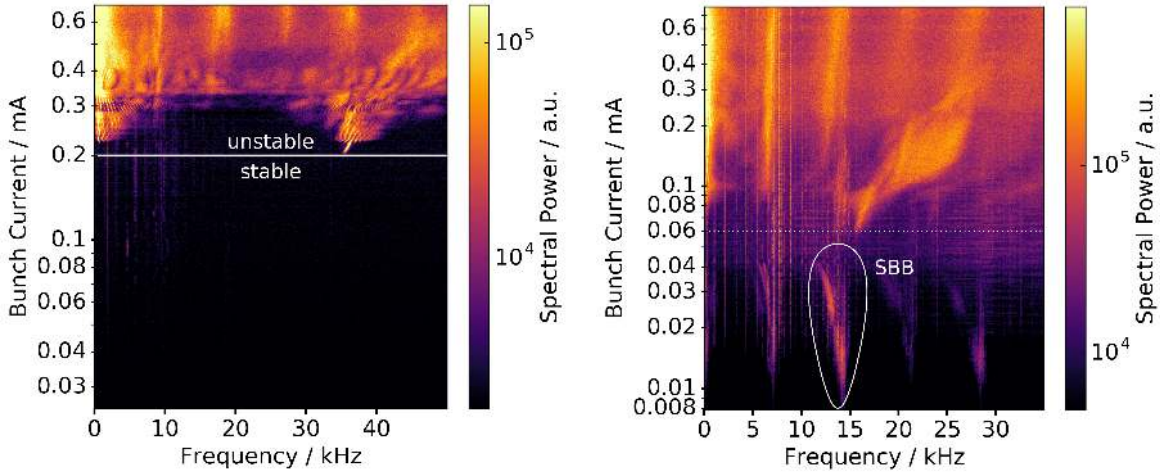

Figure 9.1: Spectrogram of the fluctuations of the THz power as a function of bunch current. (a) No short-bunch-length bursting occurs, as the bunch was not compressed strongly enough. The measurement was taken for settings resulting in a shielding of $\Pi \approx 1.41$ ($f_s = 9.4\,\mathrm{kHz}$, $V_{RF} = 1048\,\mathrm{kV}$). (b) shows the additional region of instability (indicated by white circle) below the standard bursting threshold (white dotted line). Taken at $\Pi \approx 0.81$ ($f_s = 7.2\,\mathrm{kHz}$, $V_{RF} = 1397\,\mathrm{kV}$).

First observations at KARA were reported in [89; Bro16b]. This additional region of instability was previously observed as well at the Metrology Light Source (MLS) [90] and

indications can be seen in measurements at the Diamond Light Source (see [3], Fig. 6), though there it was not discussed further.

Additionally, it was predicted by simulations in [13]. The simple scaling law for the main threshold of the instability (Equation 2.25), as described in Section 2.9, was obtained from a linear fit to simulated thresholds. This fit ignores a dip around $\Pi \approx 0.7$, where the calculated thresholds deviate from the simple linear scaling law [13]. A closer look at the calculated energy spread at this dip revealed a second unstable region in the bunch current, with a threshold below the one expected from the linear scaling law. For the values of Π accessible at KARA, it is separated by a stable region from the main instability (see Figure 9.1b). This new region corresponds to the short-bunch-length bursting discussed in the following. The upper and lower limits of this additional region of instability are predicted to not only depend on the bunch length and thus the shielding parameter, but also on the relation between the synchrotron frequency f_s and the longitudinal damping time τ_d [13; 36]. This relation is described by $\beta = 1/(2\pi\, f_\mathrm{s}\, \tau_\mathrm{d})$. The instability is termed a weak instability due to its dependency on the damping time [13].

In the following, measurements of the SBB instability at KARA are discussed and compared to existing theoretical predictions as well as detailed numerical simulations.

9.1 Bursting Behavior

The spectrogram in Figure 9.2 was obtained by a snapshot measurement (see Subsection 6.1.2) within one second. To compensate for the limited current resolution of this measurement method the filling pattern was chosen in such a way that the region of interest at small bunch currents is sampled with a sufficient resolution . The spectrogram shows the lower bound of the main instability region and the complete occurrence of the short-bunch-length bursting. This second region of instability occurred at bunch currents between 0.038 mA and 0.016 mA for the measured machine settings.

The frequencies of the power fluctuations (in Figure 9.2) are, for currents above the main bursting threshold, slightly above twice the synchrotron frequency ($2 \times f_\mathrm{s} = 2 \times 6.55\,\mathrm{kHz}$). For the SBB, they are slightly below twice the synchrotron frequency and approach this frequency for decreasing bunch current. A second frequency line at the first harmonic of the power fluctuation is visible (below $4 \times f_\mathrm{s}$). More spectrograms of snapshot measurements at different machine settings can be found in Appendix A.9.

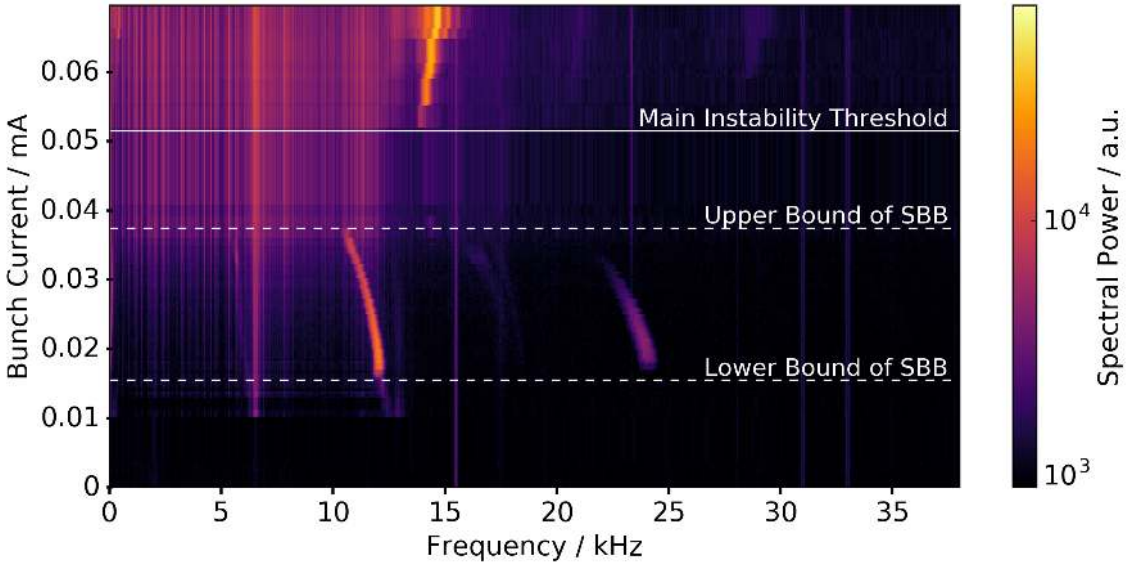

Figure 9.2: Snapshot spectrogram of the fluctuations of the THz power as a function of bunch current for a shielding parameter of $\Pi \approx 0.74$ ($f_s = 6.55\,\mathrm{kHz}$, $V_{RF} = 1400\,\mathrm{kV}$). Below the end of the micro-bunching instability (main bursting threshold) around 0.052 mA, a second unstable region is clearly visible between 0.038 mA and 0.016 mA. The current bins were chosen such that a high bunch-current resolution in the region of the short-bunch-length bursting was achieved.

9.2 Threshold and Bounds

Snapshot measurements of the lower current range, similar to Figure 9.2, were taken for different values of the momentum compaction factor and the natural bunch length by changing the magnet optics as well as the acceleration voltage. The scanned parameter range reached for α from $9.94 \cdot 10^{-3}$ down to $1.51 \cdot 10^{-3}$ and for V_{RF} from 524 kV up to 1500 kV. The bunch currents at the lower and upper bounds of the short-bunch-length bursting as well as the main bursting threshold for each measurement are displayed in Figure 9.3 using the dimensionless parameters S_{CSR} and Π (Equation 2.26 and Equation 2.27). The combination with bursting thresholds measured at machine settings, where no short-bunch-length bursting occurs, shows that the main bursting threshold is described by Equation 2.24 (see Subsection 7.2.1) and is independent of the occurrence of short-bunch-length bursting. The highest value of the shielding parameter Π where the short-bunch-length bursting occurs at KARA (rightmost red square in Figure 9.3) is $\Pi_{SBB}^{max} = 0.845 \pm 0.013$. The smallest value of the shielding parameter where the short-bunch-length bursting does not occur (leftmost green diamond in Figure 9.3) is at $\Pi_{\text{no SBB}}^{min} = 0.835 \pm 0.017$, slightly smaller than Π_{SBB}^{max}, but still within the measurement errors. Nevertheless, it would not

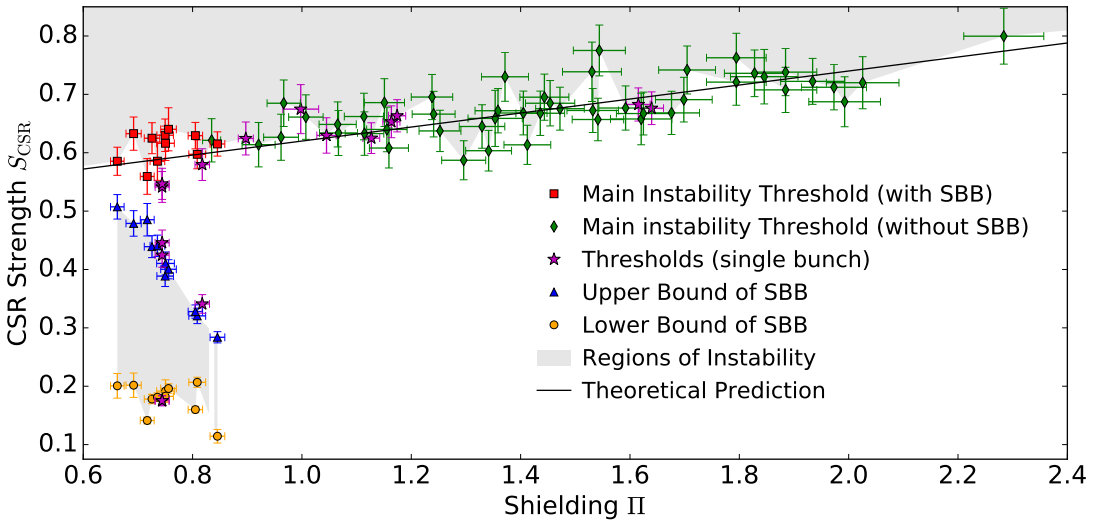

Figure 9.3: CSR strength vs. shielding of thresholds from snapshot measurements at different settings of the machine parameters compared to the linear scaling law given by Eq. 2.24 (line). The lower bound (orange discs) as well as the upper bound (blue triangles) of the short-bunch-length bursting (SBB) are shown. The main bursting threshold is shown in red (squares) for machine settings where short-bunch-length bursting occurred and in green (diamonds) for settings where it did not occur. The purple stars represent thresholds and bounds which were obtained from a full decay of a single bunch and not from snapshot measurements. The error bars display the one standard deviation uncertainties calculated from the measurement errors.

be a contradiction to the expectation, if $\Pi^{\mathrm{min}}_{\mathrm{no\,SBB}}$ would be smaller than $\Pi^{\mathrm{max}}_{\mathrm{SBB}}$, as the two measurements (at $\Pi^{\mathrm{min}}_{\mathrm{no\,SBB}}$ and $\Pi^{\mathrm{max}}_{\mathrm{SBB}}$) were obtained for different combinations of the momentum compaction factor and the acceleration voltage resulting in similar values of Π, however, significant different values for β. As described in [78], the range of Π where the weak instability occurs is bigger the smaller β is. Thus, this would be supported by the measurements showing a dependence of the presence of the second region of instability on β.

For the measurements conducted at KARA the damping time is fix (at 10.6 ms) due to the constant energy, so β only changes due to the changes in the synchrotron frequency. The synchrotron frequency is changed by the acceleration voltage and the momentum compaction factor. As discussed in Section 7.2, reducing Π via the acceleration voltage leads to an increase in f_{s} and while reducing Π via the momentum compaction factor changes f_{s} in the opposite direction (decreases it). Therefore, Π and β are not uncorrelated for the conducted measurements. This is visible in Figure 9.4, where β is displayed for each measurement and the corresponding Π. The points mostly group in four curves, caused by

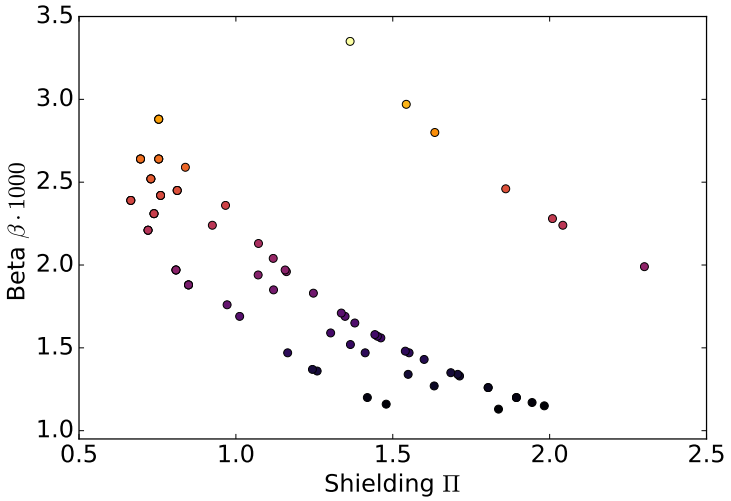

Figure 9.4: Value of β as a function of Π for the measurements shown in Figure 9.3. β and Π can not be changed independently as both depend on the synchrotron frequency f_s. The points are colored according to their value of $\beta \cdot 1000$ (y-axis).

the four acceleration voltages used in the measurements. The points along each curve were taken at the same V_{RF} and different α_c. This means that for measurements at KARA the values of Π and β can not be set completely independent.

Coloring the thresholds and bounds shown in Figure 9.3 according to the value of β of each measurement results in Figure 9.5. Looking at the main bursting threshold, mostly darker points (lower values of β) and some brighter points (higher value of β) are present at higher values of Π and all points scatter around the expected threshold independently of color. This shows that the value of β has no influence on the value of the threshold for the main bursting region, confirming the expectation that the main threshold is not dependent on β. As discussed before, the β-dependence of the region in Π, where the short-bunch-length bursting occurs, is visible in the measurements at $\Pi^{\mathrm{min}}_{\mathrm{no\,SBB}}$ and $\Pi^{\mathrm{max}}_{\mathrm{SBB}}$. The orange point (indicated by an arrow in Figure 9.5) at $\Pi^{\mathrm{min}}_{\mathrm{no\,SBB}} = 0.835 \pm 0.017$ has a β value of $\beta = 2.59 \cdot 10^{-3}$ and shows no sign of the short-bunch-length bursting. While the dark point directly to the right, at $\Pi^{\mathrm{max}}_{\mathrm{SBB}} = 0.845 \pm 0.013$, has a smaller β value ($\beta = 1.88 \cdot 10^{-3}$) and shows the SBB resulting in a second region of instability. This supports the simulation results in [78], showing that for lower values of beta the short-bunch-length bursting occurs up to higher values of Π than for higher values of β. These simulations also predicts that the upper and lower bound (values of S_{CSR}) where this second region of instability occurs depends not only on Π but on β as well. This can be seen in the measurements shortly above $\Pi = 0.8$, where two measurements (see ellipse around upper and lower bound of both measurements in Figure 9.5) are nearly at the same values of Π but again with different

values of β. For the measurement with a higher value of β ($\beta = 2.45 \cdot 10^{-3}$, orange points) the range where the short-bunch-length bursting occurs is smaller, ending already at higher values of $S_{\mathrm{CSR}} = 0.206$. The second measurement with $\beta = 1.97 \cdot 10^{-3}$ shows the SBB down to a significantly lower value of $S_{\mathrm{CSR}} = 0.160$. For lower values of Π this phenomena is not visible anymore, probably because for these measurements the values of β are to similar, leading to differences too small to be observed in the conducted measurements.

To study these effects in more detail, it would be helpful if β could be changed independently from Π. In future measurements, this might be accomplished by changing the damping time with the help of the CLIC damping ring wiggler, similar to the studies discussed in Section 7.3.

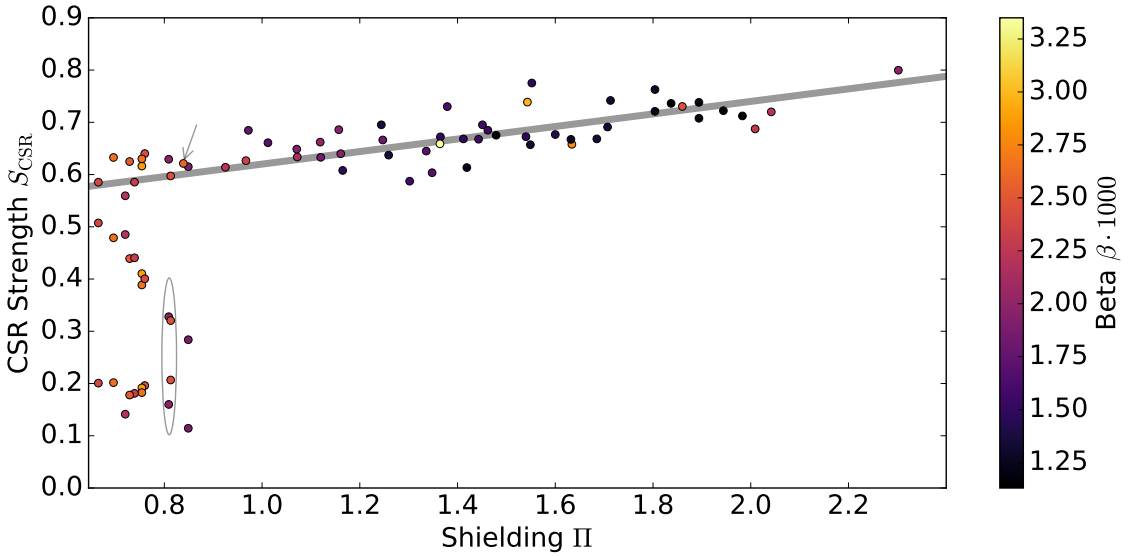

Figure 9.5: CSR strength at the bursting thresholds as a function of the shielding parameter for measurements at different machine settings. The points are colored according to the corresponding value of beta. The arrow indicates the measurement at the lowest value of Π where no SBB occurs ($\Pi^{\mathrm{min}}_{\mathrm{no\,SBB}}$), which is lower than the highest value of Π for which SBB occurs ($\Pi^{\mathrm{max}}_{\mathrm{SBB}}$). The ellipse marks two measurement sets with have nearly the same value in Π but different values of β and show a different lower bound.

9.3 Comparison with Simulations

The observed overall limit of the occurrence of the short-bunch-length bursting agrees within the uncertainties with the results obtained by Bane, Cai, and Stupakov using their VFP solver [13]. There, the authors observed a dip around $\Pi = 0.7$, while the threshold for $\Pi = 1$ is again on the theoretical calculated linear scaling law given by Equation 2.24.

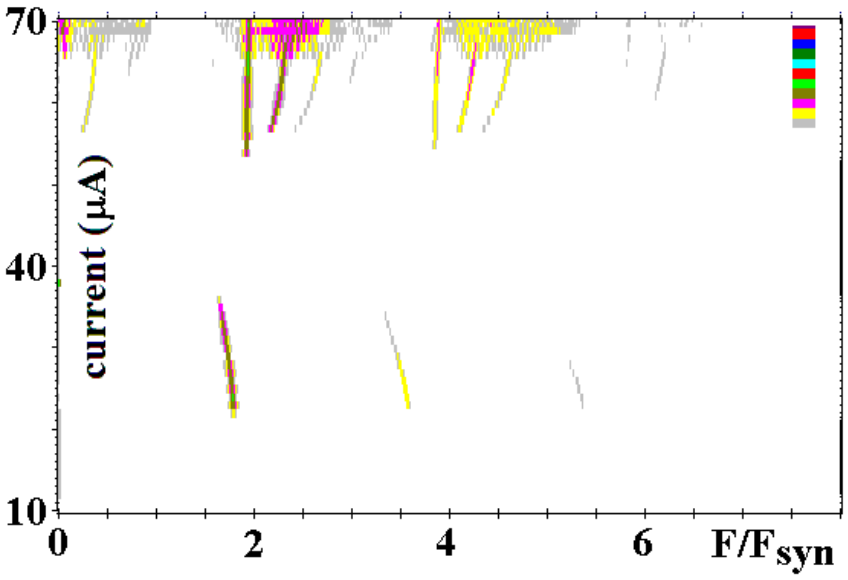

Figure 9.6: Simulated spectrogram showing the end of the micro-bunching instability (main bursting threshold) around 54 µAas well as the short-bunch-length bursting between 36 µA and 22 µA. The frequencies are directly below 2 and 4 times the synchrotron frequency, similar to the frequencies observed in the corresponding measurements (see Figure 9.2). Adapted from [Bro19b].

Values below $\Pi = 0.66$ were not accessible for our measurements, which precludes the possibility to check if the short-bunch-length bursting vanishes for even smaller values of the shielding parameter, as predicted by their calculations in [13].

As discussed above, the upper and lower limits in the bunch current of the short-bunch-length bursting are expected to depend not only on the natural bunch length $\sigma_{z,0}$ but also on $\beta = 1/(2\pi f_s \tau_d)$, which relates the longitudinal damping time τ_d and the synchrotron frequency f_s. In the measurements presented here, β ranges from $\beta = 1.13 \cdot 10^{-3}$ to $\beta = 3.33 \cdot 10^{-3}$. As the simulations in [13] were carried out only for the fixed value $\beta = 1.25 \cdot 10^{-3}$, new simulations were performed by Peter Kuske (HZB) for each measurement point using the exact parameters of the respective measurement. The VFP solver used for these additional simulations is presented in [32], and a comparison between simulation results and measurement performed at MLS and BESSY (Berliner Elektronenspeicherring-Gesellschaft für Synchrotronstrahlung m.b.H.) is given in [36].

Figure 9.6 shows a spectrogram calculated from the simulated phase space [78; Bro19b] for the machine settings used to obtain the measurement shown in Figure 9.2. Like in the measurement, a second region of instability corresponding to the short-bunch-length bursting is visible between 20 µA and 41 µA, well below the main bursting threshold at 54 µA. The dominant frequencies above the main threshold as well as in this second

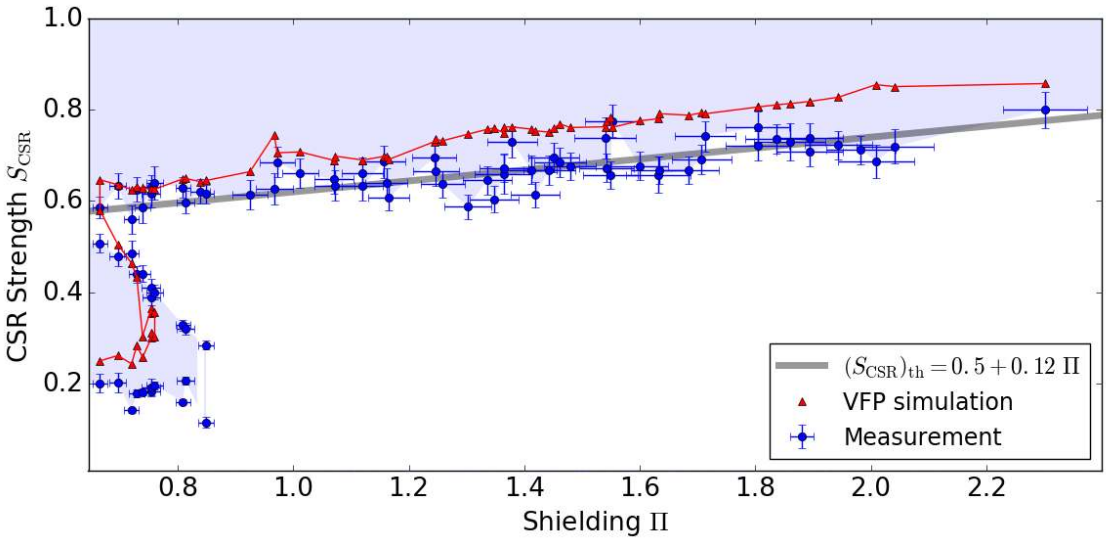

Figure 9.7: CSR strength at the bursting thresholds as a function of the shielding parameter for measurements and VFP solver simulations for different machine settings. The measured area of instability is indicated as a light blue area and confined by the measured thresholds (blue disks, already shown in Figure 9.3) with the error bars displaying the standard deviation error of each measurement. The red triangles show the results from the VFP solver simulations at the corresponding machine settings (red line to guide the eye). The gray line indicates the linear scaling law for the main bursting threshold given by Equation 2.24.

instability region are close to 2 and 4 times the synchrotron frequency, showing the same structure as the corresponding measurement (Figure 9.2). The similarity between the fluctuation frequencies in the main and in the SBB region, indicating similar dynamics of the fluctuations in the longitudinal charge distribution in both regions.

The CSR strengths at the thresholds obtained from the new VFP solver simulations are shown in Figure 9.7 (red triangles) as a function of the shielding parameter. These simulations (by Peter Kuske, HZB) yield thresholds which are higher by about 10% in comparison to the linear scaling law (grey straight line). As described in Section 2.9, the simple linear scaling law fits best for values of $\Pi > 3$ and deviates to lower threshold values for $\Pi < 3$ from the simulation points it was based on. The measurements (blue discs), however, coincide very well with the linear scaling law as was already shown in Subsection 7.2.1. Overall, the behavior of the simulations is still in agreement with the measurements. Figure 9.7 shows again clearly that in the measurement as well as in the new VFP simulations, a range of Π exists where unstable THz emission also occurs below the threshold given by the simple linear scaling law, as already predicted by [13]. The measurements as well as the simulations show a stable area between the two regions of instability.

The range in Π as well as in S_{CSR} where the short-bunch-length bursting occurs depends on β. For the parameters in our measurements, the simulations give an upper limit for the occurrence of short-bunch-length bursting of $\Pi = 0.76$, while the measurements show short-bunch-length bursting up to $\Pi_{\mathrm{SBB}}^{\mathrm{max}} = 0.845 \pm 0.013$, resulting in a small range of Π where short-bunch-length bursting is observed by measurements and not in the simulations. Also, the lower bound of the short-bunch-length bursting in the CSR strength differs slightly between the simulations and the measurements. The measurements show instability at a lower CSR strength (corresponding to a lower bunch current) than the simulations. This could be related to the fact that, in general, the threshold values obtained by the simulation are systematically slightly higher than the ones measured. Meaning, the simulated thresholds could have an systematic offset compared to the measurements. The average difference is 7 µA for the main threshold current, which ranges from 40 µA to 400 µA.

Lower values for the thresholds in the measurements cannot be explained by too-insensitive THz detectors, as this would result in an overestimation of the measured thresholds. Also, systematic influences, of this size, on the measured thresholds due to multi-bunch effects in the used snapshot measurements can be excluded, because the upper limit of multi-bunch effects in the thresholds was found to be much lower, which will be shown in the next chapter (Section 10.1). Additionally, thresholds measured in pure single-bunch decays agree, within the uncertainties considered, with the ones obtained from snapshot measurements (see Figure 9.3).

A small difference, consistent with the one observed, could be caused due to our measurement method. For small fluctuations of the machine settings, the measurements would give the absolute floor of the corresponding thresholds, while the simulation gives a value corresponding more to the average threshold for the machine settings, leading to a small deviation. Such fluctuations in the machine could occur in the acceleration voltage and the current in the magnets and, thus, the magnet optics and the momentum compaction factor.

Another potential source for deviations could originate from the assumptions used in the simulation. For example, the longitudinal damping time, an essential component in the solution of the VFP equation, was obtained by beam dynamics calculations which did not include the additional energy loss due to coherent synchrotron radiation emission. Furthermore, the VFP simulations consider only the simple parallel plates model for the CSR impedance (Section 2.6). The small difference between the measured thresholds and the calculated ones could indicate additional impedance contributions. For example, considering an additional geometric impedance for an aperture like a scraper leads to a

slightly lower simulated threshold [31]. Also, the impedance of edge radiation is mainly resistive and would lead, if considered in the simulation, to a lower threshold. In [91], the parallel plates model was extended to the case of a rectangular vacuum chamber and the micro-bunching thresholds were simulate for different aspect ratios of chamber width to chamber height (KARA: 72 mm width and 32 mm height). The results for an aspect ratio corresponding to the one at KARA, gave threshold values slightly below the prediction by the simple scaling law. Last but not least, a stronger CSR interaction than expected from the simple circular orbit simulated could be caused by an interaction extending into the straights behind the dipoles [78].

In conclusion, it was found that the Vlasov-Fokker-Planck simulations based on the simple parallel plates model deviate quantitatively from the measurement results. Further measurements, best with the possibility to change the damping time and therefore β independently of Π and at even lower values of Π (even lower natural bunch length), would allow an even more thorough comparison with different impedance models.

10 Multi-bunch Effects on the Micro-Bunching Instability

With the fast THz detectors and KAPTURE, described in Chapter 5, it is possible to measure the bursting behavior for all bunches in a multi-bunch fill individually. This allows to study possible differences in the behavior of the individual bunches caused by the presence of the surrounding bunches. Parts of this section have also been published in [Bro17a].

The description of the micro-bunching instability via the simplified parallel plates model of the CSR impedance (see Section 2.6) reflects the observed micro-bunching instability quite well [Bro16a; Sch17a] (and was used in the chapters above for the simulations). However, this description does not consider interactions between the bunches due to its short-range wakefield. Yet, such interactions can be facilitated by different structures present in real machines, like RF-cavities, passive cavities, scrapers, and other sources of long-ranging wake fields. First indications for multi-bunch effects at ANKA were measured in 2004 [92] caused by the influence of scrapers and in 2012 based on the emitted THz power [93]. Moreover, possible effects through CSR based on whispering gallery modes were theoretically discussed and simulated [94].

In the following, the threshold current, the bursting frequency, and the low bursting frequency, as the most prominent features of the instability, will be compared between the individual bunches.

10.1 Threshold Current

The bursting threshold for each bunch is determined (Subsection 6.3.1) via the power of the fluctuation in the emitted CSR power per turn. As described in Subsection 6.3.1, there can be some fluctuations in the detected CSR power even below the bursting threshold, mainly due to the synchrotron oscillation and 50 Hz noise. The influence of such unwanted fluctuations on the determined threshold can be reduced by considering only the fluctuation power in a certain frequency range around the bursting frequency (see Figure 6.6).

Figure 10.1 shows the integrated fluctuation power in the frequency range of $34 - 44\,\mathrm{kHz}$ for each bunch within one fill with the filling pattern shown in the right panel. The kink indicating the bursting threshold is clearly visible around $\approx 214\,\mu\mathrm{A}$. The used frequency range has to be adjusted for each measurement, as the bursting frequency at the threshold depends on the used machine settings (see Subsection 7.2.2). In the following, this integrated fluctuation power in a certain frequency range will often be referred to as THz fluctuations or just fluctuation strength for simplification. The threshold detection algorithm used in Subsection 6.3.1 (from [Bro14]) works best for snapshot measurements (due to the limited number of data points over current) and unfortunately shows a quite big uncertainty on the determined threshold in some decay measurements. For a multi-bunch decay measurement this is not feasible while at the same time it would be unpractical to determine the threshold for every single bunch in the fill by hand. Thus, instead of using the position of the kink, the bursting threshold was redefined as the point where the fluctuation power exceeds a certain level, which is chosen for each fill individually by eye. This method might lead to a slight shift of the determined mean value of the thresholds of all bunches. Which is not problematic as the important point of the measurements below is not to compare the mean value between the fills, but to have the best resolution on the distribution of the threshold currents of the individual bunches in each fill.

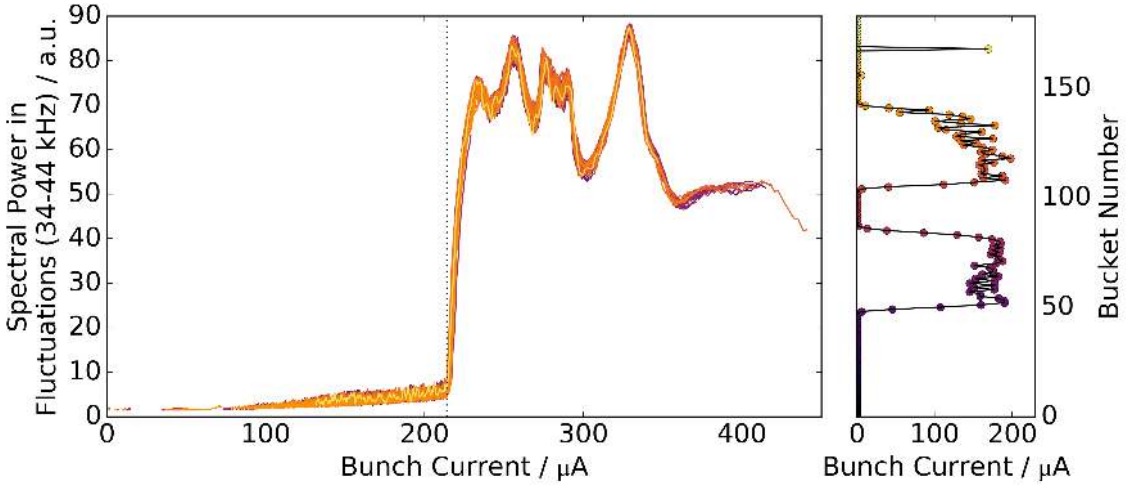

Figure 10.1: Integrated fluctuation power in the frequency range of $34-44\,\mathrm{kHz}$ as a function of the bunch current for each bunch. The filling pattern is displayed in the right panel and indicates the colors corresponding to the bunches. All curves show a kink around $\approx 214\,\mu\mathrm{A}$ (dashed vertical line) corresponding to the bursting threshold. (Also presented in [Bro17b])

The bunch current of each bunch is determined with time-correlated single photon counting (TCSPC, Subsection 4.3) and the measurement of the beam current (Section 4.2). As

described in Subsection 6.2, to get the current of each bunch at a certain point in time (the times of the THz measurements) a fit on the current decrease of each bunch is used to interpolate between the single current measurements. It is noteworthy that for some machine settings the same fit function (e.g. double exponential decay to model two possible contributions in the lifetime) was applicable for some bunches while other bunches in the same fill, showed small but systematic differences from the fitted behavior. For the studies presented up until now, this effect was minimal and if present it was considered in the uncertainties on the determined bunch currents. For the study of possible differences between bunches in a multi-bunch fill, the uncertainties on the determined bunch current need to be reduced as far as possible. Additionally, this effect needs to be avoided, as it could possibly lead to an artificial systematic on the distribution of the determined threshold currents. Thus, a slightly modified method was chosen. For all bunches the fit was applied only on a part of the current decay, namely the same fixed current range around the threshold current. A simple exponential function (including an offset) proved to be sufficient (in the following referred to as partial exponential fit). By fitting only a range around the threshold current, the fit result can not be influenced by the fact that the bunches start their decay at different bunch currents, depending on the filling pattern. For example, a current decay ranging from high currents to shortly below the threshold current could follow a slightly different function than a decay ranging from shortly above the threshold current to well below, due to bunch and/or beam current-dependent effects in the lifetime. Further investigations are necessary to show what exactly causes the same fit model to fail for one part of the bunches in a multi-bunch environment while working well for the rest. These differences between the bunches in the evolution of their bunch current as as function of time could hint at different beam dynamical behaviors of bunches in a multi-bunch environment.

The error on the bunch current measurement at the mean threshold current of all bunches (given in Table 10.1) is determined using the same method as described in Subsection 6.2. Instead of using the approximation given there, the error is calculated for each fill individually from the count rate at the corresponding threshold current, to have the most accurate estimation possible. How to handle measurement artifacts looking like multi-bunch effects, in this case caused by the dead time of the time correlated single photon counting (TCSPC) setup, is described in Subsection 4.3.2. Figure 10.2 shows how the dead time of the TCSPC setup affects the measurement. Due to the resulting artificial distortion of the filling pattern, the bunch current to time mapping is wrong and thus the observed threshold (kink) is shifted to different bunch currents differently for each bunch (see Figure 10.2b). In result, it looks like the bunches crossed the bursting threshold at significantly

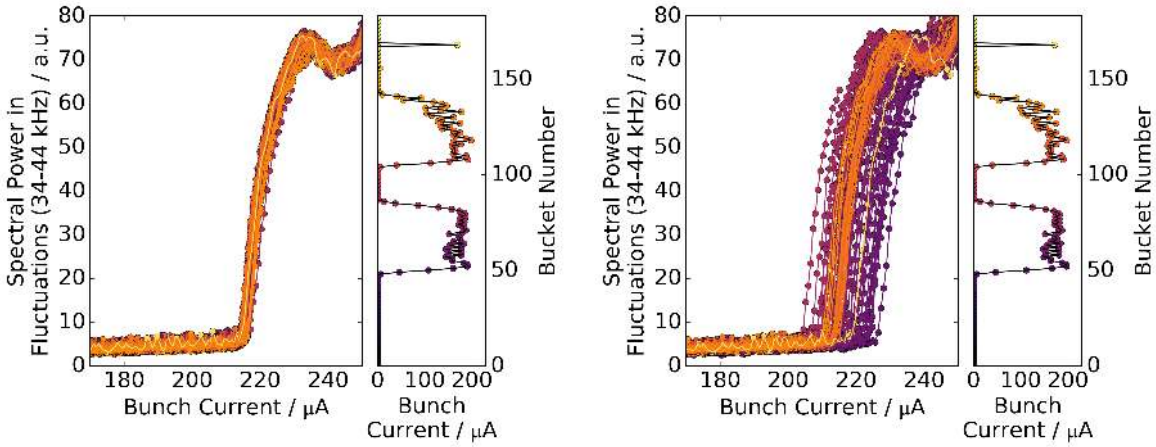

(a) (b)

Figure 10.2: (a) Zoom into Figure 10.1 at the threshold current. (b) Same data but with out the correction of the dead time effect in the bunch currents. The dead time effect in the filling pattern measurement leads to a systematic error in the determination of the threshold current. (Also presented in [Bro17b])

different currents. When the dead time effect is corrected, the spread of the bunch currents at which the kink in the fluctuations due to the threshold is observed, shrinks drastically (see Figure 10.2a). For the measurements in the following, the count rate of the TCSPC setup was kept at an intermediate level (as discussed in Subsection 4.3.2) and the remaining dead time effect was corrected.

Table 10.1: Spread of the threshold currents vs. statistical error on the measured bunch current at the threshold for different fills. The (quadratic) difference between the standard deviation of the threshold currents I_{th} of the different bunches and the statistic error of the bunch current measurement at the mean threshold current $\sigma_{I_{\mathrm{b,th}}}$ is given. The difference in the uncertainty on the threshold currents for the fitted data compared to the Poisson error, shows that the fit improves the quality of the bunch currents. All values are given in µA. [Bro17a]

Fill number	6212	6258	6283	6284	6288	6292	6296
$\mu\left(I_{\mathrm{th}}\right)$	106.02	207.32	179.44	67.64	116.15	128.13	243.17
$\sigma_{I_{\mathrm{b,th}},\ \mathrm{Poisson}}$	1.98	17.26	1.79	1.20	1.38	1.45	2.10
$\sigma_{I_{\mathrm{b,th}},\ \mathrm{Fit}}$	0.48	4.12	0.62	0.29	0.34	0.29	0.72
$\sigma\left(I_{\mathrm{th}}\right)$	0.55	4.28	1.065	0.49	0.50	0.43	0.98
$\sqrt{\sigma\left(I_{\mathrm{th}}\right)^2 - \sigma^2_{I_{\mathrm{b,th}}}}$ (par. exp. fit)	0.27	1.16	0.87	0.39	0.37	0.32	0.66

The measured average threshold current $\mu\left(I_{\mathrm{th}}\right)$ of the bunches in multi-bunch fills is given in Table 10.1 for several fills. Due to different settings of the acceleration voltage and the momentum compaction factor the resulting threshold currents I_{th} differ between the fills.

Figure 10.3a shows the fluctuation strength as a function of the bunch current (around the bursting threshold) for all bunches in one fill (6296). All bunches show a similar behavior, with a small variation in the current where the signal increases strongly crossing the power level, indicating the instability threshold (see dotted line in Figure 10.3a). A second example (in Figure 10.3b) shows a similar variation of the threshold currents of the individual bunches in another fill (6288).

The statistical uncertainty $\sigma_{I_{\mathrm{b,th}},\,\mathrm{Poisson}}$ on the bunch current measurement at the threshold current, calculated by the Poisson statistic (Equation 4.1), is around 1 to 2 µA for the different fills. With the exception of fill 6258 for which the optical attenuation of the TCSPC setup was chosen stronger, leading to a lower count rate. The usage of the partial exponential fit (described above) reduces the statistical fluctuations and therefore improves the uncertainty on the bunch current $\sigma_{I_{\mathrm{b,th}},\,\mathrm{Fit}}$ by a factor of 3 or more to values below 1 µA for most cases. The spread of the threshold currents $\sigma\left(I_{\mathrm{th}}\right)$ of the bunches was found to be mostly below 1 µA (see Table 10.1).

Nevertheless, the difference between the threshold spread and the current uncertainty indicates an additional contribution to the spread in threshold currents. For the presented measurements, an upper limit for a possible influence of multi-bunch effects on the threshold current of the longitudinal micro-bunching instability can be given with approx. 0.5 µA. A possible systematic in the distribution of the threshold currents, for example depending on the position of a bunch in the train or on the current in the preceding bunch, would probably be convolved with the scattering of the threshold currents due to the statistical error of the bunch current measurement. As the effects are at best in the same order of magnitude it could be impossible to see the original systematic distribution.

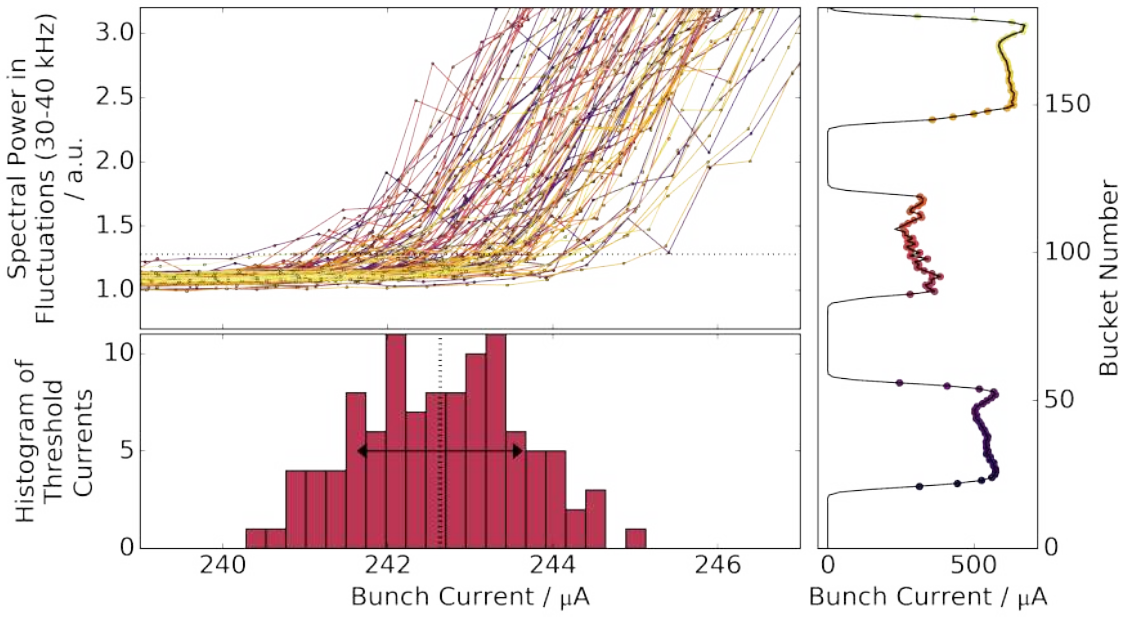

(a)

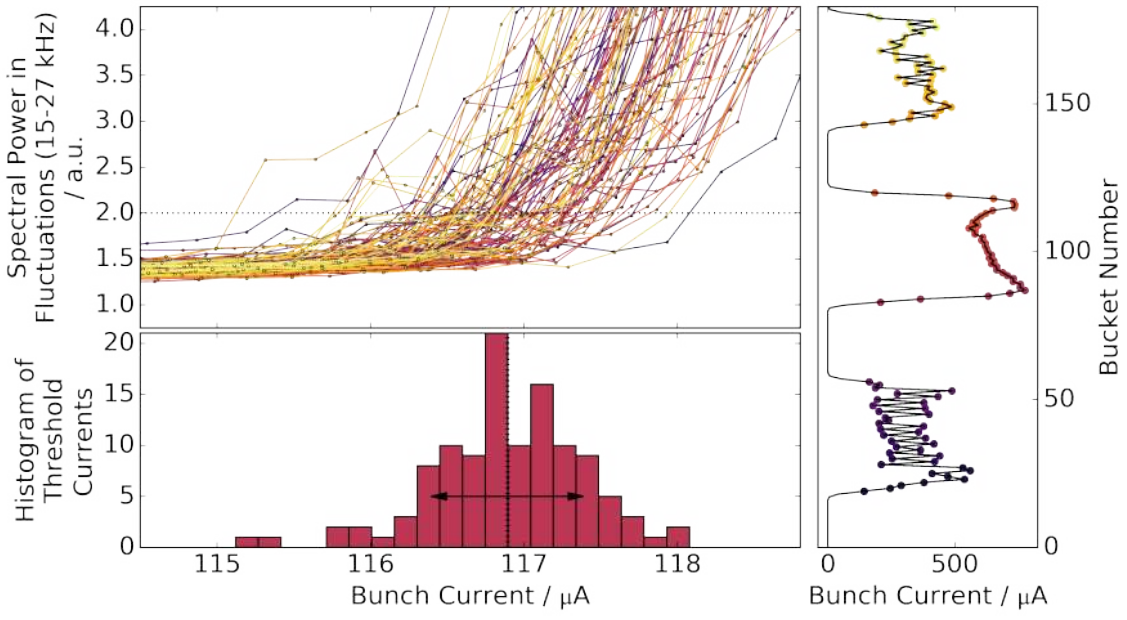

(b)

Figure 10.3: THz fluctuations as function of bunch current for all bunches in a multi-bunch fill. (a) Fill 6296 and (b) Fill 6288 in Table 10.1. The vertical (doted) line in the histogram of the threshold currents of each bunch (lower panel) indicates the average of the threshold currents $\mu(I_{\mathrm{th}})$ while the horizontal arrows indicate the spread (standard deviation) of threshold currents $\sigma(I_{\mathrm{th}})$. The filing pattern at the start of the decay is indicated in the right plot.

10.2 Bursting Frequency

The bursting frequency is the fluctuation frequency in the emitted CSR power at the bursting threshold. In the previous section, it was discussed that bunches in a multi-bunch fill show a slight variation in the observed threshold current which is in the order of the bunch current accuracy. The bursting frequency at the threshold, however, can be determined without the knowledge of the bunch current. This was first studied in a bachelor thesis under my supervision [95]. In the following, a simpler and faster approach to determine the bursting frequency was used. For each individual bunch, the main fluctuation frequency is determined in the dataset taken right before the bunch crosses the thresholds from the unstable to the stable regime (the kink in the fluctuation power is observed). For the different fills studied in the previous section, the determined spreads in bursting frequency between the different bunches are listed in Table 10.2. For fill 6284 no reliable values can be determined due to strong noise lines in the spectrogram. The measurements show maximal deviations ranging from 156 Hz to 441 Hz. This matches the findings in [95] where maximal deviations of 200 Hz, 250 Hz, and 350 Hz were observed for three examined fills.

Table 10.2: Spread of bursting frequencies between different bunches in different multi-bunch fills (also discussed in Table 10.1). The mean value of the determined bursting frequency is $\mu(f_{\mathrm{th}})$. The standard deviation is given as $\sigma(f_{\mathrm{th}})$ while the maximal deviation gives the difference between the minimal and the maximal value. All values are in Hz.

Fill number	6212	6258	6283	6284	6288	6292	6296
$\mu(f_{\mathrm{th}})$	18894	35648	31500	-	19493	20991	33452
max. deviation f_{th}	156	188	369	-	441	253	386
$\sigma(f_{\mathrm{th}})$	42	36	114	-	80	61	84

Figure 10.4a shows the bursting frequency determined for each bunch (for fill 6296). A short segment of the Fourier transform of the emitted CSR power in the frequency range of the determined bursting frequency, can be seen in Figure 10.4b. Each column gives the signal for one bunch. The bursting frequency is not a smooth, sharp peak in the FFT, but has a width of about 150 Hz (FWHM), which is reflected in Figure 10.4a as error bars. As the frequency was determined by just finding the maximum in the FFT, a moving average with a width of 75 Hz was applied to smooth the noise spikes which are visible in Figure 10.4b on the broad peaks.

The bursting frequency of the different bunches lies between 33.2 kHz and $\approx$ 33.6 kHz. The bunches in the middle train, which had lower bunch currents at the start of the

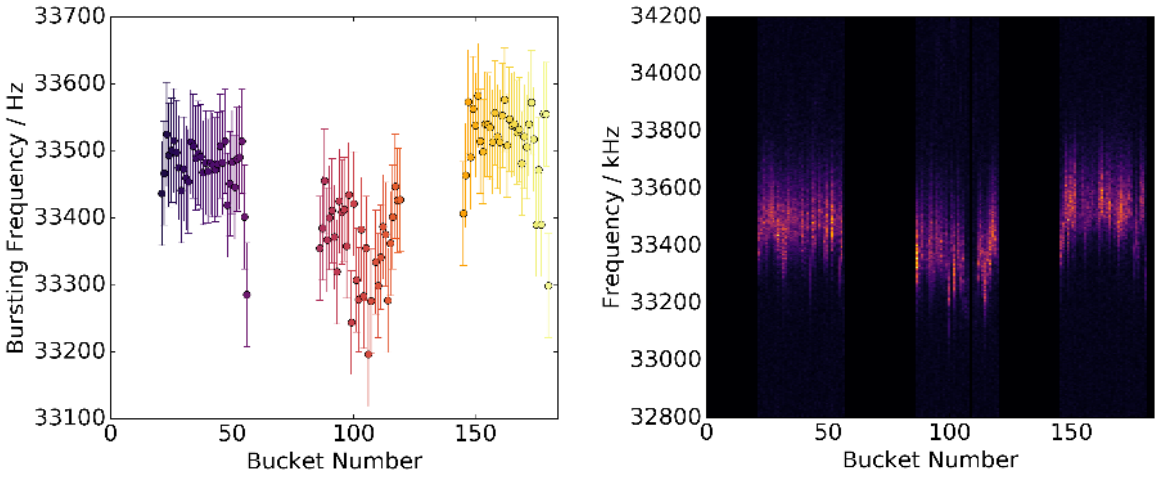

(a) (b)

Figure 10.4: (a) Bursting frequency of each bunch in a multi-bunch fill (6296) with the error bars indicating the width of the frequency peak at the bursting threshold. (b) Each column shows a short segment of the Fourier transform of the emitted CSR power of each bunch. The frequency peak of the bursting frequency is quite broad and ragged.

measurement (for filling pattern at the start of the decay see Figure 10.3a, right panel) show a slightly lower bursting frequency. In Figure 10.5a and Figure 10.5b, the same plots are shown for another fill (6288). Here, the bursting frequency lies between 19.3 kHz and ≈ 19.7 kHz. And the bunches in the middle train (which had higher bunch currents at the start of the measurement, see Figure 10.3b right panel) show a slightly higher bursting frequency.

Extrapolating from these two examples it seems[1] that bunches with a comparably lower initial bunch current at the start of the measurement show a slightly lower bursting frequency at the threshold.

One possible explanation could be as follows. Bunches starting with a lower bunch current reach the threshold at early times, where the total beam current is still high whereas bunches starting from higher currents cross the threshold current at later times, where the total beam current is lower. This could influence the machine parameter slightly, for example the actual acceleration voltage observed by each bunch could change slightly due to a change in the strength of beam loading effects with the total beam current.

From the studied measurements, three (including the two examples) show these systematics. While one other measurement shows no clear correlation between the initial bunch current

[1] Note, the different measurements show different behaviors as discussed below.

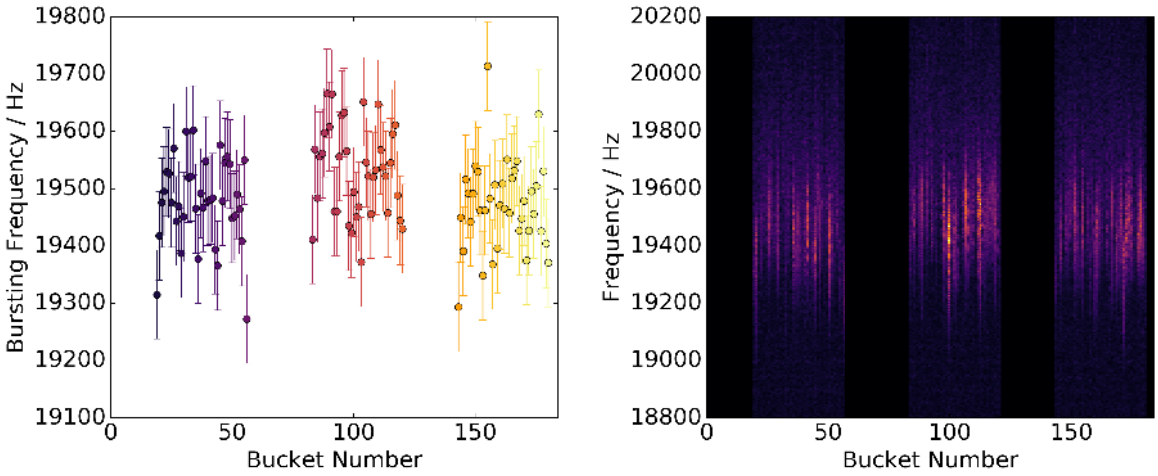

(a) (b)

Figure 10.5: (a) Bursting frequency of each bunch in a multi-bunch fill (6288) with the error bars indicating the width of the frequency peak at the bursting threshold. (b) Each column shows a short segment of the Fourier transform of the emitted CSR power of each bunch. The frequency peak of the bursting frequency is quite broad and ragged.

and the bursting frequency and the remaining two measurements even show a slight inverse correlation (see Appendix A.10). It seems there are some systematic effects, but they probably depend on more parameters than the initial bunch current, like for example the filling pattern or even the machine settings during the different measurements. More systematic studies are necessary to pin point the source for such systematic effects. For example, any long ranging wake fields present in the machine and not considered in the simulations, could have a slight influence on the bursting behavior.

Another option not considered up until now, is that the determination of the bursting frequency from the measurement could be not as accurate as thought. For example, the frequency line starting at the bursting frequency at the threshold increases in frequency for increasing bunch current (see Figure 10.6). This could have an effect because, for most measurements a dataset containing one second of data is taken every ten seconds. Which means, it happens that there is no measurement at the exact time the bunch crosses the bursting threshold, with a deviation between 0 and 10 seconds. This leads to a shift in the determined frequency as the frequency line is not vertical (Figure 10.6). So, if one bunch passes the threshold and the previous dataset was taken directly before while for a second bunch the previous dataset was taken up to ten seconds earlier, the determined bursting frequency differs. While this could explain the spread, it can not directly explain the systematics observed.

The cause of these systematics in the small spread of the bursting frequency for different bunches in a multi-bunch fill could also have an effect on the threshold, which would not be directly visible due to the convolution with the scattering of the bunch currents due to the uncertainty in the bunch current determination. With further knowledge of the relation between the bursting frequency and the threshold current, it might be possible to use the former to study the latter circumventing the limitations due to the uncertainties on the bunch current measurements.

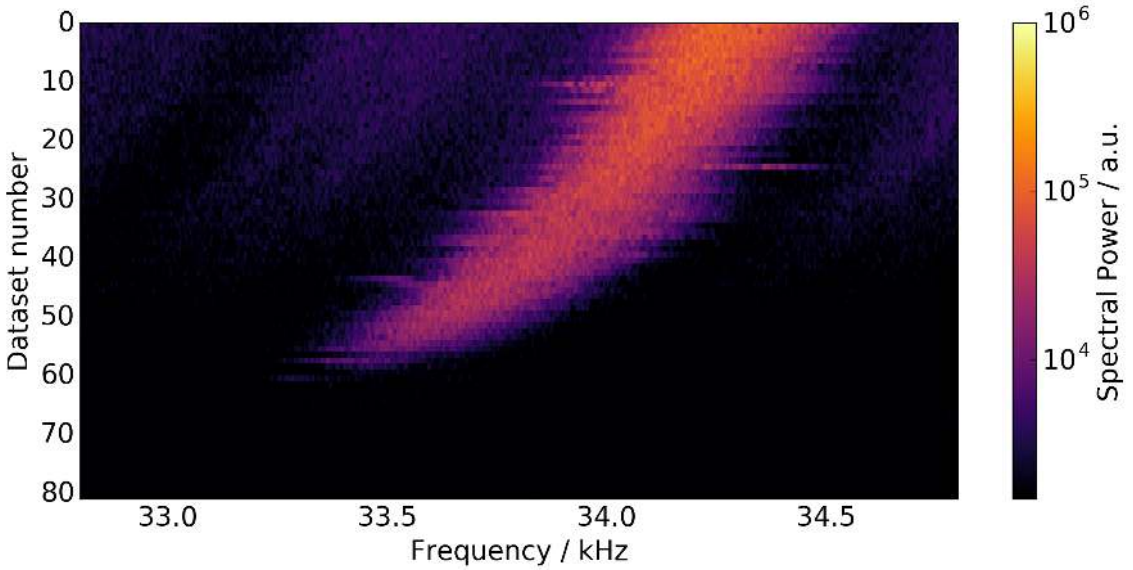

Figure 10.6: Small section of a spectrogram showing the frequency line which starts at the threshold current with the bursting frequency. The frequency line shifts with increasing bunch current (decreasing number of dataset). (Fill 6296)

10.3 Low Bursting Frequency

For the low bursting frequency visible in the fluctuations of the CSR power emitted by bunches under the influence of the micro-bunching instability, it is not yet clear what determines the behavior as a function of the bunch current (as discussed in Subsection 7.2.3 and Section 7.3). Thus, it is an interesting point to see if it is influenced by the presence of other bunches.

First studies of this ([95]) were conducted before the influence of the dead time effect in the filling pattern measurement on multi-bunch studies became apparent. The found differences in the low bursting frequency of different bunches in multi-bunch fills are drastically reduced when dead time effects are considered (and corrected, Subsection 4.3.2) in the measurements discussed in [95].

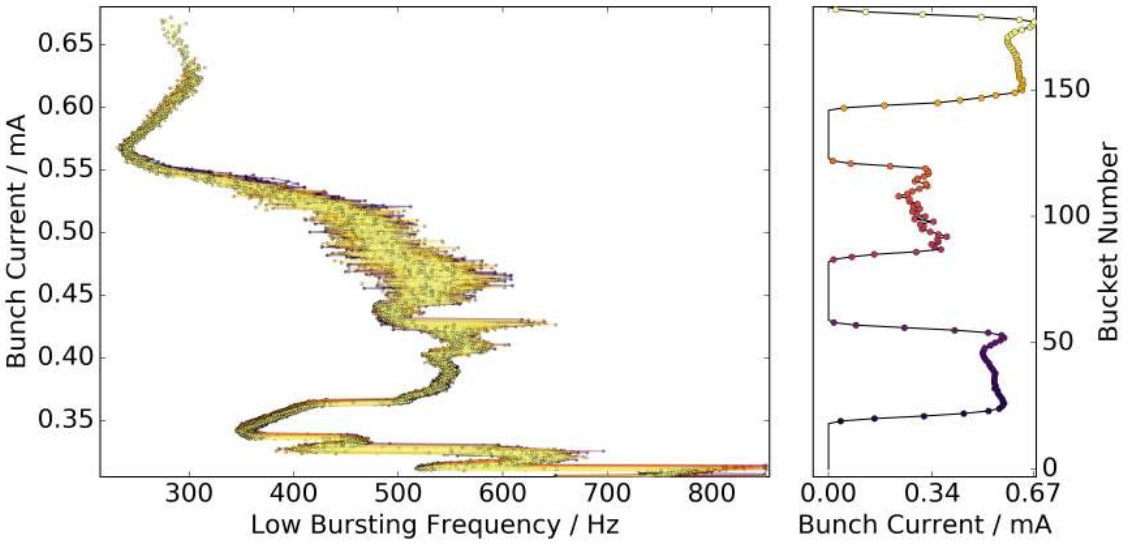

Figure 10.7: Behavior of the low bursting frequency during the bunch current decay, displayed for each bunch in a multi-bunch fill (6296). The line colors correspond to the different bunches indicated with the same color in the filling pattern in the right panel.

For one of the fills (6296) studied in the previous sections, Figure 10.7 shows the low bursting frequency as a function of current during the decay (similar to Figure 7.13) for each bunch shown in the filling pattern in the right panel. It is clearly visible that the low bursting frequencies of all bunches show overall the same behavior. As described before, for the study of the threshold current of different bunches only a certain part of the bunch current decay (around the mean threshold current of each fill) was fitted, as this reduced the uncertainty further and described the current decay better. For the study of the low bursting frequency the whole current range is necessary. Thus, a fit over the whole current was performed accepting the potentially higher uncertainty in the determined bunch currents. In Figure 10.8, a zoom into the low bursting frequency in the current range from 0.33 mA to 0.39 mA is shown. It is visible that the lines are not exactly the same. For example, at a frequency of 475 Hz the bunches have a current between 362.0 µA and 367.3 µA. This span of 5.3 µA is close to the total span of the threshold currents (4.8 µA) seen in the same fill (Figure 10.3a). Taking into account the slightly higher uncertainty on the fitted bunch currents due to the different fit function, the spread can be mostly explained by the uncertainty on the determined bunch currents. Probably a small contribution by a different effect can not be ruled out, similar to the threshold currents in Table 10.1.

The inset in Figure 10.8 zooms into the kink of the low bursting frequency around 342 µA. Due to the temporal vertical trend of the low bursting frequency at this current, the

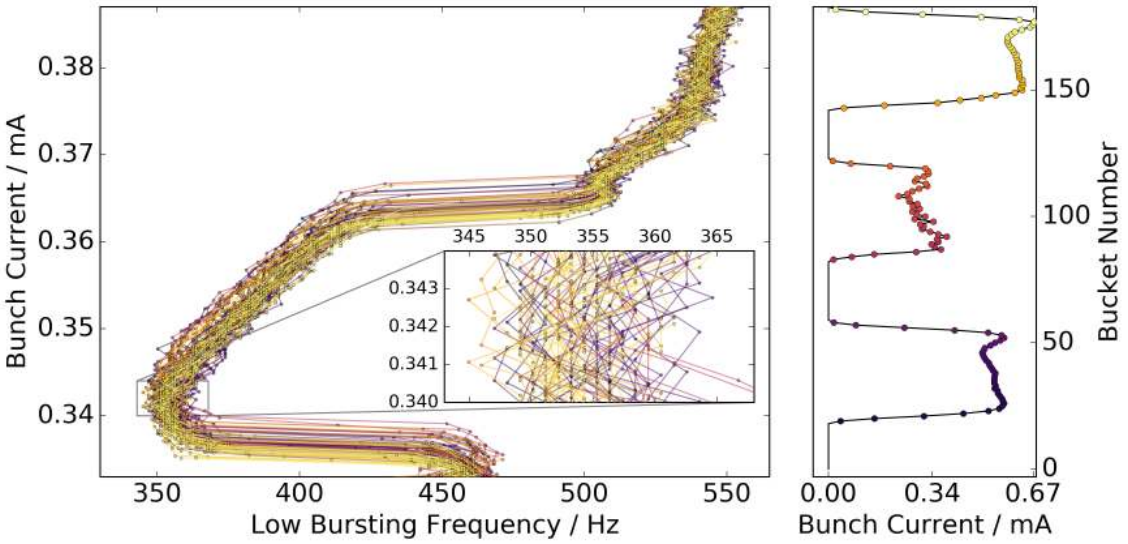

Figure 10.8: Zoom into Figure 10.7 providing a more detailed view of the low bursting frequency behavior for different bunches in a multi-bunch fill (6296). In the inset, the change in the determined frequency for each bunch from one measurement (points) to the next measurement is visible.

observed current spread, discussed above, should not have a big influence on the observed spread in frequency. At 342 µA, the low bursting frequency of the different bunches ranges from approximately 345 Hz to 365 Hz giving a frequency spread of 20 Hz. The frequency resolution is ≈ 1 Hz due to the measurement duration of one second. As the low bursting frequency is not a narrow frequency line but more a broad peak, a moving average (with a window width of 10 Hz) was used on the frequency data to smooth out noise spikes and, therefore, improve the search for the strongest frequency component (Subsection 6.3.3). Nevertheless, some of the bunches still show a jitter in the determined frequency of up to 10 Hz from one measurement point to the next.

Similar to the above mentioned spread in bunch current at a fixed value of the low bursting frequency or the spread in threshold current of the different bunches, the spread in the low bursting frequency at a fixed bunch current is in the same order as the spread of a single bunch. This makes a possible multi-bunch systematic effect hardly visible, but the spread could still contain a small additional component. This additional component could lead to the presence of small differences in the behavior of individual bunches in multi-bunch fills. Nevertheless, these potential components are small compared to the overall dynamics confirming that the micro-bunching instability is mainly a single bunch effect.

11 Summary

The micro-bunching instability is a longitudinal, coherent instability caused by the self-interaction of a short electron bunch in a storage ring with the coherent synchrotron radiation (CSR) it is emitting in wavelengths longer than itself. Above the instability's threshold current, the interaction leads to the formation of substructures on the charge distribution in the longitudinal phase space. This can be observed in measurements as fluctuations in the CSR power which is typically emitted in the hundred GHz to THz frequency range.

This thesis studied systematically the influence of different machine parameters as well as special conditions like a multi-bunch environment or short bunch lengths combined with low bunch currents on the behavior of a bunch under the influence of the micro-bunching instability. This was mainly conducted on the three most characteristic features of the instability: the threshold current and two fluctuation frequencies, the bursting frequency occurring directly at the threshold current of the instability and the low bursting frequency, corresponding to the repetition rate of the bursts in the emitted CSR power further above the threshold current.

For these systematic studies, the dedicated data acquisition system KAPTURE was developed further and improved in a KIT-internal cooperation with the IPE[1], resulting in the new version KAPTURE-2. In combination with fast THz detectors, this allows to continuously detect the emitted CSR power of each bunch in a multi-bunch fill at every revolution with up to eight different detectors synchronously. Enabled by this capability to measure all bunches in a multi-bunch fill simultaneously, the "snapshot" measurement method was developed to study current-dependent effects with a drastically reduced measurement time of as short as one second. Additionally, this thesis, and the measurements therein, brought up the necessity to reduce the uncertainties on the measured bunch currents and contributed to the implementation and testing of a dead time correction scheme for the time-correlated single photon counting setup used to measure the bunch currents.

[1] Institute for Data Processing and Electronics

These improvements were for example necessary to systematically study the dependence of the threshold current from the momentum compaction factor α_c and the acceleration voltage V_{RF}. It could be shown that the predicted simple linear scaling law of the threshold current, based on the simple parallel plates model of the CSR impedance, describes the measurement results at KARA. Similarly, the dependence of the bursting frequency at the threshold current on Π was studied. The steps observed in the measured bursting frequency as a function of Π, support the simulation-based expectation that the number of substructures in the charge distribution changes for different settings. On the other hand, the observations revealed a discrepancy between the measurements and the simulations. The measured steps are significantly more pronounced than the ones in the simulations. Additionally, the behavior over bunch current of the slow repetition rate of the bursts (low bursting frequency) in the emitted CSR power was studied. The behavior is also not exactly reproduced by the simulations based on the parallel plates impedance. There is still no explanation for its exact behavior over the bunch current. Nevertheless, it could be shown that the frequency range it spans over for different bunch currents depends on Π. With this knowledge, it is now possible to shift the threshold current, the bursting frequency as well as the low bursting frequency to specific values as needed. Nevertheless, it needs to be considered that changes of these parameters via the momentum compaction factor and the acceleration voltage are not independent.

In further studies it could be demonstrated that the longitudinal damping time changes the low bursting frequency but has no influence on the bursting frequency as well as the threshold current. The damping time was influenced by increasing the synchrotron radiation loss with the CLIC damping ring wiggler prototype installed at KARA. This provides the possibility to change the low bursting frequency, and therefore the repetition rate of the bursts in emitted CSR power, independently of the other two parameters.

With the development of the acquisition systems KAPTURE and recently KAPTURE-2, it was also possible to investigate how the frequency range in which the emitted CSR is detected, influences the observed behavior. The observations showed that the detected frequency range influences the shape of the bursts but not the repetition rate of the bursts. This indicates that both, the power of the emitted CSR fluctuates and the spectrum of the emitted CSR, changes due to the formation of substructure on the longitudinal charge distribution. Measurements with two different waveguide-coupled Schottky diode detectors showed no dependence on the detected frequency range for the current where first fluctuations caused by the instability become visible. This indicates that the determination of the threshold current is independent from the detector. Further investigations with the shortly tested on-chip Schottky diode array, containing eight detectors sensitive in different

frequency ranges, will help to gain further insight into the turn-by-turn changes in the emitted CSR spectrum.

For further understanding, also additional diagnostics available at KARA were utilized. Synchronous measurements of the longitudinal and the horizontal bunch profile and the emitted CSR power made it possible to observe changes in different bunch parameters, like the bunch length, energy spread and longitudinal phase, connected to each other. This provided a further understanding of the influence of the instability on the longitudinal dynamics of a bunch. It is, for example, possible to see the connection between the occurrence of substructures on the longitudinal bunch profile and the increase in detected CSR power. Furthermore, a small shift in the bunch's phase relative to the acceleration voltage was observed during the increased emission of CSR in a burst. This proved independently of any THz detector that not only the emitted spectrum changes but also the total amount of power emitted and therefore lost by the bunch changes. This demonstrates the potential of these synchronous measurements and makes them an ideal candidate for further studies and tests of the dynamics under the influence of the micro-bunching instability.

In the second half of this thesis, the influence of the micro-bunching instability under special conditions was investigated. First, measurements of an additional region of instability occurring at KARA for low bunch currents combined with short bunch lengths confirmed the presence of a weak instability predicted by simulations. As predicted, a dependence of the upper and lower current limits of this instability on the ratio β of the longitudinal damping time and the synchrotron period was found. Additionally, it was possible to confirm the predictions that also the region in Π, where the instability occurs, depends on β. A direct comparison between the measurements and individual simulations at the exact parameters of the measurements revealed small deviations. For example, the thresholds were simulated to be about 10% higher than measured. Also, the simulated region containing the weak instability was smaller than the one measured. So overall, the measurements revealed the regions of instability to be bigger in all dimensions than it is expected by the simulations. These deviations indicate further effects not yet considered in the simple parallel plates model of the CSR impedance. The simulated threshold currents could be change if additional impedances, for example from apertures in the vacuum pipe or from the edge radiation, were to be considered. And the CSR interaction could turn out to be stronger than expected from the simple circular orbit in the parallel plates model if the interaction extends into the straight sections behind the dipoles.

Secondly, it was shown that the threshold currents of bunches in a multi-bunch fill deviate slightly from each other, while the overall bursting behavior is roughly the same as in

single-bunch operation. The implemented dead time correction reduced the uncertainty on the measured bunch currents below this difference observed in the threshold currents. This leaves a small difference indicating an additional contribution. For the presented measurements of the threshold current, this possible contribution by multi-bunch effects was determined to be less than 0.5 . Similarly, a small difference is observed between individual bunches in a multi-bunch fill in the repetition rate of the bursts. As the spread is in the same order than the jitter observed in a single bunch for different measurements, it is not possible to separate a possible multi-bunch effect from the jitter of a single bunch. For some measurements a small, systematic difference is observed in the bursting frequency (finger frequency) at the threshold current. It is noteworthy that this effect is visible in three of the presented six measurements. However, one of the measurements does not show this systematic and the remaining two measurements even show a slight inverse correlation. Therefore, further systematic studies are necessary, to figure out which parameters differ between these measurements and lead to this difference in the observed small, systematic effect on the bursting frequency of bunches in a multi-bunch fill. Nevertheless, all the observed differences in a multi-bunch environment are small compared to the overall dynamics of the micro-bunching instability. Therefore, it could be shown that a possible usage of the produced coherent THz radiation is not limited to single-bunch operation alone.

With the systematic studies conducted in this thesis, the influence of important machine parameters as well as special operation conditions on the behavior of bunches subject to the micro-bunching instability was thoroughly mapped, discussed and compared to simulations. This has led to a deeper understanding of the dynamics in the longitudinal phase space caused by this instability. It was found that the Vlasov-Fokker-Planck simulations based on the description of the micro-bunching instability via the simplified parallel plates model of the CSR impedance deviate quantitatively from the measurement results. In the future, the conducted measurements will prove helpful in testing different impedance models as well as in figuring out which impedances and parameters are actively contributing and influencing the micro-bunching behavior observed in short electron bunches. This instability, caused by the self-interaction of a bunch with its own CSR, has to be understood and described with a model as complete as possible, in order to develop and test future efforts to influence and control the instability in existing machines or suppress and avoid it already in the design phase of new machines.

A Appendix

A.1 Typical Machine Settings

In the table the typical machine parameters during the measurements in this thesis are listed. Some parameters are given with ranges as they could be varied to study the resulting changes in the micro-bunching instability.

Table A.1: Parameters during study of the micro-bunching instability.

Electron beam energy	$E \approx 1.3\,\mathrm{GeV}$
RF frequency	$f_{\mathrm{RF}} \approx 499.705\,\mathrm{MHz}$
Revolution frequency	$f_{\mathrm{rev}} \approx 2.7157\,\mathrm{MHz}$
Synchrotron frequency	$f_{\mathrm{s}} \approx 4.5\,\mathrm{kHz}$ to $13.5\,\mathrm{kHz}$
Acceleration voltage	$V_{\mathrm{RF}} \approx 500\,\mathrm{kV}$ to $1400\,\mathrm{kV}$
Radiated energy/particle/revolution	$U_0 \approx 45.5\,\mathrm{keV}$
Relative energy spread	$\sigma_\delta \approx 0.47 \times 10^{-3}$
Momentum compaction factor	$\alpha_{\mathrm{c}} \approx 1.5 \times 10^{-4}$ to 1×10^{-3}

A.2 Schottky Diode Detectors

The different narrow-band waveguide-coupled VDI detectors available at KARA (Subsection 5.2) are sensitive in frequency bands ranging from $90 - 140\,\mathrm{GHz}$ to $500 - 750\,\mathrm{GHz}$ (see Figure A.1). They have a higher responsivity in their individual frequency band than the quasi-optical broad-band detector from ACST, which has a lower responsivity but over a significantly wider spectral range. The different analog output bandwidths can be seen in Figure A.2, where the pulse response of the ACST and of one of the VDI detectors to a short THz pulse, measured with an oscilloscope, is displayed.

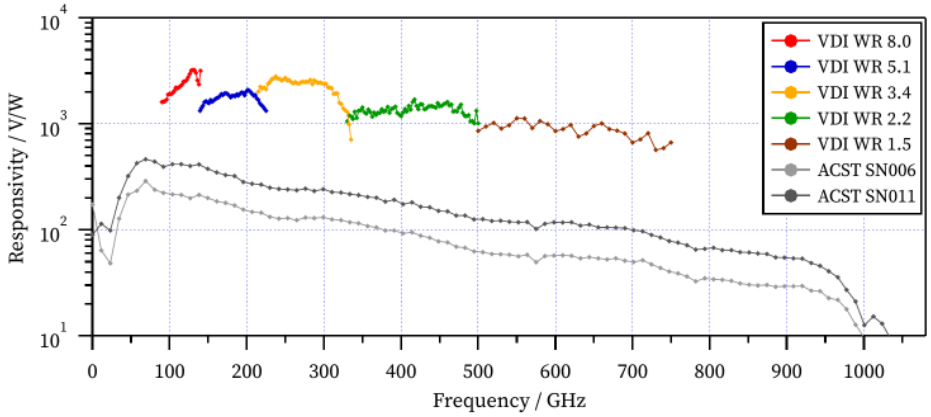

Figure A.1: Spectral responsivity of the used narrow-band waveguide-coupled Schottky barrier diode detectors from VDI and the broad-band quasi-optical SBD detectors from ACST. Courtesy of Johannes Steinmann. [20]

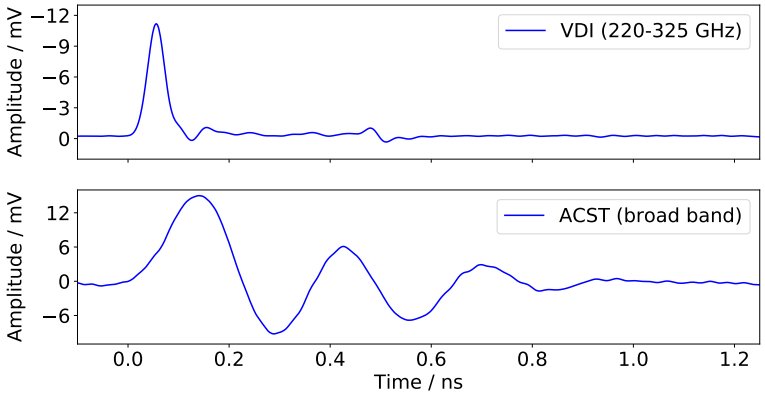

Figure A.2: Pulse response to a $< 10\,\mathrm{ps}$ pulse for the broad-band ACST detector and one of the narrow-band VDI detectors. The different pulse length resulting from the different analog output band width is clearly visible. The ACST detector is limited by the internal 4 GHz amplifier. As the signals were taken at a different time and input power, they can not be compares quantitatively. Data courtesy of J. L. Steinmann.

A.3 RF-System Calibration Cross-Check

In Section 3.3, it is described how the old RF-system was calibrated using Compton back scattering measurements. As an additional cross check, the measured threshold currents are compared in Figure A.3 to the theoretical predictions calculated from Equation 7.1. While the solid lines were calculated with the calibrated voltages and match the measured thresholds very well, the dashed lines were calculated using the set-values of the acceleration voltage and clearly do not match the measurements. This proves that the calibration determined in Section 3.3 is valid.

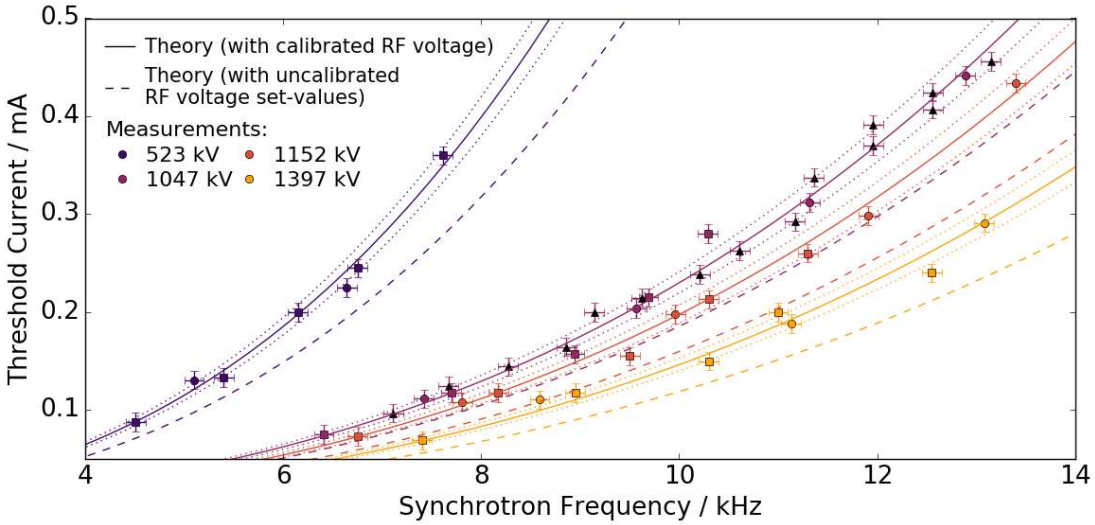

Figure A.3: Threshold currents as a function of the synchrotron frequency. The solid lines show the theoretical prediction using the threshold current for the calibrated acceleration voltage and their dotted 1σ-uncertainty bands. While the dashed curves show the prediction based on the set-values of the acceleration voltage.

A.4 Momentum Compaction Factor Scan

For the scan over different values of the momentum compaction factor α_c mentioned in Section 7.1, α_c was stepwise decreased for each snapshot measurement while the acceleration voltage was kept constant. A shift of the bursting frequency to lower values with decreasing α_c is clearly visible. Similarly, the threshold current decreases for decreasing α_c. It is also visible that the shape of the frequency component starting at the threshold current changes for the different values of the momentum compaction factor.

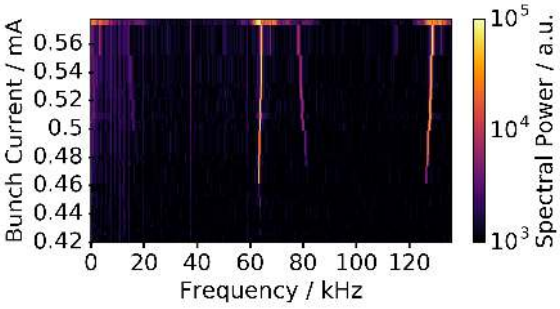

(a) $\alpha_c = 9.93 \cdot 10^{-4}$

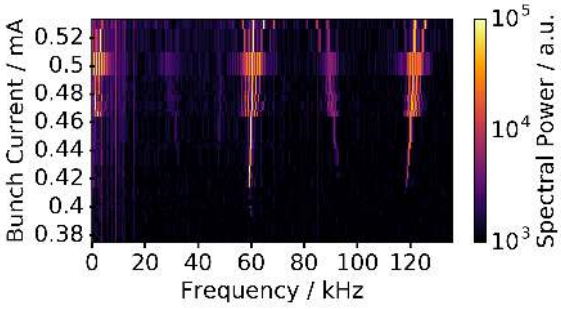

(b) $\alpha_c = 9.06 \cdot 10^{-4}$

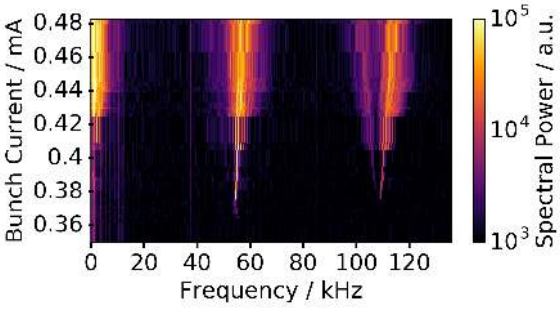

(c) $\alpha_c = 8.22 \cdot 10^{-4}$

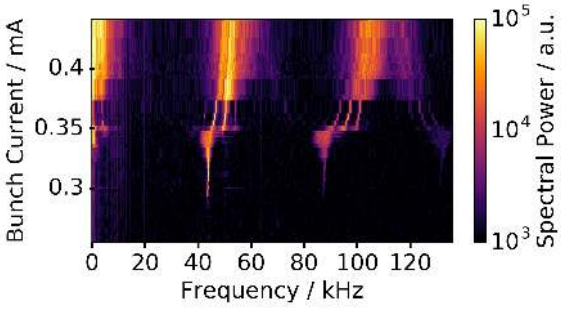

(d) $\alpha_c = 7.17 \cdot 10^{-4}$

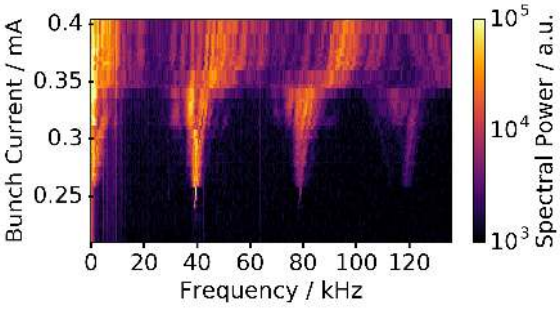

(e) $\alpha_c = 5.99 \cdot 10^{-4}$

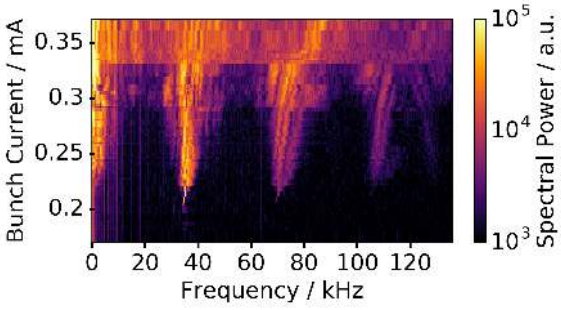

(f) $\alpha_c = 4.80 \cdot 10^{-4}$

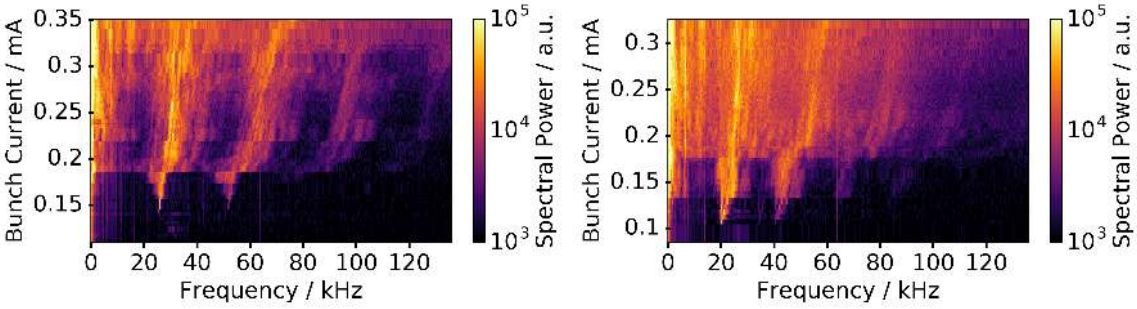

(g) $\alpha_c = 3.93 \cdot 10^{-4}$ (h) $\alpha_c = 2.90 \cdot 10^{-4}$

Figure A.4: Spectrograms showing the fluctuation frequencies of the emitted CSR power as a function of the bunch current were recorded with snapshot measurements at decreasing values of the momentum compaction factor. The momentum compaction factor α_c was stepwise changed between the measurements from $9.93 \cdot 10^{-4}$ to $2.90 \cdot 10^{-4}$.

A.5 Span of Low Bursting Frequency

As discussed in Subsection 7.2.3 the low bursting frequency corresponds to the repetition rate of the bursts in emitted CSR power. Figure 7.14 shows the extracted low bursting frequency as a function of bunch current for multiple different measurements with different values of Π. It is visible that for lower values of Π (shorter natural bunch length) the span between minimum and maximum frequency of the low bursting frequency over current is smaller than for higher values of Π.

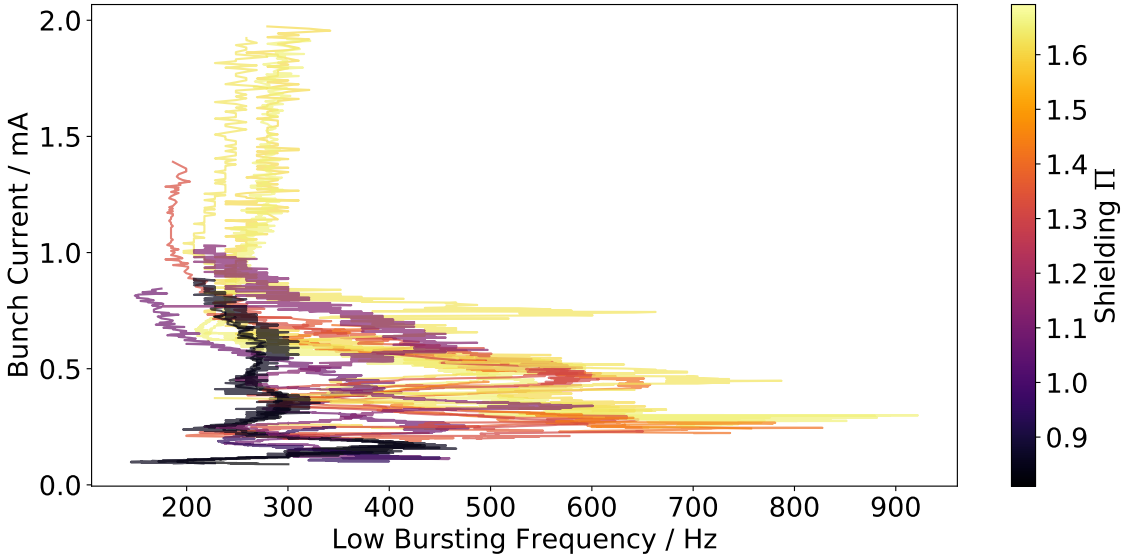

Figure A.5: Low bursting frequency as a function of bunch current for multiple measurements with different shielding parameter. The darker the color of the curve the lower the value of Π is.

A.6 Damping Time Dependency of Bunch Length Shrinking After Burst

In the second half of Section 7.3, the energy spread was used for the discussion of damping time-dependent effects in the micro-bunching instability. Especially the dependency of the low bursting frequency (corresponding to the repetition rate of the bursts in emitted CSR power) on the synchrotron radiation damping was studied. The discussions and calculations based on the minimal and maximal value of the energy spread at each bunch current, can be done equally well on the bunch length and yield the same results, which is shown in the following two figures.

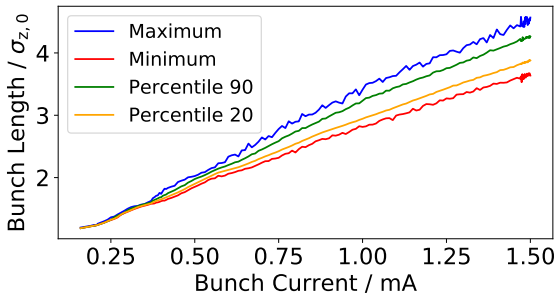

Figure A.6: The minimal and maximal bunch length as well as the 90th and 20th percentile of the bunch length at each bunch current as a function of the bunch current.

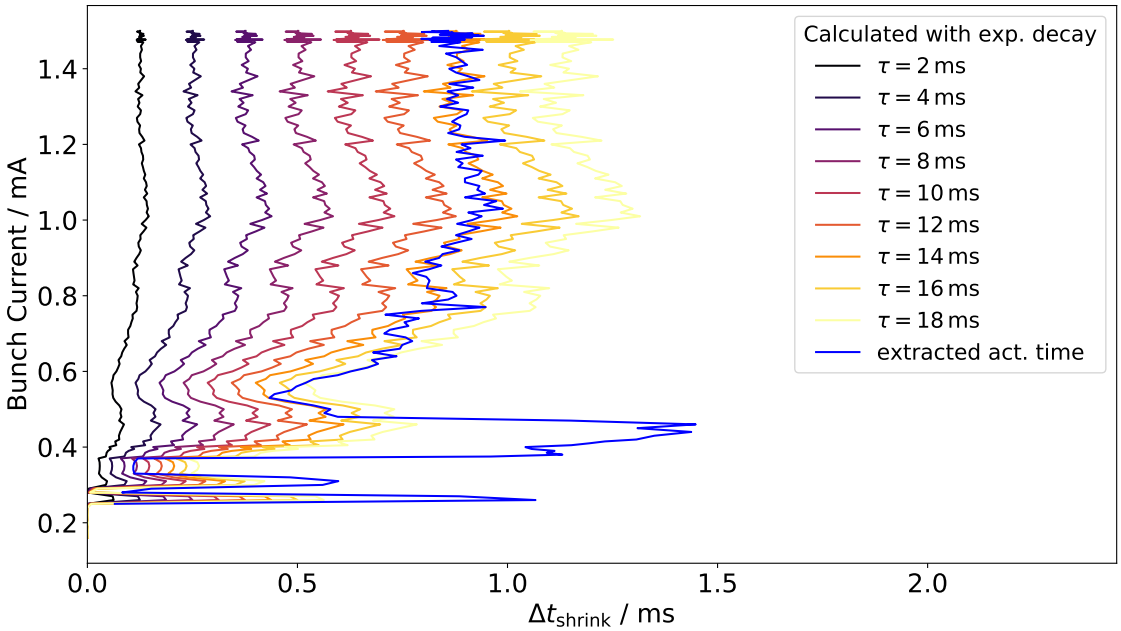

Figure A.7: Time it would take the bunch length to shrink down between bursts calculated based on the model that it is damped down from $\sigma_{z,\mathrm{max}}$ to $\sigma_{z,\mathrm{min}}$ with a pure exponential damping with damping time τ. For $\sigma_{z,\mathrm{max}}$ and $\sigma_{z,\mathrm{min}}$ the values displayed in Figure A.6 are used and the damping time is varied. Additionally, the actual shrinking time it took in the simulation was extracted with a Schmitt trigger and is displayed in blue. The simulation this is based on was run with a damping time of 9 ms.

A.7 Simultaneous Measurement with Two Schottky Diode Detectors

As described in Section 8.1, the fluctuations in the emitted CSR power were simultaneously measured with two waveguide-coupled Schottky diode detectors at different bunch currents. The following figures show the signal detected with the two detectors. As the detectors are sensitive for different frequency ranges (A: $140 - 220\,\mathrm{GHz}$ and B: $325 - 500\,\mathrm{GHz}$) difference are visible in the fluctuations.

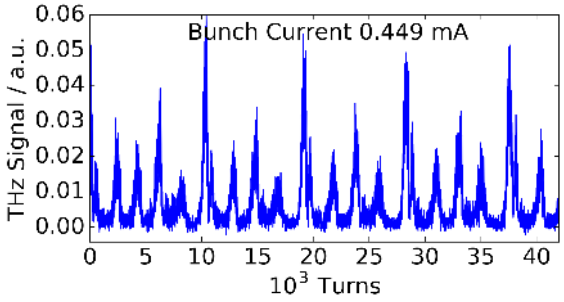

(a) 140 to 220 GHz

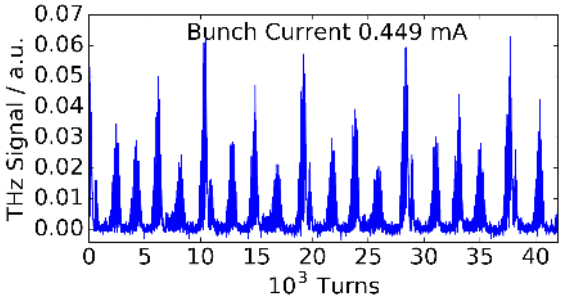

(b) 325 to 500 GHz

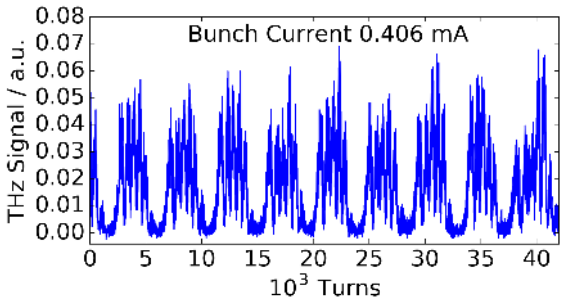

(c) 140 to 220 GHz

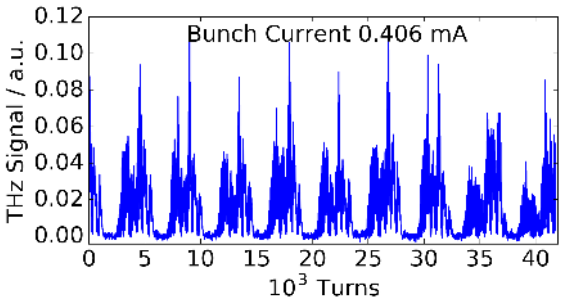

(d) 325 to 500 GHz

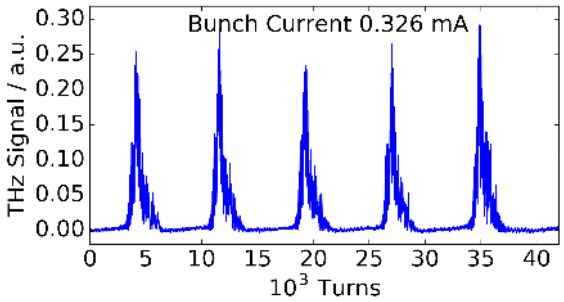

(e) 140 to 220 GHz

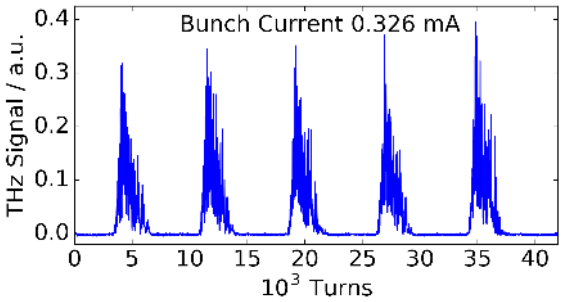

(f) 325 to 500 GHz

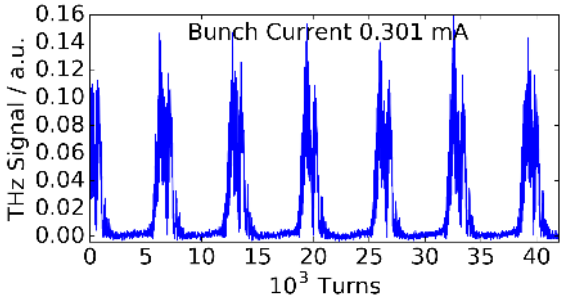

(g) 140 to 220 GHz

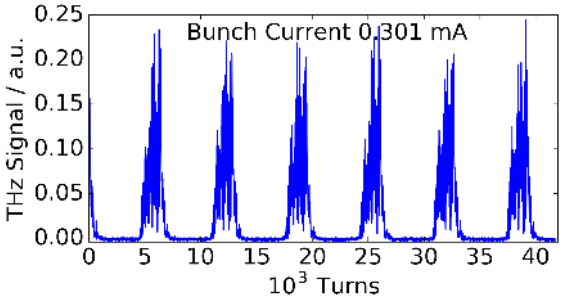

(h) 325 to 500 GHz

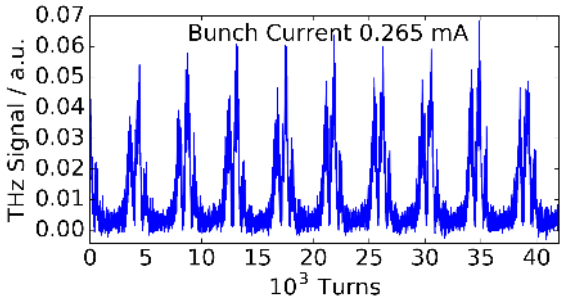

(i) 140 to 220 GHz

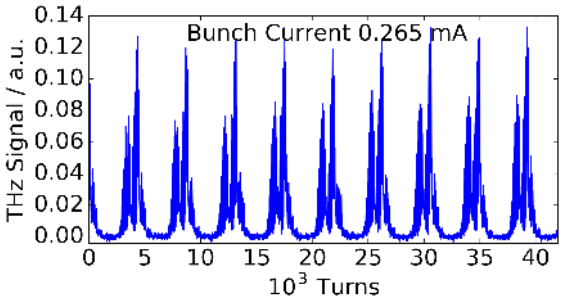

(j) 325 to 500 GHz

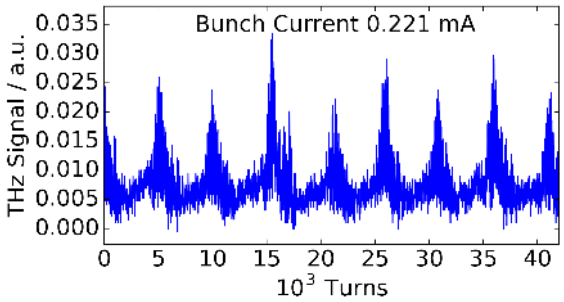

(k) 140 to 220 GHz

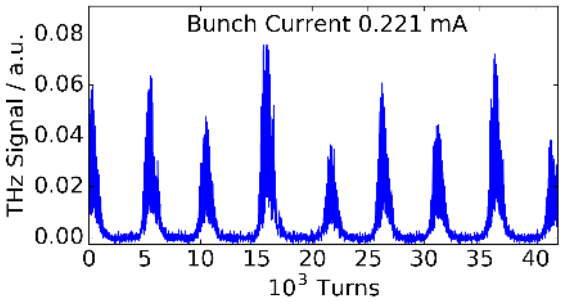

(l) 325 to 500 GHz

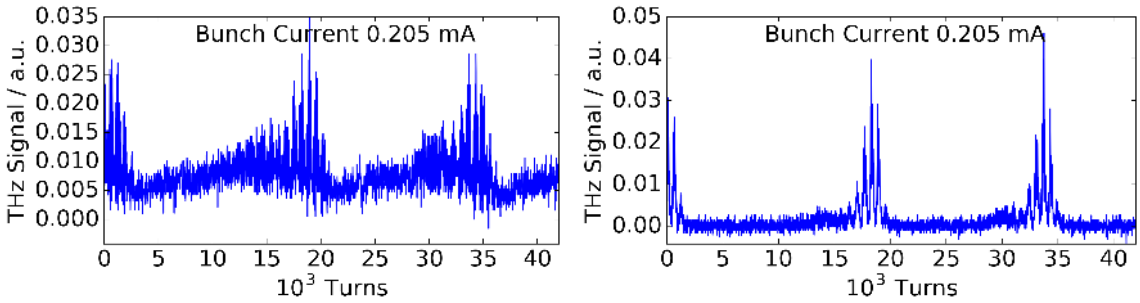

(m) 140 to 220 GHz

(n) 325 to 500 GHz

Figure A.8: CSR power per turn simultaneously detected with two waveguide-coupled Schottky diode detectors sensitive in different frequency ranges (A: $140 - 220\,\mathrm{GHz}$ and B: $325 - 500\,\mathrm{GHz}$). The signals displayed in the subfigures on the left hand side were measured with detector A and signals in the subfigures on the right hand side were measured with detector B, at different bunch currents.

A.8 Decay Measurement with the Schottky Diode Array

The on-chip Schottky diode array ([86], Section 8.1) was used as THz detector to measure the fluctuations in the emitted CSR power as a function of the decreasing bunch current. The following figures show the spectrograms calculated from the signals recorded with each of the eight detector channels of the diode array. The channels are sensitive in different frequency ranges and therefore recored the fluctuations in different parts of the emitted CSR spectrum. While all spectrograms show overall the same behavior, there are also some distinct differences visible in the relative power between different spectral components in each spectrogram.

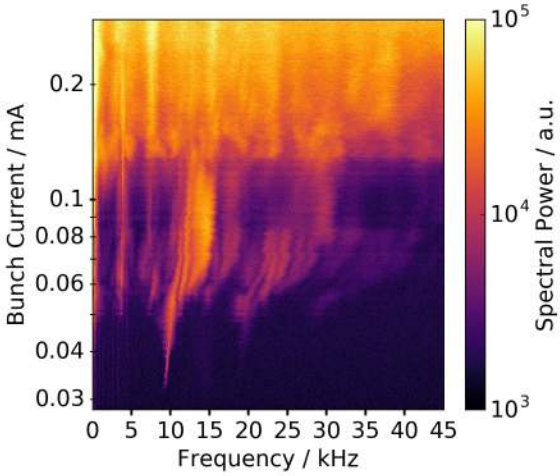

(o) 50GHZ

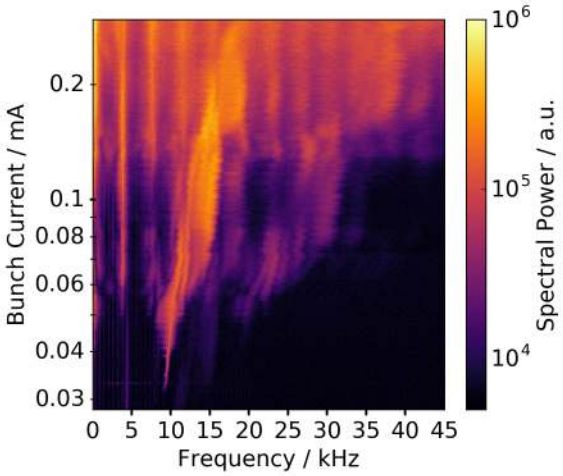

(p) 100GHZ

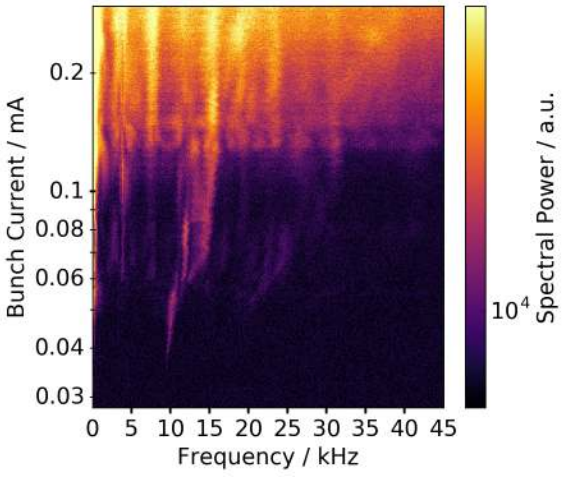

(q) 200GHZ

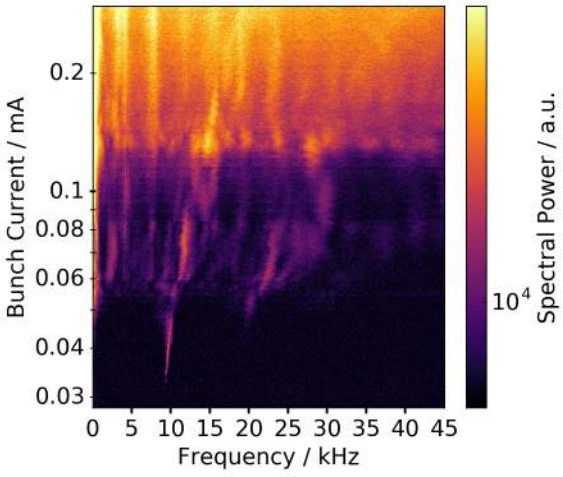

(r) 300GHZ

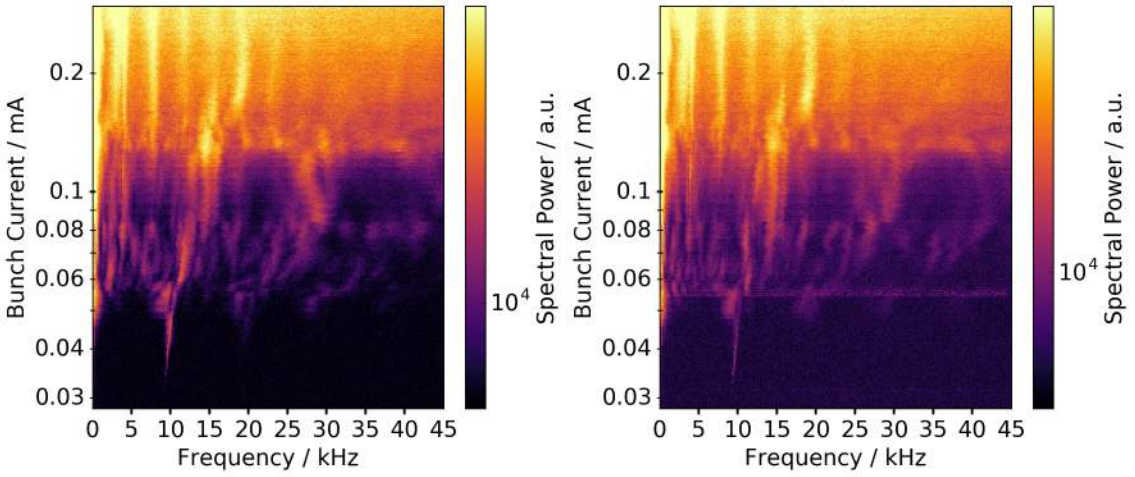

(s) 400GHZ

(t) 500GHZ

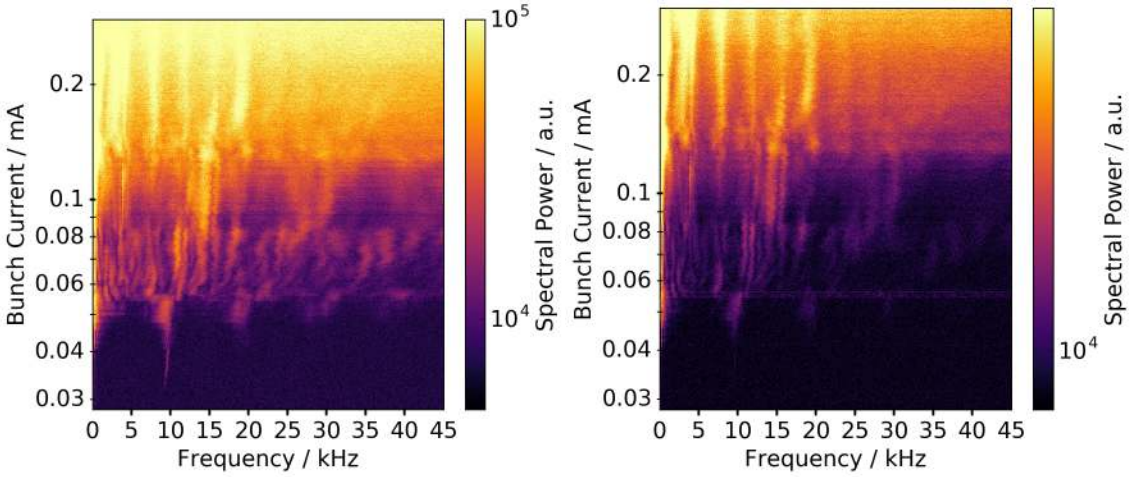

(u) 600GHZ

(v) 700GHZ

Figure A.9: Spectrograms of the fluctuation in the emitted CSR power detected simultaneously with the eight channels of the on-chip Schottky diode array from TU Dresden. (a) to (h) show the spectrograms for the different channels sensitive for frequencies from 50 GHz to 700 GHz.

A.9 Snapshot Measurements of Short-Bunch-Length Bursting

The following figures show snapshot measurements of the second region of instability caused by the weak instability (short-bunch-length bursting, Chapter 9) at different machine settings. The first measurement was taken at a slightly higher momentum compaction factor than the others. Between the other measurements, the acceleration voltage was increase step wise. In all measurements, the short-bunch-length bursting is visible as one dominant frequency line slightly below the bursting frequency of the main micro-bunching instability (visible at high bunch current in each measurement). The frequency increases with decreasing bunch current. In the last measurement (with the lowest value of Π, Figure A.14), the instability occurs over the biggest range in bunch current. Additionally a broadening of the dominant frequency line is visible around 0.03 mA which is not visible in the other measurements. At the same bunch current as the broadening also a low frequency component (≈ 130 Hz) is present, and can be seen when the frequency axis is displayed in a logarithmic scale (see Figure A.14b).

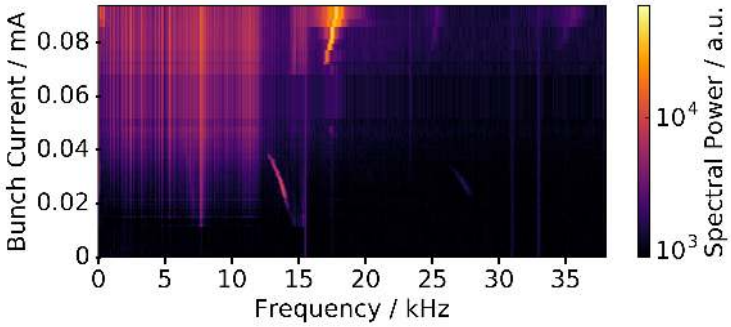

Figure A.10: Snapshot spectrogram of the short-bunch-length bursting at $V_{\mathrm{RF}} = 1500$ kV, $f_{\mathrm{s}} = 7.7$ kHz, and $\Pi = 0.81$.

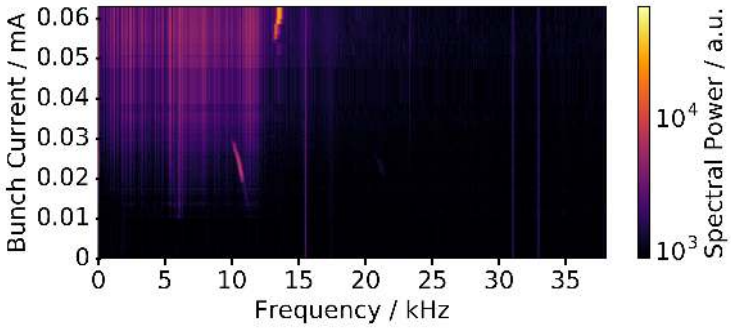

Figure A.11: Snapshot spectrogram of the short-bunch-length bursting at $V_{\mathrm{RF}} = 1200$ kV, $f_{\mathrm{s}} = 6.11$ kHz, and $\Pi = 0.80$.

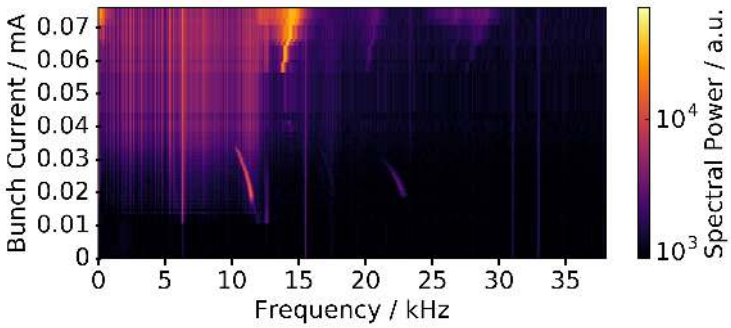

Figure A.12: Snapshot spectrogram of the short-bunch-length bursting at $V_{\mathrm{RF}} = 1300\,\mathrm{kV}$, $f_{\mathrm{s}} = 6.31\,\mathrm{kHz}$, and $\Pi = 0.76$.

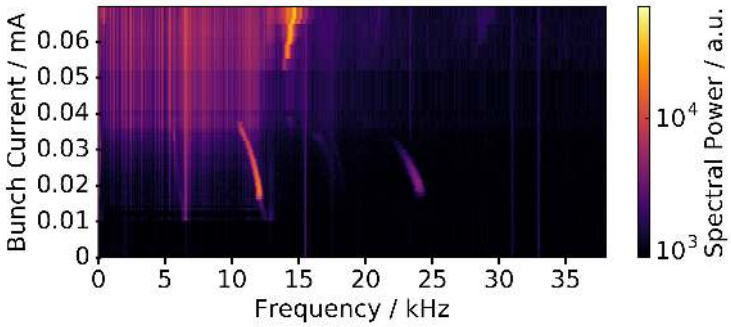

Figure A.13: Snapshot spectrogram of the short-bunch-length bursting at $V_{\mathrm{RF}} = 1400\,\mathrm{kV}$, $f_{\mathrm{s}} = 6.51\,\mathrm{kHz}$, and $\Pi = 0.73$.

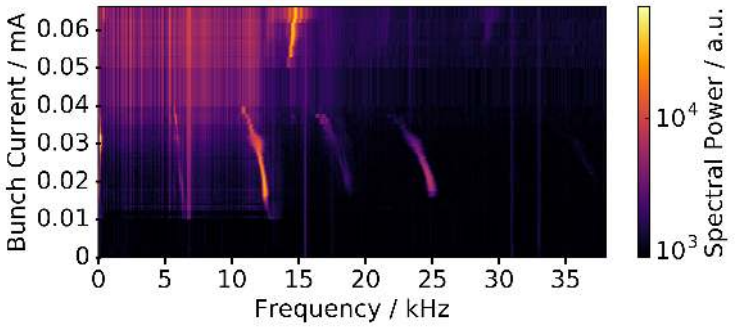

(a)

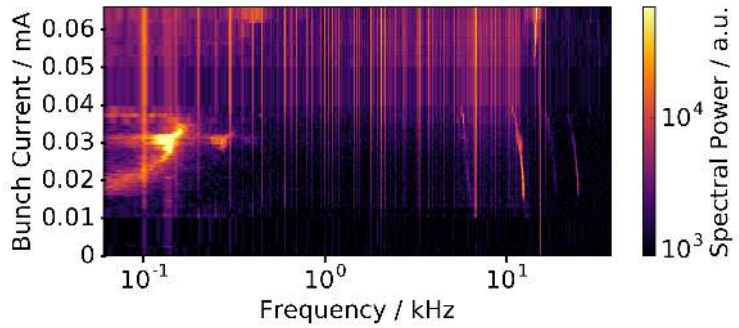

(b)

Figure A.14: Snapshot spectrogram of the short-bunch-length bursting at $V_{\mathrm{RF}} = 1500\,\mathrm{kV}$, $f_{\mathrm{s}} = 6.77\,\mathrm{kHz}$, and $\Pi = 0.71$.

A.10 Measurements of the Bursting Frequency in Multi-Bunch Fills

In the following figures, the bursting frequency of the bunches in a multi-bunch fill are displayed as a function of the initial bunch current of each individual bunch. The calculated spread of the bursting frequencies for the shown fills is given in Table 10.2. The measurements during the fills with number 6296, 6288, and 6292 show systematically a lower bursting frequency for bunches with a lower initial bunch currents (as described in Section 10.2). In fill 6283 and slightly also in fill 6258 the opposite direction of this behavior is visible. And fill 6212 shows not clear dependency.

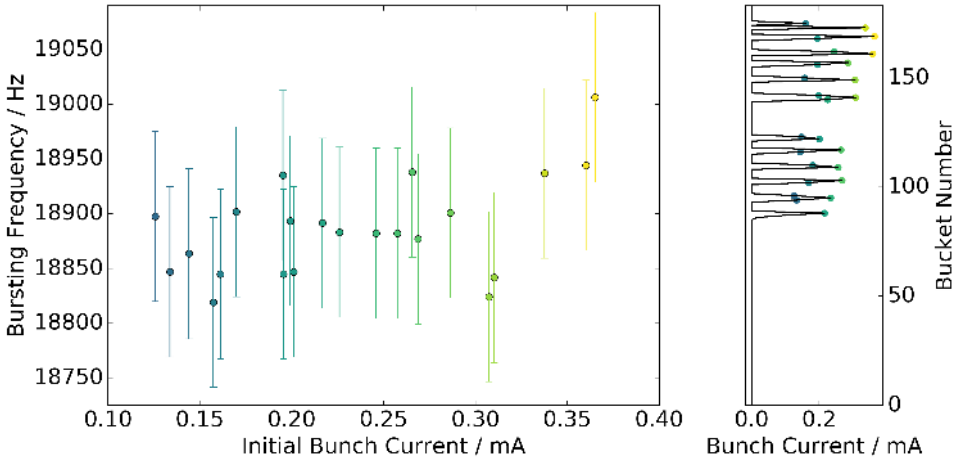

(a) Fill 6212

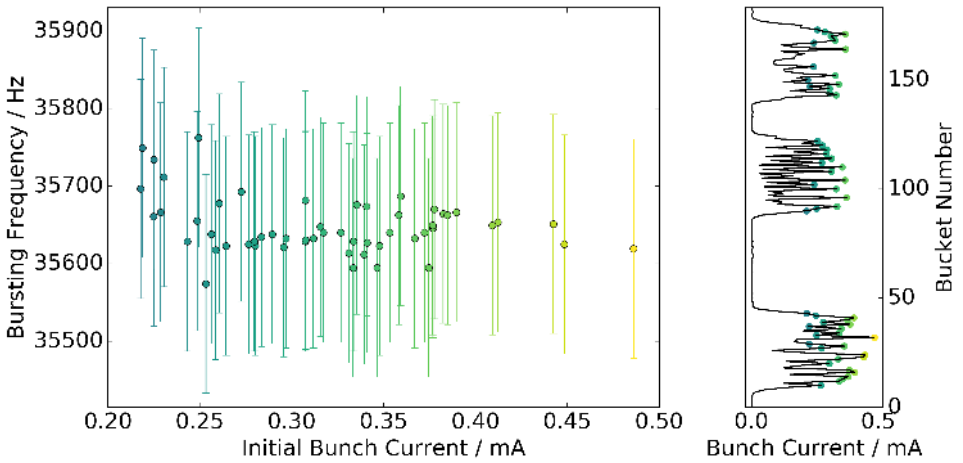

(b) Fill 6258

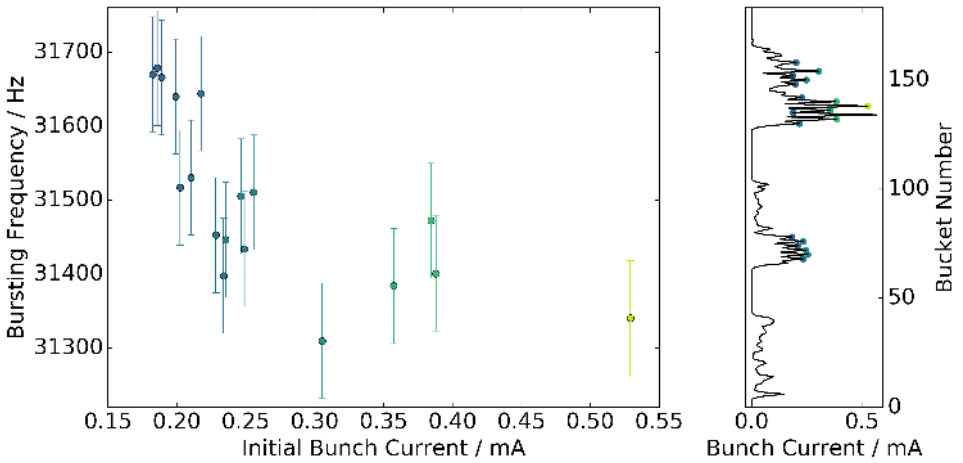

(c) Fill 6283

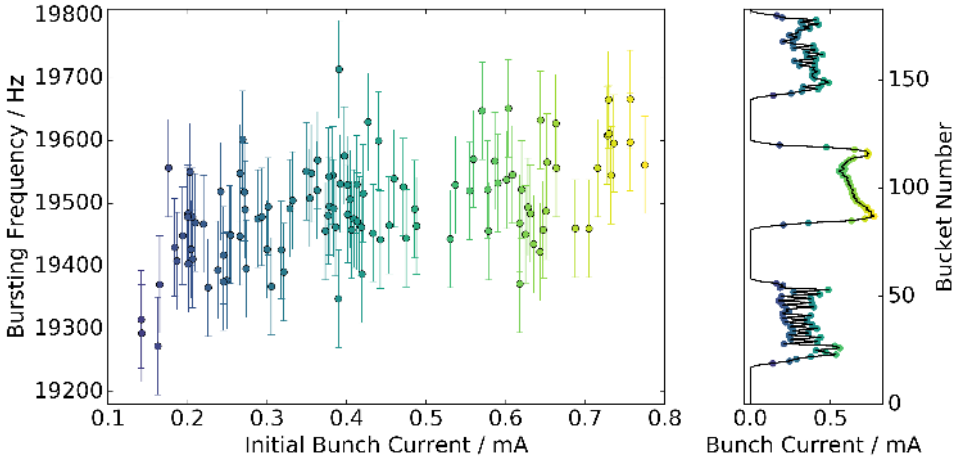

(d) Fill 6288

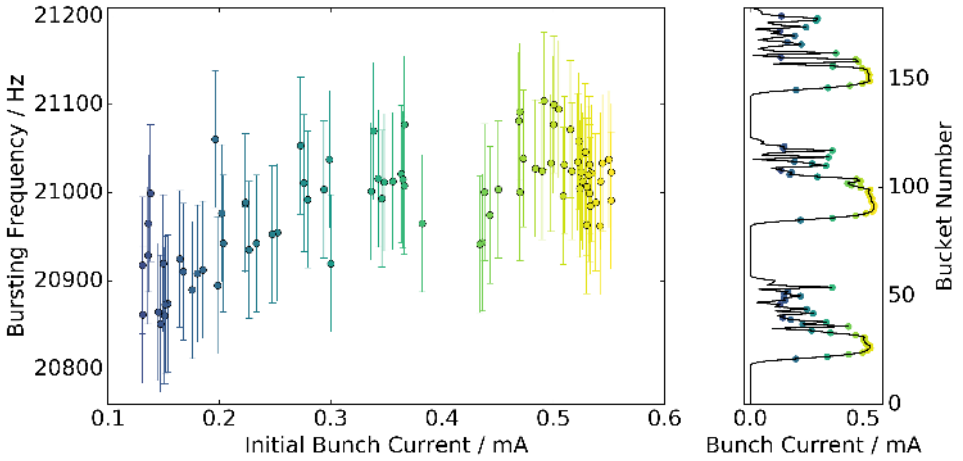

(e) Fill 6292

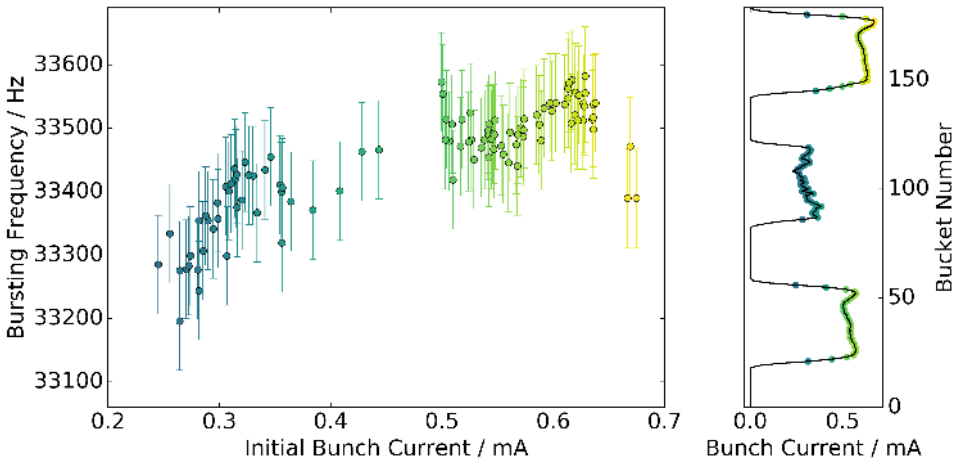

(f) Fill 6296

Figure A.15: Bursting frequency of each bunch in a multi-bunch fill as a function of the initial bunch current with the error bars indicating the average width of the frequency peak at the bursting threshold.

Publications

[Sch18c] P. Schönfeldt, P. Schreiber, M. Brosi, M. Blaicher, Julian, and J. Schestag. *Inovesa/Inovesa: Gamma Two*. 2018. DOI: 10.5281/zenodo.1321580.

[Sch17a] P. Schönfeldt, M. Brosi, M. Schwarz, J. L. Steinmann, and A.-S. Müller. "Parallelized Vlasov-Fokker-Planck solver for desktop personal computers". In: *Phys. Rev. Accel. Beams* 20 (3 2017), p. 030704. DOI: 10.1103/PhysRevAccelBeams.20.030704.

[Sch17b] P. Schönfeldt, M. Brosi, M. Schwarz, J. L. Steinmann, and A.-S. Müller. "Parallelized Vlasov-Fokker-Planck solver for desktop personal computers". In: *Phys. Rev. Accel. Beams* 20 (3 2017), p. 030704. DOI: 10.1103/PhysRevAccelBeams.20.030704.

[Bro16a] M. Brosi, J. L. Steinmann, E. Blomley, E. Bründermann, M. Caselle, N. Hiller, B. Kehrer, Y.-L. Mathis, M. J. Nasse, L. Rota, M. Schedler, P. Schönfeldt, M. Schuh, M. Schwarz, M. Weber, and A.-S. Müller. "Fast mapping of terahertz bursting thresholds and characteristics at synchrotron light sources". In: *Phys. Rev. Accel. Beams* 19 (11 2016), p. 110701. DOI: 10.1103/PhysRevAccelBeams.19.110701.

[Bol19a] T. Boltz, E. B. M. Brosi, B. Härer, A.-S. Müller, P. Schreiber, P. Schönfeldt, and M. Yan. "Perturbation of Synchrotron Motion in the Micro-Bunching Instability". In: *Proc. 10th International Partile Accelerator Conference (IPAC'19), Melbourne, Australia, 19-24 May 2019* (Melbourne, Australia). International Partile Accelerator Conference 10. Geneva, Switzerland: JACoW Publishing, 2019, pp. 108–111. ISBN: 978-3-95450-208-0. DOI: doi:10.18429/JACoW-IPAC2019-MOPGW018.

[Ste16] J. L. Steinmann, E. Blomley, M. Brosi, E. Bründermann, M. Caselle, J. L. Hesler, N. Hiller, B. Kehrer, Y.-L. Mathis, M. J. Nasse, J. Raasch, M. Schedler, P. Schönfeldt, M. Schuh, M. Schwarz, M. Siegel, N. Smale, M. Weber, and A.-S. Müller. "Frequency-Comb Spectrum of Periodic-Patterned Signals". In: *Phys. Rev. Lett.* 117 (17 2016), p. 174802. DOI: 10.1103/PhysRevLett.117.174802.

[Pap19] A. Papash, E. Blomley, T. Boltz, M. Brosi, E. Bründermann, S. Casalbuoni, J. Gethmann, E. Huttel, B. Kehrer, A. Mochihashi, A.-S. Müller, R. Ruprecht, M. Schuh, and J. Steinmann. "New Operation Regimes at the Storage Ring KARA at KIT". In: *Proc. 10th International Partile Accelerator Conference (IPAC'19), Melbourne, Australia, 19-24 May 2019* (Melbourne, Australia). International Partile Accelerator Conference 10. Geneva, Switzerland: JACoW Publishing, 2019, pp. 1422–1425. ISBN: 978-3-95450-208-0. DOI: doi:10.18429/JACoW-IPAC2019-TUPGW016.

[Keh18b] B. Kehrer, M. Brosi, J. L. Steinmann, E. Blomley, E. Bründermann, M. Caselle, S. Funkner, N. Hiller, M. J. Nasse, G. Niehues, L. Rota, M. Schedler, P. Schönfeldt, M. Schuh, P. Schütze, M. Weber, and A.-S. Müller. "Synchronous detection of longitudinal and transverse bunch signals at a storage ring". In: *Phys. Rev. Accel. Beams* 21 (10 2018), p. 102803. DOI: 10.1103/PhysRevAccelBeams.21.102803.

[Bro17a] M. Brosi, E. Blomley, E. Bründermann, M. Caselle, B. Kehrer, A. Kopmann, A.-S. Müller, L. Rota, M. Schedler, P. Schönfeldt, M. Schuh, M. Schwarz, J. L. Steinmann, and M. Weber. "Studies of the Micro-Bunching Instability in Multi-Bunch Operation at the ANKA Storage Ring". In: *Proc. of International Particle Accelerator Conference (IPAC'17), Copenhagen, Denmark, 14-19 May, 2017* (Copenhagen, Denmark). International Particle Accelerator Conference 8. Geneva, Switzerland: JACoW, 2017, pp. 3645–3648. ISBN: 978-3-95450-182-3. DOI: https://doi.org/10.18429/JACoW-IPAC2017-THOBA1.

[Keh17] B. Kehrer, E. Blomley, M. Brosi, E. Bründermann, N. Hiller, A.-S. Müller, M. J. Nasse, M. Schedler, P. Schönfeldt, M. Schuh, M. Schwarz, P. Schütze, N. Smale, and J. L. Steinmann. "Time-Resolved Energy Spread Studies at the ANKA Storage Ring". In: *Proc. of International Particle Accelerator Conference (IPAC'17), Copenhagen, Denmark, 14-19 May, 2017* (Copenhagen, Denmark). International Particle Accelerator Conference 8. Geneva, Switzerland: JACoW, 2017, pp. 53–56. ISBN: 978-3-95450-182-3. DOI: https://doi.org/10.18429/JACoW-IPAC2017-MOOCB1.

[Ste18c] J. L. Steinmann, M. Brosi, E. Bründermann, M. Caselle, S. Funkner, B. Kehrer, G. Nasse Micheal Niehues, L. Rota, P. Schönfeldt, M. Schuh, M. Siegel, M. Weber, and A.-S. Müller. "Turn-by-Turn Measurements for Systematic Investigations of the Micro-Bunching Instability". In: *Proc. of 60th ICFA Advanced Beam Dynamics Workshop on Future Light Sources (FLS2018), Shanghai, China, 5-9 March, 2018* (Shanghai, China). ICFA Advanced Beam Dynamics Workshop

on Future Light Sources 60. Geneva, Switzerland: JACoW, 2018. DOI: https://doi.org/10.18429/JACoW-FLS2018-TUP2WD03.

[Keh19a] B. Kehrer, M. Brosi, E. Bründermann, S. Funkner, A.-S. Müller, G. Niehues, M. Patil, M. Schuh, and J. Steinmann. "Turn-by-Turn Horizontal Bunch Size and Energy Spread Studies at KARA". In: *Proc. 10th International Partile Accelerator Conference (IPAC'19), Melbourne, Australia, 19-24 May 2019* (Melbourne, Australia). International Partile Accelerator Conference 10. Geneva, Switzerland: JACoW Publishing, 2019, pp. 2498–2500. ISBN: 978-3-95450-208-0. DOI: doi:10.18429/JACoW-IPAC2019-WEPGW016.

[Bie19] S. Bielawski, E. Blomley, M. Brosi, E. Bründermann, E. Burkard, C. Evain, S. Funkner, N. Hiller, M. J. Nasse, G. Niehues, E. Roussel, M. Schedler, P. Schönfeldt, J. L. Steinmann, C. Szwaj, S. Walther, and A.-S. Müller. "From self-organization in relativistic electron bunches to coherent synchrotron light: observation using a photonic time-stretch digitizer". In: *Scientific Reports* 9.1 (2019). DOI: 10.1038/s41598-019-45024-2.

[Nie18] G. Niehues, E. Blomley, M. Brosi, E. Bründermann, M. Caselle, S. Funkner, N. Hiller, A.-S. Müller, M. Nasse, L. Rota, M. Schuh, P. Schönfeldt, and M. Weber. "High Repetition Rate, Single-Shot Electro-Optical Monitoring of Longitudinal Electron Bunch Dynamics Using the Linear Array Detector KALYPSO". In: *Proc. 9th International Particle Accelerator Conference (IPAC'18), Vancouver, BC, Canada, April 29-May 4, 2018* (Vancouver, BC, Canada). International Particle Accelerator Conference 9. Geneva, Switzerland: JACoW Publishing, 2018, pp. 2216–2218. ISBN: 978-3-95450-184-7. DOI: doi:10.18429/JACoW-IPAC2018-WEPAL026.

[Cas14a] M. Caselle, M. Brosi, S. Chilingaryan, T. Dritschler, N. Hiller, V. Judin, A. Kopmann, A.-S. Müller, L. Petzold, J. Raasch, L. Rota, M. Siegel, N. Smale, J. Steinmann, M. Vogelgesang, M. Weber, and S. Wuensch. "A Picosecond Sampling Electronic 'KAPTURE' for Terahertz Synchrotron Radiation". In: *IBIC'14 Monterey, CA, USA*. 2014. URL: http://accelconf.web.cern.ch/AccelConf/IBIC2014/papers/moczb1.pdf.

[Cas14b] M. Caselle, M. Brosi, S. Chilingaryan, T. Dritschler, E. Hertle, V. Judin, A. Kopmann, A.-S. Müller, J. Raasch, M. Schleicher, M. Siegel, N. Smale, J. Steinmann, M. Vogelgesang, M. Weber, and S. Wuensch. "Commissioning of an Ultra-fast Data Acquisition System for Coherent Synchrotron Radiation Detection". In: *Proceedings of 2014 International Particle Accelerator Conference.*

2014, p. 3497. URL: http://accelconf.web.cern.ch/accelconf/IPAC2014/papers/thpme113.pdf.

[Cas17] M. Caselle, L. A. Perez, M. Balzer, A. Kopmann, L. Rota, M. Weber, M. Brosi, J. Steinmann, E. Bründermann, and A.-S. Müller. "KAPTURE-2. A picosecond sampling system for individual THz pulses with high repetition rate". In: *Journal of Instrumentation* 12.01 (2017), p. C01040. DOI: 10.1088/1748-0221/12/01/c01040.

[Bro14] M. Brosi. "Untersuchung des Burstingverhaltens von Synchrotronstrahlung im THz-Bereich". Master thesis. Karlsruhe, Deutschland: Karlsruhe Institute of Technology (KIT), 2014.

[Bro15] M. Brosi, M. Caselle, E. Hertle, N. Hiller, A. Kopmann, A.-S. Müller, P. Schönfeldt, M. Schwarz, J. L. Steinmann, and M. Weber. "Online Studies of THz-Radiation in the Bursting Regime at ANKA". In: *Proc. 6th International Particle Accelerator Conference (IPAC'15), Richmond, VA, USA, May 3-8, 2015* (Richmond, VA, USA). International Particle Accelerator Conference 6. Geneva, Switzerland: JACoW, 2015, p. 882. ISBN: 978-3-95450-168-7. DOI: https://doi.org/10.18429/JACoW-IPAC2015-MOPHA042.

[Ste18b] J. L. Steinmann, T. Boltz, M. Brosi, E. Bründermann, M. Caselle, B. Kehrer, L. Rota, P. Schönfeldt, M. Schuh, M. Siegel, M. Weber, and A.-S. Müller. "Continuous bunch-by-bunch spectroscopic investigation of the microbunching instability". In: *Phys. Rev. Accel. Beams* 21 (11 2018), p. 110705. DOI: 10.1103/PhysRevAccelBeams.21.110705.

[Jud14] V. Judin, M. Brosi, C. Caselle, E. Hertle, N. Hiller, A. Kopmann, A.-S. Müller, M. Schuh, N. Smale, J. Steinmann, and M. Weber. "Studies of Bursting CSR in Multi-bunch Operation at the ANKA Storage Ring". In: *Proceedings of 2014 International Particle Accelerator Conference*. 2014, p. 225.

[Bro18b] M. Brosi, J. Gethmann, A. Bernhard, B. Kehrer, A. Papash, P. Schönfeldt, P. Schreiber, J. L. Steinmann, and A.-S. Müller. "Studies of the Micro-Bunching Instability in the Presence of a Damping Wiggler". In: *Journal of Physics: Conference Series* 1067.6 (2018), p. 062017. URL: http://stacks.iop.org/1742-6596/1067/i=6/a=062017.

[Bro18a] M. Brosi, A. Bernhard, J. Gethmann, B. Kehrer, A.-S. Müller, A. Papash, P. Schreiber, P. Schönfeldt, and J. Steinmann. "Studies of the Micro-Bunching Instability in the Presence of a Damping Wiggler". In: *Proc. 9th International Particle Accelerator Conference (IPAC'18), Vancouver, BC, Canada, April*

29-May 4, 2018 (Vancouver, BC, Canada). International Particle Accelerator Conference 9. Geneva, Switzerland: JACoW Publishing, 2018, pp. 3273–3276. ISBN: 978-3-95450-184-7. DOI: doi:10.18429/JACoW-IPAC2018-THPAK029.

[Bro19a] M. Brosi, T. Boltz, E. Bründermann, S. Funkner, B. Kehrer, A.-S. Müller, M. Nasse, G. Niehues, M. Patil, P. Schreiber, P. Schönfeldt, and J. Steinmann. "Synchronous Measurements of Electron Bunches Under the Influence of the Microbunching Instability". In: *Proc. 10th International Partile Accelerator Conference (IPAC'19), Melbourne, Australia, 19-24 May 2019* (Melbourne, Australia). International Partile Accelerator Conference 10. Geneva, Switzerland: JACoW Publishing, 2019, pp. 3119–3122. ISBN: 978-3-95450-208-0. DOI: doi:10.18429/JACoW-IPAC2019-WEPTS015.

[Keh18a] B. Kehrer, E. Blomley, M. Brosi, E. Bründermann, A.-S. Müller, M. Schuh, P. Schönfeldt, and J. Steinmann. "Filling Pattern Measurements Using Dead-Time Corrected Single Photon Counting". In: *Proc. 9th International Particle Accelerator Conference (IPAC'18), Vancouver, BC, Canada, April 29-May 4, 2018* (Vancouver, BC, Canada). International Particle Accelerator Conference 9. Geneva, Switzerland: JACoW Publishing, 2018, pp. 2219–2222. ISBN: 978-3-95450-184-7. DOI: doi:10.18429/JACoW-IPAC2018-WEPAL027.

[Keh16] B. Kehrer, E. Blomley, M. Brosi, E. Bründermann, N. Hiller, A.-S. Müller, M. J. Nasse, M. Schedler, P. Schönfeldt, M. Schuh, P. Schütze, N. Smale, and J. L. Steinmann. "Simultaneous Detection of Longitudinal and Transverse Bunch Signals at ANKA". In: *Proc. of International Particle Accelerator Conference (IPAC'16), Busan, Korea, May 8-13, 2016* (Busan, Korea). International Particle Accelerator Conference 7. Geneva, Switzerland: JACoW, 2016, pp. 109–111. ISBN: 978-3-95450-147-2. DOI: doi:10.18429/JACoW-IPAC2016-MOPMB014.

[Bro19b] M. Brosi, J. L. Steinmann, E. Blomley, T. Boltz, E. Bründermann, J. Gethmann, B. Kehrer, Y.-L. Mathis, A. Papash, M. Schedler, P. Schönfeldt, P. Schreiber, M. Schuh, M. Schwarz, A.-S. Müller, M. Caselle, L. Rota, M. Weber, and P. Kuske. "Systematic studies of the microbunching instability at very low bunch charges". In: *Phys. Rev. Accel. Beams* 22 (2 2019), p. 020701. DOI: 10.1103/PhysRevAccelBeams.22.020701.

[Bro16b] M. Brosi, E. Blomley, E. Bründermann, N. Hiller, B. Kehrer, A.-S. Müller, M. Schedler, M. Schuh, P. Schönfeldt, and J. L. Steinmann. "Systematic Studies of Short Bunch-Length Bursting at ANKA". In: *Proc. of International Particle Accelerator Conference (IPAC'16), Busan, Korea, May 8-13, 2016* (Busan,

Korea). International Particle Accelerator Conference 7. Geneva, Switzerland: JACoW, 2016, pp. 1662–1665. ISBN: 978-3-95450-147-2. DOI: doi:10.18429/JACoW-IPAC2016-TUPOR006.

[Bro17b] M. Brosi, E. Blomley, E. Bründermann, M. Caselle, B. Kehrer, A. Kopmann, A.-S. Müller, L. Rota, M. Schedler, P. Schönfeldt, M. Schuh, M. Schwarz, J. L. Steinmann, and M. Weber. "Studies of the Micro-Bunching Instability in Multi-Bunch Operation at the ANKA Storage Ring". In: *Proc. of International Particle Accelerator Conference (IPAC'17), Copenhagen, Denmark, 14-19 May, 2017*. JACoW, 2017, presentation slides. ISBN: 978-3-95450-182-3. DOI: https://doi.org/10.18429/JACoW-IPAC2017-THOBA1.

Bibliography

[1] J. M. Byrd et al. “Observation of Broadband Self-Amplified Spontaneous Coherent Terahertz Synchrotron Radiation in a Storage Ring”. In: *Physical Review Letters* 89.22 (2002).

[2] M Abo-Bakr et al. “Coherent emission of synchrotron radiation and longitudinal instabilities”. In: *Particle Accelerator Conference, 2003. PAC 2003. Proceedings of the*. Vol. 5. IEEE. 2003, pp. 3023–3025.

[3] W Shields et al. “Microbunch Instability Observations from a THz Detector at Diamond Light Source”. In: *Journal of Physics: Conference Series* 357.1 (2012), p. 012037. URL: http://stacks.iop.org/1742-6596/357/i=1/a=012037.

[4] A. Andersson et al. “Observation of coherent synchrotron radiation from a 1-mm electron bunch at the MAX-I storage ring”. In: (1999), pp. 77–87. DOI: 10.1117/12.366631.

[5] G. Wüstefeld et al. “Coherent THz Measurements at the Metrology Light Source”. In: *Proceedings of the 1st International Particle Accelerator Conference*. 2010, p. 2508.

[6] G. Carr et al. “Investigation of coherent emission from the NSLS VUV ring”. In: *Particle Accelerator Conference, 1999. Proceedings of the 1999*. Vol. 1. IEEE. 1999, pp. 134–136.

[7] B. Podobedov et al. “Sawtooth instability studies in the Stanford Linear Collider damping rings”. In: *Conf.Proc.* C970512 (1997), p. 1629.

[8] C Evain et al. “Spatio-temporal dynamics of relativistic electron bunches during the micro-bunching instability in storage rings”. In: *EPL (Europhysics Letters)* 98.4 (2012), p. 40006.

[9] U. Arp et al. “Spontaneous coherent microwave emission and the sawtooth instability in a compact storage ring”. In: *Phys. Rev. ST Accel. Beams* 4 (5 2001), p. 054401. DOI: 10.1103/PhysRevSTAB.4.054401.

[10] R. L. Warnock et al. “A General method for propagation of the phase space distribution, with application to the sawtooth instability”. In: *The physics of high brightness beams. Proceedings, 2nd ICFA Advanced Accelerator Workshop, Los Angeles, USA, November 9-12, 1999*. 2000, pp. 322–348. URL: http://www-public.slac.stanford.edu/sciDoc/docMeta.aspx?slacPubNumber=SLAC-PUB-8404.

[11] G. Stupakov et al. “Beam instability and microbunching due to coherent synchrotron radiation”. In: *Phys. Rev. ST Accel. Beams* 5 (5 2002), p. 054402. DOI: 10.1103/PhysRevSTAB.5.054402.

[12] M. Venturini et al. “Bursts of Coherent Synchrotron Radiation in Electron Storage Rings: a Dynamical Model”. In: *Physical Review Letters* 89 (2002), p. 224802.

[13] K. L. F. Bane et al. “Threshold studies of the microwave instability in electron storage rings”. In: *Phys. Rev. ST Accel. Beams* 13 (10 2010), p. 104402. DOI: 10.1103/PhysRevSTAB.13.104402.

[14] J. D. Jackson. *Classical Electrodynamics*. 2nd edition. John Wiley & Sons, Inc., 1975.

[15] H. Wiedemann. *Particle Accelerator Physics*. 4th. Springer International Publishing, 2015. DOI: 10.1007/978-3-319-18317-6.

[16] K. Wille. *Physik der Teilchenbeschleuniger und Synchrotronstrahlungsquellen*. B. G. Teubner Stuttgart, 1992.

[17] J. Liouville. “Note sur la Théorie de la Variation des constantes arbitraires”. In: *Journal de Mathématiques Pures et Appliquées, Sér. I, . (1838)* I.3 (1838), pp. 342–349.

[18] M. Sand. “The Physics of Electron Storage Rings: An Introduction”. In: *International School of Physics, Enrico Fermi, Course XLVI: Physics with Intersecting Storage Rings*. Vol. C6906161. 1969. URL: http://slac.stanford.edu/pubs/slacreports/reports02/slac-r-121.pdf.

[19] A.-S. Müller. *Physik der Teilchenbeschleuniger*. Vorlesungsfolien. 2012.

[20] J. Steinmann. “Strahldiagnose von kurzen Elektronenpaketen mit THz-Detektoren an Teilchenbeschleunigern”. Ph.D. thesis. Karlsruhe Institute of Technology, 2018. DOI: 10.5445/KSP/1000090017.

[21] K. W. Robinson. “Radiation Effects in Circular Electron Accelerators”. In: *Phys. Rev.* 111 (2 1958), pp. 373–380. DOI: 10.1103/PhysRev.111.373.

[22] H. Wiedemann. “Handbook of Accelerator Physics and Engineering”. In: ed. by A. W. Chao et al. 2nd. WORLD SCIENTIFIC, 2013. Chap. 3.1.4 Synchrotron Radiation in Storage Rings, pp. 220–223.

[23] H. Wiedemann. *Particle Accelerator Physics*. 3rd edition. Berlin, Heidelberg: Springer Verlag, 2007.

[24] A. W. Chao et al. *Handbook of Accelerator Physics and Engineering*. World Scientific Publishing Co. Pte. Ltd., 1999.

[25] K. Y. Ng. *Physics of intensity dependent beam instabilities*. Hoboken, NJ: World Scientific, 2006. ISBN: 9789812563422. DOI: 10.1142/5835.

[26] K. Ng et al. *Explicit expressions of impedances and wake functions*. Oct. 2010. DOI: 10.2172/1002001.

[27] J. B. Murphy et al. "Longitudinal wakefield for synchrotron radiation". In: *Proceedings Particle Accelerator Conference*. Vol. 5. 1995, 2980–2982 vol.5. DOI: 10.1109/PAC.1995.505757.

[28] J. Murphy et al. "Longitudinal Wakefield for an Electron Moving on a Circular Orbit". In: *Particle Accelerators* 57 (1997), pp. 9–64. URL: http://cds.cern.ch/record/1120287/files/p9.pdf.

[29] T. Agoh. "Steady fields of coherent synchrotron radiation in a rectangular pipe". In: *Phys. Rev. ST Accel. Beams* 12 (9 2009), p. 094402. DOI: 10.1103/PhysRevSTAB.12.094402.

[30] K. Y. Ng. *Physics of Intensity Dependent Beam Instabilities*. World Scientific, 2006.

[31] P. Schönfeldt. "Simulation and measurement of the dynamics of ultra-short electron bunch profiles for the generation of coherent THz radiation". Ph.D. thesis. http://dx.doi.org/10.5445/IR/1000084466: Karlsruhe Institute of Technology, 2018.

[32] P. Kuske. "Calculation of Longitudinal Instability Threshold Currents for Single Bunches". In: *Proceedings of ICAP2012, Rostock-Warnemünde, Germany. , 2012*. THSDC3. 2012. URL: accelconf.web.cern.ch/AccelConf/ICAP2012/papers/thsdc3.pdf.

[33] The HDF Group. *Hierarchical Data Format, version 5*. 1997-2019. URL: https://www.hdfgroup.org/HDF5/.

[34] J. Haïssinski. "Exact longitudinal equilibrium distribution of stored electrons in the presence of self-fields". English. In: *Il Nuovo Cimento* 18 (1 1973), pp. 72–82. ISSN: 0369-3554. DOI: 10.1007/BF02832640.

[35] K. L. F. Bane et al. "Impedance calculation and verification in storage rings". In: (2005). DOI: 10.5170/CERN-2005-006.143.

[36] P. Kuske. "CSR-driven Longitudinal Single Bunch Instability Thresholds". In: *Proceedings, 4th International Particle Accelerator Conference (IPAC 2013): Shanghai, China*. WEOAB102. 2013. URL: https://accelconf.web.cern.ch/accelconf/IPAC2013/papers/weoab102.pdf.

[37] KIT IBPT construction department. 2019.

[38] S. L. Kramer. "Direct observation of beam impedance above cutoff". In: *Phys. Rev. ST Accel. Beams* 5 (11 2002), p. 112001. DOI: 10.1103/PhysRevSTAB.5.112001.

[39] L. Præstegaard. "Investigations of the ANKA Injector: Lattice, Beam Properties and Performance". Ph.D. thesis. Denmark: University of Aarhus, 2001. URL: https://phys.au.dk/fileadmin/site_files/publikationer/phd/Lars_Praestegaard.pdf.

[40] E. Huttel et al. "OPERATION WITH A LOW EMITTANCE OPTICS AT ANKA". In: *Proceedings of 2005 Particle Accelerator Conference*. 2005.

[41] L. Wang et al. "Suppression of beam-ion instability in electron rings with multibunch train beam fillings". In: *Phys. Rev. ST Accel. Beams* 14 (8 2011), p. 084401. DOI: 10.1103/PhysRevSTAB.14.084401.

[42] C. Chang et al. "First Results of Energy Measurements with a Compact Compton Backscattering Setup at ANKA". In: *Proceedings of 2015 International Particle Accelerator Conference*. 2015, p. 876.

[43] C. Chang. "Precise determination of the electron beam energy with Compton backscattered laser photons at ANKA". Ph.D. thesis. Karlsruhe, Germany: KIT, 2016.

[44] Dimtel, Inc. URL: https://www.dimtel.com/ (visited on 12/04/2019).

[45] A. Hofmann et al. "Single Bunch Operation at ANKA: Gun Performance, Timing and First Results". In: *Proceedings of 2010 International Particle Accelerator Conference*. MOPD094. 2010, p. 924.

[46] Micro-Research Finland Oy. URL: www.mrf.fi (visited on 12/04/2019).

[47] M. Aicheler et al. *The Compact Linear Collider (CLIC) – Project Implementation Plan*. Ed. by M. Aicheler. CERN Yellow Reports: Monographs. 247 p. 2019. DOI: 10.23731/CYRM-2018-004.

[48] A. Bernhard et al. "A CLIC Damping Wiggler Prototype at ANKA: Commissioning and Preparations for a Beam Dynamics Experimental Program". In: *Proc. of International Particle Accelerator Conference (IPAC'16), Busan, Korea, May 8-13, 2016* (Busan, Korea). International Particle Accelerator Conference 7. doi:10.18429/JACoW-

IPAC2016-WEPMW002. Geneva, Switzerland: JACoW, 2016, pp. 2412–2415. ISBN: 978-3-95450-147-2. DOI: doi:10.18429/JACoW-IPAC2016-WEPMW002.

[49] J. Gethmann et al. "Non-Linear Beam Dynamics Studies of the CLIC Damping Wiggler Prototype". In: *Proc. of International Particle Accelerator Conference (IPAC'17), Copenhagen, Denmark, 14-19 May, 2017* (Copenhagen, Denmark). International Particle Accelerator Conference 8. Geneva, Switzerland: JACoW, 2017, pp. 3087–3090. ISBN: 978-3-95450-182-3. DOI: https://doi.org/10.18429/JACoW-IPAC2017-WEPIK068.

[50] B. Kehrer. "Time-resolved studies of the micro-bunching instability at KARA". PhD thesis. Karlsruher Institut für Technologie (KIT), 2019. 143 pp. DOI: 10.5445/IR/1000098584.

[51] E. Hertle et al. "First Results of the new bunch-by-bunch feedback system at ANKA". In: *Proceedings of 2014 International Particle Accelerator Conference*. 2014, p. 1739. DOI: 10.18429/JACoW-IPAC2014-TUPRI074.

[52] E. Blomley et al. "Beam Studies with a New Longitudinal Feedback System at the ANKA Storage Ring". In: *Proc. of International Particle Accelerator Conference (IPAC'16), Busan, Korea, May 8-13, 2016* (Busan, Korea). International Particle Accelerator Conference 7. Geneva, Switzerland: JACoW, 2016, pp. 2658–2660. ISBN: 978-3-95450-147-2. DOI: doi:10.18429/JACoW-IPAC2016-WEPOR001.

[53] P. Schütze. *Transversale Strahldynamik bei der Erzeugung kohärenter Synchrotronstrahlung*. BestMasters. Springer Spektrum, Wiesbaden, 2018. DOI: 10.1007/978-3-658-20386-3.

[54] Bergoz Instrumentation. URL: https://www.bergoz.com/ (visited on 06/26/2019).

[55] C. Sax. "Aufbau einer Messeinrichtung zur 2-D Charakterisierung von THz-Strahlprofilen". Bachelor thesis. Karlsruhe, Germany: Karlsruhe Institute of Technology, 2017.

[56] B Kehrer et al. "Visible Light Diagnostics at the ANKA Storage Ring". In: *Proceedings of 2015 International Particle Accelerator Conference*. 2015, p. 866. DOI: 10.18429/JACoW-IPAC2015-MOPHA037.

[57] PicoQuant. *PicoHarp 300 - Stand-alone TCSPC Module*. 2014. URL: http://www.picoquant.com/products/category/tcspc-and-time-tagging-modules/picoharp-300-stand-alone-tcspc-module-with-usb-interface.

[58] M. Patting et al. "Dead-time effects in TCSPC data analysis". In: *Proceedings of SPIE - The International Society for Optical Engineering* 6583 (May 2007), p. 658307. DOI: 10.1117/12.722804.

[59] L. Rota et al. “KALYPSO: A Mfps Linear Array Detector for Visible to NIR Radiation”. en-us. In: *Proceedings of the 5th Int. Beam Instrumentation Conf., IBIC2016, Barcelona, Spain* (2017). DOI: 10.18429/jacow-ibic2016-wepg46.

[60] N. Hiller. “Electro-Optical Bunch Length Measurements at the ANKA Storage Ring”. Ph.D. thesis. Karlsruhe, Germany: Karlsruhe Institute of Technology, 2013. DOI: 10.5445/IR/1000041159.

[61] S. Funkner et al. “High throughput data streaming of individual longitudinal electron bunch profiles”. In: *Physical Review Accelerators and Beams* 22.2 (2019), p. 022801. ISSN: 2469-9888. DOI: 10.1103/PhysRevAccelBeams.22.022801.

[62] L. Rota. “KALYPSO, a novel detector system for high-repetition rate and real-time beam diagnostics”. Ph.D. thesis. Karlsruhe: Karlsruhe Institute of Technology, 2018. DOI: 10.5445/IR/1000082349.

[63] A.-S. Müller et al. “Accelerator-Based THz Radiation Sources”. In: *Synchrotron Light Sources and Free-Electron Lasers: Accelerator Physics, Instrumentation and Science Applications*. Ed. by E. Jaeschke et al. Cham: Springer International Publishing, 2019, pp. 1–35. ISBN: 978-3-319-04507-8. DOI: 10.1007/978-3-319-04507-8_6-2.

[64] A.-S. Müller. “Accelerator-Based Sources of Infrared and Terahertz Radiation”. In: *Reviews of Accelerator Science and Technology* 3 (2010).

[65] Y.-L. Mathis et al. “Terahertz Radiation at ANKA, the New Synchrotron Light Source in Karlsruhe”. In: *Journal of Biological Physics* 29.2 (2003), pp. 313–318. ISSN: 1573-0689. DOI: 10.1023/A:1024429801191.

[66] A.-S. Müller et al. “Far Infrared Coherent Synchrotron Edge Radiation at ANKA”. In: *Synchrotron Radiation News* 19.3 (2006), pp. 18–24. eprint: https://doi.org/10.1080/08940880600755202. DOI: 10.1080/08940880600755202.

[67] Y.-L. Mathis et al. *Coherent Synchrotron Edge Radiation and Applications at ANKA*. Tech. rep. ISS Institute for Synchrotron Radiation, 2007. URL: http://www.uvsor.ims.ac.jp/WIRMS2007/UVSORWSonCSR/presentation/Mathis.pdf.

[68] P. F. Goldsmith. *Quasioptical Systems: Gaussian Beam Quasioptical Propogation and Applications*. IEEE, 1998. DOI: 10.1109/9780470546291.

[69] Advanced Compound Semiconductor Technologies (ACST) GmbH. URL: http://www.acst.de/ (visited on 07/09/2014).

[70] Advanced Compound Semiconductor Technologies (ACST) GmbH. *UWB Quasi-optical Detectors up to 2THz*. URL: http://www.acst.de/downloads/ACST_Flyer_Quasi_Optical_Detector.pdf.

[71] A. Semenov et al. “Schottky Diode Detectors for Monitoring Coherent THz Synchrotron Radiation Pulses”. In: *Proceedings, 5th International Particle Accelerator Conference (IPAC 2014): Dresden, Germany, June 15-20, 2014*. 2014. DOI: 10.18429/JACoW-IPAC2014-THPME097.

[72] Virginia Diodes, Inc. URL: http://vadiodes.com/ (visited on 07/09/2014).

[73] Python Software Foundation. *Python Language Reference, version 2.7*. URL: http://www.python.org.

[74] M. Schwarz et al. “Bursting Patterns of Coherent Synchrotron Radiation in the ANKA Storage Ring”. In: *Proceedings of 2013 International Particle Accelerator Conference*. 2013, p. 2516.

[75] T. Boltz. “Working title: On the Perturbation of Synchrotron Motion in the Micro-Bunching Instability”. In: *paper in preparation* (2020).

[76] B. E. Billinghurst et al. “Longitudinal bunch dynamics study with coherent synchrotron radiation”. In: *Phys. Rev. Accel. Beams* 19 (2 2016), p. 020704. DOI: 10.1103/PhysRevAccelBeams.19.020704.

[77] T. Boltz. *personal communication*. 2019.

[78] P. Kuske. “Short Bunches at the Transition From Strong to Weak Longitudinal Instability”. In: *Proc. of International Particle Accelerator Conference (IPAC'17), Copenhagen, Denmark, 14-19 May, 2017* (Copenhagen, Denmark). International Particle Accelerator Conference 8. https://doi.org/10.18429/JACoW-IPAC2017-THPAB007. Geneva, Switzerland: JACoW, 2017, pp. 3696–3699. ISBN: 978-3-95450-182-3. DOI: https://doi.org/10.18429/JACoW-IPAC2017-THPAB007.

[79] T. Boltz. “Comprehensive analysis of micro-structure dynamics in longitudinal electron bunch profiles”. MA thesis. Karlsruhe, [2017]. URL: http://dx.doi.org/10.5445/IR/1000068253.

[80] Y. Papaphilippou et al. “Conceptual Design of the CLIC damping rings”. In: *Proc. 3rd Int. Particle Accelerator Conf. (IPAC'12)*. TUPPC086. 2012, pp. 1368–1370. URL: http://accelconf.web.cern.ch/Accelconf/IPAC2012/papers/tuppc086.pdf.

[81] J. Gethmann. Ph.D. thesis. Karlsruhe Institute of Technology, 2019. Forthcoming.

[82] R. P. Walker. “Wigglers”. In: (1995). DOI: 10.5170/CERN-1995-006.807.

[83] K. L. F. Bane et al. “Simulations of the longitudinal instability in the SLC damping rings”. In: *Proc. 15th Particle Accelerator Conf. (PAC'93), Washington D.C., USA*. 1993, pp. 3339–3341. URL: accelconf.web.cern.ch/AccelConf/p93/PDF/PAC1993_3339.PDF.

[84] M. Borland. *elegant: A Flexible SDDS-Compliant Code for Accelerator Simulation*. Advanced Photon Source. 2000. URL: http://www.aps.anl.gov/Accelerator_Systems_Division/Accelerator_Operations_Physics/manuals/elegant_latest/elegant.pdf.

[85] J Safranek. "Experimental determination of storage ring optics using orbit response measurements". In: *Nuclear Instruments and Methods in Physics Research Section A: Accelerators, Spectrometers, Detectors and Associated Equipment* 388.1 (1997), pp. 27–36. ISSN: 0168-9002. DOI: https://doi.org/10.1016/S0168-9002(97)00309-4.

[86] M. Laabs et al. "On-chip THz spectrometer for bunch compression fingerprinting at fourth-generation light sources". In: *Journal of Synchrotron Radiation* 25.5 (2018), pp. 1509–1513. DOI: 10.1107/S1600577518010184.

[87] P. Schönfeldt et al. "Elaborated Modeling of Synchrotron Motion in Vlasov-Fokker-Planck Solvers". In: *Journal of Physics: Conference Series* 1067.6 (2018), p. 062025. URL: http://stacks.iop.org/1742-6596/1067/i=6/a=062025.

[88] K. W. Ormond et al. "Synchrotron oscillation driven by RF phase noise". In: *Proceedings of the 1997 Particle Accelerator Conference (Cat. No.97CH36167)*. Vol. 2. 1997, 1822–1824 vol.2. DOI: 10.1109/PAC.1997.751029.

[89] A.-S. Müller et al. "Studies of Bunch-bunch Interactions in the ANKA Storage Ring with Coherent Synchrotron Radiation using an Ultra-fast Terahertz Detection System". In: *Proceedings of IPAC*. 2013, p. 109. URL: http://accelconf.web.cern.ch/AccelConf/IPAC2013/papers/mopea019.pdf.

[90] M. Ries et al. "THz Bursting Thresholds Measured at the Metrology Light Source". In: *Proceedings of 2012 International Particle Accelerator Conference*. 2012, p. 3030.

[91] Y. Cai. "Scaling law of coherent synchrotron radiation in a rectangular chamber". In: *Phys. Rev. ST Accel. Beams* 17 (2 2014), p. 020702. DOI: 10.1103/PhysRevSTAB.17.020702.

[92] A.-S. Müller et al. "Investigation of Scraper Induced Wake Fields at ANKA". In: *Proc. 9th European Particle Accelerator Conf. (EPAC'04), Lucerne, Switzerland*. WEPLT069. 2004. URL: https://www.google.com/url?sa=t&rct=j&q=&esrc=s&source=web&cd=1&ved=2ahUKEwjgvqCJgMrhAhVE-qQKHX3yAKsQFjAAegQIAhAC&url=http%3A%2F%2Faccelconf.web.cern.ch%2Faccelconf%2Fe04%2FPAPERS%2FWEPLT069.PDF&usg=AOvVaw0csH25DiUidP99BLREFmER.

[93] A.-S. Müller et al. "Experimental Aspects of CSR in the ANKA Storage Ring". In: *Beam Dynamics Newsletter No. 57*. Ed. by Y. Cai et al. Vol. 57. International Committee for Future Accelerators, 2012.

[94] R. Warnock et al. “INTER-BUNCH COMMUNICATION THROUGH CSR IN WHISPERING GALLERY MODES”. In: *North American Particle Accelerator Conference 2013, At Pasadena, CA*. Oct. 2013. DOI: 10.13140/2.1.2725.9688.

[95] P. Schreiber. “Vergleich der zeitlichen Strukturen von Strahlungsausbrüchen der kohärenten Synchrotronstrahlung”. Bachelor thesis. Karlsruhe, Germany: Karlsruhe Institute of Technology, 2015.

Acknowledgements

I want to take this opportunity to thank everyone who was involved over the last years in the creation of this work and without whose support the completion of this thesis would not have been possible.

Many thanks to Prof. Anke-Susanne Müller for providing me with the opportunity to do my PhD thesis at KARA and facilitating that I can follow my research interests and present my work at so many meetings, workshops, and conferences.

I would like to thank Prof. Marc Weber for kindly taking on the role of the co-referent and also for all the comments provided for joint publications and this thesis.

Additionally, I want to thank Erik Bründermann who took care of a lot of administrative matters so I could concentrate on my research and who always had an friendly ear for my many questions.

I feel grateful for the support (financial and otherwise) of the Helmholtz International Research School for Teratronics (HIRST) which accompanied me through the years with the interesting and enriching HIRST seminars.

For one of the biggest contributions to the success of this thesis, my thanks go to the entire THz group (and all the people somehow attached to it ;-) who provided not only a pleasant and friendly but also a humorous and fun working atmosphere. Special thanks go to Marcel Schuh, Nigel Smale, and Edmund Blomley for their help as operators and in teaching me the operational tricks for KARA. I would like to thank Nicole Hiller, Stephan Funkner, and Gudrun Niehues for their EO expertise during synchronous measurements. My thanks also go to Julian Gethmann for the joint measurements with the CLIC wiggler. Many thanks to Yves-Laurent Mathis for providing the opportunity to use the IR beamlines, and Michael Süpfle for the friendly and competent technical support. I also want to thank Michele Caselle and Lorenzo Rota from IPE for the successful cooperation and their help by improving and debugging the KAPTURE systems.

For their awesome support the following colleagues deserve special thanks:
Johannes Steinmann for his infinite knowledge of everything concerning electronics and so much more. And also for the perfect alignment of the detectors at times when I didn't have the necessary calmness.

Patrik Schönfeldt for long discussions at any time, the endless support with Inovesa, even when I found yet another bug (sorry ... feature) and his expertise in evaluating EO data.

Benjamin Kehrer for his help with measurements, especially the PicoHarp measurements and for always ensuring that laughter echoes down the corridors.

Tobias Boltz for not going easy during our fruitful discussions on the mechanisms and dynamics of the micro-bunching instability.

And last but not least my office mate Patrick Schreiber for the many discussions and conversations on and off topic we had. Thank you that you always (easily) endured my stressed self and calmed my nerves and reassured me.

I am particularly indebted to my parents and my brother. This work would not have been possible without the sympathy, support, encouragement, and motivation that I have always received from you.

Thank You All!